

Graduate School of  
Systemic Neurosciences  
LMU Munich

## Functional Dissociation of Neural Circuits for Motion Vision in *Drosophila*

Georg Ammer

Dissertation at the  
Graduate School of Systemic Neurosciences at the  
Ludwig Maximilians-Universität München

23<sup>rd</sup> of August 2017



**Supervisor**

Prof. Dr. Alexander Borst

**Second Reviewer**

Prof. Dr. Herwig Baier

**Date of Defense**

June 5<sup>th</sup>, 2018



## ABSTRACT

Understanding how neural circuits of the brain perform fundamental computations is a central goal of neuroscience. A classic example of such a computation is the detection of visual motion, which is critical for all sighted animals to navigate the environment, avoid predators or detect conspecifics. More than half a century ago, algorithmic models were proposed that describe the computation of motion direction remarkably well. How this operation is implemented at the neuronal and biophysical level, however, remains elusive. The visual system of the fruit fly *Drosophila melanogaster* lends itself particularly well to addressing this question. Recent advances in genetic and anatomical methodology for *Drosophila* hold promise in mapping the neural elements and biophysical mechanisms to proposed algorithmic structures. Moreover, the small size of the fly brain makes it feasible to understand how the motion vision circuit interacts with parallel and downstream circuits to ultimately guide behavioral responses of the animal.

All of the studies presented in this cumulative thesis investigate the *Drosophila* motion vision circuit. In particular, they do so by addressing different mechanistic levels. In the first study, we identified T4 and T5 neurons as representing the direction-selective output stage of elementary ON and OFF motion detectors (**Manuscript 1**). This was followed by characterizing and assessing the functional contribution of their presynaptic input elements, with a focus on the ON motion pathway (**Manuscript 2**). Moreover, we tried to refine the algorithmic architecture of the motion detection circuit and assign specific neuronal cell types to the elements of that algorithmic structure (**Manuscripts 2,3**).

The second half of this thesis tries to relate the computation of motion direction to the challenges that this system faces during natural behavior of the fly. First, we asked how natural environments have shaped the properties of *Drosophila* ON and OFF motion detectors (**Manuscript 4**). Furthermore, we explored the functional interaction of the motion vision system with parallel visual circuits and the influence of these interactions on fly behavior (**Manuscripts 5,6**). Lastly, we investigated the evolutionary functional conservation of a single identified visual neuron across two fly species of different sizes (**Manuscript 7**). Taken together, the manuscripts contained in this thesis broaden our knowledge on how flies compute the direction of motion at several different levels – and might shed light onto how neural circuits compute in general.



## TABLE OF CONTENTS

1. Introduction .....	1
1.1 Understanding Brain Function .....	1
1.2 Motion Vision as a Model System for Studying Neural Computation.....	1
1.3 Tools for Investigating Neural Circuits .....	2
1.3.1 Genetic Dissection of Neural Circuits in <i>Drosophila</i> .....	2
1.3.2 Anatomical Reconstruction of Neural Circuits .....	5
1.4 Algorithmic Models of Motion Detection.....	6
1.5 Neural Circuits for Motion Detection in <i>Drosophila</i> .....	8
1.5.1 The ON Motion Pathway - Input Elements to T4 .....	11
1.5.2 Neural Circuits for OFF Motion Detection .....	13
1.6 Motion Vision and Behavior.....	15
1.6.1 Behavioral State-dependent Modulation of Motion Detection.....	15
1.6.2 Motion Detection in Natural Environments .....	16
1.7 Beyond Motion Detection Circuits.....	17
1.8 Comparative Studies of Neuronal Function .....	18
1.9 Conclusion .....	18
2. Manuscripts .....	21
Manuscript I: A Directional Tuning Map of <i>Drosophila</i> Elementary Motion Detectors.....	21
Manuscript II: Functional Specialization of Neural Input Elements to the <i>Drosophila</i> ON Motion Detector .....	33
Manuscript III: The Temporal Tuning of the <i>Drosophila</i> Motion Detectors Is Determined by the Dynamics of Their Input Elements .....	57
Manuscript IV: Asymmetry of <i>Drosophila</i> ON and OFF Motion Detectors Enhances Real-World Velocity Estimation .....	95
Manuscript V: Object Tracking in Motion-Blind Flies.....	123
Manuscript VI: Neural Mechanisms for <i>Drosophila</i> Contrast Vision .....	145
Manuscript VII: Preserving Neural Function under Extreme Scaling.....	179

<b>3. Discussion.....</b>	<b>193</b>
3.1 Defining the Algorithm of Motion Detection.....	193
3.2 Towards the Cellular Implementation of Motion Detection .....	195
3.3 Biophysical Implementation of the Core Computations.....	198
3.3.1 Temporal Delay Mechanism .....	198
3.3.2 Mechanism of Non-linear Input Interaction.....	200
3.4 Parallels with Direction-selective Circuits in the Mammalian Retina.....	201
3.5 Limitations of Current Anatomical and Genetic Tools .....	202
3.5.1 Tools for Blocking Synaptic Transmission.....	202
3.5.2 Connectomic Circuit Reconstruction .....	204
3.6 Downstream Circuits and Behavior .....	204
3.7 Visual Circuit Function during Natural Behavior.....	205
3.8 Conclusions and Outlook.....	206
<b>4. References.....</b>	<b>209</b>
<b>5. Supplements</b>	
Acknowledgements .....	221
List of Publications and Author Contributions .....	223
Curriculum Vitae.....	225
Affidavit .....	227

## LIST OF FIGURES

Figure 1. Algorithmic Models of Motion Detection .....	7
Figure 2. Anatomy of the <i>Drosophila</i> Visual System.....	9
Figure 3. Proposed Neural Implementation of the <i>Drosophila</i> ON Motion Detector .....	12
Figure 4. Neural Circuits and Temporal Properties of the OFF Motion Detector .....	14
Figure 5. The HR/BL Motion Detector Unites PD-Enhancement and ND-Suppression.....	194
Figure 6. An Improved Medulla Connectome Reveals Additional Inputs to T4 Cells.....	196



# 1. INTRODUCTION

## 1.1 Understanding Brain Function

Brains have evolved to transform information from the environment as well as the animal's internal state into appropriate behavioral actions. To understand how neural circuits of the brain perform this task is one of the central goals of neuroscience.

Between the reception of a sensory stimulus and a behavioral reaction, the brain usually performs a high number of complex operations. In order to understand brain function it is valuable to study these smaller building blocks – often referred to as computations – individually. One reason for this is that brains perform basic neural computations repeatedly – independent of sensory modality, processing hierarchy and even organism. Well-studied examples of such fundamental computations are linear filtering (Carandini et al., 2005), normalization (Carandini and Heeger, 2011) or decorrelation (Vinje and Gallant, 2000; Wiechert et al., 2010). The majority of this thesis revolves around the neural implementation of one such fundamental computation – the correlation of signals over time and space (Parise and Ernst, 2016). This operation is crucial for all circuits that detect visual motion, as the direction of motion is not represented explicitly at the photoreceptor level, but must be extracted by correlating signals from neighboring receptors (i.e. spatially) over time. Studying the neural circuits for motion detection thus holds promise for providing insight into how brains work in general.

## 1.2 Motion Vision as a Model System for Studying Neural Computation

Major insights into how brains perform neural computations often arise from studying simple innate behaviors or reflexes (Götz, 1964; Kandel, 2001; Marder and Goaillard, 2006). Neural circuits that detect the direction of motion are a good example for several reasons. First, motion detection is important for a multitude of survival-critical tasks such as visual navigation, predator avoidance, or detection of potential mating partners (Borst, 2014a; Mauss and Borst, 2017). Such essential behaviors are particularly robust and thus well suited for scientific investigation. Second, motion detection circuits, at least in invertebrates, are most likely hardwired and not subject to experience-dependent plasticity (Karmeier et al., 2001). This allows the exact same circuit to be studied in multiple individuals. Third, the problem of motion detection is at an intermediate level of complexity. It is complex enough that it can serve as

an example of a sophisticated neural computation, but still simple enough that a complete understanding, ranging from the circuit level down to biophysics, seems plausible within the next decade.

The study of fly vision has a long tradition (Exner, 1891). Clearly, a reason for this is that flies heavily rely on vision, which allows them to perform aerial maneuvers at rotational speeds up to 3000 degrees per second (Land and Collett, 1974). A well-studied visual behavior of flies is the so-called optomotor response. When a fly is tethered inside a cylindrical drum with a patterned surface and the drum is rotated in one or the other direction, the fly shows a turning response following the direction of motion (Fermi and Reichardt, 1963; Götz, 1964). This behavioral paradigm has been widely used to study several properties of the fly visual system such as its spatial tuning, contrast sensitivity or light adaptation (Dvorak et al., 1980; Pick and Buchner, 1979; Srinivasan and Dvorak, 1980). Only a few years later, nerve cells in the visual system of flies – the lobula plate tangential cells (LPTCs) – were discovered that respond to motion in a direction-selective way (Dvorak et al., 1975). These cells provided an entry point to the neural substrate of motion detection and their response properties have been characterized in great detail (Hausen, 1982; Hengstenberg, 1982). However, dissection of the neural elements that are upstream of these motion-sensitive interneurons and thus directly compute the direction of motion had to await the small fruit fly *Drosophila* to enter center stage.

### 1.3 Tools for Investigating Neural Circuits

Investigating the structure and function of a neural circuit critically depends on the available methodological tools. During the last decades, scientists have developed a vast array of such tools, both for functional and anatomical dissection of brain circuits, that are being widely used by the *Drosophila* community.

#### 1.3.1 Genetic Dissection of Neural Circuits in *Drosophila*

The fruit fly *Drosophila melanogaster*, thanks to its long tradition as a genetic model organism (Adams et al., 2000; Morgan, 1910; Rubin and Spradling, 1982), is a powerful animal system to study motion detection. The recent decade has witnessed the advent of a large variety of sophisticated tools to manipulate neural circuits at the cellular and subcellular level (Borst, 2009; Venken et al., 2011). Large libraries of fly lines, for example, based on the binary Gal4-UAS expression system, were generated that allow for a cell type-specific targeting of any genetically encodable tool of interest (Brand and Perrimon, 1993; Jenett et al., 2012; Kvon et

al., 2014; Pfeiffer et al., 2008). This system uses heterologous expression of the yeast transcription factor Gal4 driven by an endogenous enhancer fragment. Hence, the enhancer fragment's activity determines the spatial and temporal specificity of Gal4 expression. A second transgene, the so-called reporter or effector gene, is under the control of an upstream-activating-sequence (UAS) which is recognized by Gal4. Thereby, this effector transgene is only expressed in the subset of cells that expresses Gal4. Recently, complementary binary expression systems that are either orthogonal to the Gal4-UAS system or allow intersectional genetic strategies were developed to increase the versatility of these tools (Lai and Lee, 2006; Luan et al., 2006).

Effector genes can come in a variety of different flavors and can be as simple as fluorescent proteins for visualization of cell morphology (Chalfie et al., 1994). Of special importance for neuroscientists are proteins that interfere with the electrical signaling or synaptic release of neurotransmitters and thereby silence their output. One of these tools, Tetanus toxin (TNT), cleaves synaptobrevin, which is an essential component of the SNARE complex that is necessary for synaptic vesicle release (Sweeney et al., 1995). Tetanus toxin is highly potent since a single toxin molecule can cleave multiple targets. However, it was reported that some synapses are resistant to TNT (Rister and Heisenberg, 2006). Expression of the transgene shibire<sup>ts</sup> also blocks the release of neurotransmitters but by a different mechanism (Kitamoto, 2001). Shibire<sup>ts</sup> is a temperature-sensitive dominant negative allele of dynamin, a small GTPase that is required for vesicle reuptake. Overexpression of shibire<sup>ts</sup> thus interferes with neurotransmitter release by depleting the pool of synaptic vesicles. A major advantage of shibire<sup>ts</sup> is its temperature-sensitivity. This property renders it inefficient at low (permissive) temperatures, but effective at higher (restrictive) temperatures. Therefore, the same individual can be used for both control and inactivation experiments. Furthermore, such conditional manipulations are not susceptible to possible long-term compensation mechanisms. It must be taken into account, however, that both cellular physiology and behavior are highly temperature dependent. Neuronal activity can also be suppressed by overexpressing the inwardly rectifying potassium channel Kir2.1 that hyperpolarizes the cell (Baines et al., 2001). This is assumed to block not only chemical transmitter release, but also signaling through electrical synapses, as the hyperpolarization will spread through gap junctions.

In addition to the aforementioned transgenes, recently developed optogenetic actuators allow for a light-dependent control of the electrical activity of a cell with high temporal precision (Boyden et al., 2005; Feno et al., 2011). Optogenetic tools are light-sensitive ion channels (commonly channelrhodopsins) or ion pumps (e.g. halorhodopsin). Depending on

the ion selectivity of the protein, they can have either an inhibitory or excitatory effect. A key advantage of channelrhodopsins over the previously mentioned tools is that their gating by light permits a millisecond-precise control of neural activity. However, the light must be delivered to the region of interest and visible light, if detected by the photoreceptors of the animal, can interfere with visual behaviors. To circumvent this problem, channelrhodopsin variants were developed with absorption spectra outside of the visible wavelength range of *Drosophila* (Klapoetke et al., 2014; Lin et al., 2013).

Another methodological milestone for neuroscience has been the development and improvement of genetically encoded fluorescent sensors for calcium (Grienberger and Konnerth, 2012). Calcium can enter the cell directly through neurotransmitter receptors or through voltage-gated calcium channels. The calcium concentration of a cell can thus be used as a proxy for the activity of a neuron. Cell type-specific expression of calcium indicators can therefore be employed to optically monitor the activity of a subset of neurons or subcellular compartments (Akerboom et al., 2012; Chen et al., 2013; Mank et al., 2008). The microscopic method of choice for calcium imaging is two-photon excitation microscopy (Denk et al., 1990). Here, two low energy photons with a wavelength in the infrared spectrum are absorbed quasi-simultaneously by the fluorophore, which then emits fluorescence in the visible range. Due to the quadratic relationship between the simultaneous absorption of the two photons and the light intensity, the localization of excitation is restricted to the focal plane. This property, together with the fact that the excitation light is in the non-visible range, makes this microscopic technique ideally suitable for studying visual systems (Helmchen and Denk, 2005; Reiff et al., 2010). A key advantage of two-photon calcium imaging over whole-cell patch clamp recordings is that multiple cells can be imaged at once, and cells that are inaccessible to electrical recordings can be optically imaged. However, calcium indicators are inherently slow. They act as low-pass filters with time constants of hundreds of milliseconds, thus making it impossible to resolve fast events. Additionally, calcium is only a very indirect reporter of the neuron's membrane voltage, usually related to it in a non-linear fashion. Novel voltage-sensitive indicators are constantly improving in performance and start being used *in vivo*, but still suffer from poor signal-to-noise ratio (Cao et al., 2013; Yang et al., 2016).

Apart from tools to manipulate neural activity, the possibility to perturb the function of single genes cell type-specifically offers a variety of avenues for understanding neural computations. Genome-wide RNAi libraries, for example, allow for the cell type-specific knockdown of any protein of interest (Dietzl et al., 2007; Perkins et al., 2015). These resources have been widely used in *Drosophila* neuroscience (Pimentel et al., 2016; Yapici et al., 2008). However, off-target effects and partially low knockdown efficiency are confounding factors.

Great expectations rest on the recently developed CRISPR/Cas9 system for genome engineering ([Heidenreich and Zhang, 2016](#)). This approach allows for the targeted modification of any endogenous DNA sequence of interest and has already been successfully applied in many organisms including *Drosophila* ([Pankova and Borst, 2017](#); [Zhang et al., 2014](#)).

### 1.3.2 Anatomical Reconstruction of Neural Circuits

In addition to the wide array of genetic tools that are available to *Drosophila* researchers, a second advantage is the small size of its brain, which lies in the order of some hundred thousands of neurons. This permits a dense reconstruction of its anatomy by newly developed microscopy techniques. Maps of neural circuits have been assembled by using different approaches. Light microscopic imaging of single or few neurons at a time, and subsequent registration of these images onto a common reference brain have created mesoscopic maps, for example of the neural circuit for *Drosophila* courtship behavior ([Yu et al., 2010](#)). The gold standard, however, is to use electron microscopy (EM) which has a spatial resolution that is up to a hundred-times higher than that of light microscopy. Therefore, it allows for the dense reconstruction of very fine neuronal processes and the detection of individual synaptic contacts. The ultimate goal for neural circuit anatomists is the entire connectome of an organism – a map of all its neurons and all synaptic connections between them. The first nervous system to be completely reconstructed was that of the roundworm *Caenorhabditis elegans* that comprises only 302 neurons ([Varshney et al., 2011](#); [White et al., 1986](#)). The visual system of *Drosophila* alone, however, harbors more than two orders of magnitude more nerve cells, which makes its reconstruction a daunting task.

Two different methods for acquiring EM images are widely used in neuroanatomy ([Briggman and Bock, 2012](#)). Serial-section transmission electron microscopy (ssTEM) requires cutting the sample into thin sections, collecting them, scanning each of them individually with a transmission electron beam and subsequently registering them before tracing the neuronal connections ([Harris et al., 2006](#)). An alternative method is serial block-face scanning electron microscopy (SBF-SEM). Here, the block-face of the embedded sample is imaged and the backscattered electrons are detected. Either a diamond knife or a focused ion beam then removes a thin section of the sample before the next block-face is imaged. The sections that were previously imaged are lost and cannot, as with ssTEM, be imaged again. This cycle is repeated until the entire sample is scanned. Registration of SBF-SEM images is easier than that of ssTEM images as the block-face is always in the same orientation and not deformed. Furthermore, this process can be highly automated ([Denk and Horstmann, 2004](#);

Xu et al., 2017). Recent technological improvements have also allowed ssTEM to be automated by collecting the individual sections on a tape (Hildebrand et al., 2017; Kasthuri et al., 2015). The bottleneck for both connectomic approaches, however, is not the acquisition of images, but the tracing of the neurites. Manual tracing is very labor intense and limits the speed at which circuits can be reconstructed. Recently, the application of deep neural nets has greatly simplified reconstruction efforts and holds promise for future applications (Dorkenwald et al., 2017). The resultant dense anatomical maps of neural circuits can serve as powerful guides in formulating or excluding hypotheses about the function of neural circuits (Denk et al., 2012). This is especially true for the visual system of *Drosophila*, where large-scale projects have generated several circuit diagrams for substructures of the optic lobe (Rivera-Alba et al., 2011; Takemura et al., 2013). However, as discussed later in more depth, connectivity maps are necessarily incomplete and physiological studies are required to verify functional circuit architectures.

#### 1.4 Algorithmic Models of Motion Detection

Hypotheses about functional architectures that instruct experimental approaches need not only come from anatomical circuit structures. Historically, conceptual or algorithmic models have played and continue to play an at least equally important role (Exner, 1894; Hubel and Wiesel, 1962; McCulloch and Pitts, 1943). This is especially true for the quest of finding the neural implementation of motion detection. Visual motion is defined as the spatial displacement of a visual object (or stimulus) over time. Every circuit that detects motion must thus fulfill three key requirements: First, it needs to sample the environment with at least two spatially segregated sensors. Second, the signal coming from one of these inputs must be temporally delayed with respect to the other input. Finally, to generate direction selectivity, the signals originating from the two input lines must interact in a non-linear manner.

Two particularly successful models of motion detection that fulfill these requirements were historically described. Both of them belong to the class of so-called correlation-type motion detectors. The only difference between the two models lies in the nature of their non-linear operation and the location of the delayed and direct arm, respectively. The Hassenstein-Reichardt (HR) correlator was proposed following observations of the turning behavior of the beetle *Chlorophanus viridis* to apparent motion stimuli (Hassenstein and Reichardt, 1956). These experiments led the authors to suggest a model in which the non-linearity is multiplicative, thus leading to a non-linear amplification of motion signals in the preferred direction (PD) of the detector (**Figure 1A**). Subtraction of two mirror-symmetrical subunits of such a “half-detector” leads to a fully opponent direction-selective signal (**Figure 1B**). This

means that the detector responds positively if a stimulus moves to one direction and with a negative sign when it moves to the other direction. The Barlow-Levick (BL) model was proposed to explain the response properties of direction-selective ganglion cells (DSGCs) in the rabbit retina (Barlow and Levick, 1965). In contrast to the Hassenstein-Reichardt detector, it performs a suppression of motion signals in the non-preferred, or null, direction (ND) (Figure 1C). Even such simple models as the Hassenstein-Reichardt correlator describe several non-trivial aspects of fly visual behavior and electrophysiological signatures of motion-sensitive cells remarkably well (Borst et al., 2010). First, correlation-type motion detectors, unlike a speedometer, exhibit a velocity optimum at which the response of the detector is maximal. Furthermore, this optimum depends on the spatial structure of the visual stimulus. For a moving sine-wave grating, the optimal velocity is linearly dependent on the spatial wavelength of the grating such that the detector always responds maximally at a fixed temporal frequency. The Hassenstein-Reichardt detector makes several further non-intuitive predictions, for example a transient ringing response that is observed when a static grating starts moving instantaneously, as well as a velocity-dependent gain control mechanism. All these signatures of correlation-type motion detectors were experimentally confirmed in motion-sensitive neurons of the fly, making them powerful algorithmic models to guide experimental approaches (Borst, 2014b).

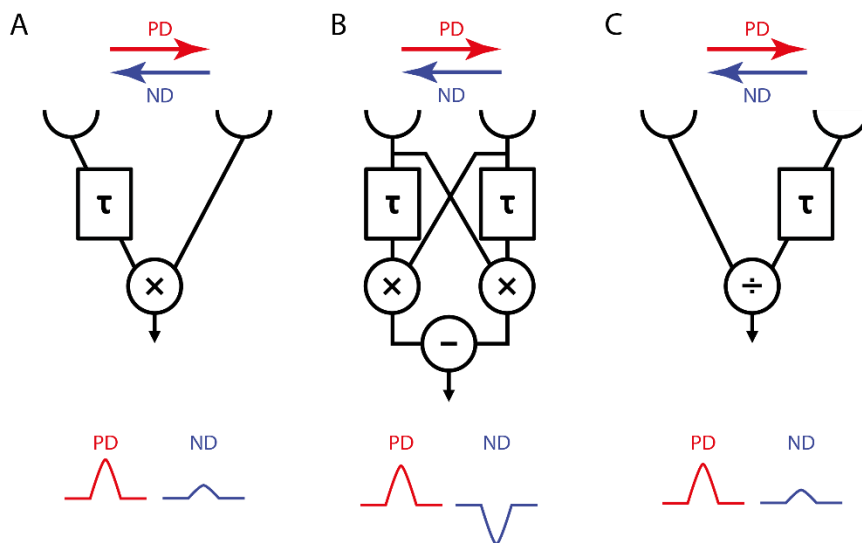


**Figure 1. Algorithmic Models of Motion Detection**

**(A)** The elementary subunit of the Hassenstein-Reichardt correlator generates direction-selective output by multiplying signals from a delayed ( $\tau$ ) and a direct input line which leads to an enhancement of signals moving in the preferred direction (PD).

**(B)** Subtraction of two mirror-symmetrical units of a Hassenstein-Reichardt half-detector generates a fully-opponent motion signal.

**(C)** The non-linear operation of the Barlow-Levick detector is divisive, leading to a suppression of signals moving in the null direction (ND). Note that the side of delayed line is flipped with respect to the Hassenstein-Reichardt detector.

Defining the algorithms that the brain uses to extract motion information from its visual environment is a valuable goal in itself. The Holy Grail, however, is to find a correspondence between computational modules and neural mechanisms in the brain. Fully describing the neural implementation of motion detection in the fly brain minimally requires the completion of the three following tasks:

- Identifying the cell types that constitute the detector (i.e. are necessary for generating a direction-selective signal)
- Uncovering the cellular and biophysical mechanisms that account for the asymmetrical temporal filtering
- Identifying the biophysical mechanisms that combine the input signals in a non-linear way to generate a direction-selective signal

## 1.5 Neural Circuits for Motion Detection in *Drosophila*

The neural circuits that compute motion direction reside in the optic lobes of the fly brain. The fact that the optic lobes are by far the largest sensory neuropils in the fly brain argues for the importance of this sensory modality for fly behavior and survival (**Figure 2A**). The optic lobe can be anatomically subdivided into five different neuropils: retina, lamina, medulla, lobula and lobula plate. Each of these neuropils exhibits a columnar structure, which is arranged retinotopically such that each column corresponds to one point in visual space (**Figure 2B**).

Motion vision begins when photons are absorbed by photoreceptors in the fly's retina. Of the eight photoreceptor subtypes found in *Drosophila*, only R1 to R6 contribute significantly to motion detection ([Heisenberg and Buchner, 1977](#); [Rister et al., 2007](#); [Yamaguchi et al., 2008](#)) (but see ([Wardill et al., 2012](#)), who reported a contribution of R7 and R8). These photoreceptors provide strong synaptic input via tetrad synapses to lamina monopolar cells L1 and L2 and somewhat weaker input to L3 cells ([Rivera-Alba et al., 2011](#)). Silencing synaptic output from L1 and L2 in conjunction renders flies completely blind to motion. Rescuing synaptic transmission from photoreceptors to L1 and L2 restores behavioral responses to motion stimuli ([Rister et al., 2007](#)). Thus, L1 and L2 together provide the major input to downstream motion detection circuits. At this stage, the motion vision circuit, similar as in the mammalian retina, splits into two parallel pathways. One of the pathways, fed by L1, is specialized in detecting moving brightness increments (ON motion) whereas the pathway postsynaptic to L2 extracts information about moving brightness decrements (OFF motion) ([Joesch et al., 2010](#)). The L3 pathway has long been speculated to be involved in the detection of form and color ([Bausenwein et al., 1992](#)). However, recent anatomical and functional studies found that neurons postsynaptic to L3 are involved in the detection of motion as well

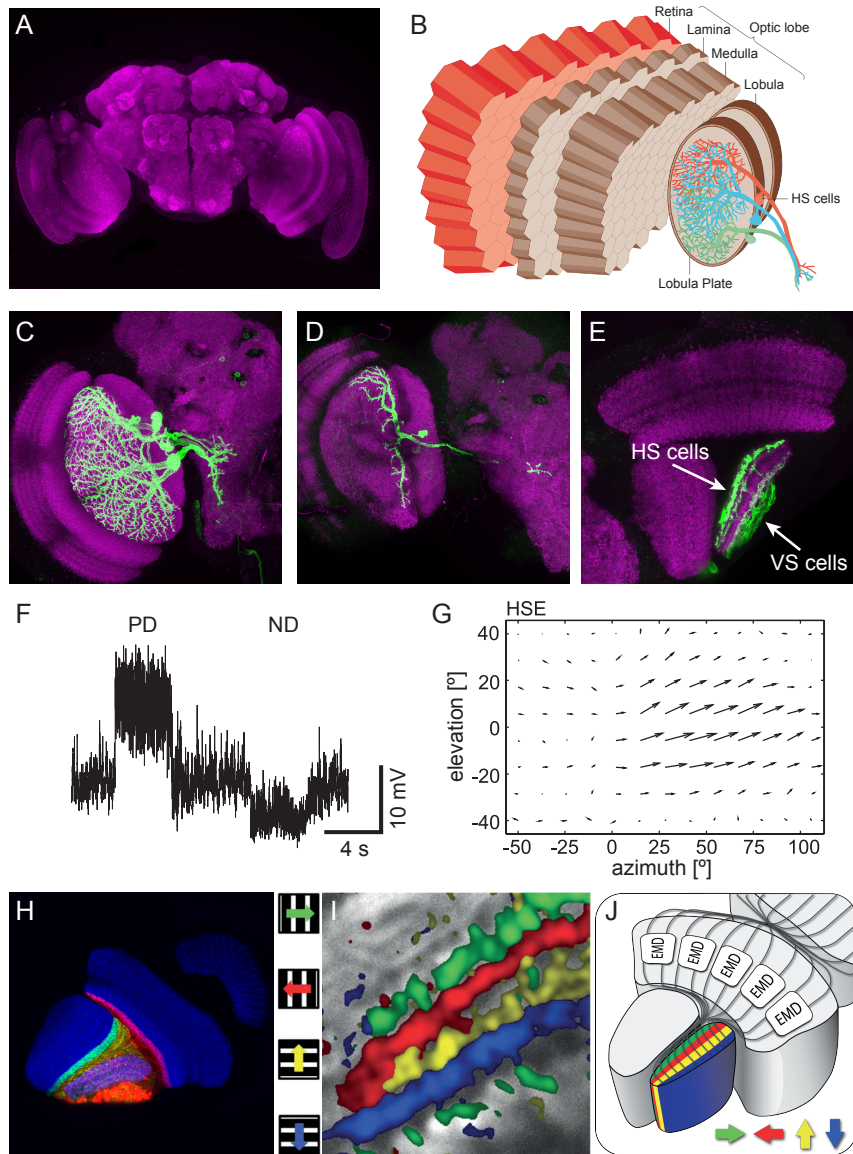


**Figure 2. Anatomy of the *Drosophila* Visual System**

(A) Frontal view of the *Drosophila* brain stained against the presynaptic marker nc82.

(B) Schematic of the fly optic lobe emphasizing the columnar structure of its distinct neuropils (from [Borst, 2014a](#) with permission).

(C) Optic lobe of a fly brain with multiple VS and HS cells labelled (green). Note the dendritic arbors that, together, span the whole lobula plate and the axon terminals arborizing in the central brain.

(D) Single-cell labelling of a putative VS6 cell depicting its large dendritic arbor.

(E) Horizontal section of the fly visual system with multiple VS and HS cells. Whereas VS cells mainly arborize in lobula plate layer 4, the dendrites of HS cells are restricted to layer 1.

(F) Electrophysiological response of a LPTC to motion in preferred direction (PD) and null direction (ND) revealing the motion opponency displayed by these cells.

(G) Receptive field of a *Drosophila* HSE cell. This cell would be maximally stimulated by a rotation of the fly along the yaw axis or by forward movement (from [Schnell et al., 2010](#)).

(H) T4 (red) and T5 (green) cells have their dendrites in the medulla and lobula, respectively, and project to the four layers of the lobula plate.

(I) T4 and T5 cells respond to different cardinal directions of motion, depending on their layer of projection in the lobula plate (from [Borst, 2014b](#)).

(J) Schematic of the fly visual system. Elementary motion detectors (EMD) tuned to different directions project to distinct lobula plate layers thus forming a directional tuning map (from [Mauss et al., 2017](#)).

(Shinomiya et al., 2014; Silies et al., 2013). In addition to L1, L2 and L3, also other lamina cells were shown to play a, mainly modulatory, role in motion detection (Meier et al., 2014; Tuthill et al., 2013; Tuthill et al., 2014). This is not surprising given the high degree of interconnectedness in the lamina neuropil (Rivera-Alba et al., 2011).

At the other end of the motion detection circuit in the lobula plate, only three synapses downstream of the lamina monopolar cells, reside the large lobula plate tangential cells (LPTCs), of which vertical system (VS) and horizontal system (HS) cells are the best-studied representatives. These cells project to the central brain and were the first direction-selective neurons to be described in the fly brain (Hausen, 1982; Hengstenberg, 1982; Joesch et al., 2008; Schnell et al., 2010) (**Figure 2C-E**). HS and VS cells are fully motion-opponent, in line with the responses of a full Hassenstein-Reichardt detector (**Figure 2F**). Different from all cells in their upstream circuit, LPTCs cover a large part of visual space and are tuned to the optic flow generated by ego-motion of the fly (Krapp and Hengstenberg, 1996) (**Figure 2G**). Notably, LPTCs that arborize in different layers of the lobula plate show different preferred directions. HS cells, with dendrites restricted to layer 1, respond preferentially to front-to-back motion. VS cells, which arborize mainly in layer 4, respond preferentially to downward motion. Furthermore, when using the uptake of radioactively labeled deoxyglucose as a measure for neural activity, the four layers of the lobula plate were labeled selectively when the fly was confronted with motion in one of the four cardinal directions (Buchner et al., 1984). Later, functional imaging of calcium in small dendritic branches of LPTCs revealed signals that were already direction selective (Single and Borst, 1998). This raised the hypothesis that LPTCs integrate signals from an array of presynaptic direction-selective small-field neurons.

Which cells are then presynaptic to LPTCs and provide them with direction-selective input? The T4 and T5 cells, described more than a hundred years ago (Cajal and Sanchez, 1915), have long been strong candidates for playing this role (**Figure 2H**). First, T4 and T5 cells both come in four different subtypes, each of which sends its axon only to one of the four layers of the lobula plate (Fischbach and Dittrich, 1989). Second, an electron microscopic study has identified synaptic connections between a T4 cell and an HS cell (Strausfeld and Lee, 1991). Third, blocking synaptic transmission from T4 and T5 cells together renders LPTCs unresponsive to moving gratings (Schnell et al., 2012).

The test of the assumption that T4 and T5 themselves are direction selective, however, had to await the development of tools for cell type-specific imaging of calcium activity in the fly visual system (see section on genetic tools above). Expressing the calcium indicator GCaMP5 selectively in T4 and T5 neurons led to the definitive proof that these cells are indeed

direction selective. In the first study presented in this thesis (**Manuscript 1** - ([Maisak et al., 2013](#))), we could show that each of the four subtypes of T4 and T5 cells responds, depending on its layer of projection in the lobula plate, maximally to one of the four cardinal directions. The directional preference of each of the subtypes is in agreement with earlier deoxyglucose labeling experiments of lobula plate layers ([Buchner et al., 1984](#)) (**Figure 2I-J**). Furthermore, T4 and T5 cells functionally segregate with respect to their contrast polarity preference. When imaging calcium responses from a specific T4 or T5 line, respectively, T4 cells responded selectively to moving bright edges whereas T5 cells responded mainly to moving dark edges. Thus, T4 and T5 represent the direction-selective output stages of the ON and OFF motion detection pathways. However, are these cells indeed necessary to drive direction-selective responses in downstream circuits? To address this question we performed experiments in which synaptic release of either T4 or T5 cells was blocked and the activity of postsynaptic LPTCs was measured electrophysiologically (**Manuscript 1** - ([Maisak et al., 2013](#))). These experiments revealed that T4 and T5 indeed provide the main, if not only, direction-selective input to downstream circuits.

### 1.5.1 The ON Motion Pathway - Input Elements to T4

Having identified T4 and T5 neurons as representing the output stage of ON and OFF elementary motion detectors, the next step was to identify and characterize the neurons that provide synaptic input to these cells. These inputs to T4 and T5 would be strong candidates for constituting the delayed and direct lines of the motion detector. Throughout this thesis, I focused on investigating the neural circuit for ON motion detection. Therefore, I will also discuss this pathway in more detail below.

Early anatomical studies have already speculated on the existence of at least two separate pathways in the *Drosophila* visual system ([Bausenwein et al., 1992](#)). One of these pathways starts from L1 and, via medulla cell Mi1, impinges onto T4. The second pathway goes from L2 via Tm1 to T5. A key advance in the anatomical description of the fly visual system has come from electron microscopic reconstructions of visual system subregions ([Rivera-Alba et al., 2011; Takemura et al., 2013](#)). Using serial-section TEM, Takemura and colleagues imaged and densely reconstructed a whole medulla column and many neighboring cells that provide synaptic input to this column ([Takemura et al., 2013](#)). In agreement with the early anatomical studies mentioned above, clustering analyses of this “medulla connectome” revealed three separate neural pathways (starting from lamina cells L1, L2 and L3 respectively), albeit with considerable crosstalk at early stages. Furthermore, this connectome identified medulla cells Mi1 and Tm3 as being postsynaptic to L1 and providing the majority

(> 85%) of input synapses to T4 cells (**Figure 3A**). When mapping the receptive fields of all Mi1 and Tm3 cells that synapse onto a single T4 cell into visual space, a small offset between the conjunctive receptive field centers of these cells, corresponding to 1° of visual space, was discovered (**Figure 3B**). This offset, calculated from Tm3 to Mi1, aligned with the preferred direction of postsynaptic T4 cells in 3 out of 4 cases. Since any motion detector requires a spatial segregation of its inputs, this finding led the authors to postulate that Mi1 and Tm3 represent the direct and delayed line of the *Drosophila* ON motion detector. Furthermore, it was concluded that a Barlow-Levick-like implementation would require Mi1 to be delayed with respect to Tm3, and a Hassenstein-Reichardt detector-like mechanism would require Tm3 to be delayed with respect to Mi1. Notably, a spatial segregation of only 1° of visual angle seems surprisingly small for a motion detector with such a high degree of direction selectivity as T4 ([Maisak et al., 2013](#)).

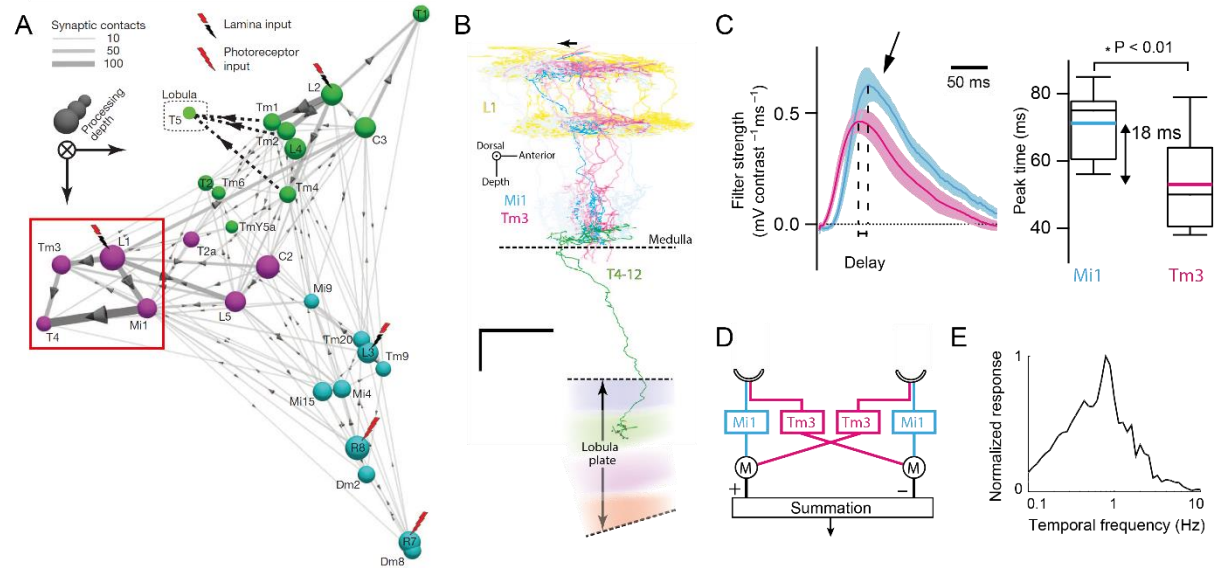


**Figure 3. Proposed Neural Implementation of the *Drosophila* ON Motion Detector**

**(A)** Wiring diagram of a single medulla column after ssTEM reconstruction as of 2013. The proposed neural substrate for ON motion detection is highlighted with a red box.

**(B)** EM reconstruction of major inputs to a given T4 cell. A small spatial offset between Mi1 and Tm3 inputs that aligns with the arborization layer in the lobula plate was reported.

**(C)** Linear temporal filters extracted for Mi1 and Tm3 cells. On average, the peak of the Mi1 filter was delayed by 18 milliseconds with respect to the Tm3 filter.

**(D)** Proposed architecture of the ON motion detector. Mi1 corresponds to the delayed and Tm3 to the direct line.

**(E)** Simulated temporal frequency tuning of the motion detector depicted in (D) after the subtraction stage. (A-B: modified from [Takemura et al., 2013](#); C-D: modified from [Behnia et al., 2014](#); with permission).

The visual response properties of Mi1 and Tm3 were subsequently measured using whole-cell patch-clamp recordings ([Behnia et al., 2014](#)). As expected from cells that receive their strongest input from L1, both cells responded with a depolarization to brightness

increments. More interestingly, the temporal filter properties, measured by using white noise stimuli followed by linear filter extraction, revealed a small difference in time to peak with Mi1 being delayed by 18 milliseconds with respect to Tm3 (**Figure 3C**). Taking into account the proposed anatomical offset between Mi1 and Tm3, the authors thus concluded that these cells correspond to the delayed and non-delayed line of a correlation-type motion detector. Thereafter, the authors used the experimentally determined filters for Mi1 and Tm3 as inputs to a Hassenstein-Reichardt correlation-type motion detector model, which resulted in a direction-selective detector with a temporal frequency optimum of 1Hz – similar to that of T4 cells (**Figure 3D,E**). However, it is important to note that this result was obtained only after subtraction of two half-detectors. The output of such a half-detector alone – which would correspond to a T4 cell – is in fact only weakly direction selective ([Salazar-Gatzimas et al., 2016](#)). Furthermore, the authors' conclusion is only correlative in nature. To verify this model requires experiments in which Mi1 and Tm3 cells are selectively removed from the circuit and the output of the motion detection circuit is measured. The proposed model leads to a very clear prediction for such experiments: Removing either Mi1 or Tm3 from the circuit should lead to a complete loss of direction selectivity under all conditions. We tested these predictions by silencing the neural activity of Mi1 or Tm3 and used electrophysiological responses of LPTCs and turning responses of walking flies as readouts of the motion detection circuit (**Manuscript 2 – (Ammer et al., 2015)**). The results of this study were inconsistent with the above-mentioned prediction and therefore challenge the proposed model.

### 1.5.2 Neural Circuits for OFF Motion Detection

Similar to the ON pathway, the neural components of the OFF pathway have been investigated in detail. Transmedulla cells Tm1, Tm2 and Tm4 are the strongest postsynaptic targets of lamina L2 cells ([Takemura et al., 2013](#)). Lamina cell L4 reciprocally connects to L2 and synapses onto Tm2 in an asymmetric manner ([Takemura et al., 2011](#)). An anatomical EM study that reconstructed cells presynaptic to T5 indeed found Tm1, Tm2 and Tm4 as inputs to T5. Quantitatively, Tm2 provides more input synapses than Tm1, and Tm4 is the weakest input ([Shinomiya et al., 2014](#)). Interestingly, in addition to these three cell types, T5 cells receive the strongest synaptic input from Tm9 cells, which themselves receive input mainly from L3 (**Figure 4A**). This is in agreement with functional studies, which suggest that multiple lamina cell types, including L3, provide input to the OFF motion detection pathway ([Jenett et al., 2012; Meier et al., 2014; Silies et al., 2013; Tuthill et al., 2013](#)). However, unlike for T4, the T5 inputs and their presynaptic partners were not reconstructed densely. Thus, their subcellular distribution on the T5 dendrite could not be remapped to their visual receptive fields, leaving any potential anatomical offset between these inputs unknown.

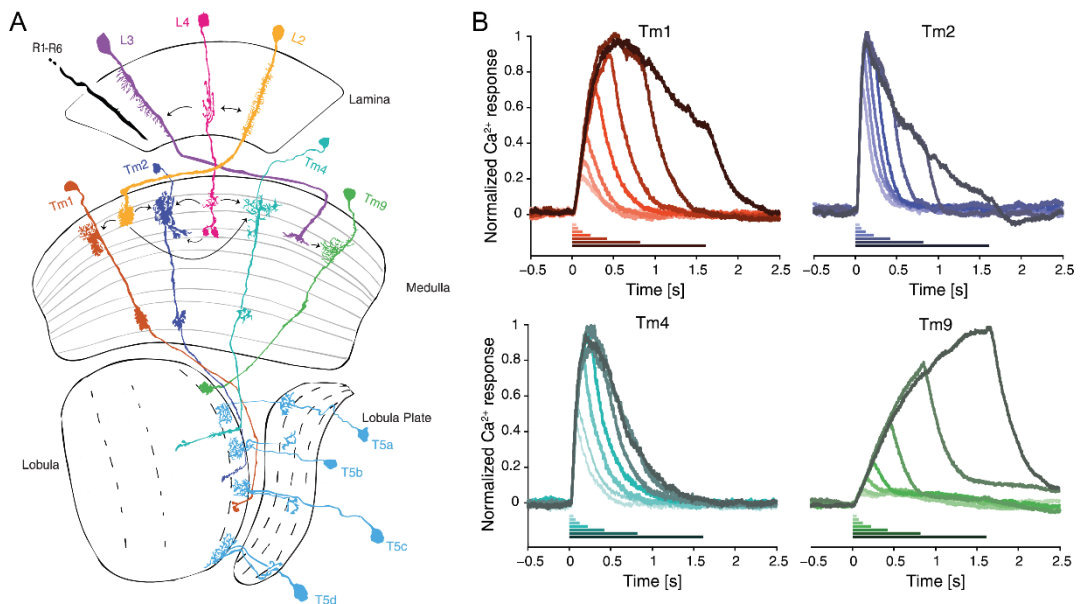


**Figure 4. Neural Elements and Temporal Properties of the *Drosophila* OFF Motion Detector**

(A) Schematic of the fly optic lobe with major neural elements of the OFF motion pathway. Note that every cell type exists in every column but is displayed only once for clarity.

(B) Temporal response properties of major inputs to T5 cells. Calcium responses to OFF steps of different durations are depicted.

(A-B from: [Serbe et al., 2016](#); with permission)

Both electrophysiological and functional imaging studies characterized the temporal and spatial response properties of T5 inputs ([Behnia et al., 2014](#); [Meier et al., 2014](#); [Serbe et al., 2016](#); [Strother et al., 2014](#)). All of the cells were shown to be OFF selective and respond to motion stimuli in a non-directional way. This suggests that direction selectivity indeed arises in the dendrites of T5 neurons. Additionally, all cells have small receptive fields, corresponding to the acceptance angle of a single photoreceptor (but see ([Fisher et al., 2015a](#)), who reported that Tm9 is a large-field neuron with a receptive field size of around 60°). In addition, the temporal properties of all four T5 inputs were measured with different techniques. Electrophysiological experiments found that the peak of the linear filter of Tm1 was delayed with respect to Tm2 by 13 milliseconds, which led to the suggestion that these cells correspond to the delayed and direct line of the OFF motion detector ([Behnia et al., 2014](#)). These results were later confirmed by a study that characterized Tm1 and Tm2 cells with voltage imaging ([Yang et al., 2016](#)). Two calcium imaging studies found that Tm9 cells respond with much slower kinetics than both Tm1 and Tm2 ([Fisher et al., 2015a](#); [Serbe et al., 2016](#)) and Tm4 cells respond similarly to Tm2 ([Serbe et al., 2016](#)). Thus, the neurons presynaptic to T5 represent a filter bank with diverse temporal properties (**Figure 4B**). Serbe and colleagues also investigated the functional contribution of T5 input elements to OFF motion detection by

using LPTC recordings and behavioral experiments as readout. These experiments showed that all of the four input elements are required for OFF motion detection to different degrees with the strongest contribution from Tm9 (Fisher et al., 2015a; Serbe et al., 2016). However, finding a correspondence between any of these cell types and a specific element of the OFF motion detector was not possible so far. Thus, as for the ON pathway, the exact functional role of the cellular elements presynaptic to T5 neurons remains largely unknown.

## 1.6 Motion Vision and Behavior

Most of the studies that investigate the fly visual system do so in tethered flies in an artificial visual environment. However, it is becoming apparent that sensory brain areas are not merely feedforward systems but receive a wealth of feedback information from higher order and motor areas. Furthermore, the visual stimuli that a fly encounters in its natural setting are drastically different from those that are routinely used in the laboratory. Thus, it is becoming increasingly important to study visual processing in a setting that mimics the natural one as closely as possible.

### 1.6.1 Behavioral State-dependent Modulation of Motion Detection

The visual stimuli impinging onto a fly's eye are markedly different for a stationary and a moving fly. In particular, the visual system of a moving fly is confronted with higher image motion speeds resulting from self-motion when compared with a stationary fly. Thus, from an efficient coding point of view, it would be highly advantageous to tune the fly's motion detection system to the range of expected image velocities (Barlow, 1961). To test this hypothesis, both electrophysiological and optical recordings of LPTCs were performed in walking and tethered flying flies, respectively (Chiappe et al., 2010; Jung et al., 2011; Maimon et al., 2010). These experiments showed that, indeed, the response amplitude of LPTCs increases and their temporal tuning optimum shifts to higher temporal frequencies when the fly is locomoting compared to when it is stationary. Furthermore, in walking flies the response gain of tangential cells is correlated with the turning velocity of the fly (Chiappe et al., 2010). Thereby, the motion detection circuit shifts its dynamic range to the higher image velocities that it experiences when the animal is moving. Further studies have found that activation of octopamine receptors either pharmacologically or by direct release of the neuromodulator itself is necessary and sufficient for this tuning shift (Jung et al., 2011; Suver et al., 2012).

Theoretically, the response optimum of a motion detector is determined by the dynamics of its input arms. The temporal frequency shift seen in flying flies, for example, could

be recapitulated in a Hassenstein-Reichardt detector model when the time constants of the input filters were changed (Jung et al., 2011). Thus, the experimentally observed shift in tuning might be accompanied by a concurrent change in the temporal dynamics of the medulla input neurons to T4 and T5. Therefore, the state-dependent modulation of the motion detector's tuning provides a promising entry point to pinpoint the functional role of its inputs elements. In a manuscript contained in this thesis, we characterized the temporal tuning properties of LPTCs as well as both ON and OFF motion detectors and all their presynaptic elements with and without the addition of an octopamine receptor agonist (**Manuscript 3** - (Arenz et al., 2017)). Based on these measurements, we generated a computational model that was able to reproduce the detector's tuning under both physiological states and thus allowed us to map the cell types to specific elements of the algorithmic motion detectors. Importantly, this model did not require the postulation of any additional delays that might be implemented downstream of the medulla input neurons.

### 1.6.2 Motion Detection in Natural Environments

Animals have evolved in natural environments. Thus, their brain circuits have adapted to extract information from the species' particular ecological sensory niche. Indeed, much of the information that would be physically available to an organism is not processed by the brain at all. Think of the lack of UV-vision or magnetosensation in humans, for example. The reason for this is that the energy reserve of an animal is limited – and the brain is an especially energy-expensive organ. Therefore, it is beneficial to allocate the limited neural processing capabilities to those sensory signals that are most informative to the animal. Sensory systems of animals thus act as “matched filters” – they extract signals crucial to the animal's survival and reject unimportant signals (Barlow, 1961; Warrant, 2016; Wehner, 1987). Consequently, the visual systems should be tuned to the particular statistics of the natural visual environment that the animal experiences. The statistics of visual stimuli under natural conditions, however, are drastically different from the stimuli that are routinely used in laboratories. Natural scenes, for example, have heavily asymmetric luminance distributions, skewed towards negative contrasts (Ratliff et al., 2010). Furthermore, low temporal as well as low spatial frequencies dominate in natural images (Van Hateren, 1992, 1993). A number of studies provide evidence that visual circuits in both flies and mammals are indeed tuned to the statistics of natural environments (Clark et al., 2014; Ratliff et al., 2010; Simoncelli and Olshausen, 2001).

In a study contained in this thesis, we investigated whether ON and OFF motion vision pathways in *Drosophila* have adapted differently to the ON/OFF statistics of natural environments (**Manuscript 4** - (Leonhardt et al., 2016)). However, why have parallel channels

for ON and OFF stimuli in the first place? A split into processing channels for positive (ON) and negative (OFF) changes of the sensory stimulus is found in multiple sensory systems ranging from olfaction, thermosensation and vision in invertebrate and mammalian model systems (Chalasani et al., 2007; Liu et al., 2015; Schiller, 1992). Interestingly, ON and OFF circuits even exist in higher order brain areas such as the fear circuit in the mouse amygdala (Herry et al., 2008). These examples suggest that an ON-OFF split might confer an evolutionary advantage to the animal. Indeed, it has been shown that ON-OFF circuits maximize information content in an energy-efficient manner (Gjorgjieva et al., 2014). For the motion detection circuit, the split into ON and OFF largely alleviates the problem of the biophysical implementation of the sign-correct multiplication postulated in the Hassenstein-Reichardt detector (Eichner et al., 2011). Additionally, segregated processing in ON and OFF channels allows evolution to act on both of these channels independently, adapting each to the properties of the natural environment individually. This suggests that the asymmetry encountered in natural environments might be reflected in functional asymmetries between these two pathways. We tested this hypothesis by first investigating velocity tuning properties of *Drosophila* ON and OFF motion detectors on a behavioral and physiological level. Computer simulations of a motion estimation model that was trained on natural scenes generated predictions of the tuning properties of an optimal detector. Comparing experimental and computational results allowed us to infer that ON and OFF detectors are indeed tuned differentially, likely as an adaptation to the statistics of natural environments (Manuscript 4 - (Leonhardt et al., 2016)).

## 1.7 Beyond Motion Detection Circuits

Fly visual behaviors are manifold, ranging from collision avoidance, fixation, landing behavior, over course stabilization to tracking of a conspecific (Borst, 2014a; Cook, 1979). In natural surroundings, multiple stimuli that induce such behaviors when presented in isolation can occur simultaneously. Thus, natural visual stimuli often engage different neural sub-circuits at the same time and the behavioral output is usually a result of the superposition and interaction of their activities. An animal that tracks an object, for example must still be able to do so in the case of additional optic flow generated by external disturbances. The neural circuits underlying these behaviors, however, may share many components of their neural hardware. To a single photoreceptor or even a medulla interneuron, for example, a transient dimming that is detected by the cell might be caused by a looming predator, a passing conspecific or simply a trunk of a tree that the fly passes in flight. Similarly, motion-sensitive T4 and T5 cells can be activated both by optic flow generated by ego-motion or a distant object that the fly wants to track and land on.

How T4 and T5 motion detector cells ultimately contribute to two specific behaviors - the optomotor response and bar fixation behavior - was investigated in another study contained in this thesis (**Manuscript 5** - ([Bahl et al., 2013](#))). Here, we took advantage of *Drosophila*'s genetic toolbox and silenced synaptic output from T4 and T5 cells. This allowed us to elucidate the role of T4 and T5 in both of these behaviors, and gain insight into their functional interplay. We discovered that T4/T5 blocked flies were motion blind and did not perform any optomotor response. However, they were still able to fixate a vertical bar, although with reduced performance. This led to the postulation of a visual circuit that detects local luminance changes – the so-called position system – which works in parallel to the motion detection circuit. When the fly fixates a distant landmark, for example, the activity of both of these circuits support the fly's behavioral performance.

In addition to local luminance changes, spatial contrast, defined as the local difference in luminance, generates strong visual percepts in humans ([Shapiro and Hamburger, 2007](#)) ([Adelson, 2000](#)). In a further study, we investigated whether flies perceive spatial contrast and performed a first step in dissecting the underlying circuit mechanisms (**Manuscript 6** - ([Bahl et al., 2015](#))).

## 1.8 Comparative Studies of Neuronal Function

Insights into how neurons perform certain computations often come from comparative studies. Circuits that fulfill the same tasks in different animals are often functionally, and in closely related species even structurally, conserved. One important question is how neurons and circuits preserve functional properties despite drastic size scaling of their individual components. The final study presented in this thesis addresses this question by comparing morphology and electrical properties of HS cells from the blowfly (*Calliphora vicina*) with their counterparts in the fruit fly (*Drosophila melanogaster*) (**Manuscript 7** - ([Cuntz et al., 2013](#))).

## 1.9 Conclusion

All of the studies presented in this cumulative thesis use the *Drosophila* motion vision circuit as a model system to investigate fundamental questions about neural computations. The studies, however, diverge with respect to the mechanistic level that was explored. The first half of the thesis is dedicated to the identification and characterization of the neurons that represent the first direction-selective stage in the fly visual system (**Manuscript 1**) and their presynaptic elements (**Manuscripts 2,3**). Moreover, we tried to define the algorithmic architecture of the motion detection circuit and assign specific neural cell types to the elements

of that algorithmic structure (**Manuscripts 2,3**). The second half of the thesis asks how natural environments have shaped the tuning properties of fly motion detectors (**Manuscript 4**) and how motion detection circuits interact with parallel visual circuits to guide fly behavior (**Manuscripts 5,6**). Lastly, we investigated how the function of a single identified visual neuron can be conserved across two species of different sizes (**Manuscript 7**). Taken together, the papers contained in this cumulative thesis extend our knowledge on how flies compute the direction of motion, ranging from the cellular to the behavioral level.



## Manuscript I

### A Directional Tuning Map of *Drosophila* Elementary Motion Detectors

Matthew S. Maisak\*, Juergen Haag\*, **Georg Ammer**, Etienne Serbe, Matthias Meier, Aljoscha Leonhardt, Tabea Schilling, Armin Bahl, Gerald M. Rubin, Aljoscha Nern, Barry J. Dickson, Dierk F. Reiff, Elisabeth Hopp, and Alexander Borst

\* equal contribution

#### Author Contributions

M.S.M. and J.H. jointly performed and, together with A.Bo. evaluated all calcium imaging experiments. **G.A.**, E.S. and M.M. recorded from tangential cells. A.L., T.S. and A.Ba. performed the behavioural experiments. G.R., B.D. and A.N. generated the driver lines and characterized their expression pattern. D.F.R. performed preliminary imaging experiments. E.H. helped with programming and developed the PMT shielding for the two-photon microscope. A.Bo. designed the study and wrote the manuscript with the help of all authors.

**Nature** 500, 212-216. doi: 10.1038/nature12320.



## A directional tuning map of *Drosophila* elementary motion detectors

Matthew S. Maisak<sup>1\*</sup>, Juergen Haag<sup>1\*</sup>, Georg Ammer<sup>1</sup>, Etienne Serbe<sup>1</sup>, Matthias Meier<sup>1</sup>, Aljoscha Leonhardt<sup>1</sup>, Tabea Schilling<sup>1</sup>, Armin Bahl<sup>1</sup>, Gerald M. Rubin<sup>2</sup>, Aljoscha Nern<sup>2</sup>, Barry J. Dickson<sup>3</sup>, Dierk F. Reiff<sup>4†</sup>, Elisabeth Hopp<sup>1</sup> & Alexander Borst<sup>1</sup>

The extraction of directional motion information from changing retinal images is one of the earliest and most important processing steps in any visual system. In the fly optic lobe, two parallel processing streams have been anatomically described, leading from two first-order interneurons, L1 and L2, via T4 and T5 cells onto large, wide-field motion-sensitive interneurons of the lobula plate<sup>1</sup>. Therefore, T4 and T5 cells are thought to have a pivotal role in motion processing; however, owing to their small size, it is difficult to obtain electrical recordings of T4 and T5 cells, leaving their visual response properties largely unknown. We circumvent this problem by means of optical recording from these cells in *Drosophila*, using the genetically encoded calcium indicator GCaMP5 (ref. 2). Here we find that specific subpopulations of T4 and T5 cells are directionally tuned to one of the four cardinal directions; that is, front-to-back, back-to-front, upwards and downwards. Depending on their preferred direction, T4 and T5 cells terminate in specific sublayers of the lobula plate. T4 and T5 functionally segregate with respect to contrast polarity: whereas T4 cells selectively respond to moving brightness increments (ON edges), T5 cells only respond to moving brightness decrements (OFF edges). When the output from T4 or T5 cells is blocked, the responses of postsynaptic lobula plate neurons to moving ON (T4 block) or OFF edges (T5 block) are selectively compromised. The same effects are seen in turning responses of tethered walking flies. Thus, starting with L1 and L2, the visual input is split into separate ON and OFF pathways, and motion along all four cardinal directions is computed separately within each pathway. The output of these eight different motion detectors is then sorted such that ON (T4) and OFF (T5) motion detectors with the same directional tuning converge in the same layer of the lobula plate, jointly providing the input to downstream circuits and motion-driven behaviours.

Most of the neurons in the fly brain are dedicated to image processing. The respective part of the head ganglion, called the optic lobe, consists of several layers of neuropile called lamina, medulla, lobula and lobula plate, all built from repetitive columns arranged in a retinotopic way (Fig. 1a). Each column houses a set of identified neurons that, on the basis of Golgi staining, have been described anatomically in great detail<sup>3–5</sup>. Owing to their small size, however, most of these columnar neurons have never been recorded from electrophysiologically. Therefore, their specific functional role in visual processing is still largely unknown. This fact is contrasted by rather detailed functional models about visual processing inferred from behavioural studies and recordings from the large, electrophysiologically accessible output neurons of the fly lobula plate (tangential cells). As the most prominent example of such models, the Reichardt detector derives directional motion information from primary sensory signals by multiplying the output from adjacent photoreceptors after asymmetric temporal filtering<sup>6</sup>. This model makes a number of rather counter-intuitive predictions all of which have been confirmed experimentally (for review, see ref. 7). Yet, the neurons corresponding to most

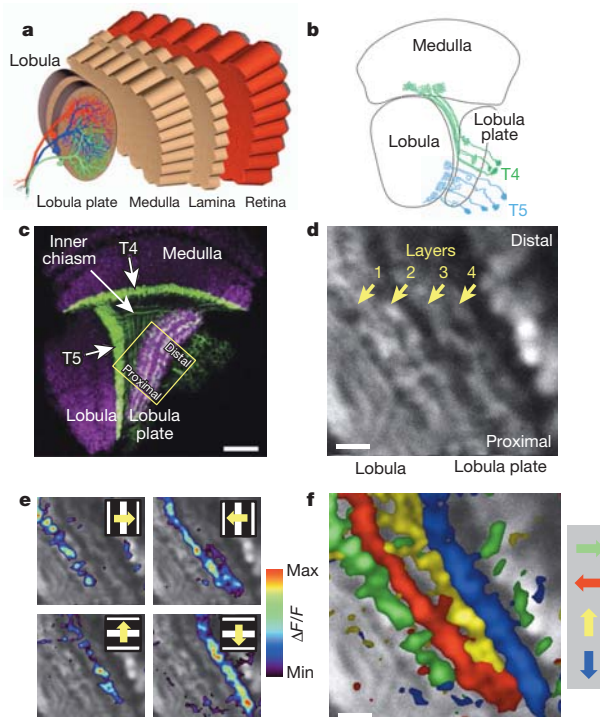


**Figure 1 | Directional tuning and layer-specific projection of T4 and T5 cells.** **a**, Schematic diagram of the fly optic lobe. In the lobula plate, motion-sensitive tangential cells extend their large dendrites over many hundreds of columns. Shown are the reconstructions of the three cells of the horizontal system<sup>22</sup>. **b**, Anatomy of T4 and T5 cells, as drawn from Golgi-impregnated material (from ref. 5). **c**, Confocal image of the R42F06, shown in a horizontal cross-section (from ref. 10). Neurons are marked in green (Kir2.1-EGFP labelled), whereas the neuropile is stained in purple by an antibody against the postsynaptic protein Dlg. Scale bar, 20  $\mu$ m. **d**, Two-photon image of the lobula plate of a fly expressing GCaMP5 under the control of the same driver line R42F06. Scale bar, 5  $\mu$ m. The size and orientation of the image approximately corresponds to the yellow square in **c**. **e**, Relative fluorescence changes ( $\Delta F/F$ ) obtained during 4-s grating motion along the four cardinal directions, overlaid on the greyscale image. Each motion direction leads to activity in a different layer. Minimum and maximum  $\Delta F/F$  values were 0.3 and 1.0 (horizontal motion), and 0.15 and 0.6 (vertical motion). **f**, Compound representation of the results obtained from the same set of experiments. Scale bar, 5  $\mu$ m. Results in **e** and **f** represent the data obtained from a single fly averaged over four stimulus repetitions. Similar results were obtained from six other flies.

<sup>1</sup>Max Planck Institute of Neurobiology, 82152 Martinsried, Germany. <sup>2</sup>Janelia Farm Research Campus, Ashburn, Virginia 20147, USA. <sup>3</sup>Institute of Molecular Pathology, 1030 Vienna, Austria. <sup>†</sup>Present address: Institute Biology 1, Albert-Ludwigs University, 79085 Freiburg, Germany.

\*These authors contributed equally to this work.

of the circuit elements of the Reichardt detector have not been identified so far. Here, we focus on a set of neurons called T4 and T5 cells (Fig. 1b) which, on the basis of circumstantial evidence, have long been speculated to be involved in motion detection<sup>1,8–10</sup>. However, it is unclear to what extent T4 and T5 cells are directionally selective or whether direction selectivity is computed or enhanced within the dendrites of the tangential cells. Another important question concerns the functional separation between T4 and T5 cells; that is, whether they carry equivalent signals, maybe one being excitatory and the other inhibitory on the tangential cells, or whether they segregate into directional- and non-directional pathways<sup>11</sup> or into separate ON- and OFF-motion channels<sup>12,13</sup>.

To answer these questions, we combined Gal4-driver lines specific for T4 and T5 cells<sup>14</sup> with GCaMP5 (ref. 2) and optically recorded the visual response properties using two-photon fluorescence microscopy<sup>15</sup>. In a first series of experiments, we used a driver line labelling both T4 and T5 cells. A confocal image (Fig. 1c, modified from ref. 10) revealed clear labelling (in green) in the medulla (T4 cell dendrites), in the lobula (T5 cell dendrites), as well as in four distinct layers of the lobula plate, representing the terminal arborizations of the four subpopulations of both T4 and T5 cells. These four layers of the lobula plate can also be seen in the two-photon microscope when the calcium indicator GCaMP5 is expressed (Fig. 1d). After stimulation of the fly with grating motion along four cardinal directions (front-to-back, back-to-front, upwards and downwards), activity is confined to mostly one of the four layers, depending on the direction in which the grating is moving (Fig. 1e). The outcome of all four stimulus conditions can be combined into a single image by assigning a particular colour to each pixel depending on the stimulus direction to which it responded most strongly (Fig. 1f). From these experiments it is clear that the four subpopulations of T4 and T5 cells produce selective calcium signals depending on the stimulus direction, in agreement with previous deoxyglucose labelling<sup>8</sup>. Sudden changes of the overall luminance evokes no responses in any of the layers (field flicker;  $n = 4$  experiments, data not shown). However, gratings flickering in counter-phase lead to layer-specific responses, depending on the orientation of the grating (Supplementary Fig. 1).

The retinotopic arrangement of this input to the lobula plate is demonstrated by experiments where a dark edge was moved within a small area of the visual field only. Depending on the position of this area, activity of T4 and T5 cells is confined to different positions within the lobula plate (Fig. 2a). Consequently, when moving a bright vertical edge horizontally from back to front, activity of T4 and T5 cells is elicited sequentially in layer 2 of the lobula plate (Fig. 2b). These two experiments also demonstrate that T4 and T5 cells indeed signal motion locally. We next investigated the question of where direction selectivity of T4 and T5 cells arises; that is, whether it is already present in the dendrite, or whether it is generated by synaptic interactions within the lobula plate. This question is hard to answer, as the dendrites of both T4 and T5 cells form a dense mesh within the proximal layer of the medulla (T4) and the lobula (T5), respectively. However, signals within the inner chiasm where individual processes of T4 and T5 cells can be resolved in some preparations show a clear selectivity for motion in one over the other directions (Fig. 2c). Such signals are as directionally selective as the ones measured within the lobula plate, demonstrating that the signals delivered from the dendrites of T4 and T5 cells are already directionally selective.

To assess the particular contribution of T4 and T5 cells to the signals observed in the above experiments, we used driver lines specific for T4 and T5 cells, respectively. Applying the same stimulus protocol and data evaluation as in Fig. 1, identical results were obtained as before for both the T4- as well as the T5-specific driver line (Fig. 3a, b). We conclude that T4 and T5 cells each provide directionally selective signals to the lobula plate, in contrast to previous reports<sup>11</sup>. Thus, both T4 and T5 cells can be grouped, according to their preferred direction, into four subclasses covering all four cardinal directions, reminiscent of ON-OFF ganglion cells of the rabbit retina<sup>16</sup>.

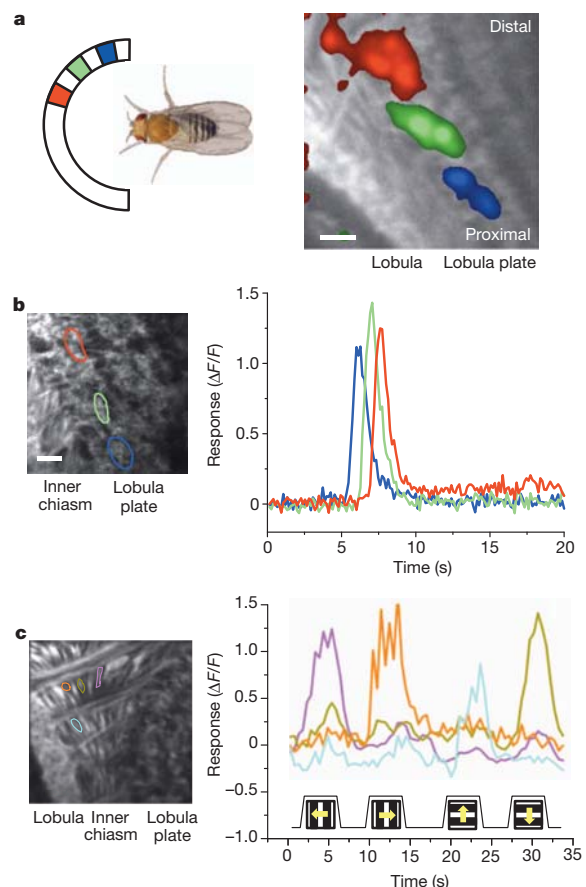


**Figure 2 | Local signals of T4 and T5 cells.** **a**, Retinotopic arrangement of T4 and T5 cells. A dark edge was moving repeatedly from front-to-back within a  $15^\circ$  wide area at different azimuthal positions (left). This leads to relative fluorescence changes at different positions along the proximal-distal axis within layer 1 of the lobula plate (right). Scale bar, 5  $\mu\text{m}$ . Similar results have been obtained in four other flies. **b**, Sequential activation of T4 and T5 cells. A bright edge was moving from back-to-front at  $15^\circ \text{ s}^{-1}$ . Scale bar, 5  $\mu\text{m}$ . Similar results have been obtained in six other flies. **c**, Signals recorded from individual fibres within the inner chiasm (left) reveal a high degree of direction selectivity (right). Scale bar, 5  $\mu\text{m}$ . Similar results were obtained from four other flies, including both lines specific for T4 and T5 cells. Response traces in **b** and **c** are derived from the region of interest encircled in the image with the same colour.

We next addressed whether T4 cells respond differently to T5 cells. To answer this question, we used, instead of gratings, moving edges with either positive (ON edge, brightness increment) or negative (OFF edge, brightness decrement) contrast polarity as visual stimuli. We found that T4 cells strongly responded to moving ON edges, but showed little or no response to moving OFF edges (Fig. 3c). This is true for T4 cells terminating in each of the four layers. We found the opposite for T5 cells. T5 cells selectively responded to moving OFF edges and mostly failed to respond to moving ON edges (Fig. 3d). Again, we found this for T5 cells in each of the four layers. We next addressed whether there are any other differences in the response properties between T4 and T5 cells by testing the velocity tuning of both cell populations by means of stimulating flies with grating motion along the horizontal axis from the front to the back at various velocities covering two orders of magnitude. T4 cells revealed a maximum response at a stimulus velocity of  $30^\circ \text{ s}^{-1}$ , corresponding to a temporal frequency of 1 Hz (Fig. 3e). T5 cell responses showed a similar dependency on stimulus velocity, again with a peak at a temporal frequency of

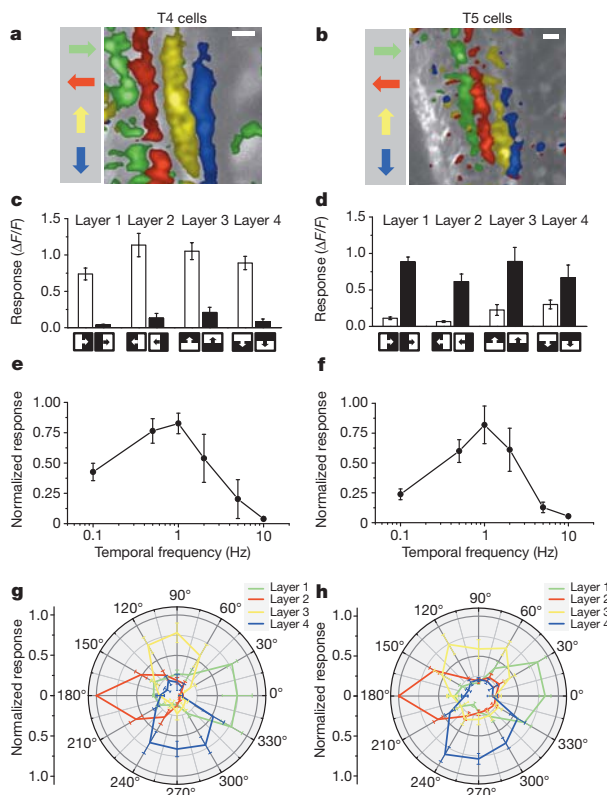


**Figure 3 | Comparison of visual response properties between T4 and T5 cells.** **a, b**, Relative fluorescence changes ( $\Delta F/F$ ) of the lobula plate terminals of T4 (a) and T5 (b) cells obtained during grating motion along the four cardinal directions. Results represent the data obtained from a single fly each, averaged over two stimulus repetitions. Scale bars, 5  $\mu\text{m}$ . Similar results have been obtained in ten other flies. **c, d**, Responses of T4 (c) and T5 (d) cells to ON and OFF edges moving along all four cardinal directions. ON (white) and OFF (black) responses within each layer are significantly different from each other, with  $P < 0.005$  except for layers 3 and 4 in T5 cells, where  $P < 0.05$ . **e, f**, Responses of T4 (e) and T5 (f) cells to gratings moving horizontally at different temporal frequencies. Relative fluorescence changes were evaluated from layer 1 of the lobula plate and normalized to the maximum response before averaging. **g, h**, Responses of T4 (g) and T5 (h) cells to gratings moving in 12 different directions. Relative fluorescence changes were evaluated from all four layers of the lobula plate normalized to the maximum response before averaging. Data represent the mean  $\pm$  s.e.m. of the results obtained in  $n = 8$  (c),  $n = 7$  (d),  $n = 6$  (e),  $n = 7$  (f),  $n = 6$  (g) and  $n = 5$  (h) different flies. Significances indicated are based on two-sample  $t$ -test.

1 Hz (Fig. 3f). Thus, there is no obvious difference in the velocity tuning between T4 and T5 cells. As another possibility, T4 cells might functionally differ from T5 cells with respect to their directional tuning width. To test this, we stimulated flies with gratings moving into 12 different directions and evaluated the relative change of fluorescence in all four layers of the lobula plate. Using the T4-specific driver line, we found an approximate half width of 60–90° of the tuning curve, with the peak responses in each layer shifted by 90° (Fig. 3g). No decrease of calcium was detectable for grating motion opposite to the preferred direction of the respective layer. When we repeated the experiments using the T5-specific driver line, we found a similar dependence of the relative change of fluorescence on the stimulus direction (Fig. 3h). We conclude that T4 cells have the same velocity and orientation tuning as T5 cells. The only functional difference we were able to detect remains their selectivity for contrast polarity.

Our finding about the different preference of T4 and T5 cells for the polarity of a moving contrast makes the strong prediction that selective

blockade of T4 or T5 cells should selectively compromise the responses of downstream lobula plate tangential cells to either ON or OFF edges. To test this prediction, we blocked the output of either T4 or T5 cells via expression of the light chain of tetanus toxin<sup>17</sup> and recorded the responses of tangential cells via somatic whole-cell patch to moving ON and OFF edges. In response to moving ON edges, strong and reliable directional responses were observed in all control flies (Fig. 4a). However, T4-block flies showed a strongly reduced response to ON edges, whereas the responses of T5-block flies were at the level of control flies (Fig. 4b, c). When we used moving OFF edges, control flies again responded with a large amplitude (Fig. 4d). However, the responses of T4-block flies were at the level of control flies, whereas the responses of T5-block flies were strongly reduced (Fig. 4e, f). These findings are reminiscent on the phenotypes obtained from blocking lamina cells L1 and L2 (ref. 13) and demonstrate that T4 and T5 cells are indeed the motion-coding intermediaries for these contrast polarities on their way to the tangential cells of the lobula plate. Whether the residual responses to ON edges in T4-block flies and to OFF edges in T5-block flies are due to an incomplete signal separation between the two pathways or due to an incomplete genetic block in both fly lines is currently unclear.

To address the question of whether T4 and T5 cells are the only motion detectors of the fly visual system, or whether they represent one cell class, in parallel to other motion-sensitive elements, we used tethered flies walking on an air-suspended sphere<sup>18</sup> and stimulated them by ON and OFF edges moving in opposite directions<sup>19</sup>. As in the previous experiments, we blocked T4 and T5 cells specifically by selective expression of the light chain of tetanus toxin. During balanced motion, control flies did not show significant turning responses to either side (Fig. 4g). T4-block flies, however, strongly followed the direction of the moving OFF edges, whereas T5-block flies followed the direction of the moving ON edges (Fig. 4h, i). In summary, the selective preference of T4-block flies for OFF edges and of T5-block flies for ON edges not only corroborates our findings about the selective preference of T4 and T5 cells for different contrast polarities, but also demonstrates that the signals of T4 and T5 cells are indeed the major, if not exclusive, inputs to downstream circuits and motion-driven behaviours.

Almost a hundred years after T4 and T5 cells have been anatomically described<sup>3</sup>, this study reports their functional properties in a systematic way. Using calcium as a proxy for membrane voltage<sup>20</sup>, we found that both T4 and T5 cells respond to visual motion in a directionally selective manner and provide these signals to each of the four layers of the lobula plate, depending on their preferred direction. Both cell types show identical velocity and orientation tuning which matches the one of the tangential cells<sup>21,22</sup>. The strong direction selectivity of both T4 and T5 cells is unexpected, as previous studies had concluded that the high degree of direction selectivity of tangential cells is due to a push-pull configuration of weakly directional input with opposite preferred direction<sup>23,24</sup>. Furthermore, as the preferred direction of T4 and T5 cells matches the preferred direction of the tangential cells branching within corresponding layers, it is currently unclear which neurons are responsible for the null-direction response of the tangential cells. As for the functional separation between T4 and T5 cells, we found that T4 cells selectively respond to brightness increments, whereas T5 cells exclusively respond to moving brightness decrements. Interestingly, parallel ON and OFF motion pathways had been previously postulated on the basis of selective silencing of lamina neurons L1 and L2 (ref. 13). Studies using apparent motion stimuli to probe the underlying computational structure arrived at controversial conclusions: whereas some studies concluded that there was a separate handling of ON and OFF events by motion detectors<sup>12,25,26</sup>, others did not favour such a strict separation<sup>19,27</sup>. The present study directly demonstrates the existence of separate ON and OFF motion detectors, as represented by T4 and T5 cells, respectively. Furthermore, our results anatomically confine the essential processing steps of elementary

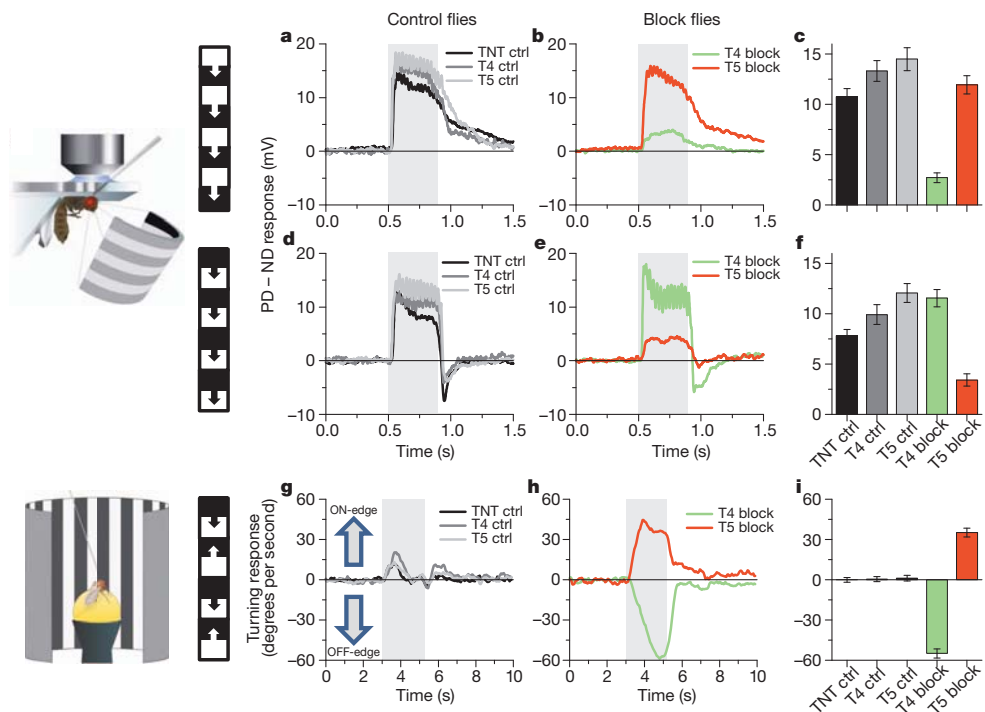


**Figure 4 | Voltage responses of lobula plate tangential cells and turning responses of walking flies to moving ON and OFF edges.** **a, d**, Average time course of the membrane potential in response to preferred direction motion minus the response to null direction motion (PD – ND response) as recorded in three types of control flies (stimulation period indicated by shaded area). **b, e**, Same as in **a, d**, but recorded in T4-block flies (green) and T5-block flies (red). The stimulus pattern, shown to the left, consisted of multiple ON- (a) or OFF-edges (d). **c, f**, Mean voltage responses (PD – ND) of tangential cells in the five groups of flies. Recordings were done from cells of the vertical<sup>12</sup> and the horizontal<sup>22</sup> system. Because no difference was detected between them, data were pooled. Data comprise recordings from  $n = 20$  (TNT control),  $n = 12$  (T4 control),  $n = 16$  (T5 control),  $n = 17$  (T4 block) and  $n = 18$  (T5 block) cells. In both T4 and T5-block flies, ON and OFF responses are significantly different

from each other with  $P < 0.001$ . In T4-block flies, ON responses are significantly reduced compared to all three types of control flies, whereas in T5-block flies, OFF responses are significantly reduced, both with  $P < 0.001$ . **g, h**, Average time course of the turning response of three types of control flies to ON and OFF edges moving simultaneously to opposite directions (stimulation period indicated by shaded area). **i**, Same as in **g**, but recorded from T4-block flies (green) and T5-block flies (red). **i**, Mean turning tendency ( $\pm$ s.e.m.) during the last second of the stimulation period averaged across all flies within each group. Data comprise average values obtained in  $n = 12$  (TNT controls),  $n = 11$  (T4 controls),  $n = 11$  (T5 controls),  $n = 13$  (T4 block) and  $n = 12$  (T5 block) flies. Values of T4 and T5-block flies are highly significantly different from zero with  $P < 0.001$ . Significances indicated are based on two-sample *t*-test.

motion detection—that is, asymmetric temporal filtering and nonlinear interaction—to the neuropile between the axon terminals of lamina neurons L1 and L2 (ref. 28) and the dendrites of directionally selective T4 and T5 cells (Supplementary Fig. 2). The dendrites of T4 and T5 cells might well be the place where signals from neighbouring columns interact in a nonlinear way, similar to the dendrites of starburst amacrine cells of the vertebrate retina<sup>29</sup>.

## METHODS SUMMARY

**Flies.** Flies used in calcium imaging experiments (Figs 1–3) had the following genotypes: T4/T5 line ( $w^-$ ;  $+/+$ ; *UAS-GCaMP5,R42F06-GAL4/UAS-GCaMP5,R42F06-GAL4*), T4 line ( $w^-$ ;  $+/+$ ; *UAS-GCaMP5,R54A03-GAL4/UAS-GCaMP5,R54A03-GAL4*), T5 line ( $w^-$ ;  $+/+$ ; *UAS-GCaMP5,R42H07-GAL4/UAS-GCaMP5,R42H07-GAL4*). Flies used in electrophysiological and behavioural experiments (Fig. 4) had identical genotypes of the following kind: TNT control flies ( $w^+/w^+$ ; *UAS-TNT-E/UAS-TNT-E*;  $+/+$ ), T4 control flies ( $w^+/w^-$ ;  $+/+$ ; *VT37588-GAL4/+*), T5 control flies ( $w^+/w^-$ ;  $+/+$ ; *R42H07-GAL4/+*), T4-block flies ( $w^+/w^-$ ; *UAS-TNT-E/+*; *VT37588-GAL4/+*), T5-block flies ( $w^+/w^-$ ; *UAS-TNT-E/+*; *R42H07-GAL4/+*).

**Two-photon microscopy.** We used a custom-built two-photon laser scanning microscope<sup>29</sup> equipped with a  $\times 40$  water immersion objective and a mode-locked Ti:sapphire laser. To shield the photomultipliers from the stimulus light, two separate barriers were used: the first was placed directly over the LEDs, the second extended from the fly holder over the arena. Images were acquired at a resolution of  $256 \times 256$  pixels and a frame rate of 1.87 Hz, except where indicated, using ScanImage software<sup>30</sup>.

**Electrophysiology.** Recordings were established under visual control using a Zeiss Microscope and a  $\times 40$  water immersion objective.

**Behavioural analysis.** The locomotion recorder was custom-designed according to ref. 18. It consisted of an air-suspended sphere floating in a bowl-shaped sphere holder. Motion of the sphere was recorded by two optical tracking sensors.

**Visual stimulation.** For calcium imaging and electrophysiological experiments, we used a custom-built LED arena covering  $180^\circ$  and  $90^\circ$  of the visual field along the horizontal and the vertical axis, respectively, at  $1.5^\circ$  resolution. For the behavioural experiments, three 120-Hz LCD screens formed a U-shaped visual arena with the fly in the centre, covering  $270^\circ$  and  $114^\circ$  of the visual field along the horizontal and the vertical axes, respectively, at  $0.1^\circ$  resolution.

**Data evaluation.** Data were evaluated off-line using custom-written software (Matlab and IDL).

**Full Methods** and any associated references are available in the online version of the paper.

Received 16 April; accepted 20 May 2013.

1. Bausenwein, B., Dittrich, A. P. M. & Fischbach, K. F. The optic lobe of *Drosophila melanogaster* II. Sorting of retinotopic pathways in the medulla. *Cell Tissue Res.* **267**, 17–28 (1992).
2. Akerboom, J. *et al.* Optimization of a GCaMP calcium indicator for neural activity imaging. *J. Neurosci.* **32**, 13819–13840 (2012).
3. Cajal, S. R. & Sanchez, D. *Contribución al conocimiento de los centros nerviosos de los insectos* (Imprenta de Hijos de Nicholas Moja, 1915).
4. Strausfeld, N. J. *Atlas of an Insect Brain* (Springer, 1976).
5. Fischbach, K. F. & Dittrich, A. P. M. The optic lobe of *Drosophila melanogaster*. I. A Golgi analysis of wild-type structure. *Cell Tissue Res.* **258**, 441–475 (1989).

6. Reichardt, W. Autocorrelation, a principle for the evaluation of sensory information by the central nervous system. In *Sensory Communication* (ed. Rosenblith, W. A.) 303–317 (MIT Press and John Wiley & Sons, 1961).
7. Borst, A., Haag, J. & Reiff, D. F. Fly motion vision. *Annu. Rev. Neurosci.* **33**, 49–70 (2010).
8. Buchner, E., Buchner, S. & Buelthoff, H. Deoxyglucose mapping of nervous activity induced in *Drosophila* brain by visual movement. 1. Wildtype. *J. Comp. Physiol. A* **155**, 471–483 (1984).
9. Strausfeld, N. J. & Lee, J. K. Neuronal basis for parallel visual processing in the fly. *Vis. Neurosci.* **7**, 13–33 (1991).
10. Schnell, B., Raghu, V. S., Nern, A. & Borst, A. Columnar cells necessary for motion responses of wide-field visual interneurons in *Drosophila*. *J. Comp. Physiol. A* **198**, 389–395 (2012).
11. Douglass, J. K. & Strausfeld, N. J. Visual motion-detection circuits in flies: Parallel direction- and non-direction-sensitive pathways between the medulla and lobula plate. *J. Neurosci.* **16**, 4551–4562 (1996).
12. Franceschini, N., Riehle, A. & Le Nestour, A. Directionally selective motion detection by insect neurons. In *Facets of Vision* (ed. Stavenga, H.) 360–390 (Springer, 1989).
13. Joesch, M., Schnell, B., Raghu, S. V., Reiff, D. F. & Borst, A. ON and OFF pathways in *Drosophila* motion vision. *Nature* **468**, 300–304 (2010).
14. Pfeiffer, B. D. *et al.* Tools for neuroanatomy and neurogenetics in *Drosophila*. *Proc. Natl. Acad. Sci. USA* **105**, 9715–9720 (2008).
15. Denk, W., Strickler, J. H. & Webb, W. W. Two-photon laser scanning fluorescence microscopy. *Science* **248**, 73–76 (1990).
16. Oyster, C. W. & Barlow, H. B. Direction-selective units in rabbit retina: distribution of preferred directions. *Science* **155**, 841–842 (1967).
17. Sweeney, S. T., Broadie, K., Keane, J., Niemann, H. & O’Kane, C. J. Targeted expression of tetanus toxin light chain in *Drosophila* specifically eliminates synaptic transmission and causes behavioral defects. *Neuron* **14**, 341–351 (1995).
18. Seelig, J. D. *et al.* Two-photon calcium imaging from head-fixed *Drosophila* during optomotor walking behavior. *Nature Methods* **7**, 535–540 (2010).
19. Clark, D. A., Bursztyn, L., Horowitz, M. A., Schnitzer, M. J. & Clandinin, T. R. Defining the computational structure of the motion detector in *Drosophila*. *Neuron* **70**, 1165–1177 (2011).
20. Egelhaaf, M. & Borst, A. Calcium accumulation in visual interneurons of the fly: Stimulus dependence and relationship to membrane potential. *J. Neurophysiol.* **73**, 2540–2552 (1995).
21. Joesch, M., Plett, J., Borst, A. & Reiff, D. F. Response properties of motion-sensitive visual interneurons in the lobula plate of *Drosophila melanogaster*. *Curr. Biol.* **18**, 368–374 (2008).
22. Schnell, B. *et al.* Processing of horizontal optic flow in three visual interneurons of the *Drosophila* brain. *J. Neurophysiol.* **103**, 1646–1657 (2010).
23. Borst, A. & Egelhaaf, M. Direction selectivity of fly motion-sensitive neurons is computed in a two-stage process. *Proc. Natl. Acad. Sci. USA* **87**, 9363–9367 (1990).
24. Single, S., Haag, J. & Borst, A. Dendritic computation of direction selectivity and gain control in visual interneurons. *J. Neurosci.* **17**, 6023–6030 (1997).
25. Eichner, H., Joesch, M., Schnell, B., Reiff, D. F. & Borst, A. Internal structure of the fly elementary motion detector. *Neuron* **70**, 1155–1164 (2011).
26. Joesch, M., Weber, F., Eichner, H. & Borst, A. Functional specialization of parallel motion detection circuits in the fly. *J. Neurosci.* **33**, 902–905 (2013).
27. Egelhaaf, M. & Borst, A. Are there separate ON and OFF channels in fly motion vision? *Vis. Neurosci.* **8**, 151–164 (1992).
28. Takemura, S. Y., Lu, Z. & Meinertzhagen, I. A. Synaptic circuits of the *Drosophila* optic lobe: the input terminals to the medulla. *J. Comp. Neurol.* **509**, 493–513 (2008).
29. Euler, T., Detwiler, P. B. & Denk, W. Directionally selective calcium signals in dendrites of starburst amacrine cells. *Nature* **418**, 845–852 (2002).
30. Polgruto, T. A., Sabatini, B. L. & Svoboda, K. ScanImage: Flexible software for operating laser scanning microscopes. *Biomed. Eng. Online* **2**, 13 (2003).

**Supplementary Information** is available in the online version of the paper.

**Acknowledgements** We thank L. Looger, J. Simpson, V. Jayaraman and the Janelia GECI team for making and providing us with the GCaMP5 flies before publication; J. Plett for designing and engineering the LED arena; C. Theile, W. Essbauer and M. Sauter for fly work; and A. Mauss, F. Gabbiani and T. Bonhoeffer for critically reading the manuscript. This work was in part supported by the Deutsche Forschungsgemeinschaft (SFB 870). M.S.M., G.A., E.S., M.M., A.L., A.Ba and A.Bo are members of the Graduate School of Systemic Neurosciences.

**Author Contributions** M.S.M. and J.H. jointly performed and, together with A.Bo, evaluated all calcium imaging experiments. G.A., E.S. and M.M. recorded from tangential cells. A.L., T.S. and A.Ba performed the behavioural experiments. G.R., B.D. and A.N. generated the driver lines and characterized their expression pattern. D.F.R. performed preliminary imaging experiments. E.H. helped with programming and developed the PMT shielding for the two-photon microscope. A.Bo designed the study and wrote the manuscript with the help of all authors.

**Author Information** Reprints and permissions information is available at [www.nature.com/reprints](http://www.nature.com/reprints). The authors declare no competing financial interests. Readers are welcome to comment on the online version of the paper. Correspondence and requests for materials should be addressed to A.Bo. (borst@neuro.mpg.de).

## METHODS

**Flies.** Flies were raised on standard cornmeal-agar medium at 25 °C and 60% humidity throughout development on a 12 h light/12 h dark cycle. For calcium imaging, we used the genetically encoded single-wavelength indicator GCaMP5, variant G, with the following mutations: T302L, R303P and D380Y (ref. 2). Expression of GCaMP5 was directed by three different Gal4 lines, all from the Janelia Farm collection<sup>14</sup>. Flies used in calcium imaging experiments (Figs 1–3) had the following genotypes: T4/T5 line (*w<sup>-</sup>*; *+/+*; *UAS-GCaMP5,R42F06-GAL4/UAS-GCaMP5,R42F06-GAL4*), T4 line (*w<sup>-</sup>*; *+/+*; *UAS-GCaMP5,R54A03-GAL4/UAS-GCaMP5,R54A03-GAL4*), T5 line (*w<sup>-</sup>*; *+/+*; *UAS-GCaMP5,R42H07-GAL4/UAS-GCaMP5,R42H07-GAL4*). All driver lines were generated by the methods described in ref. 14 and were identified by screening a database of imaged lines, followed by reimaging of selected lines<sup>31</sup>. As homozygous for both the Gal4-driver and the UAS-GCaMP5 genes, T4 flies also showed some residual expression in T5 cells, and T5 flies also in T4 cells. This unspecific expression, however, was in general less than 25% of the expression in the specific cells. Flies used in electrophysiological and behavioural experiments (Fig. 4) had identical genotypes of the following kind: TNT control flies (*w<sup>+</sup>/w<sup>+</sup>*; *UAS-TNT-E/UAS-TNT-E*; *+/+*), T4 control flies (*w<sup>+</sup>/w<sup>-</sup>*; *+/+*; *VT37588-GAL4/+*), T5 control flies (*w<sup>+</sup>/w<sup>-</sup>*; *+/+*; *R42H07-GAL4/+*), T4-block flies (*w<sup>+</sup>/w<sup>-</sup>*; *UAS-TNT-E/+*; *VT37588-GAL4/+*), T5-block flies (*w<sup>+</sup>/w<sup>-</sup>*; *UAS-TNT-E/+*; *R42H07-GAL4/+*). UAS-TNT-E flies were derived from the Bloomington Stock Center (stock no. 28837) and VT37588-Gal4 flies were derived from the VDRC (stock no. 205893). Before electrophysiological experiments, flies were anaesthetized on ice and waxed on a Plexiglas holder using bees wax. The dissection of the fly cuticle and exposure of the lobula plate were performed as described previously (for imaging experiments, see ref. 32; for electrophysiology, see ref. 21). Flies used in behavioural experiments were taken from 18 °C just before the experiment and immediately cold-anaesthetized. The head, the thorax and the wings were glued to a needle using near-ultraviolet bonding glue (Sinfony Opaque Dentin) and strong blue LED light (440 nm, dental curing-light, New Woodpecker).

**Two-photon microscopy.** We used a custom-built two-photon laser scanning microscope<sup>33</sup> equipped with a  $\times 40$  water immersion objective (0.80 NA, IR-Achroplan; Zeiss). Fluorescence was excited by a mode locked Ti:sapphire laser (<100 fs, 80 MHz, 700–1,020 nm; pumped by a 10 W CW laser; both Mai Tai; Spectraphysics) with a DeepSee accessory module attached for dispersion compensation control resulting in better pulse compression and fluorescence at the target sample. Laser power was adjusted to 10–20 mW at the sample, and an excitation wavelength of 910 nm was used. The photomultiplier tube (H10770PB-40, Hamamatsu) was equipped with a dichroic band-pass mirror (520/35, Brightline). Images were acquired at a resolution of  $256 \times 256$  pixels and a frame rate of 1.87 Hz, except in Fig. 2 (7.5 Hz), using the ScanImage software<sup>30</sup>.

**Electrophysiology.** Recordings were established under visual control using a  $\times 40$  water immersion objective (LumplanF, Olympus), a Zeiss microscope (AxioTech vario 100, Zeiss), and illumination (100 W fluorescence lamp, hot mirror, neutral density filter OD 0.3; all from Zeiss). To enhance tissue contrast, we used two polarization filters, one located as an excitation filter and the other as an emission filter, with slight deviation on their polarization plane. For eye protection, we additionally used a 420-nm LP filter on the light path.

**Behavioural analysis.** The locomotion recorder was custom-designed according to ref. 18. Briefly, it consists of an air-suspended sphere floating in a bowl-shaped sphere holder. A high-power infrared LED (800 nm, JET series, 90 mW, Roithner Electronics) is located in the back to illuminate the fly and the sphere surface. Two optical tracking sensors are equipped with lens and aperture systems to focus on the sphere behind the fly. The tracking data are processed at 4 kHz internally, read out via a USB interface and processed by a computer at  $\approx 200$  Hz. This allows real-time calculation of the instantaneous rotation axis of the sphere. A third camera (GRAS-20S4M-C, Point Grey Research) is located in the back which is essential for proper positioning of the fly and allows real-time observation and video recording of the fly during experiments.

**Visual stimulation.** For calcium imaging and electrophysiological experiments, we used a custom-built LED arena that allowed refresh rates of up to 550 Hz and 16 intensity levels. It covered 180° (1.5° resolution) and 90° (1.5° resolution) of the visual field along the horizontal and the vertical axis, respectively. The LED arena was engineered and modified based upon ref. 34. The LED array consists of  $7 \times 4$  individual TA08-81GWA dot-matrix displays (Kingbright), each harbouring  $8 \times 8$  individual green (568 nm) LEDs. Each dot-matrix display is controlled by an ATmega168 microcontroller (Atmel) combined with a ULN2804 line driver (Toshiba America) acting as a current sink. All panels are in turn controlled via an I2C interface by an ATmega128 (Atmel)-based main controller board, which reads in pattern information from a compact flash (CF) memory card. Matlab was used for programming and generation of the patterns as well as for sending the serial command sequences via RS-232 to the main controller board. The

luminance range of the stimuli was  $0.5\text{--}33 \text{ cd m}^{-2}$ . For the calcium imaging experiments, two separate barriers were used to shield the photomultipliers from the stimulus light coming from the LED arena. The first was a spectral filter with transparency to wavelengths  $>540$  nm placed directly over the LEDs (ASF SFG 10, Microchemicals). The second was a layer of black PVC extending from the fly holder over the arena. Square wave gratings had a spatial wavelength of 30° of visual angle and a contrast of 88%. Unless otherwise stated, they were moving at 30° s $^{-1}$ . Edges had the same contrast and were also moving at 30° s $^{-1}$ . For the experiments shown in Figs 1, 2b and 3, each grating or edge motion was shown twice within a single sweep, resulting in a total of eight stimulation periods. Each stimulus period lasted 4 s, and subsequent stimuli were preceded by a 3-s pause. In the experiment shown in Fig. 2a, a dark edge of 88% contrast was moved for 1 s at 15° s $^{-1}$  from the front to the back at three different positions (22°, 44°, 66° from frontal to lateral). At each position, edge motion was repeated 15 times. For the experiment shown in Fig. 2b, a bright edge of 88% contrast was moving at 15° s $^{-1}$  from the back to the front, and images were acquired at a frame rate of 7.5 Hz. For the experiments shown in Figs 3e, f, all six stimulus velocities were presented once within one sweep, with the stimulus lasting 4 s, and different stimuli being separated by 2 s. In the experiments shown in Figs 3g, h, a single sweep contained all 12 grating orientations with the same stimulus and pause length as above. For the electrophysiology experiments (Fig. 4a–f), multiple edges were used as stimuli moving simultaneously at 50° s $^{-1}$ . To stimulate cells of horizontal system (HS cells), a vertical, stationary square-wave grating with 45° spatial wavelength was presented. For ON-edge motion, the right (preferred direction, PD) or the left edge (null direction, ND) of each light bar started moving until it merged with the neighbouring bar. For OFF-edge motion, the right or the left edge of each dark bar was moving. To stimulate cells of the vertical system (VS cells), the pattern was rotated by 90° clockwise. For the behavioural experiments (Fig. 4g–i), three 120-Hz LCD screens (Samsung 2233 RZ) were vertically arranged to form a U-shaped visual arena ( $w = 31 \text{ cm} \times d = 31 \text{ cm} \times h = 47 \text{ cm}$ ) with the fly in the centre. The luminance ranged from 0 to  $131 \text{ cd m}^{-2}$  and covered large parts of the flies' visual field (horizontal,  $\pm 135^\circ$ ; vertical,  $\pm 57^\circ$ ; resolution,  $<0.1^\circ$ ). The three LCD screens were controlled via NVIDIA 3D Vision Surround Technology on Windows 7 64-bit allowing a synchronized update of the screens at 120 frames per second. Visual stimuli were created using Panda3D, an open-source gaming engine, and Python 2.7, which simultaneously controlled the frame rendering in Panda3D, read out the tracking data and temperature and streamed data to the hard disk. The balanced motion stimulus consisted of a square-wave grating with 45° spatial wavelength and a contrast of 63%. Upon stimulation onset, dark and bright edges moved into opposite directions at 10° s $^{-1}$  for 2.25 s. This stimulation was performed for both possible edge directions and two initial grating positions shifted by half a wavelength, yielding a total of four stimulus conditions.

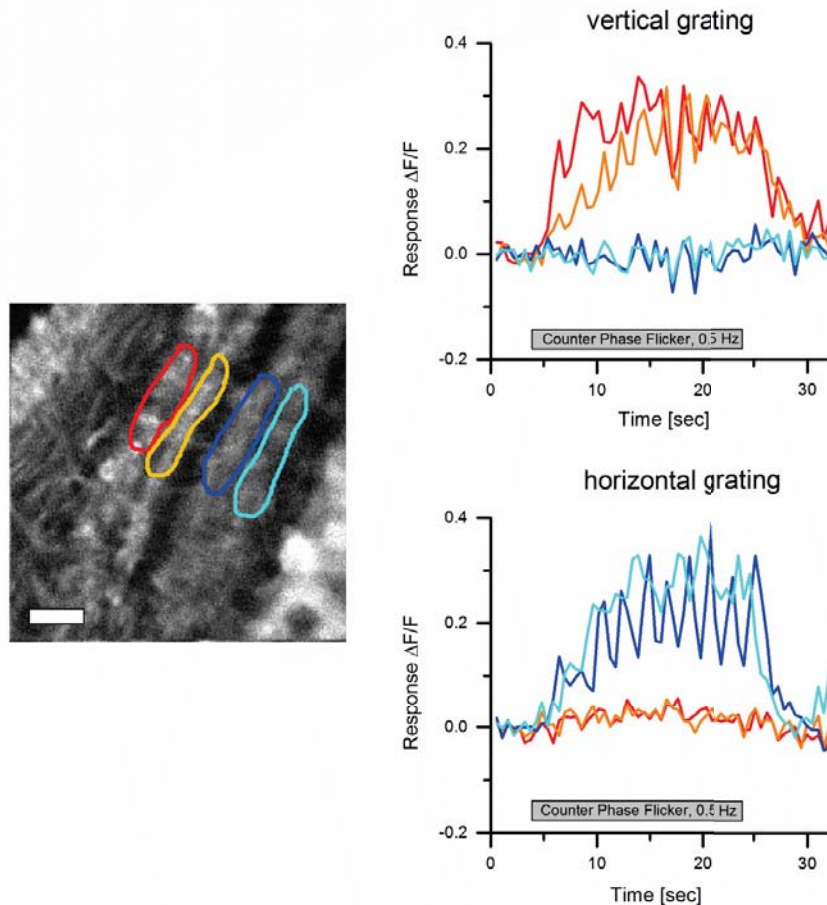
**Data evaluation.** Data were evaluated off-line using custom-written software (Matlab and IDL). For the images shown in Figs 1e, f, 2a and 3a, b, the raw image series was converted into four images representing the relative fluorescence change during each direction of grating motion:  $(\Delta F/F)_{\text{stim}} = (F_{\text{stim}} - F_{\text{ref}})/F_{\text{ref}}$ . The image representing the stimulus fluorescence ( $F_{\text{stim}}$ ) was obtained by averaging all images during stimulation; the image representing the reference fluorescence ( $F_{\text{ref}}$ ) was obtained by averaging three images before stimulation. Both images were smoothed using a Gaussian filter of 10 pixel half-width. For the images shown in Figs 1f and 3a, b,  $\Delta F/F$  images were normalized by their maximum value. Then, a particular colour was assigned to each pixel according to the stimulus direction during which it reached maximum value, provided it passed a threshold of 25%. Otherwise, it was assigned to background. The response strength of each pixel was coded as the saturation of that particular colour. For the data shown in Figs 2b, c and 3c–h, the raw image series was first converted into a  $\Delta F/F$  series by using the first three images as reference. Then, a region was defined within a raw image, and average  $\Delta F/F$  values were determined within that region for each image, resulting in a  $\Delta F/F$  signal over time. Responses were defined as the maximum  $\Delta F/F$  value reached during each stimulus presentation minus the average  $\Delta F/F$  value during the two images preceding the stimulus. For the bar graphs shown in Fig. 4c, f, the average voltage responses during edge motion (0.45 s) along the cell's preferred (PD) and null direction (ND) were calculated. For each recorded tangential cell, the difference between the PD and the ND response was determined, and these values were averaged across all recorded cells. The data shown in Fig. 4g, h were obtained from the four stimulus conditions by averaging the turning responses for the two starting positions of the grating and calculating the mean difference between the turning responses for the two edge directions. For the bar graph shown in Fig. 4i, the average turning response of each fly during the last second of balanced motion stimulation was calculated. These values were averaged across all recorded flies within each genotype.

RESEARCH LETTER

31. Jenett, A. *et al.* A Gal4-driver line resource for *Drosophila* neurobiology. *Cell Rep.* **2**, 991–1001 (2012).
32. Reiff, D. F., Plett, J., Mank, M., Griesbeck, O. & Borst, A. Visualizing retinotopic half-wave rectified input to the motion detection circuitry of *Drosophila*. *Nature Neurosci.* **13**, 973–978 (2010).
33. Euler, T. *et al.* Eyecup scope—optical recording of light stimulus-evoked fluorescence signals in the retina. *Pfluger Arch.* **457**, 1393–1414 (2009).
34. Reiser, M. B. & Dickinson, M. H. A modular display system for insect behavioral neuroscience. *J. Neurosci. Methods* **167**, 127–139 (2008).

# SUPPLEMENTARY INFORMATION

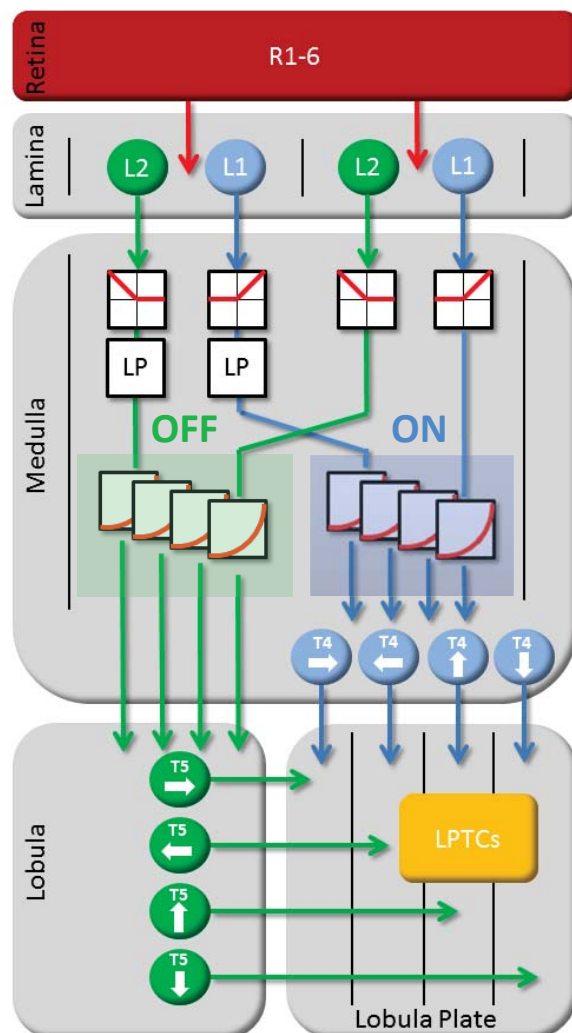
doi:10.1038/nature12320



**Supplemental Fig.1** Responses of T4 and T5 cells to counter-phase flicker. Square-wave gratings (15 deg spatial wavelength and 88% contrast) with vertical (top) and horizontal (bottom) orientation were phase-shifted every second by 180 deg for 20 seconds. Response traces are derived from the region of interest encircled in the image to the left with the same color from a single stimulation period. T4 and T5 cells in layers 1 and 2 only respond to the vertical grating, cells in layers 3 and 4 selectively respond to the horizontal grating. Similar results were obtained in  $n=4$  flies. Scale bar = 5  $\mu$ m. Together with the missing response of T4 and T5 cells to full-field flicker, these findings suggest that T4 and T5 cells receive input signals from neurons with different orientation tuning, depending on whether they respond to motion along the horizontal (layers 1 and 2) or the vertical (layers 3 and 4) axis<sup>1,2</sup>.

1 Pick, B. & Buchner, E. Visual movement detection under light- and dark-adaptation in the fly, *Musca domestica*. *J. Comp. Physiol.* **134**, 45-54 (1979).

2 Srinivasan, M.V. & Dvorak, D.R. Spatial processing of visual information in the movement-detecting pathway of the fly. *J. Comp. Physiol.* **140**, 1-23 (1980).



**Supplemental Fig.2** Circuit diagram of the fly elementary motion detector. Visual input from photoreceptors R1-6 is split into parallel pathways, L1 and L2, at the level of the lamina. Two neighboring columns are shown. The outputs from both L1 and L2 are half-wave rectified, such that downstream elements carry information about ON (L1-pathway) and OFF (L2-pathway) signals separately. After temporal low-pass filtering ('LP') the signals from one column, they interact in a supra-linear way with the instantaneous signals derived from the other column. This interaction takes place, separately in both pathways, along all four cardinal directions. Directionally selective signals are carried via T4 and T5 cells to the four layers of the lobula plate where T4 and T5 cells with the same preferred direction converge again on the dendrites of the tangential cells ('LPTCs').



## Manuscript II

### Functional Specialization of Neural Input Elements to the *Drosophila* ON Motion Detector

Georg Ammer\*, Aljoscha Leonhardt, Armin Bahl, Barry J. Dickson, and Alexander Borst\*

\* corresponding authors

#### Author Contributions

**G.A.** and A. Borst designed the study. **G.A.** performed electrophysiological experiments and anatomical characterization of expression patterns, analyzed the data, and wrote the manuscript with the help of A. Borst, A.L., and A. Bahl. A.L. and A. Bahl performed behavioral experiments and analyzed data. B.J.D. generated SplitGal4 fly lines and hosted G.A. for characterization of Gal4 lines. A. Borst performed computational modeling.

**Current Biology** 25, 2247-2253. doi: 10.1016/j.cub.2015.07.014

## Functional Specialization of Neural Input Elements to the *Drosophila* ON Motion Detector

### Highlights

- Medulla cells Mi1 and Tm3 are involved in the detection of ON motion
- Mi1 is a necessary element over all contrasts, velocities, and directions
- Tm3 is specialized in the computation of fast ON motion signals
- The effect of blocking Tm3 is direction dependent

### Authors

Georg Ammer, Aljoscha Leonhardt,  
Armin Bahl, Barry J. Dickson,  
Alexander Borst

### Correspondence

gammer@neuro.mpg.de (G.A.),  
aborst@neuro.mpg.de (A.B.)

### In Brief

Ammer et al. investigate the function of *Drosophila* medulla cells Mi1 and Tm3 in ON motion detection. They find that Mi1 is a necessary element over all stimulus conditions. Tm3, in contrast, plays a more specialized role, being specifically involved in the detection of fast movement in the preferred direction.



# Functional Specialization of Neural Input Elements to the *Drosophila* ON Motion Detector

Georg Ammer,<sup>1,\*</sup> Aljoscha Leonhardt,<sup>1</sup> Armin Bahl,<sup>1,3</sup> Barry J. Dickson,<sup>2</sup> and Alexander Borst<sup>1,\*</sup>

<sup>1</sup>Max Planck Institute of Neurobiology, Am Klopferspitz 18, 82152 Martinsried, Germany

<sup>2</sup>Janelia Research Campus, Howard Hughes Medical Institute, 19700 Helix Drive, Ashburn, VA 20147, USA

<sup>3</sup>Present address: Department of Molecular and Cell Biology, Harvard University, 16 Divinity Avenue, Cambridge, MA 02138, USA

\*Correspondence: [gambar@neuro.mpg.de](mailto:gambar@neuro.mpg.de) (G.A.), [aborst@neuro.mpg.de](mailto:aborst@neuro.mpg.de) (A.B.)

<http://dx.doi.org/10.1016/j.cub.2015.07.014>

## SUMMARY

Detecting the direction of visual movement is fundamental for every sighted animal in order to navigate, avoid predators, or detect conspecifics. Algorithmic models of correlation-type motion detectors describe the underlying computation remarkably well [1–3]. They consist of two spatially separated input lines that are asymmetrically filtered in time and then interact in a nonlinear way. However, the cellular implementation of this computation remains elusive. Recent connectomic data of the *Drosophila* optic lobe has suggested a neural circuit for the detection of moving bright edges (ON motion) with medulla cells Mi1 and Tm3 providing spatially offset input to direction-selective T4 cells, thereby forming the two input lines of a motion detector [4]. Electrophysiological characterization of Mi1 and Tm3 revealed different temporal filtering properties and proposed them to correspond to the delayed and direct input, respectively [5]. Here, we test this hypothesis by silencing either Mi1 or Tm3 cells and using electrophysiological recordings and behavioral responses of flies as a readout. We show that Mi1 is a necessary element of the ON pathway under all stimulus conditions. In contrast, Tm3 is specifically required only for the detection of fast ON motion in the preferred direction. We thereby provide first functional evidence that Mi1 and Tm3 are key elements of the ON pathway and uncover an unexpected functional specialization of these two cell types. Our results thus require an elaboration of the currently prevailing model for ON motion detection [6, 7] and highlight the importance of functional studies for neural circuit breaking.

## RESULTS

A large number of studies provide strong evidence that motion vision in flies is based on correlation-type motion detectors (Figure 1A) [8–12]. In recent years, great progress has been made in revealing the internal structure and identifying some of the cellular elements constituting the *Drosophila* motion-detection

circuit [13, 14]. In particular, it was shown that motion detection occurs in two parallel pathways that differ with respect to their preference for moving brightness increments (ON pathway) and brightness decrements (OFF pathway) [15, 16]. Genetic approaches to specifically silence neuronal cell types combined with electrophysiological and behavioral measurements have mainly focused on lamina circuits and identified cells that feed into the ON or OFF pathway, or both [15, 17–19]. T4 and T5 cells were discovered as the first cells in the *Drosophila* visual system that are direction selective and represent the output stages of ON and OFF elementary motion detectors, respectively [20]. Medulla cells that relay information from the lamina to the dendrites of T4 and T5 have been characterized anatomically [4, 21, 22] and, in part, electrophysiologically [5] or by calcium imaging [23, 24]. However, the functional role of medulla cells in generating direction-selective responses in postsynaptic T4 or T5 cells is still unknown. In this study, we focus on two medulla cell types of the ON pathway: Mi1 and Tm3. These two cell types form the great majority of synaptic inputs to T4 cells (Figure 1B) [4] and exhibit different temporal filtering properties [5]. Thus, it has been proposed that Mi1 and Tm3 constitute the delayed and direct input lines of the *Drosophila* ON motion detector, respectively (Figure 1C) [4, 5]. Here, we test this hypothesis experimentally.

### A Candidate Circuit for ON Motion Detection

We first generated a simple computational model for a fully opponent correlation-type motion detector that computes ON and OFF motion in separate channels [25]. To test the functional role of the individual input elements, we simulated their removal from the circuit by setting their output gain to zero and computed the response of the detector. As expected, when we blocked either of the two input arms of the ON channel, the detector lost its direction selectivity for ON motion completely (Figure 1D). This model thus generates a clear prediction for our subsequent physiological and behavioral investigations: if Mi1 and Tm3 indeed constitute the two input lines of the ON motion detector, then functionally silencing either of them should lead to a complete loss of direction-selective responses to moving ON stimuli in downstream circuits and behavior under all stimulus conditions.

### Mi1 Is an Essential Element of the ON Motion Vision Pathway

In order to measure the output of the motion-detection circuit, we performed *in vivo* patch-clamp recordings from direction-selective lobula plate tangential cells, which receive input from



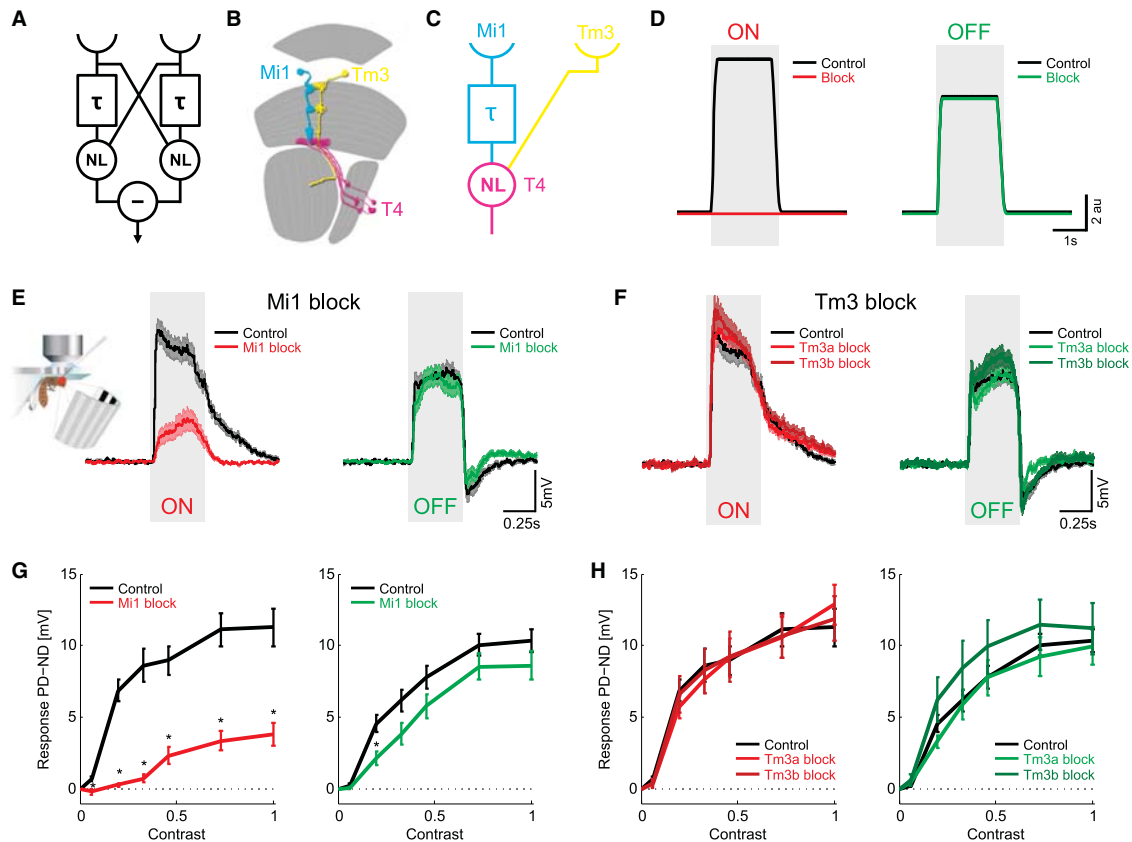


**Figure 1. Voltage Responses of Lobula Plate Tangential Cells in Mi1 and Tm3 Block Flies**

(A) Correlation-type motion detector. Two spatially separated input lines interact in a nonlinear way after one of them has been temporally delayed. Two mirror-symmetrical subunits are subtracted to yield a fully opponent direction-selective response.

(B) Anatomy of the neural input elements to T4 cells. Mi1 (cyan) and Tm3 (yellow) are the cells with the strongest input to direction-selective T4 cells (magenta).

(C) Schematic model suggesting that Mi1 and Tm3 form the delayed and non-delayed arm of a motion detector. The nonlinearity occurs in T4 cells.

(D) Response of a computational simulation of correlation-type motion detectors when removing either the delayed or the direct line. With both input lines intact, the detector produces direction-selective responses to both moving ON and OFF edges (black). Blocking either of the two input lines of the ON channel abolishes responses to ON motion (red) while leaving OFF motion (green) responses intact.

(E and F) Voltage responses of lobula plate tangential cells (calculated by subtracting the response for null direction [ND] stimulation from the response to preferred direction [PD] stimulation) to moving ON or OFF edges when Mi1 cells (E) or Tm3 cells (F) are silenced. Responses of control flies are depicted in black and of Mi1 or Tm3 block flies in red for ON motion and green for OFF motion (control,  $n = 16$ ; Mi1 block,  $n = 21$ ; Tm3a block,  $n = 23$ ; Tm3b block,  $n = 20$ ).

(G and H) Contrast dependence of lobula plate tangential cells to moving ON or OFF edges of Mi1 (G) and Tm3 (H) block flies. Control flies are depicted in black and block flies in red for ON and green for OFF motion stimuli. Null direction responses were subtracted from preferred direction responses (PD – ND) (control,  $n = 12$ ; Mi1 block,  $n = 14$ ; Tm3a block,  $n = 9$ ; Tm3b block,  $n = 10$ ).

Data are presented as mean  $\pm$  SEM.  $n$  indicates the number of recorded cells. Significant differences between control and block flies are indicated by asterisks (two-sided Student's *t* test, Benjamini-Hochberg corrected,  $*p < 0.05$ ). Detailed statistics are provided in Table S2. Recordings from vertical system (VS) and horizontal system (HS) cells were pooled. See also Figures S1 and S2 and Table S1.

a large number of T4 and T5 cells [26, 27], and stimulated flies with visual motion on an LED arena [9]. To silence the neuronal activity of Mi1 or Tm3 cells, we used the Gal4/UAS system [28] to specifically express the EGFP-tagged inward-rectifying potassium channel Kir2.1 [29]. We generated a specific SplitGal4 line [30] to target Mi1 cells and used two independent Gal4 lines for manipulation of Tm3 cells [31]. All transgenic lines showed clear expression of the Kir2.1 channel in the respective cell types when stained with antibodies against the EGFP tag (Figure S1). We selectively stimulated the ON and OFF motion vision path-

ways with either multiple ON or OFF edges moving in the same direction at a velocity of  $50^\circ \text{ s}^{-1}$ . Control flies responded with strong direction-selective responses to both moving ON and OFF edges (Figures 1E and 1F). In contrast, Mi1 block flies showed a strong reduction in response to ON motion but were unaffected for OFF motion (Figure 1E). Thus, in accordance with the predictions from the proposed model [4, 5], Mi1 is an essential element of the ON motion pathway. Surprisingly however, when we blocked Tm3 cells, responses to both ON and OFF stimuli were indistinguishable from those of control flies

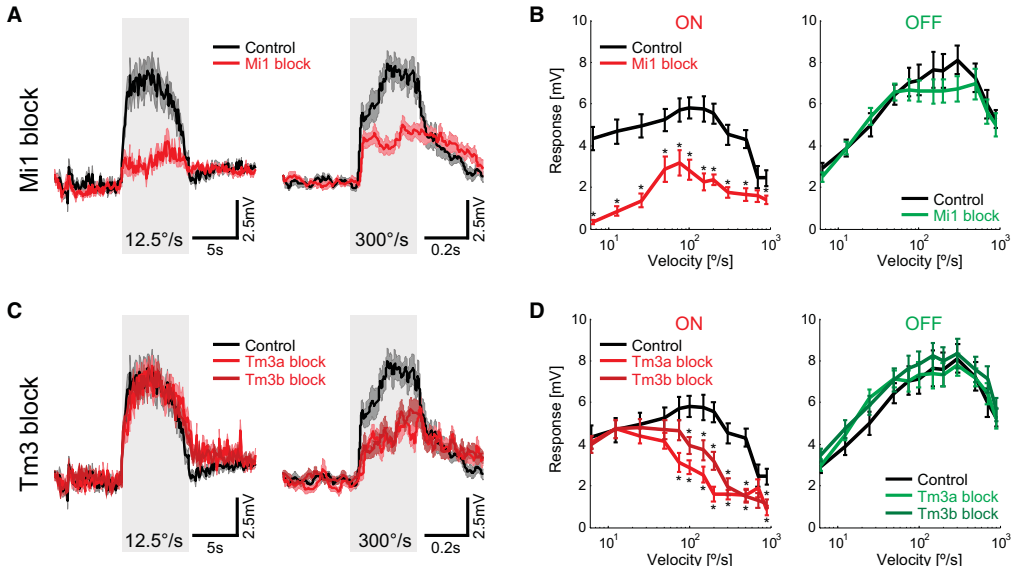


**Figure 2. Differential Velocity Tuning of Mi1 and Tm3 Block Flies**

(A) Average voltage responses of lobula plate tangential cells of control (black) and Mi1 block flies (red) to slow ( $12.5^{\circ} \text{ s}^{-1}$ ) and fast ( $300^{\circ} \text{ s}^{-1}$ ) ON edges moving in the preferred direction.

(B) Velocity tuning curves of lobula plate tangential cells of control (black) and Mi1 block flies to ON edges (red) and OFF edges (green) moving in the preferred direction (control,  $n = 13$ ; Mi1 block,  $n = 11$ ).

(C) Average voltage responses of lobula plate tangential cells of control (black) and Tm3 block (red) flies to slow ( $12.5^{\circ} \text{ s}^{-1}$ ) and fast ( $300^{\circ} \text{ s}^{-1}$ ) ON edges moving in the preferred direction.

(D) Velocity tuning curves of lobula plate tangential cells of control (black) and Tm3 block flies to ON edges (red) and OFF edges (green) moving in the preferred direction (control,  $n = 13$ ; Tm3a block,  $n = 15$ ; Tm3b block,  $n = 17$ ).

Data are presented as mean  $\pm$  SEM.  $n$  indicates the number of recorded cells. Significant differences between control and block flies are indicated by asterisks (two-sided Student's *t* test, Benjamini-Hochberg corrected,  $*p < 0.05$ ). Detailed statistics are provided in Table S2. Recordings from VS and HS cells were pooled. See also Figures S1 and S3 and Table S1.

(Figure 1F). To rule out that the strong stimulus drives the system to saturation and that possible residual Tm3 activity was sufficient to generate the observed responses, we varied the stimulus strength by reducing the contrast. Compared to control flies, Mi1 block flies showed a strong reduction to ON stimuli for all contrasts and a minor reduction to OFF stimuli in the low-contrast range (Figure 1G). However, responses of Tm3 block flies were again unaffected, even for very low contrasts (Figure 1H). Thus, we conclude, in disagreement with the proposed model [4, 5], that Tm3 cells are not necessary in general for the detection of ON motion.

#### Differential Velocity Dependence of Mi1 and Tm3 Block Flies

The finding that Tm3 is a dispensable circuit element under the tested stimulus conditions does not completely rule out its involvement in ON motion detection. It is possible that Tm3 plays an essential part under certain other stimulus conditions. In addition to the contrast tuning curve of a motion detector, another important characteristic is its dependence on velocity. We determined the velocity tuning curves by presenting single ON or OFF edges moving in the preferred direction at velocities that spanned two orders of magnitude. When blocking Mi1 cells, we found a strong response reduction for all velocities tested

(Figures 2A and 2B). The peak of the residual response was similar to that of control flies (Figure 2B). Flies in which Tm3 cells were silenced showed a drastically different phenotype: For slow velocities, responses were at control level, whereas responses to fast-moving ON edges were severely reduced (Figures 2C and 2D). The maxima of the ON tuning curves of Tm3 block flies were shifted to  $12.5^{\circ} \text{ s}^{-1}$  and  $25^{\circ} \text{ s}^{-1}$ , respectively, as compared to  $100^{\circ} \text{ s}^{-1}$  for control flies. For both Mi1 and Tm3 block flies, the responses to OFF motion remained at control levels. In conclusion, these experiments demonstrate that Tm3 cells are dispensable for the detection of slow ON edges but play a pivotal role in detecting fast ON motion.

#### Directionally Asymmetric Effect of Blocking Tm3 Cells

In addition to presenting edges moving in the preferred direction, we tested responses of Mi1 and Tm3 block flies to null direction stimulation. Control flies responded with a brief transient depolarization followed by a sustained hyperpolarization (Figure 3). For Mi1 block flies, we found a strong response reduction to moving ON edges over all tested velocities (Figures 3A and 3B). For high velocities, Mi1 block flies even showed a slight tonic depolarization, revealing an excitatory input that is largely masked in control flies. The source of this input is currently unknown but may be related to a T4/T5-independent

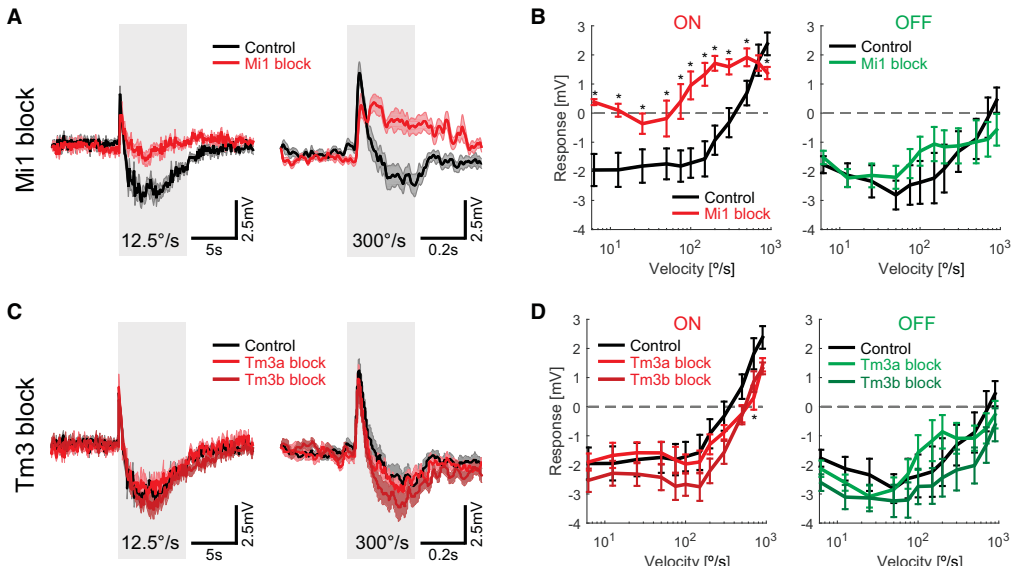


**Figure 3. Voltage Responses of Lobula Plate Tangential Cells in Mi1 and Tm3 Block Flies to Edges Moving in the Null Direction**

(A) Average voltage responses of lobula plate tangential cells of control (black) and Mi1 block flies (red) to slow ( $12.5^{\circ} \text{ s}^{-1}$ ) and fast ( $300^{\circ} \text{ s}^{-1}$ ) ON edges moving in the null direction.

(B) Velocity tuning curves of lobula plate tangential cells of control (black) and Mi1 block flies (red) to ON edges (red) and OFF edges (green) moving in the null direction (control,  $n = 13$ ; Mi1 block,  $n = 11$ ).

(C) Average voltage responses of lobula plate tangential cells of control (black) and Tm3 block (red) flies to slow ( $12.5^{\circ} \text{ s}^{-1}$ ) and fast ( $300^{\circ} \text{ s}^{-1}$ ) ON edges moving in the null direction.

(D) Velocity tuning curves of lobula plate tangential cells of control (black) and Tm3 block flies to ON edges (red) and OFF edges (green) moving in the null direction (control,  $n = 13$ ; Tm3a block,  $n = 15$ ; Tm3b block,  $n = 17$ ).

Data are presented as mean  $\pm$  SEM.  $n$  indicates the number of recorded cells. Significant differences between control and block flies are indicated by asterisks (two-sided Student's *t* test, Benjamini-Hochberg corrected,  $*p < 0.05$ ). Detailed statistics are provided in Table S2. Recordings from VS and HS cells were pooled. See also Figures S1 and S3 and Table S1.

flicker-sensitive pathway [27]. Responses to OFF motion were unaffected. Surprisingly, we did not find any effect of blocking Tm3 cells on responses to null direction motion (Figures 3C and 3D). Thus, the effect of blocking Tm3 cells is not only velocity dependent but is also dependent on the direction of stimulus motion.

Furthermore, we compared resting membrane potentials of control and Mi1 or Tm3 block flies (Table S1) and did not find significant differences. This suggests that a possible tonic synaptic transmission from Mi1 or Tm3 cells does not contribute significantly to the resting membrane potential of VS and HS cells, which otherwise might have influenced the amplitude of visual responses. Additionally, we did not observe any effect on magnitude, velocity tuning, or directional tuning of OFF motion responses for both Mi1 and Tm3 block flies (Figures 2 and 3), arguing for a strict separation of ON and OFF pathways at the level of Mi1 and Tm3.

#### Effects of Blocking Mi1 and Tm3 on Motion-Driven Behavior

In addition to the electrophysiological recordings from lobula plate tangential cells, we tested the functional contribution of Mi1 and Tm3 cells to motion-driven behaviors by blocking their synaptic output and measuring the turning responses of tethered

flies walking on an air-suspended ball [32, 33]. We used the temperature-sensitive silencing tool shibire<sup>ts</sup> [34], which allowed us to block synaptic transmission conditionally by precisely controlling the ambient temperature in our behavioral setup. Thereby, we could rule out developmental effects that may have been caused by silencing Mi1 and Tm3 with Kir2.1 [29]. In order to test the differential impairment of ON and OFF motion channels, we used a balanced motion stimulus [19] and determined velocity tuning curves. This stimulus consists of multiple bright and dark edges moving simultaneously in opposite directions. Flies turn with the direction of moving edges [19]. Thus, wild-type flies with intact ON and OFF motion pathways are expected to show little or no turning responses, whereas flies with an impairment of the ON pathway turn with the direction of moving OFF edges and vice versa [19, 20]. Indeed, control flies showed only small turning responses for all velocities (Figures 4A–4D, black traces). Flies with silenced Mi1 cells, however, turned strongly with the direction of moving OFF edges, reflecting an impairment of the ON motion pathway in accordance with the electrophysiological experiments (Figure 4A). This was true for the whole range of tested velocities (Figure 4B). In contrast, Tm3 block flies showed only small turning responses to slowly moving edges but similarly strong responses as Mi1 block flies at high stimulus velocities (Figures 4C and 4D). The differential effect of silencing Mi1

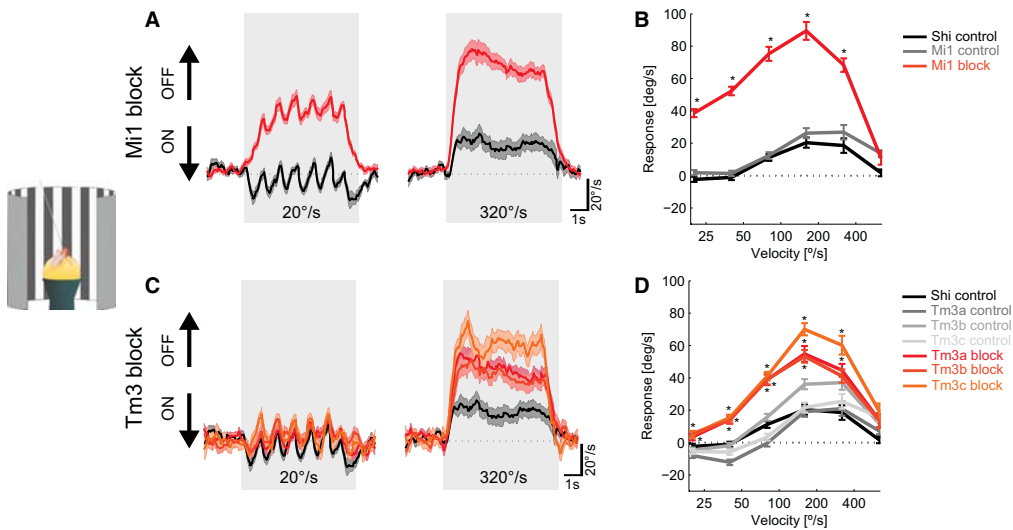


**Figure 4. Behavioral Responses of Mi1 and Tm3 Block Flies**

(A) Average turning speed of shibire control (black) and Mi1 block flies (red) to slow-moving ( $20^{\circ} \text{ s}^{-1}$ ) and fast-moving ( $320^{\circ} \text{ s}^{-1}$ ) opposing ON and OFF edges. Arrows at the left indicate the direction of moving ON and OFF edges.

(B) Velocity tuning curves for control (black and gray) and Mi1 block flies (red) to moving opposing edges (shibire control,  $n = 14$ ; Mi1 control,  $n = 12$ ; Mi1 block,  $n = 16$ ).

(C) Average turning speed of shibire control (black) and Tm3 block flies (red) to slow-moving ( $20^{\circ} \text{ s}^{-1}$ ) and fast-moving ( $320^{\circ} \text{ s}^{-1}$ ) opposing ON and OFF edges. Arrows at the left indicate the direction of moving ON and OFF edges.

(D) Velocity tuning curves for control (black and gray) and Tm3 block flies (red) to moving opposing edges (shibire control,  $n = 14$ ; Tm3a control,  $n = 12$ ; Tm3b control,  $n = 12$ ; Tm3c control,  $n = 13$ ; Tm3a block,  $n = 12$ ; Tm3b block,  $n = 15$ ; Tm3c block,  $n = 12$ ).

In (A) and (C), response traces of Gal4 controls were omitted for clarity. Data are presented as mean  $\pm$  SEM.  $n$  indicates the number of measured flies. Significant differences between both genotype controls and block flies are indicated by asterisks (two-sided Student's *t* test, Benjamini-Hochberg corrected,  $*p < 0.05$ ). Detailed statistics are provided in Table S2. See also Figures S1 and S4.

and Tm3 was again strongest for low velocities and decayed for high velocities, as was seen before in the recordings from lobula plate tangential cells. The velocity range in which Mi1 and Tm3 block flies responded in a similar manner, however, was shifted to higher values compared to the electrophysiological measurements. This discrepancy is reminiscent of the difference in the temporal frequency optimum between lobula plate tangential cells and the optomotor response of walking flies [35] and is therefore likely to be due to the same mechanisms [36, 37]. The behavioral phenotype of Tm3 block flies resembles the preferred direction-specific effect that we observed in the electrophysiological experiments. It is currently unclear whether the hyperpolarization in tangential cells that is caused by null direction stimulation has a direct effect on the turning behavior of walking flies. Our results suggest that the depolarization that is induced by movement in the preferred direction is the dominant, if not the only force that drives turning behavior. Taken together, the findings from behavioral experiments are in agreement with the electrophysiological measurements and suggest a functional specialization of Mi1 and Tm3 cells with respect to their velocity-dependent input to T4 cells.

## DISCUSSION

Direction-selective responses to moving bright edges first arise in T4 cells, but it is still unclear how these responses are shaped by T4's presynaptic inputs. Our results provide insight into this

question and demonstrate that Mi1 is an essential element for the detection of ON motion over all contrasts, velocity ranges, and directions of motion. This is consistent with Mi1 being one of the two input lines of an elementary motion detector. In contrast, Tm3 is dispensable under slow-motion stimulus conditions but necessary for the detection of fast movement in the preferred direction. Consequently, a Tm3-independent mechanism must exist that computes the direction of motion for slowly moving ON edges. Thus, ON motion is detected by at least two functionally specialized, complementary mechanisms: one detector for slow and another for fast motion, both sharing Mi1 cells as a common component. The combined action of these mechanisms allows the fly to detect visual motion over a larger range of velocities and more robustly. Additionally, modulatory or adaptive mechanisms would then be able to affect fast- and slow-motion-detection mechanisms independently.

Mechanistically, our findings give rise to two alternative hypotheses. First, Mi1 alone may be sufficient for generating direction-selective responses in T4 cells at slow velocities. In this scenario, the delay could be implemented by differential temporal filtering of Mi1 inputs that arrive at distal versus proximal locations of T4 cell dendrites. The asymmetric filtering may be due to the passive electrical properties of T4 cell dendrites which would impose a larger delay on signals arriving more distally, possibly in interaction with active dendritic conductances [38, 39]. This would offer a functional explanation for the finding that the anatomical orientation of T4 dendrites correlates with their

directional preference [4]. Indeed, such a role for dendritic morphology in conferring direction selectivity has been found in the Hb9<sup>+</sup> subtype of retinal ganglion cells [40]. For these cells, compatible with our findings, dendritically mediated direction selectivity is only apparent at slow velocities, with inhibition-mediated direction selectivity dominating at high velocities. Alternatively, the delay may be implemented by Mi1 cells that have spatially offset receptive fields and target the same T4 cell dendrite but synapse onto receptors with different temporal transduction properties. Mi1 is reported to be cholinergic [41] and both fast nicotinic and slow muscarinic acetylcholine receptors are expressed in T4 cells [21]. These two scenarios would allow a single cell type (Mi1) to act as both the direct and delayed line, depending on the postsynaptic transduction mechanisms.

As a second hypothesis, additional inputs to T4 cells, other than Mi1 and Tm3, might be essential for the detection of ON motion at low velocities. Indeed, an ongoing connectomic study encompassing a larger volume of the medulla reports additional cells apart from Mi1 and Tm3 providing input to T4 cells (<http://emanalysis.janelia.org>). The strength of these newly described inputs was severely underestimated in the previous study [4], raising the possibility that they play an essential role in generating direction-selective signals in T4. Interestingly, such a scheme has recently been proposed for the OFF pathway, with Tm2 being the instantaneous input line of a motion detector that receives the delayed input from Tm1 and Tm9 cells, which are hypothesized to possess different temporal filtering characteristics [21]. Notably, for the first hypothesis, the delay needs to be implemented postsynaptically to Mi1, whereas the second hypothesis is compatible with a cell-intrinsic delay mechanism. Clearly, a definite understanding of the underlying cellular and biophysical mechanisms will require identification of the sign and temporal characteristics of all T4 synaptic inputs as well as blocking their synaptic output under different stimulus conditions.

Furthermore, our results revealed that the effect of blocking Tm3 cells is dependent on the direction of stimulus motion, with preferred direction responses being selectively affected. This directionally asymmetric effect is reminiscent of the behavioral phenotype that was observed when blocking certain subtypes of lamina cells [18]. Most interestingly, when blocking lamina cells C3, turning responses of tethered flying flies were selectively impaired only when presenting motion from back to front, but not from front to back. As an additional parallel to our Tm3 results, this effect was only present at high stimulus speeds [18]. C3 cells, as Mi1 and Tm3, receive strong input from lamina cells L1 and L5 and form, albeit few, input synapses to T4 [4]. The direction-dependent effect of blocking C3 cells was linked to wiring asymmetries of this cell type. Such an anatomical asymmetry has not yet been reported for Tm3 cells, as the directionality of wiring was not comprehensively analyzed in the recently published medulla connectome [4]. We hypothesize that such an anatomical asymmetry might exist and that it could account for the direction-dependent effect of blocking Tm3 cells that we observed.

In addition to the specific effects of blocking Mi1 or Tm3 on responses to ON motion, we found only a very mild effect on OFF responses. This suggests that Mi1 and Tm3, in contrast to many

lamina cells [17] and in agreement with an increase of rectification from distal to proximal medulla layers [24], feed almost exclusively into the ON pathway.

In conclusion, our study is the first functional demonstration that Mi1 and Tm3 cells are indeed crucial elements of the *Drosophila* ON motion detector, as previously suggested [4, 5]. However, while Mi1 is a necessary component under all stimulus conditions tested, the functionally segregated requirement of Tm3 with respect to stimulus velocity and direction suggests that additional yet unidentified cells or circuit mechanisms are involved as well.

#### SUPPLEMENTAL INFORMATION

Supplemental Information includes Supplemental Experimental Procedures, four figures, and two tables and can be found with this article online at <http://dx.doi.org/10.1016/j.cub.2015.07.014>.

#### AUTHOR CONTRIBUTIONS

G.A. and A. Borst designed the study. G.A. performed electrophysiological experiments and anatomical characterization of expression patterns, analyzed the data, and wrote the manuscript with the help of A. Borst, A.L., and A. Bahl. A.L. and A. Bahl performed behavioral experiments and analyzed data. B.J.D. generated SplitGal4 fly lines and hosted G.A. for characterization of Gal4 lines. A. Borst performed computational modeling.

#### ACKNOWLEDGMENTS

We thank Alexander Arenz and Jesus Pujol-Marti for critical comments on the manuscript, Etienne Serbe and Matthias Meier for many helpful discussions, Christian Theile and Romina Kutlesa for excellent help with behavioral experiments, and Wolfgang Essbauer and Michael Sauter for fly work. G.A., A.L., A. Bahl, and A. Borst are members of the Graduate School of Systemic Neurosciences (GSN) Munich.

Received: May 22, 2015

Revised: July 1, 2015

Accepted: July 2, 2015

Published: July 30, 2015

#### REFERENCES

1. Hassenstein, B., and Reichardt, W. (1956). Systemtheoretische Analyse der Zeit-, Reihenfolgen- und Vorzeichenauswertung bei der Bewegungsperzeption des Ruesselkäfers *Chlorophanus*. *Z. Naturforsch. B 11b*, 513–524.
2. Barlow, H.B., and Levick, W.R. (1965). The mechanism of directionally selective units in rabbit's retina. *J. Physiol.* **178**, 477–504.
3. Borst, A., and Euler, T. (2011). Seeing things in motion: models, circuits, and mechanisms. *Neuron* **71**, 974–994.
4. Takemura, S.Y., Bharioke, A., Lu, Z., Nern, A., Vitaladevuni, S., Rivlin, P.K., Katz, W.T., Olbris, D.J., Plaza, S.M., Winston, P., et al. (2013). A visual motion detection circuit suggested by *Drosophila* connectomics. *Nature* **500**, 175–181.
5. Behnia, R., Clark, D.A., Carter, A.G., Clandinin, T.R., and Desplan, C. (2014). Processing properties of ON and OFF pathways for *Drosophila* motion detection. *Nature* **512**, 427–430.
6. Plaza, S.M., Scheffer, L.K., and Chklovskii, D.B. (2014). Toward large-scale connectome reconstructions. *Curr. Opin. Neurobiol.* **25**, 201–210.
7. Takemura, S.Y. (2015). Connectome of the fly visual circuitry. *Microscopy (Oxf.)* **64**, 37–44.
8. Buchner, E. (1976). Elementary movement detectors in an insect visual system. *Biol. Cybern.* **24**, 86–101.

9. Joesch, M., Plett, J., Borst, A., and Reiff, D.F. (2008). Response properties of motion-sensitive visual interneurons in the lobula plate of *Drosophila melanogaster*. *Curr. Biol.* 18, 368–374.
10. Götz, K.G. (1964). Optomotorische Untersuchung des visuellen Systems einiger Augenmutanten der Fruchtfliege *Drosophila*. *Kybernetik* 2, 77–92.
11. Götz, K.G. (1965). Die optischen Übertragungseigenschaften der Komplexaugen von *Drosophila*. *Kybernetik* 2, 215–221.
12. Schnell, B., Joesch, M., Forstner, F., Raghu, S.V., Otsuna, H., Ito, K., Borst, A., and Reiff, D.F. (2010). Processing of horizontal optic flow in three visual interneurons of the *Drosophila* brain. *J. Neurophysiol.* 103, 1646–1657.
13. Borst, A. (2014). In search of the Holy Grail of fly motion vision. *Eur. J. Neurosci.* 40, 3285–3293.
14. Silies, M., Gohl, D.M., and Clandinin, T.R. (2014). Motion-detecting circuits in flies: coming into view. *Annu. Rev. Neurosci.* 37, 307–327.
15. Joesch, M., Schnell, B., Raghu, S.V., Reiff, D.F., and Borst, A. (2010). ON and OFF pathways in *Drosophila* motion vision. *Nature* 468, 300–304.
16. Joesch, M., Weber, F., Eichner, H., and Borst, A. (2013). Functional specialization of parallel motion detection circuits in the fly. *J. Neurosci.* 33, 902–905.
17. Silies, M., Gohl, D.M., Fisher, Y.E., Freifeld, L., Clark, D.A., and Clandinin, T.R. (2013). Modular use of peripheral input channels tunes motion-detecting circuitry. *Neuron* 79, 111–127.
18. Tuthill, J.C., Nern, A., Holtz, S.L., Rubin, G.M., and Reiser, M.B. (2013). Contributions of the 12 neuron classes in the fly lamina to motion vision. *Neuron* 79, 128–140.
19. Clark, D.A., Bursztyn, L., Horowitz, M.A., Schnitzer, M.J., and Clandinin, T.R. (2011). Defining the computational structure of the motion detector in *Drosophila*. *Neuron* 70, 1165–1177.
20. Maisak, M.S., Haag, J., Ammer, G., Serbe, E., Meier, M., Leonhardt, A., Schilling, T., Bahl, A., Rubin, G.M., Nern, A., et al. (2013). A directional tuning map of *Drosophila* elementary motion detectors. *Nature* 500, 212–216.
21. Shinomiya, K., Karuppudurai, T., Lin, T.Y., Lu, Z., Lee, C.H., and Meinertzhagen, I.A. (2014). Candidate neural substrates for off-edge motion detection in *Drosophila*. *Curr. Biol.* 24, 1062–1070.
22. Takemura, S.Y., Karuppudurai, T., Ting, C.Y., Lu, Z., Lee, C.H., and Meinertzhagen, I.A. (2011). Cholinergic circuits integrate neighboring visual signals in a *Drosophila* motion detection pathway. *Curr. Biol.* 21, 2077–2084.
23. Meier, M., Serbe, E., Maisak, M.S., Haag, J., Dickson, B.J., and Borst, A. (2014). Neural circuit components of the *Drosophila* OFF motion vision pathway. *Curr. Biol.* 24, 385–392.
24. Strother, J.A., Nern, A., and Reiser, M.B. (2014). Direct observation of ON and OFF pathways in the *Drosophila* visual system. *Curr. Biol.* 24, 976–983.
25. Eichner, H., Joesch, M., Schnell, B., Reiff, D.F., and Borst, A. (2011). Internal structure of the fly elementary motion detector. *Neuron* 70, 1155–1164.
26. Mauss, A.S., Meier, M., Serbe, E., and Borst, A. (2014). Optogenetic and pharmacological dissection of feedforward inhibition in *Drosophila* motion vision. *J. Neurosci.* 34, 2254–2263.
27. Schnell, B., Raghu, S.V., Nern, A., and Borst, A. (2012). Columnar cells necessary for motion responses of wide-field visual interneurons in *Drosophila*. *J. Comp. Physiol. A Neuroethol. Sens. Neural Behav. Physiol.* 198, 389–395.
28. Brand, A.H., and Perrimon, N. (1993). Targeted gene expression as a means of altering cell fates and generating dominant phenotypes. *Development* 118, 401–415.
29. Baines, R.A., Uhler, J.P., Thompson, A., Sweeney, S.T., and Bate, M. (2001). Altered electrical properties in *Drosophila* neurons developing without synaptic transmission. *J. Neurosci.* 21, 1523–1531.
30. Luan, H., Peabody, N.C., Vinson, C.R., and White, B.H. (2006). Refined spatial manipulation of neuronal function by combinatorial restriction of transgene expression. *Neuron* 52, 425–436.
31. Jenett, A., Rubin, G.M., Ngo, T.T., Shepherd, D., Murphy, C., Dionne, H., Pfeiffer, B.D., Cavallaro, A., Hall, D., Jeter, J., et al. (2012). A GAL4-driver line resource for *Drosophila* neurobiology. *Cell Rep.* 2, 991–1001.
32. Bahl, A., Ammer, G., Schilling, T., and Borst, A. (2013). Object tracking in motion-blind flies. *Nat. Neurosci.* 16, 730–738.
33. Seelig, J.D., Chiappe, M.E., Lott, G.K., Dutta, A., Osborne, J.E., Reiser, M.B., and Jayaraman, V. (2010). Two-photon calcium imaging from head-fixed *Drosophila* during optomotor walking behavior. *Nat. Methods* 7, 535–540.
34. Kitamoto, T. (2001). Conditional modification of behavior in *Drosophila* by targeted expression of a temperature-sensitive shibire allele in defined neurons. *J. Neurobiol.* 47, 81–92.
35. Chiappe, M.E., Seelig, J.D., Reiser, M.B., and Jayaraman, V. (2010). Walking modulates speed sensitivity in *Drosophila* motion vision. *Curr. Biol.* 20, 1470–1475.
36. Schnell, B., Weir, P.T., Roth, E., Fairhall, A.L., and Dickinson, M.H. (2014). Cellular mechanisms for integral feedback in visually guided behavior. *Proc. Natl. Acad. Sci. USA* 111, 5700–5705.
37. Suver, M.P., Mamiya, A., and Dickinson, M.H. (2012). Octopamine neurons mediate flight-induced modulation of visual processing in *Drosophila*. *Curr. Biol.* 22, 2294–2302.
38. Branco, T., Clark, B.A., and Häusser, M. (2010). Dendritic discrimination of temporal input sequences in cortical neurons. *Science* 329, 1671–1675.
39. Hausselt, S.E., Euler, T., Detwiler, P.B., and Denk, W. (2007). A dendrite-autonomous mechanism for direction selectivity in retinal starburst amacrine cells. *PLoS Biol.* 5, e185.
40. Trenholm, S., Johnson, K., Li, X., Smith, R.G., and Awatramani, G.B. (2011). Parallel mechanisms encode direction in the retina. *Neuron* 71, 683–694.
41. Hasegawa, E., Kitada, Y., Kaido, M., Takayama, R., Awasaki, T., Tabata, T., and Sato, M. (2011). Concentric zones, cell migration and neuronal circuits in the *Drosophila* visual center. *Development* 138, 983–993.

**Current Biology**

**Supplemental Information**

**Functional Specialization of Neural Input Elements**

**to the *Drosophila* ON Motion Detector**

**Georg Ammer, Aljoscha Leonhardt, Armin Bahl, Barry J. Dickson, and Alexander Borst**

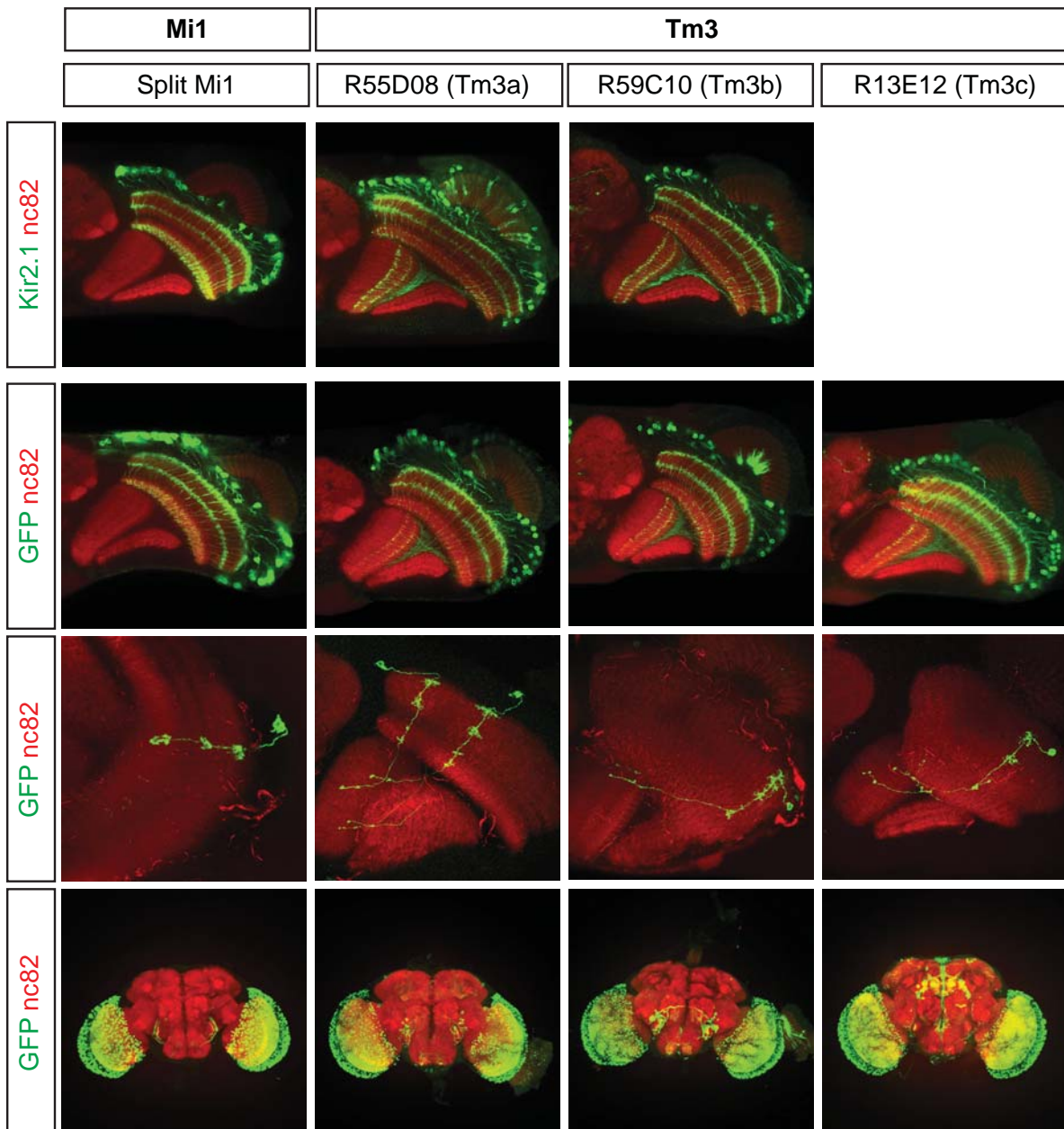


**Figure S1 related to Figures 1-4: Expression Patterns of Gal4 Lines**

Panels in the upper row show horizontal sections of brains dissected from flies with identical genotypes as in the electrophysiological experiments. Expression of Kir2.1 is visualized by staining for the EGFP tag that is fused to the Kir2.1-channel. Lower three panels show horizontal sections (top), single cell flip-outs (middle) and frontal sections (bottom) of brains of all fly lines used in this study. For characterization of expression patterns, UAS-GFP was driven by the respective Gal4 lines (see [Supplemental Experimental Procedures](#) for details).

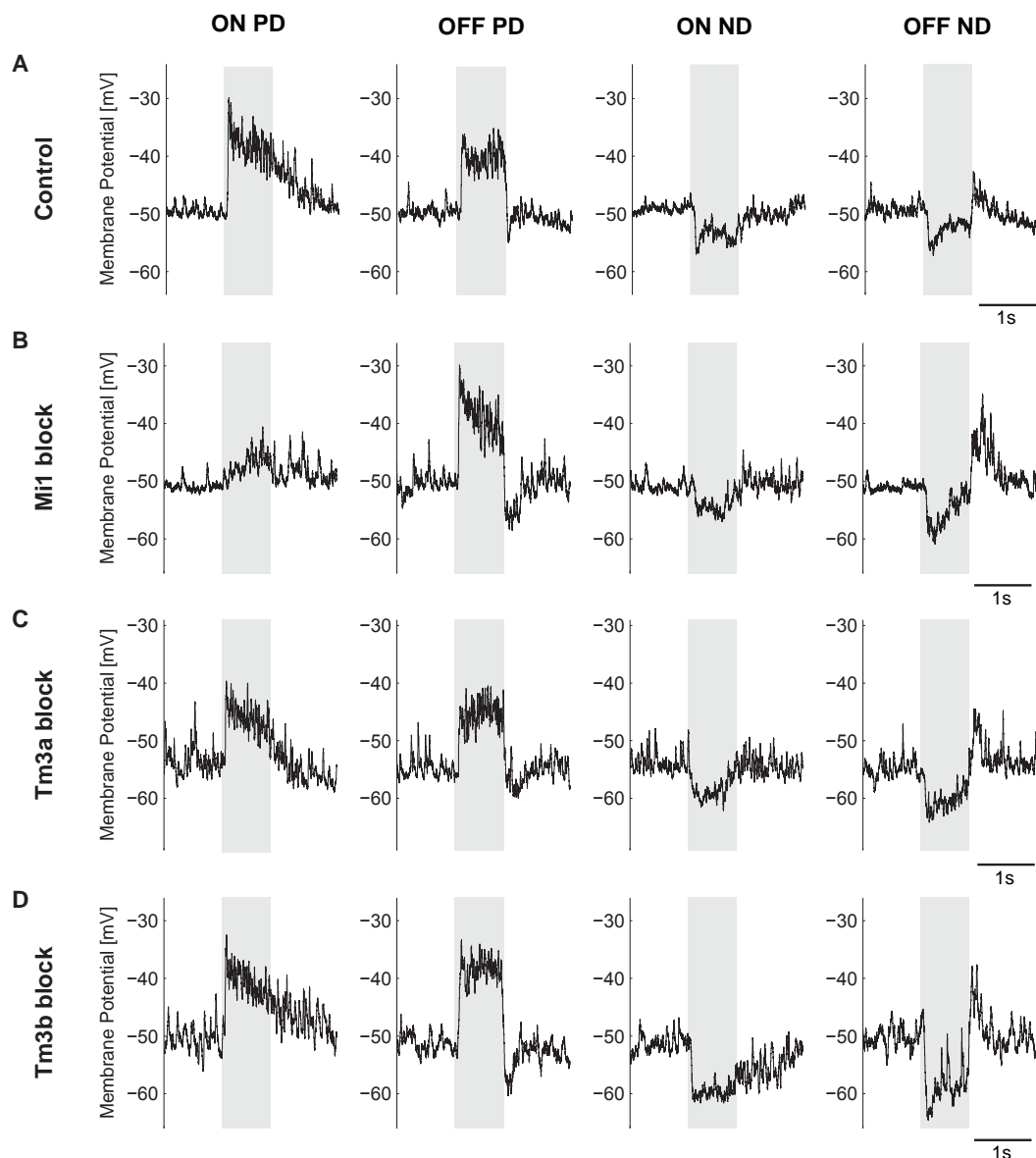


**Figure S2 related to Figure 1: Representative Raw Voltage Traces of Control and Block Flies**  
 Voltage responses of single VS or HS cells to multiple edges moving at a velocity of 50 °/s at full contrast. Traces are shown for ON and OFF edges moving in either the preferred direction (PD) or null direction (ND). (A) Single HS cell recording from a control fly. (B) Single HS cell recording from a Mi1 block fly. (C) Single HS cell recording from a Tm3a block fly. (D) Single VS cell recording from a Tm3b block fly. Grey shaded area indicates the stimulation period. Specific genotypes are listed in [Supplemental Experimental Procedures](#).

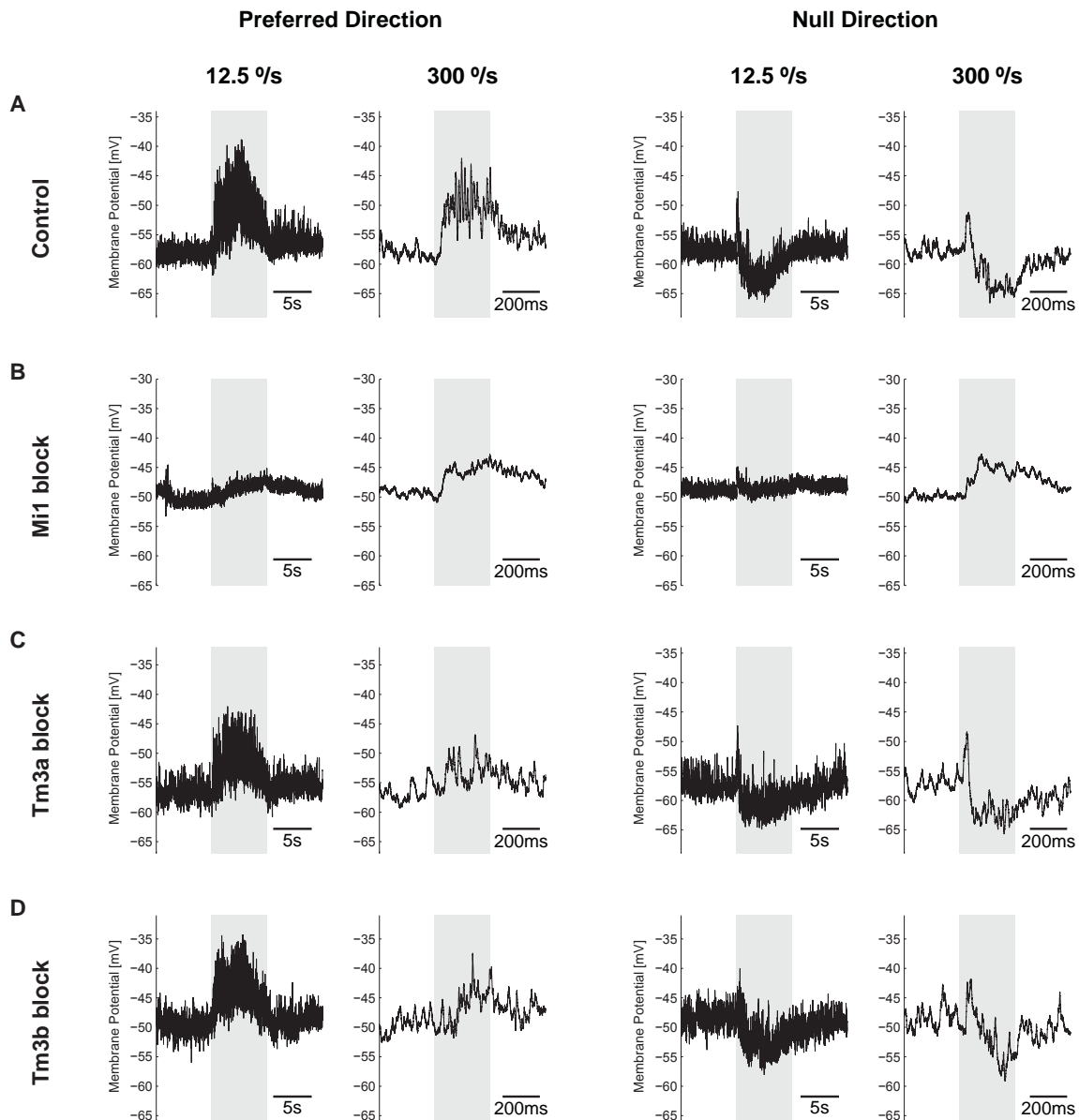


**Figure S3 related to Figures 2 and 3: Representative Raw Voltage Traces of Control and Block Flies**  
 Voltage responses of single VS or HS cells to single ON edges moving in the preferred direction (left panels) or null direction (right panels) at velocities of 12.5 %/s or 300 %/s at full contrast. (A) Single VS cell recording from a control fly. (B) Single VS cell recording from a Mi1 block fly. (C) Single VS cell recording from a Tm3a block fly. (D) Single VS cell recording from a Tm3b block fly. Grey shaded area indicates the stimulation period. Specific genotypes are listed in [Supplemental Experimental Procedures](#).

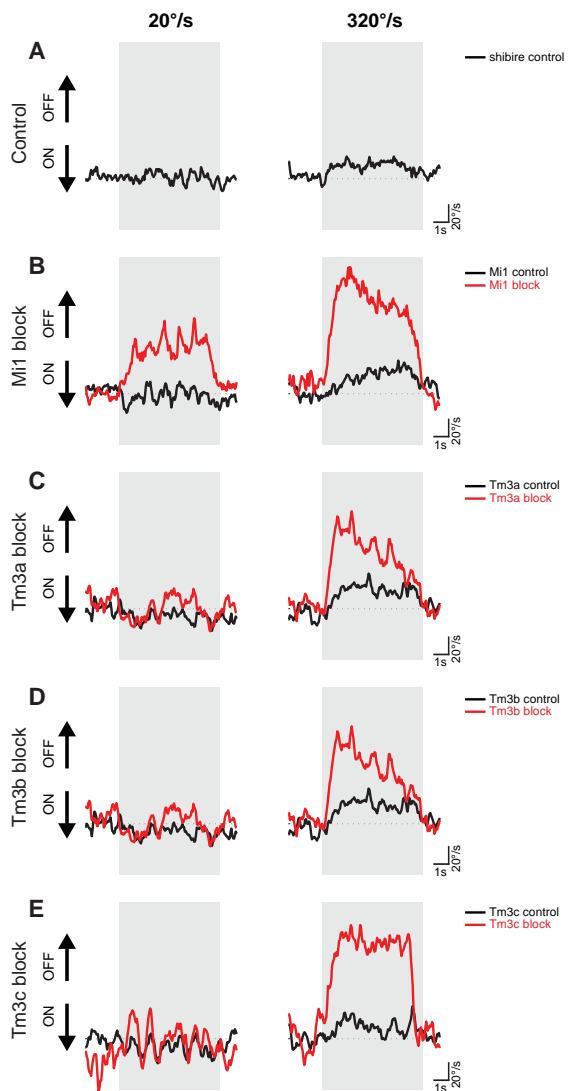


**Figure S4 related to Figure 4: Representative Single Fly Responses of Control and Block Flies**

Turning responses of single flies to multiple opposing edges moving at a velocity of either 20 °/s or 300 °/s. (A) Turning response of a single shibire control fly. (B) Turning response of a single Mi1 control fly (black) and Mi1 block fly (red). (C) Turning response of a single Tm3a control fly (black) and Tm3a block fly (red). (D) Turning response of a single Tm3b control fly (black) and Tm3b block fly (red). (E) Turning response of a single Tm3c control fly (black) and Tm3c block fly (red). Grey shaded area indicates the stimulation period. Specific genotypes are listed in [Supplemental Experimental Procedures](#).

Figure 1 E, F

Genotype	mean (mV)	s.e.m. (mV)	n (cells)
Control	-51.88	0.61	16
Mi1	-51.67	0.76	21
R55D08 (Tm3a)	-53.00	0.50	23
R59C10 (Tm3b)	-51.89	0.66	20

Figure 1 G, H

Genotype	mean (mV)	s.e.m. (mV)	n (cells)
Control	-51.75	0.65	12
Mi1	-51.64	0.63	14
R55D08 (Tm3a)	-53.44	0.69	9
R59C10 (Tm3b)	-51.75	0.98	10

Figure 2, 3

Genotype	mean (mV)	s.e.m. (mV)	n (cells)
Control	-51.58	0.81	13
Mi1	-51.50	0.70	11
R55D08 (Tm3a)	-52.07	0.52	15
R59C10 (Tm3b)	-52.06	0.71	17

**Table S1 related to Figures 1-3: Resting Membrane Potentials of Lobula Plate Tangential Cells**

Mean and s.e.m. of the resting membrane potentials of all recorded cells are listed. n denotes the number of recorded cells. Resting membrane potentials were corrected for a liquid junction potential of -12 mV. We did not find any statistically significant difference ( $p < 0.05$ ) between controls and all tested genotypes when applying an unpaired two-sided Student's t-test. Specific genotypes are listed in [Supplemental Experimental Procedures](#).

**Table S2 related to Figures 1-4: Detailed Statistics for all Figures**

n-numbers, p-values and t-values for all statistical tests applied throughout the study. Statistical significance was tested by using a two-sided Student's t-test followed by a Benjamini-Hochberg correction (\* p<0.05). Table S2 is supplied as a separate Excel spreadsheet.

## Supplemental Experimental Procedures

### Fly Stocks

Flies were reared on cornmeal agar medium under standard conditions (25° C, 60% humidity, 12hr dark/light cycle). For electrophysiology flies were used 5-30 hours post-eclosion. For behavioral experiments flies were aged 1-3 days. Only female flies were used in all experiments.

Genotypes of all fly strains used in the experiments:

### Figures 1 - 3

$w^+ / w^-$ ; 10xUAS-Kir2.1-EGFP / + ; + (Control)

$w^+ / w^-$ ; 10xUAS-Kir2.1-EGFP / VT7747AD ; VT49371DBD / + (Mi1 block)

$w^+ / w^-$ ; 10xUAS-Kir2.1-EGFP / + ; R55D08-Gal4 / + (Tm3a block)

$w^+ / w^-$ ; 10xUAS-Kir2.1-EGFP / + ; R59C10-Gal4 / + (Tm3b block)

### Figure 4

$w^+ / w^-$ ; 20xUAS-shibire<sup>ts</sup> / + ; + (Shi control)

$w^+ / w^-$ ; VT7747AD / + ; VT49371DBD / + (Mi1 control)

$w^+ / w^-$ ; + / +; R55D08-Gal4 / + (Tm3a control)

$w^+ / w^-$ ; + / +; R59C10-Gal4 / + (Tm3b control)

$w^+ / w^-$ ; + / +; R13E12-Gal4 / + (Tm3c control)

$w^+ / w^-$ ; 20xUAS-shibire<sup>ts</sup> / VT7747AD ; VT49371DBD / + (Mi1 block)

$w^+ / w^-$ ; 20xUAS-shibire<sup>ts</sup> / + ; R55D08-Gal4 / + (Tm3a block)

w<sup>+</sup> / w<sup>-</sup>; 20xUAS-shibire<sup>ts</sup> / +; R59C10-Gal4 / + (Tm3b block)

w<sup>+</sup> / w<sup>-</sup>; 20xUAS-shibire<sup>ts</sup> / +; R13E12-Gal4 / + (Tm3c block)

### Figure S1

For analysis of expression patterns:

w<sup>+</sup> / w<sup>-</sup>; UAS-mCD8-GFP, UAS-syt-HA / VT7747AD ; VT49371DBD / + (Mi1)

w<sup>+</sup> / w<sup>-</sup>; UAS-mCD8-GFP, UAS-syt-HA / + ; R55D08-Gal4 / + (Tm3a)

w<sup>+</sup> / w<sup>-</sup>; UAS-mCD8-GFP, UAS-syt-HA / + ; R59C10-Gal4 / + (Tm3b)

w<sup>+</sup> / w<sup>-</sup>; UAS-mCD8-GFP, UAS-syt-HA / + ; R13E12-Gal4 / + (Tm3c)

For single cell flip-outs:

w<sup>-</sup>, pBPhsFlp2::PEST / w<sup>-</sup>; VT7747AD / +; VT49371DBD / UAS-FRT>>FRT-myr::GFP (Mi1)

w<sup>-</sup>, pBPhsFlp2::PEST / w<sup>-</sup>; + / + ; R55D08-Gal4 / UAS-FRT>>FRT-myr::GFP (Tm3a)

w<sup>-</sup>, pBPhsFlp2::PEST / w<sup>-</sup>; + / + ; R59C10-Gal4 / UAS-FRT>>FRT-myr::GFP (Tm3b)

w<sup>-</sup>, pBPhsFlp2::PEST/w<sup>-</sup>; + / + ; R13E12-Gal4 / UAS-FRT>>FRT-myr::GFP (Tm3c)

### Immunohistochemistry and confocal microscopy

Antibody stainings were performed as previously described [S1]. We generated single cell flip-outs using a recently published method [S2]. Briefly, brains were dissected in PBS, fixed in 4% PFA (containing 0.1% Triton-X) for 25 min, washed 3x in PBT (PBS containing 0.3% Triton-X) and blocked with 10% NGS in PBT. Primary antibodies were diluted in PBT containing 5% NGS and incubated for 48 hrs at 4°C. After washing 3x in PBT, brains were incubated in secondary antibody solution for 48-72 hrs at 4°C. After washing 3x in PBT and 1x in PBS, brains were mounted in Vectashield (Vector labs). Following antibodies were used in this study:

Primary antibodies: rabbit anti-GFP (Torri Pines, 1:2000), mouse anti-nc82 (DSHB, 1:25); secondary antibodies: goat anti-rabbit 488 (Invitrogen, 1:500), goat anti-mouse 633 (Invitrogen, 1:500). Imaging was performed on a Leica SP5 confocal microscope with a 63x objective (HCx PL APO, 1.40 NA, Leica) for horizontal sections or a 20x objective (HC PL APO, 0.70 NA, Leica) for vertical sections at a resolution of 1024x1024. Images were processed in ImageJ 1.46f (NIH). Single z-slices are shown for horizontal views and maximum intensity projections for single cell flip-outs and frontal views.

## **Electrophysiology**

Flies were anesthetized on ice, waxed to a plexiglas holder, inserted into an opening cut into aluminum foil and mounted in a recording chamber. A part of the posterior side of the head cuticle and the muscle that covers the cell bodies of LPTCs was removed with a needle and fine forceps. Extracellular saline (103 mM NaCl, 3 mM KCl, 5 mM TES, 10 mM trehalose, 10 mM glucose, 7 mM sucrose, 26 mM NaHCO<sub>3</sub>, 1 mM NaH<sub>2</sub>PO<sub>4</sub>, 1.5 mM CaCl<sub>2</sub> and 4 mM MgCl<sub>2</sub>, pH 7.3, 280 mOsm) was bubbled with 95% O<sub>2</sub> and 5% CO<sub>2</sub> and perfused over the preparation. The brain of the fly was visualized with an upright microscope (Axiotech Vario 100, Zeiss) equipped with a 40x water-immersion objective (LumPlanFL, NA 0.8, Olympus), an Hg-light source (HXP-120, Visitron Systems) and polarization filters for contrast enhancement. A glass electrode filled with collagenase (Collagenase IV, Gibco, 0.5 mg ml in extracellular saline) was used to expose the somata of LPTCs. Somata of VS and HS cells were patched with a glass electrode (5–9 MΩ) filled with internal solution (140 mM potassium aspartate, 10 mM HEPES, 4 mM Mg-ATP, 0.5 mM Na-GTP, 1 mM EGTA, 1 mM KCl and 0.03 mM Alexa 568-hydrazide sodium, pH 7.26, 265 mOsm). Recordings were performed with an NPI BA-1S amplifier (NPI electronics) in

current-clamp bridge mode, low-pass filtered with a cut-off frequency at 3 kHz and digitized at 10 kHz. Data acquisition was performed with Matlab (version R2011a, MathWorks). Cell types were identified on the basis of their typical response profiles to moving gratings. In addition, the majority of recorded cells were dye filled and their identity verified anatomically.

### **Visual stimulation**

Visual stimulation was performed with a custom-built LED arena that had dimensions of 170° in azimuth and 90° in elevation and a spatial resolution of approximately 1.4° per LED. The arena allowed refresh rates of up to 600 Hz and had a maximum luminance of 80 cd m<sup>-2</sup>. Data analysis was performed with Matlab (version R2011b, MathWorks) using custom-written scripts. Multiple moving edges were presented as standing square wave gratings with a wavelength of 42°. During stimulation, either all the bright or all the dark edges of the grating moved at a velocity of 50° s<sup>-1</sup> for 0.45 s. To measure contrast tuning curves we varied the contrast of the gratings from 6% to 100% while keeping the mean luminance constant. To determine velocity tuning curves we used single edges at full contrast that covered at distance of 90° moving at the following velocities: 6.25, 12.5, 25, 50, 75, 100, 150, 200, 300, 500, 700 and 900 ° s<sup>-1</sup>. Different velocities were presented in randomized order. Edges moved in the horizontal direction when recording from HS cells and in the vertical direction when recording from VS cells.

### **Data Analysis**

For all stimuli, we averaged voltage traces during the whole stimulation period and calculated the mean and standard errors over cells.

## Behavioral experiments

Flies were cold anesthetized before the experiment. Head, thorax, and wings were glued to a needle with near-UV bonding glue (Sinfony Opaque Dentin) and blue LED light (440 nm, dental curing-light, New Woodpecker). Flies were then placed on an air-suspended polyurethane ball in a virtual environment projected onto three monitors spanning approximately 270° (vertical) and 114° (horizontal) of the fly's visual field. This stimulation system offered less than 0.1° of angular pixel size, a value well below *Drosophila*'s optical resolution capability. We used six such setups for recording fly locomotion as described previously [S3]. On two setups, stimuli were presented at a screen refresh frequency of 120 Hz; on four setups, the refresh frequency was 144Hz. We never observed qualitative or quantitative differences between these setups in any of the experiments. All monitors were equilibrated in brightness and contrast. Temperature within the immediate surround of the fly was controlled using a custom-built closed-loop thermoregulation system. We employed the following temperature protocol for all experiments and genotypes: Temperature was kept at 25°C for the first 5 minutes and then, within 10 minutes, raised to a restrictive temperature of 34°C.

## Visual Stimulation

Our balanced motion stimulus resembled the one used in previous studies [S4, S5]. Briefly, we presented flies with a stationary square wave grating that had an initial spatial wavelength of 45° visual angle and Michelson contrast of 50%. Each individual trial lasted 9s. Between 2s and 7s, bright edges moved in one direction at a fixed velocity while dark edges moved in the other direction at the same velocity. In contrast to previous versions, we reset the stimulus to the initial state after edges had traversed 20° of visual angle. This allowed us to keep the stimulus duration

fixed for varying edge velocities. Additionally, we applied a random phase shift after each reset in order to rule out symmetry effects. This was done for 6 velocities (20, 40, 80, 160, 320, and  $640^{\circ} \text{ s}^{-1}$ ) and 2 possible edge directions (dark edge leftwards/bright edge rightwards and vice versa), resulting in 12 conditions that were repeated 50 times per fly. The stimulus was rendered in real-time using Panda3D, an open source game engine, and Python 2.7.

## Data Analysis

We analyzed the data as described previously [S5]. Briefly, optical tracking sensors were equipped with lens and aperture systems to focus on the sphere behind the fly. The tracking data were processed at 4 kHz internally, read out via a USB interface and processed by a computer at 100 Hz. This allowed real-time calculation of the instantaneous rotation axis of the sphere. We resampled the rotation traces to 20Hz for further processing and applied a first-order low pass filter with a time constant of 100ms to each trace. For all flies, we manually selected 20 consecutive trials out of the 50 available that fulfilled the following criteria: First, the temperature was at a stable  $34^{\circ}\text{C}$ . Second, the average turning tendency of the fly was approximately  $0^{\circ} \text{ s}^{-1}$ . Third, the average forward velocity of the fly was at least  $5\text{mm s}^{-1}$ , indicating a visually responsive state. Flies were selected without blinding. Application of the criteria excluded, on average, 20% of all measured flies. For further processing, we subtracted responses for the two symmetrical edge directions in order to reduce the impact of walking asymmetries. Trials were then averaged. For statistical purposes, we calculated the turning tendency of each fly for each velocity condition as the mean of the turning response between 3s (walking onset) and 7s (stimulus offset). Other evaluation time frames produced qualitatively equivalent results. All data analysis was performed using Python 2.7 and the NumPy library.

## Modeling

Modeling the motion detection pathway followed Eichner et al., 2011 [S6]. Briefly, stimuli were represented as brightness values between 0 and 1 at the level of 40x40 photoreceptors with an angular resolution of 5° at a temporal resolution of 10 ms. Signals of lamina cells L1 and L2 were calculated by high-pass filtering (time-constant 250 ms) the photoreceptor input plus 10% of their DC level. The ON (L1) signal was obtained by half-wave rectifying the signal at a threshold of 0, the OFF (L2) signal was inverted and half-wave rectified at a threshold of 0.05. These signals were then processed by separate ON- and OFF-motion detectors. Within each detector (Figure 1A), the output signal of the lamina cell at one location was low-pass filtered ( $\tau = 50$  ms) and subsequently multiplied with the instantaneous signal of the lamina cell from the adjacent location. This was done twice in a mirror-symmetrical way and the results subtracted from each other. Finally, the output signals of all ON- and OFF-motion detectors were added.

## Statistics

Throughout the paper we tested for statistical significance by using a two-sided Student's t-test followed by a Benjamini-Hochberg correction (\*  $p < 0.05$ ). Detailed statistics are documented in [Table S2](#).

## Supplemental References

- S1. Yu, J.Y., Kanai, M.I., Demir, E., Jefferis, G.S., and Dickson, B.J. (2010). Cellular organization of the neural circuit that drives *Drosophila* courtship behavior. *Curr Biol* 20, 1602-1614.
- S2. Nern, A., Pfeiffer, B.D., and Rubin, G.M. (2015). Optimized tools for multicolor stochastic labeling reveal diverse stereotyped cell arrangements in the fly visual system. *PNAS* 112, 2967-2976.

- S3. Bahl, A., Ammer, G., Schilling, T., and Borst, A. (2013). Object tracking in motion-blind flies. *Nat Neurosci* *16*, 730-738.
- S4. Clark, D.A., Burszty, L., Horowitz, M.A., Schnitzer, M.J., and Clandinin, T.R. (2011). Defining the computational structure of the motion detector in *Drosophila*. *Neuron* *70*, 1165-1177.
- S5. Maisak, M.S., Haag, J., Ammer, G., Serbe, E., Meier, M., Leonhardt, A., Schilling, T., Bahl, A., Rubin, G.M., Nern, A., et al. (2013). A directional tuning map of *Drosophila* elementary motion detectors. *Nature* *500*, 212-216.
- S6. Eichner, H., Joesch, M., Schnell, B., Reiff, D.F., and Borst, A. (2011). Internal structure of the fly elementary motion detector. *Neuron* *70*, 1155-1164.

## Manuscript III

### The Temporal Tuning of the *Drosophila* Motion Detectors Is Determined by the Dynamics of Their Input Elements

Alexander Arenz\*, Michael S. Drews\*, Florian G. Richter, **Georg Ammer**, and Alexander Borst

\* equal contribuiton

#### Author Contributions

A.A., M.S.D., and A.B. conceived the study and designed the experiments. A.A. conducted and analyzed the measurements of T4/T5 cell responses. M.S.D. designed the projector-based stimulation arena and performed and analyzed the measurements of the OFF-pathway elements. F.G.R. performed and analyzed the experiments describing the ON-pathway neurons. **G.A.** performed and analyzed the patch-clamp recordings from lobula plate tangential cells. M.S.D. performed the computer simulations. A.A. wrote the manuscript with the help of all authors.

**Current Biology** 27, 929-944. doi: 10.1016/j.cub.2017.01.051.

# Current Biology

## The Temporal Tuning of the *Drosophila* Motion Detectors Is Determined by the Dynamics of Their Input Elements

### Highlights

- Input neurons to the fly motion detectors show diverse temporal filter properties
- Octopamine activation accelerates detector velocity tuning and input cell dynamics
- Dynamics of input neurons correctly predict velocity tuning of motion detectors

### Authors

Alexander Arenz, Michael S. Drews,  
Florian G. Richter, Georg Ammer,  
Alexander Borst

### Correspondence

arenz@neuro.mpg.de

### In Brief

Recent algorithmic models of visual motion detection in the fly rely on processing of three input channels. By characterizing the spatiotemporal response properties of the neurons presynaptic to fly motion-sensing cells across two tuning states, Arenz, Drews, et al. predict functional roles for these neurons in computing the direction of motion.



Arenz et al., 2017, Current Biology 27, 929–944  
April 3, 2017 © 2017 Elsevier Ltd.  
<http://dx.doi.org/10.1016/j.cub.2017.01.051>

CellPress

# The Temporal Tuning of the *Drosophila* Motion Detectors Is Determined by the Dynamics of Their Input Elements

Alexander Arenz,<sup>1,2,3,\*</sup> Michael S. Drews,<sup>1,2</sup> Florian G. Richter,<sup>1</sup> Georg Ammer,<sup>1</sup> and Alexander Borst<sup>1</sup>

<sup>1</sup>Department of Circuits—Computation—Models, Max Planck Institute of Neurobiology, Am Klopferspitz 18, 82152 Martinsried, Germany

<sup>2</sup>Co-first author

<sup>3</sup>Lead Contact

\*Correspondence: arenz@neuro.mpg.de

<http://dx.doi.org/10.1016/j.cub.2017.01.051>

## SUMMARY

Detecting the direction of motion contained in the visual scene is crucial for many behaviors. However, because single photoreceptors only signal local luminance changes, motion detection requires a comparison of signals from neighboring photoreceptors across time in downstream neuronal circuits. For signals to coincide on readout neurons that thus become motion and direction selective, different input lines need to be delayed with respect to each other. Classical models of motion detection rely on non-linear interactions between two inputs after different temporal filtering. However, recent studies have suggested the requirement for at least three, not only two, input signals. Here, we comprehensively characterize the spatiotemporal response properties of all columnar input elements to the elementary motion detectors in the fruit fly, T4 and T5 cells, via two-photon calcium imaging. Between these input neurons, we find large differences in temporal dynamics. Based on this, computer simulations show that only a small subset of possible arrangements of these input elements maps onto a recently proposed algorithmic three-input model in a way that generates a highly direction-selective motion detector, suggesting plausible network architectures. Moreover, modulating the motion detection system by octopamine-receptor activation, we find the temporal tuning of T4 and T5 cells to be shifted toward higher frequencies, and this shift can be fully explained by the concomitant speeding of the input elements.

## INTRODUCTION

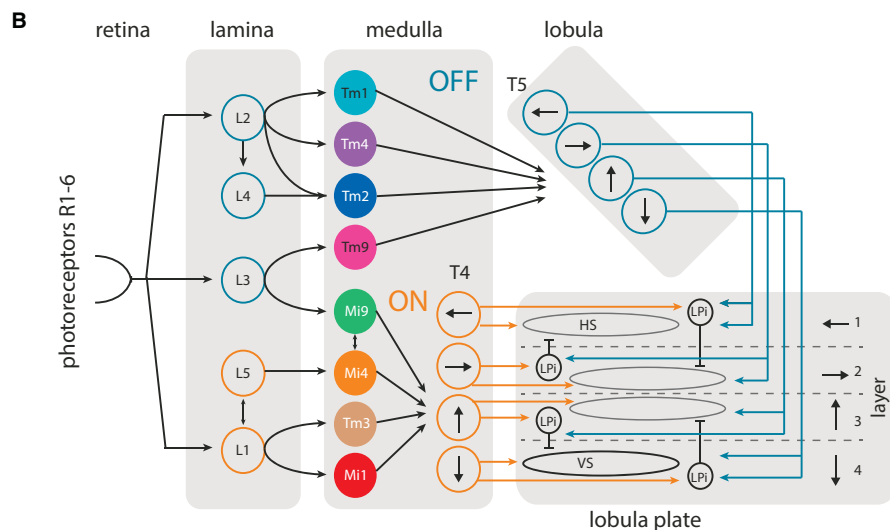
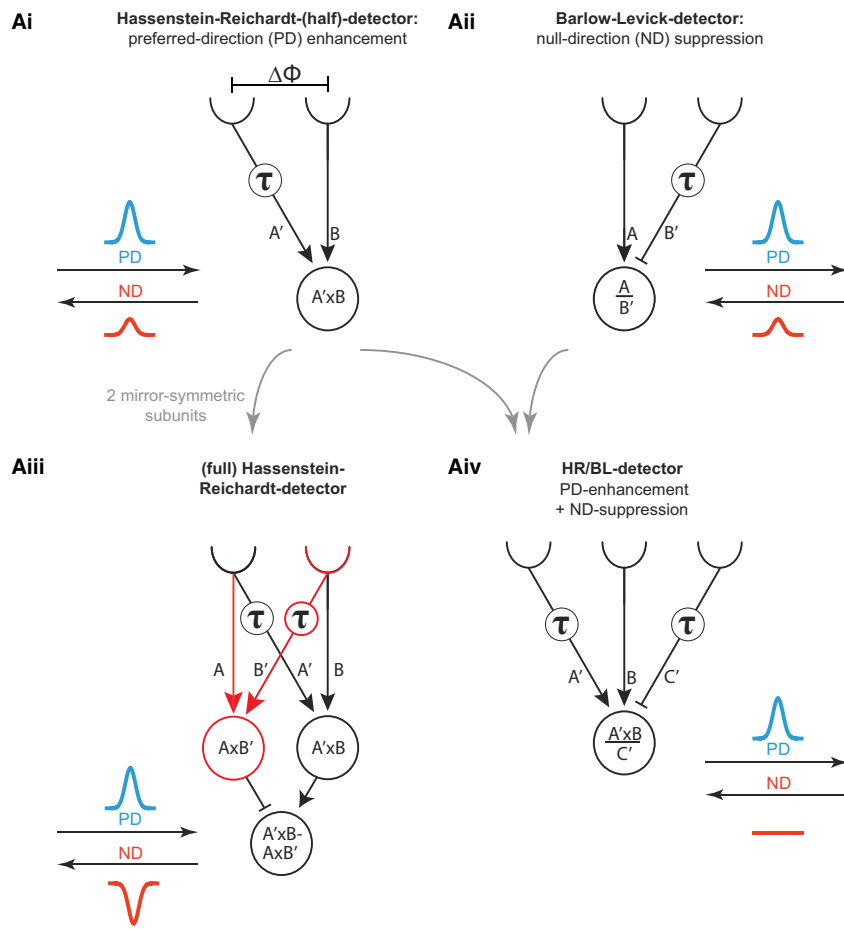
The detection of visual motion arising from ego-motion is crucial for course stabilization in flies [1]. Sets of large tangential cells in the lobula plate of the fly optic lobe respond selectively to the optic flow resulting from whole-body rotation around different axes. As single photoreceptors respond to local luminance

changes in a non-direction-selective way, the intervening circuitry of the optic lobe [2–5] (Figure 1) must serve to extract the feature of visual motion by spatiotemporal comparison of the responses of neighboring photoreceptors.

Two competing algorithmic models of motion detectors have been proposed (Figure 1A). Both models rely on asymmetric temporal filtering of two input signals that are then fed into a non-linearity. They differ by the type of non-linearity employed and the location of the delay filter. In the Barlow-Levick (BL) detector (Figure 1Aii) [6], the delay is located on the preferred side and the non-linearity is inhibitory, leading to a suppression of signals moving in the null direction (ND). In the Hassenstein-Reichardt (HR) detector (Figure 1Ai) [7], the delay is located on the null side and the non-linearity is excitatory, leading to an enhancement of signals moving in the preferred direction (PD). In the full HR detector (Figure 1Aiii), two of those subunits, or half-detectors, are arranged in a mirror-symmetric fashion and subtracted from each other to yield a fully opponent detector (for review, see [8]).

How do the proposed elements of these algorithmic models map onto the neural circuits of the fly, and how does direction selectivity arise? The fly optic lobe consists of four neuropils downstream of the retina: the lamina, medulla, lobula, and lobula plate (Figure 1B). Photoreceptors synapse onto lamina monopolar cells. These lamina cells feed into two separate pathways encoding for different contrast polarities [9–11]: the ON pathway encodes brightness increments, and the OFF pathway encodes brightness decrements. In each pathway, the direction of visual motion is computed separately [12, 13]. In both pathways, lamina neurons connect onto a distinct set of medulla neurons. In the ON pathway, these medulla neurons have axon terminals in layer 10 of the medulla, where they overlap with the dendrites of T4 neurons [4]. In the OFF pathway, transmedulla neurons project to the lobula, where they synapse onto the dendrites of T5 neurons [5]. T4 and T5 neurons each fall into four subclasses, which respond selectively to visual motion in one of the four cardinal directions (front-to-back, back-to-front, up, and down) and project their axons according to this preference to one of the four layers of the lobula plate [14]. There, T4 and T5 cells converge and provide direct excitatory cholinergic input onto wide-field lobula plate tangential cells [15]. In addition, T4 and T5 cells synapse onto lobula plate intrinsic (LPI) neurons, which in turn inhibit tangential cells in the adjacent, oppositely tuned layer [16], making tangential cells fully motion opponent. Hence, T4 and T5





(legend on next page)

neurons would represent the half-detector units of the fully opponent motion detector model just before the subtraction stage. Although the HR detector describes the responses of lobula plate tangential cells well, the responses of T4 and T5 neurons are more directionally selective than would be expected for the half-detectors of the HR model [14, 17].

In the ON pathway, medulla intrinsic neuron 1 (Mi1) and transmedullary neuron 3 (Tm3) were originally suggested as the main inputs onto T4 neurons from electron-microscopic reconstructions [4]. These data showed a small spatial offset of about a fifth of a column, about 1° in visual space, between Mi1 and Tm3 synapsing onto the same T4 neuron, with Tm3 located toward the null side of the T4 neuron. Based on this spatial offset, two possible implementations of the motion detector were suggested: a HR correlator with Tm3, or a BL detector with Mi1, as the delayed arm. Subsequent patch-clamp recordings showed a small temporal delay of ~20 ms for Mi1 with regard to Tm3, as well as a similar temporal offset of Tm1 with respect to Tm2 in the OFF pathway [18]. This led to the suggestion of HR correlator implementations with Mi1 and Tm1 as the delayed and Tm3 and Tm2 as the direct arms in the ON and the OFF pathway, respectively [18, 19].

However, new findings from several recent studies question this model. First, new electron-microscopic circuit reconstructions show additional synaptic input from Mi4 and Mi9 cells onto T4 cells (Lou Scheffer, personal communication; [https://web.archive.org/web/20150218101857/http://emanalysis.janelia.org/flyem\\_tables.php](https://web.archive.org/web/20150218101857/http://emanalysis.janelia.org/flyem_tables.php)), and from the transmedulla neurons Tm4 and Tm9 onto T5 cells [5]. Second, when all four input cell types in the OFF pathway were considered, large differences in their temporal response kinetics to flashes of dark bars were revealed [20]. Whereas Tm1, Tm2, and Tm4 respond like band-pass filters with different time constants, Tm9 has the response characteristic of a pure low-pass filter, together forming a filter bank that lends itself well to the construction of motion detectors. Third, whereas blocking the synaptic output of Mi1 severely reduces responses of tangential cells to moving ON edges, blocking Tm3 output only affects responses to edges moving at higher angular velocities but leaves responses to lower velocities unchanged [21]. This again argues against Tm3 being one of the two arms of the motion detector under all conditions. Similarly, in the OFF pathway, all four cell types were shown to contribute to the detection of moving OFF edges. Blocking their synaptic output decreased the responses of downstream tangential cells and

reduced the optomotor response to OFF edges [20]. However, no blocks of single cell types or of two types in combination fully abolished the responses to dark edges, suggesting either redundancy or a more complicated implementation than previously suggested. Fourth, recent experiments based on the sequential stimulation of individual laminar cartridges revealed that the elementary motion detectors in the ON pathway, T4 neurons, implement ND suppression [17] in addition to PD enhancement [22] (Figure 1Aiv). Spatiotemporal receptive fields of T5 neurons are consistent with a similar model in the OFF pathway [23]. This more elaborate motion detector implementation could explain the high direction selectivity. However, in contrast to both HR and BL detectors, it relies on at least three input elements.

Taken together, in both pathways, evidence mounts for a neural implementation that is more complicated than either the BL or the HR model alone, and there is a multitude of combinations possible to place the known columnar input elements into the proposed algorithmic three-arm model of the *Drosophila* motion detectors.

In order to dissect the roles and contributions of individual cell types, it would be helpful to modify their temporal response dynamics and observe the effect on the downstream motion detectors. One remarkable property of tangential cells is that their velocity tuning is not fixed but dependent on the behavioral state of the fly, as has been observed in *Drosophila* and *Lucilia*. In walking [24] as well as in tethered flying flies [25, 26], the temporal-frequency tuning shifts toward higher frequencies, corresponding to higher velocities, potentially matching the expected change of the stimulus statistics from resting to active locomotion. The behavioral effect can be mimicked in resting flies by pharmacological activation of octopamine receptors with octopamine [26] or the octopamine agonist chlordimeform (CDM) [25, 27]. The physiological source of this neuromodulation is octopaminergic neurons that project to the medulla, lobula, and lobula plate [28, 29]. They become activated during flight and are both necessary and sufficient for the increase in responses to higher temporal frequencies [26]. Importantly, this change in the temporal tuning could be reproduced in computer simulations by decreasing the low-pass filter time constant in the HR detector [25], indicating that identifying the input elements that change their kinetics under octopamine activation might help to pinpoint their functional roles in the detector.

#### Figure 1. Theoretical Models for Visual Motion Detection and the Underlying Neuronal Circuitry

(A) Algorithmic models of motion detectors based on variations of a common theme of spatiotemporal correlations of local luminance changes detected by photoreceptors. (Ai) In the Hassenstein-Reichardt (HR) correlator (of which a half-detector is shown here), a delay ( $\tau$ ) on the first of two arms activated by motion in the preferred direction (PD) causes coincidence of the two signals from neighboring photoreceptors (separated by an angle,  $\Delta\phi$ ). A multiplicative non-linearity results in a PD enhancement. (Aii) In the Barlow-Levick (BL) detector the delay is located on the opposite arm, and the non-linearity is suppressive/inhibitory, causing a null-direction (ND) suppression. (Aiii) In the full HR correlator, two mirror symmetric subunits from (Ai) are subtracted, resulting in a fully opponent detector, which not only depolarizes in PD but also hyperpolarizes in ND. (Aiv) A recently proposed model, based on the responses of T4 neurons to apparent motion stimuli, combines PD enhancement and ND suppression along the PD axis.

(B) Schematic of the circuitry of the *Drosophila* optic lobe showing neuron classes suggested to be involved in visual motion detection. Local luminance changes are detected by photoreceptors in the retina and relayed via lamina monopolar neurons (classes L1–L5) and medulla neurons (Mi1, Tm3, Mi4, Mi9, Tm1, Tm2, Tm4, and Tm9) to T4 and T5 neurons. The latter are the first neurons in the visual pathway that respond selectively to motion. Both T4 and T5 form four subtypes that respond to one of the cardinal directions and project accordingly to the four layers of the lobula plate, thus forming a map of visual motion directions. In the lobula plate, they synapse onto large-field tangential cells (horizontal system [HS] and vertical system [VS] cells), as well as onto lobula plate intrinsic (LPi) cells that in turn form inhibitory synapses onto tangential cells in the adjacent layer of opposite PD. This inhibition corresponds to the subtraction stage in the full HR correlator (Aiii) and endows lobula plate tangential cells with full motion opponency.

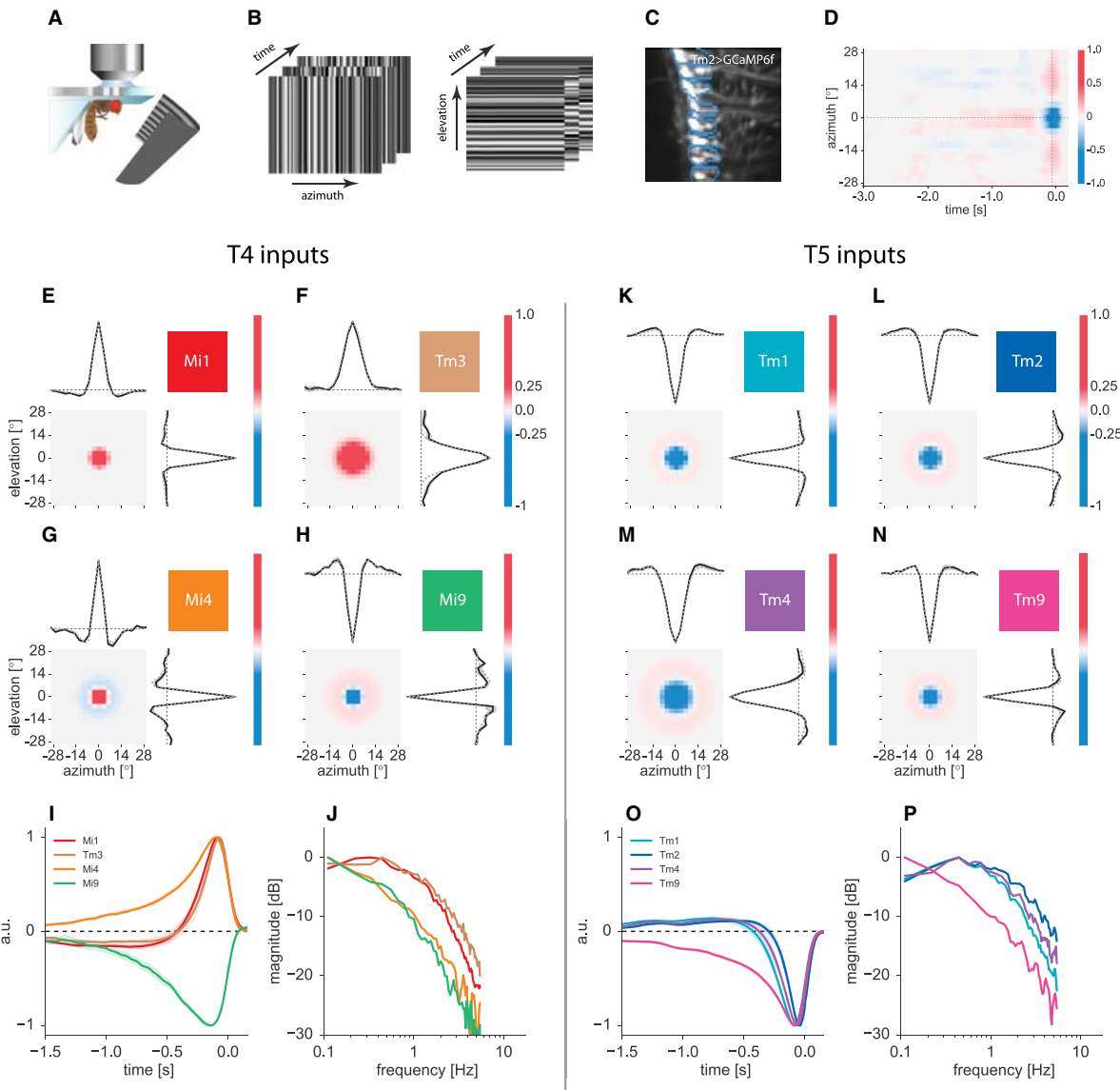


**Figure 2. Response Properties of the ON- and OFF-Pathway Medulla Columnar Elements**

(A) Two-photon calcium imaging of immobilized flies.

(B) Schematic of vertical (left) and horizontal (right) white-noise stimulus illustrated by three frames.

(C) Terminals of Tm2 neurons expressing the genetically encoded calcium indicator GCaMP6f. Regions of interest (ROIs) for the analysis of calcium indicator fluorescence changes encompass single terminals.

(D) Average aligned spatiotemporal receptive field of all Tm2 cells from (C) for a white-noise stimulus consisting of vertical bars. Along the vertical axis, the center-surround structure of the OFF-center receptive field is visible in the heat color code (vertical dashed line at the time of the peak of the response). The section along the time axis through the receptive field center reveals the temporal response kernel.

(E–H) Receptive fields of Mi1 (E), Tm3 (F), Mi4 (G), and Mi9 (H) for vertical (upper left) and horizontal (lower right) white-noise bar stimulation. From these, the two-dimensional receptive fields were constructed as a two-dimensional difference of Gaussians (Supplemental Experimental Procedures).

(I) Temporal kernels resulting from the reverse correlation of the calcium response with the white-noise stimulus for Mi1, Tm3, Mi4, and Mi9.

(J) Temporal kernels in frequency-space (constructed from the temporal kernels in (I) revealing Mi1 and Tm3 as band-pass filters and Mi4 and Mi9 as low-pass filters. (For the measurements of the spatial receptive fields: Mi1: N = 5 flies, n = 35 cells; Tm3: N = 6, n = 37; Mi4: N = 5, n = 33; Mi9: N = 7, n = 29. For the determination of the temporal kernels twice as many measurements, from the horizontal and vertical one-dimensional noise stimulus, could be used.)

(legend continued on next page)

In this study, we comprehensively characterize the spatiotemporal response profiles of all known columnar input elements of both the ON and OFF motion detectors in the fruit fly *Drosophila melanogaster* and take advantage of the motion detectors' state-dependent tuning characteristics. Using computer simulations, we test which combinations of input elements result in the observed properties of T4 and T5 neurons and thereby narrow down their possible cellular implementation. In particular, we address the question of whether the response dynamics of the input elements are sufficient to yield realistic motion detectors, or whether additional mechanisms on the synaptic or dendritic level are required to further modify the dynamics of the input signals.

## RESULTS

### Characterization of the Columnar Input Neurons to T4 Cells

The functional role of the input neurons to the elementary motion detectors and their correspondence to elements of any detector model depend crucially on their spatiotemporal response characteristics. For this reason, we characterized the spatial extent of the receptive fields as well as the response dynamics of all putative input elements to the T4 and T5 cells: Mi1, Tm3, Mi4, and Mi9 in the ON pathway, and Tm1, Tm2, Tm4, and Tm9 in the OFF pathway. Expressing the genetically encoded calcium indicator GCaMP6f [30] with cell-type-specific Gal4-driver lines, we imaged calcium signals in single terminals in layer 10 of the medulla or the proximal lobula for the ON- and OFF-pathway elements, respectively.

To precisely map the receptive fields of the input elements, we used a one-dimensional white-noise stimulus consisting of 2.8° wide horizontal or vertical bars covering the full extent of the arena (Figures 2A–2D; Figure S1; [Supplemental Experimental Procedures](#)). The spatiotemporal receptive fields were then determined from the neuron's calcium response by reverse correlation. The spatial components of these are the one-dimensional horizontal and vertical projections of the underlying two-dimensional spatial receptive field of the cell. In all cases, they strongly resembled a difference of Gaussians (DOG; also called a "Mexican hat"). Because they were similar for both the horizontal and vertical dimensions, we fitted a two-dimensional DOG to reconstruct two-dimensional spatial receptive fields (Figures 2E–2H and 2K–2N). The temporal component of the spatiotemporal receptive field reflects the temporal filtering properties of the neuron (impulse response). The extracted temporal filters were validated by predicting held-out test sequences of neuronal responses from the stimulus for two example neuron types (Mi1 and Tm9) (Figure S2; see [Supplemental Experimental Procedures](#)).

All four cell types in the ON pathway, Mi1, Tm3, Mi4, and Mi9, showed locally confined receptive fields that appeared isotropic in the horizontal and vertical dimensions (Figures 2E–2H). Mi1, Mi4, and Mi9 cells revealed a receptive field center with a half-

width diameter of approximately 6°–7°, corresponding to about one optical column. In contrast, the receptive field center of Tm3 was substantially larger, with a half-width diameter of about 12°. Mi4 and Mi9, and to a lesser degree Mi1, also revealed a significant antagonistic surround, giving them spatial band-pass characteristics. This antagonistic surround had a half-width diameter of approximately 20° for both Mi4 and Mi9 (Table S1). Because the area and thus the volume under the curve are proportional to the square of the radius, the amplitude ratio of surround to center should equal the inverse of the ratio of the squares of their half-widths for the center and the antagonistic surround to cancel perfectly. Notably, this relation is fulfilled for both low-pass elements, and the integrals of their surrounds perfectly match their respective centers, thus predicting no responses to wide-field flicker stimuli. At the same time, the spatial band-pass filter enhances responses to edges within the visual scene. In the case of Mi1, the integral of the surround reached about 50% of the one of the center. For Tm3, surround inhibition was completely absent, such that those cells have a pure low-pass characteristic in the spatial domain.

The temporal component of the spatiotemporal receptive field centers yielded the impulse responses, which reflect the temporal filtering properties of the respective cell type. Mi1 and Tm3 showed band-pass filter characteristics, as can be seen in their biphasic impulse responses (Figure 2I) and in their response spectra (Figure 2J). In contrast, Mi4 and Mi9 appeared as pure low-pass filters (Figures 2I and 2J). Surprisingly, and in contrast to the other elements of the ON pathway, Mi9 showed the inverse contrast preference, with an increased calcium response to darkening in its receptive field center (OFF response). However, apart from the polarity, the time course and filter characteristics of Mi9 were very similar to those of Mi4 (Figures 2I and 2J). Thus, the four ON-pathway elements can essentially be grouped into two classes: two fast-transient cells (Mi1 and Tm3) and two slow-sustained cells (Mi4 and Mi9). Within each class, the cells' impulse responses revealed only small differences.

### Characterization of the Columnar Input Neurons to T5 Cells

We next performed analogous experiments on the OFF-pathway elements Tm1, Tm2, Tm4, and Tm9. Mirroring the situation in the ON pathway, all four neurons of the OFF pathway had locally confined isotropic receptive fields (Figures 2K–2N). In agreement with previous reports [18, 20], they were all excited by luminance decrements. Accordingly, they revealed an OFF receptive field center. The receptive fields of all four cells also had an antagonistic surround component, giving them a spatial band-pass characteristic. In contrast to Mi4 and Mi9, however, the surround inhibition, with respect to the center, was weaker, which should render them more responsive to wide-field flicker. As a parallel to the ON-pathway elements, three of the neurons, Tm1, Tm2, and Tm9, showed a receptive field center with a half-width diameter of about 7°, whereas one element, Tm4, had a larger receptive field center, with a half-width diameter of approximately 10°.

(K–P) Characterization of the inputs to T5 cells in the OFF pathway. Spatial receptive fields of Tm1 (K), Tm2 (L), Tm4 (M), and Tm9 (N). Temporal kernels in the time (O) and frequency domain (P) for the four input elements in the OFF pathway. (Tm1: N = 8 flies, n = 71 cells; Tm2: N = 9, n = 93; Tm4: N = 5, n = 35; Tm9: N = 5, n = 32.)

Graphs depict the mean. Shaded areas around the line, where displayed, represent  $\pm$ SEM. See also Figures S1 and S2 and Tables S1 and S2.

The half-width of the antagonistic surround amounted to about 25° for Tm1, Tm2, and Tm9 and to 35° for Tm4 (Table S2). As for Mi1, and in contrast to Mi4 and Mi9, the antagonistic surround strength for all OFF input elements reached about 50% of the center, as calculated above on the basis of the amplitude and half-width ratios.

As for the ON-pathway elements, we assessed the temporal filter dynamics by measuring the impulse responses within the receptive field centers (Figures 2O and 2P). This revealed a clear band-pass characteristic for Tm1, Tm2, and Tm4 with rather short low-pass time constants of about 100–270 ms. In contrast, the impulse response of Tm9 reflected a pure low-pass filter with a much longer time constant of about 500 ms. Within the group of band-pass filters, Tm1, Tm2, and Tm4 responses have different time courses (Figure 2O) and response spectra (Figure 2P), corroborating a previous study [20]. Thus, as a striking difference from the ON-pathway elements, where two fast and two slow cells are found, the OFF pathway comprises three fast and only one slow cell.

#### Application of the Octopamine Agonist CDM Changes the Temporal Frequency Tuning of T4 and T5 Cells

It has previously been shown that activation of the octopamine system modulates the temporal-frequency tuning of lobula plate tangential cells [25, 26]. This effect could be implemented directly at the level of the tangential cells, or indirectly, by modifying the temporal tuning properties of its presynaptic input neurons, i.e., the T4/T5 cells. The latter case would give a handle to manipulate the elementary motion detectors and potentially allow narrowing down of their cellular implementation.

We first confirmed that the activation of the octopamine system with the octopamine agonist CDM [31] at a concentration of 20  $\mu$ M [25] shifts the temporal tuning of tangential cells in the lobula plate of immobilized *Drosophila* to higher frequencies (Figure S3), corroborating earlier findings using octopamine [26].

Next we focused on T4 and T5 neurons. We performed two-photon  $\text{Ca}^{2+}$  imaging in *Drosophila* expressing the genetically encoded calcium indicator GCaMP6m in the subset of T4/T5 neurons that are upward motion selective and project their axons to layer 3 of the lobula plate (T4c/T5c) (Figure 3A). Visual stimulation was presented on a semi-cylindrical LED arena and consisted of full-contrast square-wave gratings with a spatial wavelength of 24°, moving at 12 different velocities ranging from 1.2°/s to 480°/s, corresponding to temporal frequencies from 0.05 to 20 Hz, in PD and ND. Responses of T4 and T5 neurons were quantified as relative change of fluorescence (DF/F) amplitudes within small regions of interest in lobula plate layer 3 (example traces in Figure 3B). We found a temporal-frequency optimum of 1 Hz for motion in PD (Figure 3C, black traces). Application of CDM shifted the temporal-frequency optimum from 1 Hz in control to about 2.5 Hz (Figure 3C, magenta traces). Recording  $\text{Ca}^{2+}$  signals from the dendrites of either T4 or T5 cells, we found that T4 and T5 cells, considered separately, exhibited a similar temporal-frequency tuning, under control conditions as well as after application of CDM, and a similar shift in their tuning with CDM (Figures 3D and 3E).

In order to distinguish changes in the response to isolated motion stimuli from changes in the temporal integration of periodic signals, we also tested the velocity tuning of T4 and T5 neu-

rons to moving edges. For this, we presented bright and dark edges of full contrast moving at different speeds ranging from 3°/s to 300°/s in PD (Figures 3F and 3G). Corroborating previous results [14], T4 neurons responded selectively to bright edges, whereas T5 neurons were found to be selective for motion of dark edges. Measuring the calcium responses in the axon terminals in the lobula plate, we found that under control conditions the responses were highest to edges moving at the slowest velocity of 3°/s for both ON and OFF edges, i.e., T4 and T5 neurons, respectively (Figures 3F and 3G, black traces). As was seen for the grating stimuli above, application of CDM shifted the optimal stimulus condition to higher velocities of 12°/s (Figures 3F and 3G, magenta traces).

Therefore, the shift of the temporal tuning properties of lobula plate tangential cells during flight or mimicked by the application of octopamine-receptor agonists (Figure S3 [25, 26]) is already present at the level of the T4 and T5 cells, thus affecting the tuning of the elementary motion detectors.

#### Octopamine-Receptor Activation Speeds the Input Elements of T4 and T5 Cells

Different possible mechanisms could explain this shift of temporal tuning in T4/T5 cells. On the one hand, octopamine signaling could affect the synaptic inputs onto T4 and T5 neurons by changing the kinetics of neurotransmitter receptors or the dendritic integration of those signals in T4/T5 neurons. Different input elements with different response kinetics could differentially contribute to the postsynaptic signals in different states through changes in their response amplitude or via their synaptic weight. On the other hand, the kinetics of some or all input elements could speed up. We set out to test the latter hypothesis, i.e., that the response characteristics and tuning of the elementary motion detectors result directly from the temporal dynamics of the respective input elements.

For this, we characterized the spatiotemporal receptive fields of all input elements in both the ON and OFF pathways after activation of the octopamine system with CDM and compared them to control conditions. Application of CDM left the spatial receptive fields of all four input neurons in the ON pathway unaffected (Figure 4A). However, it accelerated the response kinetics of all four cell types to different degrees, with much stronger effects on the fast band-pass elements Mi1 and Tm3 than on the slow low-pass filters Mi4 and Mi9 (Figures 4B and 4C, magenta traces; Figures S4A, S5Ai, and S5Bi). As for control conditions, response kinetics of Mi1 and Tm3, as well as of Mi4 and Mi9, remained similar to each other after addition of CDM. In the OFF pathway, the results were very similar. The spatial receptive fields appeared unchanged by CDM for any of the columnar input neurons (Figure 4D). However, in the temporal domain, addition of CDM to the bath sped up the impulse responses significantly (Figures 4E and 4F, magenta traces; Figures S4B, S6Ai, and S6Bi), as was seen in the ON-pathway band-pass elements.

#### Computer Simulations Based on the Input Elements' Temporal Filters Suggest Candidate Motion Detectors

The input elements to the motion-detecting neurons T4 and T5 can be roughly grouped into two classes: temporal low-pass filters with large time constants, and band-pass filters with

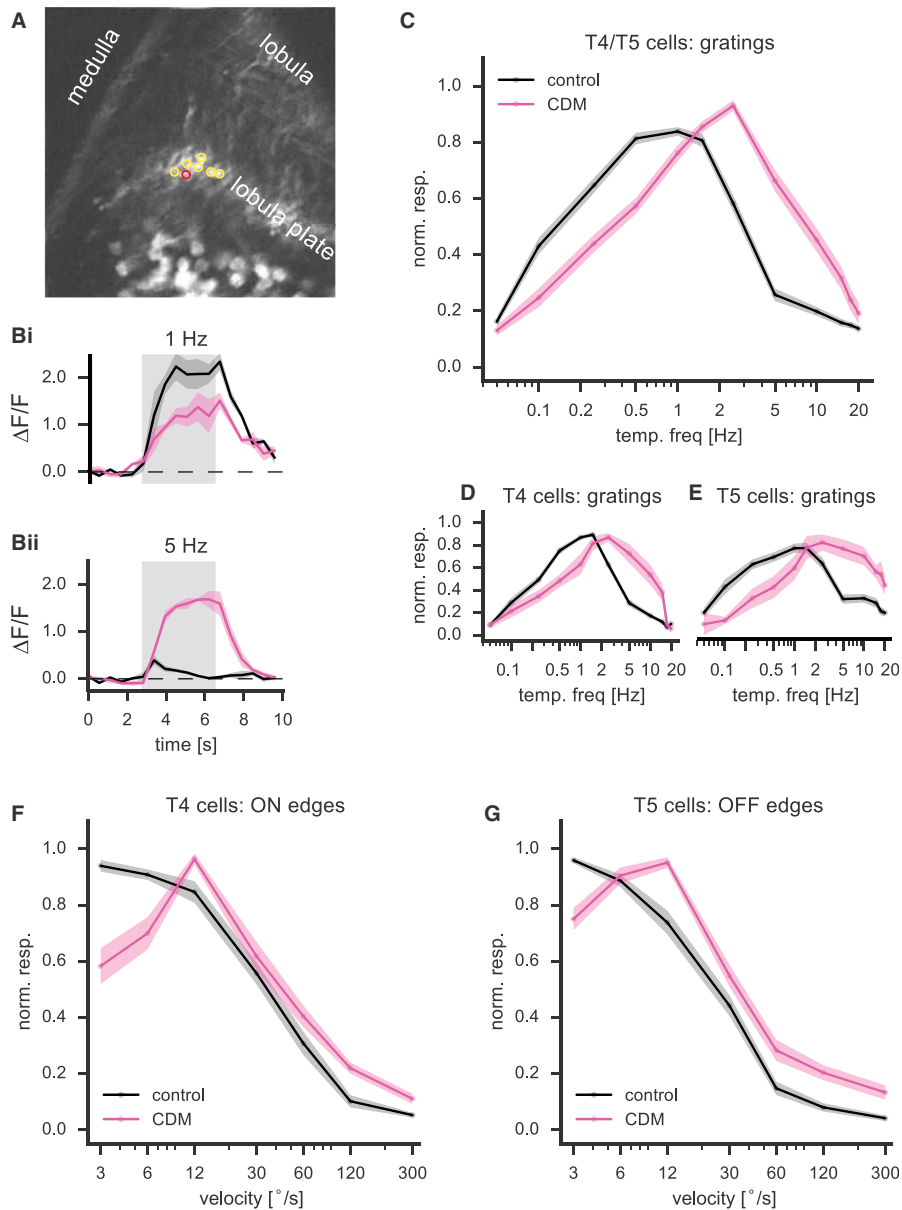


**Figure 3. Application of CDM Shifts the Temporal-Frequency and Velocity Tunings of T4/T5 Cells to Higher Velocities**

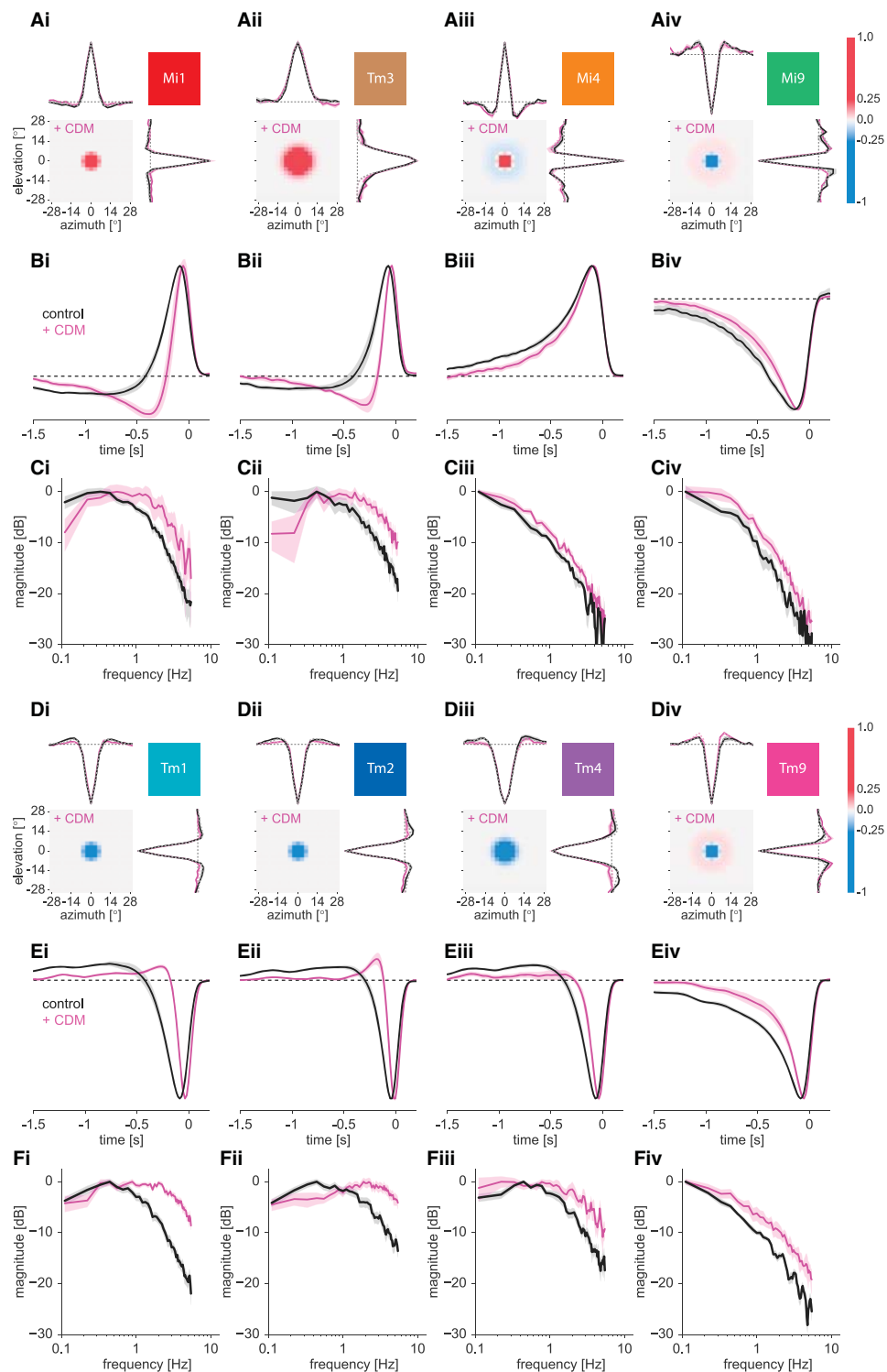
(A) T4/T5 neurons of the upward motion-selective subtype “c” projecting their axons to layer 3 of the lobula plate, expressing the genetically encoded calcium indicator GCaMP6m. The circles mark ROIs in the lobula plate; the red circle corresponds to the example calcium traces in (B).

(B) Example of calcium responses (fluorescence changes) in the axon terminals of T4/T5 cells in response to square-wave gratings moving at temporal frequencies of 1 Hz (Bi) and 5 Hz (Bii) in control (black) and after application of CDM (magenta).

(C) Population average of responses of T4/T5 axon terminals to square-wave gratings moving in the PD (up). Application of CDM leads to a shift of the temporal tuning optimum ( $N_{\text{cont}} = 36$  flies,  $n_{\text{cont}} = 80$  ROIs;  $N_{\text{CDM}} = 15/39$ ).

(D and E) Characterization of the temporal-frequency tuning in T4 (D) and T5 dendrites (E). As observed for the axon terminals, application of CDM (magenta) shifts the temporal-frequency tunings of both T4 and T5 cells to higher frequencies, as compared to control (black) (T4:  $N_{\text{cont}} = 27$  flies,  $n_{\text{cont}} = 52$  ROIs,  $N_{\text{CDM}} = 9/14$ ; T5:  $N_{\text{cont}} = 18/27$ ,  $N_{\text{CDM}} = 7/9$ ).

(F and G) Population average of responses of T4 and T5 axon terminals in the lobula plate to bright (F; T4) and dark edges (G; T5), moving at different velocities, in control (black) and after application of CDM (magenta) ( $N_{\text{cont}} = 9$  flies,  $n_{\text{cont\_T4}} = 21$ ,  $n_{\text{cont\_T5}} = 37$  ROIs;  $N_{\text{CDM}} = 6$ ,  $n_{\text{CDM\_T4}} = 16$ ,  $n_{\text{CDM\_T5}} = 17$ ). Graphs depict the mean. Shaded areas around the line represent  $\pm$ SEM. See also Figure S3.



(legend on next page)

significantly shorter time constants. We used the above-determined spatial receptive fields and response kinetics of the input elements and asked whether these could predict the responses of their postsynaptic targets, the elementary motion detector T4/T5 cells, without the necessity of additional filters or delays implemented either at the level of the synapses between the inputs and the T4/T5 cells or within the dendrites of the T4/T5 cells itself. In addition, we asked whether the observed shift in the temporal tuning in T4/T5 cells after application of the octopamine agonist CDM could be fully explained by the change of filter properties of the respective input neurons.

Although GCaMP6f has relatively fast kinetics when compared with other calcium indicators, it still possesses a decay time constant on the order of hundreds of milliseconds [30, 32]—long enough to significantly prolong the calcium signals of cells that have temporal dynamics on the same order of magnitude. In order to correct for this temporal filtering by the calcium indicator itself, we deconvolved the impulse responses in the frequency domain with a GCaMP6f low-pass filter (Figures S5 and S6). These corrected spectra were used as an approximation of the underlying filter properties of the input cells by fitting first-order filters to the average corrected frequency responses (Tables S1 and S2). We then used these values as well as the spatial filter characteristics in our computer simulations of a motion detector. Because the synaptic transmitters and postsynaptic receptors, and therefore the sign of the synaptic inputs, are not known, we decided not to make any assumptions about the sign of the synapses and ignored the response polarities of the determined receptive fields in our simulations.

Our simulations were based on a motion detector that combines PD enhancement and ND suppression, resembling a hybrid of a HR half-detector and a BL detector, as described in Haag et al. [17] (Figure 1Aiv). In this detector, three inputs with receptive fields offset by 5° each along the PD axis are processed such that an enhancing input A on the null side (left) forms a multiplicative non-linearity with the central, direct input (B), whereas a suppressing input (C) on the preferred side (right) implements a divisive non-linearity. The response of this detector equals the product of the input signals on the enhancing and the direct arm, divided by the signal from the suppressing arm (see the [Supplemental Experimental Procedures](#)).

There are 24 possible permutations that map the four input elements of each pathway onto the three positions of this detector, each one resulting in a detector with different tuning properties. Without making any further assumptions, we asked whether some of these combinations would yield more direction-select-

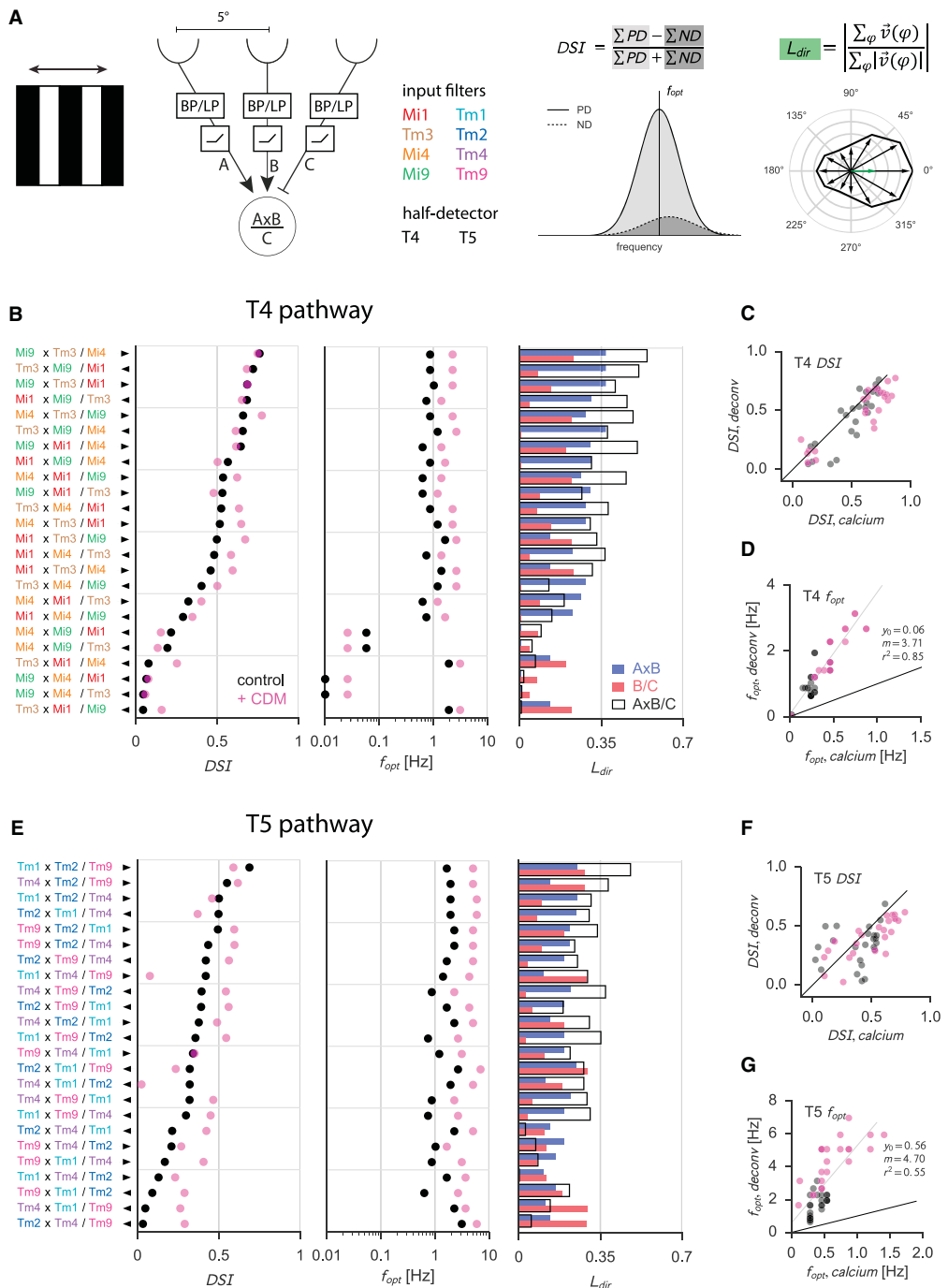
tive motion detectors than others. Each simulated detector was tested with moving square-wave gratings, and the responses were quantified in three ways (Figure 5A): (1) To assess how well the particular detector model discriminates between motion along PD and ND across velocities, we simulated square-wave gratings moving in PD and ND at different speeds covering more than three orders of magnitude. From the simulated responses, we calculated a direction selectivity index (DSI) as the relative difference between PD and ND responses, averaged over all grating velocities/temporal frequencies. (2) To judge the frequency tuning, we determined the temporal frequency evoking the maximum response in PD (temporal-frequency optimum,  $f_{opt}$ ). (3) To characterize the direction tuning beyond PD and ND, emphasizing tuning sharpness, we simulated gratings moving in 12 equally spaced directions at the  $f_{opt}$  of each detector, as determined above. From those simulated responses, the normalized length of the tuning vector ( $L_{dir}$ ) was calculated [33]. This tuning vector length of the hybrid detector was furthermore compared with the ones of the constituting HR and BL modules (Figures 1Ai and 1Aii, respectively).

In general, detectors with the low-pass filters Mi4 and Mi9 on both the outer enhancing and suppressing arms, flanking one of the band-pass elements Mi1 or Tm3, performed extremely well: they showed a rather high degree of direction selectivity and tuning sharpness (Figure 5B), in good agreement with the experimental data from T4 cells (compare with [14]), and their temporal-frequency optimum matched that of T4 cells as well (Figure 5B, right; compare with Figures 3C and 3D).

In addition, most combinations with one central low-pass neuron, Mi4, or, particularly, Mi9, flanked by the two band-pass elements Mi1 and Tm3, also achieved high direction-selectivity values. The PD (see arrows in Figure 5B, left) of these detectors is inverted as a consequence of the position of the delay in the HR and BL sub-modules. However, when considering both sub-modules separately (blue and red bars, respectively, in Figure 5B, right), the BL alone showed very low tuning sharpness ( $L_{dir}$ ) and thus contributed little to the hybrid detector. This affects the tuning specificity of the hybrid detector, as can be seen when comparing, for example, Tm3xMi9/Mi1 with Mi9xTm3/Mi4. Both detectors are built on the same HR detector (using the same cells), but the one that employs Mi4 for the BL part of the model has a higher tuning sharpness. The same is true for all other pairs of this kind: given one pair of cells for the HR module, the implementation that places two low-pass filters on the outer arms of the detector always has the sharper tuning.

#### Figure 4. Activation of Octopamine Receptors Accelerates the Temporal Filters of the ON- and OFF-Pathway Medulla Columnar Elements

- (A) Spatial receptive fields of Mi1 (Ai), Tm3 (Aii), Mi4 (Aiii), and Mi9 (Aiv) for vertical (upper left) and horizontal (lower right) white-noise bar stimulation under control conditions (black traces) and after application of CDM (magenta traces and two-dimensional receptive fields).
- (B) Temporal kernels for Mi1 (Bi), Tm3 (Bii), Mi4 (Biii), and Mi9 (Biv) revealing the faster time course after application of CDM (magenta) as compared to control (black).
- (C) Temporal kernels in frequency-space, constructed from the temporal kernels in (B). Application of CDM (magenta) leads to a shift of the center frequency of the band-pass filters as compared to control (black). (For the measurements of the spatial receptive fields [controls are as in Figure 2]: Mi1:  $N_{CDM} = 5$ ,  $n_{CDM} = 31$ ; Tm3:  $N/n_{CDM} = 6/34$ ; Mi4:  $N/n_{CDM} = 5/38$ ; Mi9:  $N/n_{CDM} = 7/37$ . Again, the temporal kernel results determined from the horizontal and vertical one-dimensional noise stimuli were pooled, resulting in twice as many measurements.)
- (D–F) Analogous to (A)–(C), the spatial receptive fields (Di–Div), temporal kernels (Ei–Eiv), and frequency spectra (Fi–Fiv) of the OFF-pathway elements Tm1, Tm2, Tm4, and Tm9. (Controls are as in Figure 2; Tm1: CDM:  $N_{CDM} = 8$ ,  $n_{CDM} = 67$ ; Tm2:  $N/n_{CDM} = 9/93$ ; Tm4:  $N/n_{CDM} = 5/28$ ; Tm9:  $N/n_{CDM} = 5/42$ .) Graphs depict the mean. Shaded areas around the line represent  $\pm$ SEM. See also Figure S4 and Tables S1 and S2.

**Figure 5. Computer Simulations of Elementary Motion Detectors**

(A) Left: schematic of a three-arm detector combining a multiplicative PD enhancement and a divisive ND suppression. The positions of the enhancing ("A"), central ("B"), and suppressing ("C") input can be occupied by any but different input elements. Those input elements are described by their temporal filtering characteristics, implemented as a band-pass (BP) and low-pass filter (LP) with subsequent rectification. The receptive fields of the three inputs are offset by 5° each. The simulated detectors are stimulated with square-wave gratings moving at different temporal frequencies in PD and ND. Middle: the direction selectivity

(legend continued on next page)

Similarly, detectors that incorporated two elements with similar temporal response properties (such as Mi1 and Tm3) on two adjacent positions tended to perform worse, especially with respect to the  $L_{dir}$  value, indicating poor tuning sharpness. This can be easily explained by the fact that both the HR and BL modules of the hybrid detector rely on temporal differences in their respective two input arms. Inputs with more similar kinetics thus render the corresponding module less effective in creating direction selectivity. In fact, the best detectors were those where both halves showed high direction selectivities on their own (Figure 5B, right), provided the PDs of both modules were aligned.

Interestingly, almost all combinations showed a shift in their tuning toward higher temporal-frequency optima by about a factor of 2 when the filter properties after application of the octopamine agonist CDM were used, matching the experimental data. As a control that the direction selectivities in our simulations were not dependent on the used deconvolution filter, we repeated the simulations with the raw temporal kernels derived from the calcium responses. The same arrangements of input elements led to the motion detectors with the highest direction-selectivity values (Figure 5C), consistent with the notion that it is the relative filter properties that are crucial. Deconvolution merely changes the temporal frequency of the visual stimulus that leads to the maximum response (Figure 5D).

In the above simulations, we followed an unbiased approach with all inputs separated by 5°, thus having receptive fields arising from neighboring neuro-ommatidia. However, electron-microscopic reconstructions have shown a spatial offset between Tm3 and Mi1 cells projecting to the same T4 cell of about 1° in this order along the PD of the postsynaptic T4 cell [4]. The smaller spatial offset could counterbalance the small differences in temporal kinetics between these cells. Repeating the above simulations of the three-arm detector under these constraints still resulted in poorly direction-selective detectors for these combinations, with  $L_{dir}$  values of 0.38 (for Mi9xTm3/Mi1, as compared to 0.41 for a 5° offset) or less. In fact, when considering only a simple two-arm detector (HR or BL type), any detector that consisted of Tm3 and Mi1 with a spatial offset of 1° resulted in  $L_{dir}$  values of less than 0.06 for both types of detectors (in comparison to 0.13 for a 5° offset).

Although the evidence is weaker for the structure of the motion detector implementation in T5, we constructed analogous motion detectors for the OFF pathway with the measured receptive fields and response kinetics of the columnar inputs onto T5 neurons (Figure 5E). In contrast to the ON pathway, only one out of

the four input elements, Tm9, constitutes a low-pass filter, whereas the other three, Tm1, Tm2, and Tm4, exhibit band-pass characteristics. Most input element combinations resulted in motion detectors with low direction selectivity. Notably, the highest direction selectivity resulted from detectors with the low-pass filter Tm9 on the suppressing arm. Naturally, detectors with the fastest input (principally Tm2) in the central position flanked by two slower elements achieved higher direction selectivities, as with this arrangement the PDs of the HR and BL subunits are aligned. Arrangements with the sole low-pass filter, Tm9, in the central position resulted in detectors with poor directional tuning, both measured as DSI across all frequencies and  $L_{dir}$ , resulting from a virtually ineffective BL half (Figure 5E, right). Interestingly, combinations with the band-pass filters Tm1 and Tm4 constituting either half of the detector tended to perform comparatively poorly—and sometimes even showed a complete breakdown of direction selectivity—in at least one of the simulated physiological states. This can be explained by the fact that the small differences in the temporal response kinetics of these neurons were not stable between control and under CDM (Figure S6). As was seen for the ON pathway, using the spatiotemporal filters extracted under CDM in the simulations led to an increase of the temporal-frequency optimum by about a factor of 2 across all detectors (Figure 5E, middle, magenta dots). Again, the simulations were robust to the deconvolution applied to account for the filtering by the calcium indicator (Figure 5F). The best arrangements were the same irrespective of whether the raw or deconvolved filters were used, and only the temporal-frequency optimum was affected (Figure 5G).

Taken together, we find distinctly different response kinetics of the input elements in both the ON and the OFF pathway, from band-pass filters to pure low-pass filters. These map naturally onto hybrid elementary motion detectors implementing PD enhancement and ND suppression. The best-performing detectors arise when the fastest element occupies the central arm, flanked by slower inputs on the enhancing and suppressing arms. In the ON pathway, two low-pass inputs, Mi4 and Mi9, are found to fill this role. In the OFF pathway, the single low-pass element, Tm9, appears to be best positioned on the suppressing arm to achieve the highest direction selectivity.

## DISCUSSION

To understand how motion detection is implemented on the dendrites of T4 and T5 cells, we describe in this study the response

of the detector is assessed across all temporal frequencies based on the area under the temporal-frequency tuning curves in PD and ND as the direction selectivity index:  $DSI = (\Sigma PD - \Sigma ND) / (\Sigma PD + \Sigma ND)$ . The dotted line indicates the temporal-frequency optimum ( $f_{opt}$ ) for responses in PD. Right: Illustration of the normalized tuning vector length ( $L_{dir}$ ) as a measure for direction selectivity and tuning sharpness.  $L_{dir}$  is calculated as the vector sum of all responses according to the direction of stimulus motion, normalized to the sum of all response vector lengths.

(B–D) Characterization of the simulated motion detectors for the ON pathway.

(B) Direction selectivity (left), temporal-frequency optimum (middle), and normalized tuning vector length (right) for all possible permutations of the four ON-pathway input elements on the three positions of the simulated detector. The magenta dots indicate the effect of CDM application on direction selectivity and temporal-frequency tuning resulting from the accelerated temporal filters of the input elements. Arrows indicate the PD with respect to the corresponding cell arrangements. For the tuning vector length, the hybrid detectors (black open bars) were compared to their constituting HR ("AxB"; blue) and BL modules ("B/C"; red).

(C and D) Direction-selectivity indices (C) and temporal-frequency optima (D) of all detectors based on the deconvolved filter kernels as shown in (B) plotted against the detectors based on the raw calcium kernels.

(E–G) Same as (B)–(D) but for the OFF pathway.

See also Figures S5 and S6.

properties of the elementary motion detectors in *Drosophila*, the T4 and T5 neurons, as well as all of their known columnar synaptic input neurons, under two different tuning regimes. With this comprehensive characterization, we are able to narrow down the cellular implementation of the motion detectors and suggest probable wiring diagrams.

All of these input elements possess spatially restricted receptive fields with centers spanning one to two ommatidia. All, with the exception of the ON-pathway band-pass neuron Tm3, have pronounced antagonistic surrounds. Particularly for the low-pass filter elements Mi4 and Mi9, the strong antagonistic surround fully counterbalances the excitatory center. This should not only eliminate sensitivity to large-field flicker stimuli but more importantly curtail the otherwise tonic responses of pure low-pass filters to moving edges, and thus strongly improve direction selectivity. The locally confined receptive fields are in agreement with previous studies [18, 20, 34] but in contradiction to [35], which described Tm9 as a wide-field neuron. In both pathways, one neuron shows a larger receptive field (Tm3 in the ON pathway, and Tm4 in the OFF pathway). The larger receptive field sizes of Tm3 [18] and Tm4 neurons are consistent with the multi-columnar input these neurons receive based on electron-microscopic reconstructions [4, 5].

All elements of the OFF pathway respond to light OFF in the center of their receptive fields, consistent with [20]. In the ON pathway, Mi1, Tm3 [18], and Mi4 analogously show an ON-center response. Mi9, however, despite being an element in the ON pathway, responds positively to OFF stimuli. This could suggest a sign reversal through an inhibitory synapse onto T4. However, it is not known what neurotransmitter is released by Mi9, and thus whether it excites or inhibits T4 neurons.

Within each of the two pathways, we find a diversity of temporal filter characteristics from fast band-pass filters to pure low-pass filters with slow-sustained responses. These differences in temporal dynamics make them ideal components for motion detection without the need of postulating further processing by slow synaptic signaling or electrotonic filtering within the dendrites of T4 and T5 cells. Where the response kinetics of these cells have been previously described, our data are consistent. In particular, Mi1, Tm3, Tm1, Tm2, and Tm4 have previously been shown to respond transiently to sustained stimuli, i.e., to possess band-pass characteristics [18, 20, 34]. Tm3 appears faster than Mi1 [18] (but see [36]), and Tm2 faster than Tm1 [18, 20, 36]. However, these temporal differences are often very small. On the other hand, Tm9 in the OFF pathway has been described as a low-pass filter [20, 35], which matches our results. In the ON pathway, we find that the previously uncharacterized cell types Mi4 and Mi9 also show pure temporal low-pass response characteristics. Thus, in both pathways, input elements with slow-sustained and fast-transient responses are found, which then converge onto the dendrites of T4 and T5 cells, respectively. Yet the relative distribution differs. In the ON pathway, two input elements show pure low-pass characteristics (Mi4 and Mi9), whereas in the OFF pathway, Tm9 constitutes the only pure low-pass filter. Two of the three input elements that constitute pure low-pass filters, namely Mi9 in the ON and Tm9 in the OFF pathway, receive their lamina input primarily from the lamina monopolar neuron L3 [37]. As L3 has been shown to respond in a slower and more sustained fashion [38] than,

e.g., the transient L2 [10, 11], this could explain the low-pass characteristics of Mi9 and Tm9. L3, like all lamina neurons, responds positively to light decrements, and it releases the excitatory neurotransmitter acetylcholine, explaining the OFF response of Tm9 and Mi9. The response dynamics of Mi4 are likely to be heavily shaped by the strong reciprocal connections with Mi9 [37]. These reciprocal connections, and thus likely the cells themselves, would have to be inhibitory, as these cells show opposite response polarities.

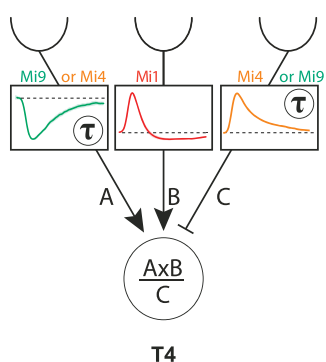
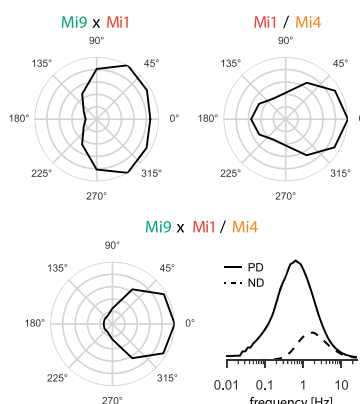
Based on the spatial receptive fields and response kinetics, we could ask which input neurons could play which role in the motion detector. Previous computer simulations based on the measured dynamics of Tm cells in the OFF pathway have shown that most combinations of two elements result in classical (full) HR detectors with similar temporal tuning optima roughly matching the tuning of tangential cells [20]. In that study, only the combination of Tm2 and Tm4 could be excluded, as their filter time constants were too similar to each other to result in a functioning detector. However, subtraction of oppositely tuned half-detectors not only leads to motion opponency but increases direction selectivity of otherwise poorly tuned half-detectors. Consequently, the tuning of lobula plate tangential cells represents a rather indirect readout. By comparing simulations of the half-detector stage with recordings from T4 and T5 neurons, we can exclude the majority of possible combinations of input elements based on their temporal-frequency optimum or directional selectivity (see below).

Based on visual stimulation of single individual columns, T4 neurons have recently been shown to implement both PD enhancement and ND suppression [17]. The receptive fields of these interactions are spatially offset along the PD axis in this order. The corresponding hybrid of an HR half-detector and a BL detector requires a minimum of three columnar inputs: a fast central input, flanked by two outer inputs providing signals that are delayed relative to the central one.

In our computer simulations for the ON pathway (Figure 5), the majority of detectors with the highest direction selectivity fall into two groups: (1) the two low-pass filter elements Mi4 and Mi9 on the outer enhancing and suppressing arms, and either of the fast band-pass elements Mi1 and Tm3 on the central arm, matching the above layout, and (2) the inverted arrangement, with one central low-pass filter, flanked by the band-pass filter elements Mi1 and Tm3. This also resulted in an inverted PD.

In the latter case, however, the BL subunit considered alone contributed very little to the directional tuning (Figure 5B, right), as the low-pass-filtered central excitatory input tends to outlast the corresponding suppression from the band-pass outer arm. This reduces the tuning sharpness of these detectors. Furthermore, this implementation does not match the arrangement of PD-enhancement and ND-suppression receptive fields along the PD in this order found for T4 cells [17]. Additionally, this arrangement would require Mi1 and Tm3 on the outer arms of the model, which is in stark contrast to their reported 1° spatial offset [4].

Among the more direction-selective detectors was also one combination with Tm3 on the central and Mi1 on the suppressing arm. However, the resulting BL subunit considered alone shows very poor directional tuning, and the direction selectivity arises

**A****ON pathway****B**

**Figure 6. Proposed Implementation of the Elementary Motion Detectors in the ON Pathway**

(A) T4 neurons implement both PD enhancement and ND suppression with receptive fields offset in this order along the PD axis. This requires one central fast arm being flanked by two delayed or stronger low-pass-filtered inputs. The relatively fast kinetics of Mi1 or Tm3 would suggest either or both for the central input. Mi4 and Mi9, on the other hand, show pure low-pass characteristics in their temporal kernels fitting the requirements of the two outer arms. The signs of both outer-arm synapses depend on the arrangement of Mi4 and Mi9 to accommodate their respective response polarity and match them to the required enhancing and suppressive inputs.

(B) Simulated detector responses for gratings moving across the visual field in 12 different directions, separated from each other by 30°. Top: directional tuning for the two sub-modules of this

detector. Top left: the pure HR (half) detector Mi9xMi1 shows some direction selectivity but has a low tuning sharpness. Top right: the pure BL detector Mi1/Mi4. This hybrid detector is very sharply tuned to rightward motion (left), whereas its direction selectivity remains high across stimulus frequencies (right).

virtually exclusively from the HR subunit. Even taking the reported small anatomical offset of about 1° between these cells into account [4] did not compensate for the small temporal differences but actually resulted in even worse directional tuning. This indicates that sizable differences not only in the temporal but also in the spatial domain are a prerequisite for direction selectivity. Similar considerations are true for all combinations that place neurons with similar response kinetics on neighboring arms. In general, the most effective hybrid detectors result from combinations of cells that are arranged such that the respective HR and BL sub-detectors are as direction selective as possible and aligned in their PD.

For detectors where two low-pass filters flank a central band-pass filter element, both Mi1 and Tm3 seem feasible to fill the role of the latter. However, a previous study blocking the synaptic output of Tm3 found an effect on the response of tangential cells to moving ON edges only at high but not at low to moderate velocities [21]. Hence, although we do not exclude a functional role for Tm3 in ON motion detection, this finding argues against Tm3 as the (sole) central arm of the detector in the ON pathway, as the interference especially with the central arm should fully abolish the detection of motion.

Taken together, an implementation of the ON elementary motion detector as depicted in Figure 6 seems most likely: Mi1 as the fast central input, flanked by the low-pass elements Mi4 and Mi9 constituting the suppressing and enhancing arm in either order. Depending on the location, these neurons need to be either both excitatory or both inhibitory to accommodate their respective response polarity and fulfill the required role of enhancing and suppressing input. Considering their opposite polarity and reciprocal connection, it is more likely that both neurons are inhibitory. This would place Mi9 on the enhancing arm ("A" in Figure 6A), and Mi4 on the suppressing arm ("C" in Figure 6A). Importantly, with the observed range of temporal response characteristics in the input elements, it is not necessary to postulate further delays at the synaptic or dendritic level.

In the OFF pathway, the algorithmic structure of motion detection is less clear. On the one hand, spatiotemporal receptive field measurements of T5 neurons reveal excitatory and inhibitory sub-fields that are offset along the PD axis and appropriately tilted in space and time to support PD enhancement and ND suppression [23]. This would suggest a similar architecture as for T4. On the other hand, other studies have only reported PD enhancement for T5 [22, 39]. Nevertheless, we performed analogous simulations based on the measured T5 input kinetics and receptive fields assuming a similar detector architecture. The two detectors with the highest direction selectivity incorporated the low-pass filter, Tm9, into their suppressing arm (Figure 5E). Lacking a second pure low-pass filter input in the OFF pathway, the central and enhancing arms were occupied with band-pass filters. Because the PDs of PD enhancement and ND suppression need to be aligned, the fastest element of the combination, principally Tm2, must be located in the central position. This is also illustrated by the two worst combinations (Figure 5E, right), where even though the BL module on its own performs quite well, the oppositely oriented HR module destroys the direction selectivity of the hybrid detector. As above, hybrid detectors with the low-pass filter, Tm9, on the central arm perform poorly, as the constituting BL half contributes little to direction selectivity in those combinations (Figure 5E, right; e.g., Tm2xTm9/Tm4).

According to our simulations, and if the structure for T5 resembles the hybrid detector proposed for T4, the arrangement of a central Tm2, flanked on the null side by an enhancing Tm1 and on the preferred side by a suppressing Tm9 input, achieves by far the best direction selectivity. This implementation would predict inhibitory/suppressing input from Tm9 onto T5, which could be experimentally tested. Consistent with this arrangement, out of all four T5 columnar inputs, blocking the synaptic output from Tm4 cells results in the lowest reduction in OFF-edge responses in tangential cells [20]. Nevertheless, those blocking experiments indicate that Tm4 plays a role in the detector that awaits resolving.

In this study, we have shown that the activation of the octopamine system by CDM shifts the temporal-frequency and velocity tuning of T4 and T5 neurons to higher temporal frequencies/velocities, mirroring the temporal tuning shift in tangential cells of the lobula plate observed under active locomotion or octopaminergic activation [24–27]. At the level of T4 and T5 neurons, we find a temporal-frequency optimum of about 1–1.5 Hz for moving gratings under control conditions, corroborating previous studies [14, 17, 22]. Application of CDM shifts the temporal-frequency optimum to 2.5 Hz. T4 and T5 cells show a velocity optimum for moving edges at 3°/s or lower under control conditions, which shifts to about 12°/s under CDM. The much higher velocity optimum observed in tangential cells [40] results from the summation of synaptic inputs from the larger number of T4 and T5 neurons swept by the edge during the same time interval at higher velocities.

In parallel to the temporal-frequency tuning shift in T4 and T5 neurons, the temporal response properties of the input elements, in particular of the band-pass filter elements, accelerate. Indeed, the shift in the tuning of T4 and T5 neurons (Figure 3) can be fully accounted for by the speeding of their input elements (Figures 4 and 5). This further supports the hypothesis that the temporal kinetics of the input elements alone, without any further filtering at the synaptic or T4/T5 dendritic levels, represent the delay stage of the elementary motion detectors.

Interestingly, we observe that whereas the order of input elements with respect to their filter characteristics generally remained the same under CDM, Tm1 became faster than Tm4 (Figure S6). As a consequence, simulated motion detectors using combinations that relied on temporal differences between these two cell types suffered a strong reduction or complete breakdown of direction selectivity under CDM (Figure 5). Considering cell-to-cell variability and such changes under different physiological conditions, detectors relying on small differences in the dynamics of their input elements [18, 39] will not be robust.

Octopaminergic neurons broadly innervate the optic lobes, specifically the medulla, lobula, and lobula plate [26, 28, 29]. They activate during flight and are necessary and sufficient for the observed change in the temporal tuning profile of tangential cells [26]. Although the molecular and cellular mechanisms of action on the medulla neurons and T4/T5 cells, as well as the precise physiological activation of the octopamine system, are beyond the scope of this study, a few points are worth noting. Four different types of octopamine receptors exist in *Drosophila* that are all G protein-coupled receptors but act via different pathways and thus will have different effects [41, 42]. Of those four types, only the octopamine receptors Oamb and to a lesser degree Oct1βR appear to be expressed in the optic lobes [42]. The expression pattern of these octopamine receptors is not known at the cellular level. Considering that all input elements in both the ON and the OFF pathway are accelerated in their responses, albeit to different degrees, it is entirely possible that those changes are indirect and inherited from neurons in the lamina or even the retina. For example, an accelerated response in L1 and L2, and to a smaller degree in L3, could explain the observed response changes in the medulla neurons described here. So far, octopaminergic neurons have not been shown to innervate the retina and lamina directly [26, 28, 29], yet octopamine might nevertheless directly or indirectly affect

photoreceptors or lamina neurons. For example, lamina wide-field neurons, projecting from the medulla back into the lamina and forming synaptic inputs to lamina neurons [43], are modulated by the behavioral state and octopamine signaling [44]. Although it cannot be excluded that octopamine acts at multiple levels, including on T4/T5 neurons directly, we have shown that the observed tuning shift in T4/T5 neurons can be fully accounted for by the changes in the temporal dynamics of their input elements.

Pharmacological activation, like any optogenetic or other exogenous activation of the octopamine system, is unlikely to capture all subtleties of the physiological changes during active locomotion, yet it can serve as a tool to manipulate the tuning of the visual motion detection system. At the same time, considering the match between pharmacological manipulation and physiological state changes observed at the level of lobula plate tangential cells [24–26], it is highly likely that the speeding of the filter characteristics in the medulla neurons described here is relevant under physiological conditions.

We have shown that it is possible to construct a hybrid HR/BL detector (as proposed in [17]) with the measured filters for the cellular elements for both the ON and the OFF pathway across different network states. From these, we can predict anatomical arrangements that would give rise to the observed response characteristics of the elementary motion detectors. Although we cannot rule out additional synaptic or dendritic filter mechanisms, we show that the temporal dynamics of the input elements alone are sufficient to explain the response properties of the elementary motion detectors across different tuning regimes. Future studies using the genetic toolbox of *Drosophila* to activate or block individual input neurons and studying the effects on visual responses in the T4 and T5 cells, as well as neurotransmitter and receptor expression pattern analyses and electron-microscopic reconstructions of the wiring, will be required to verify and further confine the proposed circuitry.

## EXPERIMENTAL PROCEDURES

Experimental procedures are described in detail in the [Supplemental Experimental Procedures](#).

## SUPPLEMENTAL INFORMATION

Supplemental Information includes Supplemental Experimental Procedures, six figures, and two tables and can be found with this article online at <http://dx.doi.org/10.1016/j.cub.2017.01.051>.

## AUTHOR CONTRIBUTIONS

A.A., M.S.D., and A.B. conceived the study and designed the experiments. A.A. conducted and analyzed the measurements of T4/T5 cell responses. M.S.D. designed the projector-based stimulation arena and performed and analyzed the measurements of the OFF-pathway elements. F.G.R. performed and analyzed the experiments describing the ON-pathway neurons. G.A. performed and analyzed the patch-clamp recordings from lobula plate tangential cells. M.S.D. performed the computer simulations. A.A. wrote the manuscript with the help of all authors.

## ACKNOWLEDGMENTS

We thank Stefan Prech for help in designing the projector-based stimulus arena, Jürgen Haag for sharing his expertise in two-photon microscopy, and

Wolfgang Essbauer and Michael Sauter for fly husbandry. We are very grateful to Michael Reiser, Gerry Rubin, and Aljoscha Nern (Janelia) for sharing unpublished fly lines. We would also like to thank Aljoscha Leonhardt for many helpful discussions, and Alex Mauss for critically reading the manuscript. This work was supported by an EMBO Long-Term Fellowship (A.A.), the Deutsche Forschungsgemeinschaft (SFB 870), and the Max Planck Society.

Received: October 28, 2016

Revised: December 19, 2016

Accepted: January 25, 2017

Published: March 23, 2017

## REFERENCES

1. Borst, A. (2014). Fly visual course control: behaviour, algorithms and circuits. *Nat. Rev. Neurosci.* 15, 590–599.
2. Fischbach, K.F., and Dittrich, A.P.M. (1989). The optic lobe of *Drosophila melanogaster*. I. A Golgi analysis of wild-type structure. *Cell Tissue Res.* 258, 441–475.
3. Bausenwein, B., Dittrich, A.P., and Fischbach, K.F. (1992). The optic lobe of *Drosophila melanogaster*. II. Sorting of retinotopic pathways in the medulla. *Cell Tissue Res.* 267, 17–28.
4. Takemura, S.-Y., Bharioke, A., Lu, Z., Nern, A., Vitaladevuni, S., Rivlin, P.K., Katz, W.T., Olbris, D.J., Plaza, S.M., Winston, P., et al. (2013). A visual motion detection circuit suggested by *Drosophila* connectomics. *Nature* 500, 175–181.
5. Shinomiya, K., Karuppudurai, T., Lin, T.-Y., Lu, Z., Lee, C.-H., and Meinertzhagen, I.A. (2014). Candidate neural substrates for off-edge motion detection in *Drosophila*. *Curr. Biol.* 24, 1062–1070.
6. Barlow, H.B., and Levick, W.R. (1965). The mechanism of directionally selective units in rabbit's retina. *J. Physiol.* 178, 477–504.
7. Hassenstein, B., and Reichardt, W. (1956). Systemtheoretische Analyse der Zeit-, Reihenfolgen-und Vorzeichenauswertung bei der Bewegungsperzeption des Rüsselkäfers Chlorophanus. *Z. Naturforsch. B* 11, 513–524.
8. Borst, A., and Helmstaedter, M. (2015). Common circuit design in fly and mammalian motion vision. *Nat. Neurosci.* 18, 1067–1076.
9. Joesch, M., Schnell, B., Raghu, S.V., Reiff, D.F., and Borst, A. (2010). ON and OFF pathways in *Drosophila* motion vision. *Nature* 468, 300–304.
10. Strother, J.A., Nern, A., and Reiser, M.B. (2014). Direct observation of ON and OFF pathways in the *Drosophila* visual system. *Curr. Biol.* 24, 976–983.
11. Clark, D.A., Bursztyn, L., Horowitz, M.A., Schnitzer, M.J., and Clandinin, T.R. (2011). Defining the computational structure of the motion detector in *Drosophila*. *Neuron* 70, 1165–1177.
12. Eichner, H., Joesch, M., Schnell, B., Reiff, D.F., and Borst, A. (2011). Internal structure of the fly elementary motion detector. *Neuron* 70, 1155–1164.
13. Joesch, M., Weber, F., Eichner, H., and Borst, A. (2013). Functional specialization of parallel motion detection circuits in the fly. *J. Neurosci.* 33, 902–905.
14. Maisak, M.S., Haag, J., Ammer, G., Serbe, E., Meier, M., Leonhardt, A., Schilling, T., Bahl, A., Rubin, G.M., Nern, A., et al. (2013). A directional tuning map of *Drosophila* elementary motion detectors. *Nature* 500, 212–216.
15. Mauss, A.S., Meier, M., Serbe, E., and Borst, A. (2014). Optogenetic and pharmacologic dissection of feedforward inhibition in *Drosophila* motion vision. *J. Neurosci.* 34, 2254–2263.
16. Mauss, A.S., Pankova, K., Arenz, A., Nern, A., Rubin, G.M., and Borst, A. (2015). Neural circuit to integrate opposing motions in the visual field. *Cell* 162, 351–362.
17. Haag, J., Arenz, A., Serbe, E., Gabbiani, F., and Borst, A. (2016). Complementary mechanisms create direction selectivity in the fly. *eLife* 5, e17421.
18. Behnia, R., Clark, D.A., Carter, A.G., Clandinin, T.R., and Desplan, C. (2014). Processing properties of ON and OFF pathways for *Drosophila* motion detection. *Nature* 512, 427–430.
19. Behnia, R., and Desplan, C. (2015). Visual circuits in flies: beginning to see the whole picture. *Curr. Opin. Neurobiol.* 34, 125–132.
20. Serbe, E., Meier, M., Leonhardt, A., and Borst, A. (2016). Comprehensive characterization of the major presynaptic elements to the *Drosophila* OFF motion detector. *Neuron* 89, 829–841.
21. Ammer, G., Leonhardt, A., Bahl, A., Dickson, B.J., and Borst, A. (2015). Functional specialization of neural input elements to the *Drosophila* ON motion detector. *Curr. Biol.* 25, 2247–2253.
22. Fisher, Y.E., Silies, M., and Clandinin, T.R. (2015). Orientation selectivity sharpens motion detection in *Drosophila*. *Neuron* 88, 390–402.
23. Leong, J.C.S., Esch, J.J., Poole, B., Ganguli, S., and Clandinin, T.R. (2016). Direction selectivity in *Drosophila* emerges from preferred-direction enhancement and null-direction suppression. *J. Neurosci.* 36, 8078–8092.
24. Chiappe, M.E., Seelig, J.D., Reiser, M.B., and Jayaraman, V. (2010). Walking modulates speed sensitivity in *Drosophila* motion vision. *Curr. Biol.* 20, 1470–1475.
25. Jung, S.N., Borst, A., and Haag, J. (2011). Flight activity alters velocity tuning of fly motion-sensitive neurons. *J. Neurosci.* 31, 9231–9237.
26. Suver, M.P., Mamiya, A., and Dickinson, M.H. (2012). Octopamine neurons mediate flight-induced modulation of visual processing in *Drosophila*. *Curr. Biol.* 22, 2294–2302.
27. Longden, K.D., and Krapp, H.G. (2010). Octopaminergic modulation of temporal frequency coding in an identified optic flow-processing interneuron. *Front. Syst. Neurosci.* 4, 153.
28. Sinakevitch, I., and Strausfeld, N.J. (2006). Comparison of octopamine-like immunoreactivity in the brains of the fruit fly and blow fly. *J. Comp. Neurol.* 494, 460–475.
29. Busch, S., Selcho, M., Ito, K., and Tanimoto, H. (2009). A map of octopaminergic neurons in the *Drosophila* brain. *J. Comp. Neurol.* 513, 643–667.
30. Chen, T.-W., Wardill, T.J., Sun, Y., Pulver, S.R., Renniger, S.L., Baohan, A., Schreiter, E.R., Kerr, R.A., Orger, M.B., Jayaraman, V., et al. (2013). Ultrasensitive fluorescent proteins for imaging neuronal activity. *Nature* 499, 295–300.
31. Roeder, T. (1995). Pharmacology of the octopamine receptor from locust central nervous tissue (OAR3). *Br. J. Pharmacol.* 114, 210–216.
32. Schnell, B., Weir, P.T., Roth, E., Fairhall, A.L., and Dickinson, M.H. (2014). Cellular mechanisms for integral feedback in visually guided behavior. *Proc. Natl. Acad. Sci. USA* 111, 5700–5705.
33. Mazurek, M., Kager, M., and Van Hooser, S.D. (2014). Robust quantification of orientation selectivity and direction selectivity. *Front. Neural Circuits* 8, 92.
34. Meier, M., Serbe, E., Maisak, M.S., Haag, J., Dickson, B.J., and Borst, A. (2014). Neural circuit components of the *Drosophila* OFF motion vision pathway. *Curr. Biol.* 24, 385–392.
35. Fisher, Y.E., Leong, J.C.S., Sporar, K., Ketkar, M.D., Gohl, D.M., Clandinin, T.R., and Silies, M. (2015). A class of visual neurons with wide-field properties is required for local motion detection. *Curr. Biol.* 25, 3178–3189.
36. Yang, H.H., St-Pierre, F., Sun, X., Ding, X., Lin, M.Z., and Clandinin, T.R. (2016). Subcellular imaging of voltage and calcium signals reveals neural processing in vivo. *Cell* 166, 245–257.
37. Takemura, S.-Y., Xu, C.S., Lu, Z., Rivlin, P.K., Parag, T., Olbris, D.J., Plaza, S., Zhao, T., Katz, W.T., Umayam, L., et al. (2015). Synaptic circuits and their variations within different columns in the visual system of *Drosophila*. *Proc. Natl. Acad. Sci. USA* 112, 13711–13716.
38. Silies, M., Gohl, D.M., Fisher, Y.E., Freifeld, L., Clark, D.A., and Clandinin, T.R. (2013). Modular use of peripheral input channels tunes motion-detecting circuitry. *Neuron* 79, 111–127.

39. Salazar-Gatzimas, E., Chen, J., Creamer, M.S., Mano, O., Mandel, H.B., Matulis, C.A., Pottackal, J., and Clark, D.A. (2016). Direct measurement of correlation responses in *Drosophila* elementary motion detectors reveals fast timescale tuning. *Neuron* 92, 227–239.

40. Leonhardt, A., Ammer, G., Meier, M., Serbe, E., Bahl, A., and Borst, A. (2016). Asymmetry of *Drosophila* ON and OFF motion detectors enhances real-world velocity estimation. *Nat. Neurosci.* 19, 706–715.

41. Farooqui, T. (2007). Octopamine-mediated neuromodulation of insect senses. *Neurochem. Res.* 32, 1511–1529.

42. El-Kholi, S., Stephano, F., Li, Y., Bhandari, A., Fink, C., and Roeder, T. (2015). Expression analysis of octopamine and tyramine receptors in *Drosophila*. *Cell Tissue Res.* 361, 669–684.

43. Rivera-Alba, M., Vitaladevuni, S.N., Mishchenko, Y., Lu, Z., Takemura, S.Y., Scheffer, L., Meinertzhagen, I.A., Chklovskii, D.B., and de Polavieja, G.G. (2011). Wiring economy and volume exclusion determine neuronal placement in the *Drosophila* brain. *Curr. Biol.* 21, 2000–2005.

44. Tuthill, J.C., Nern, A., Rubin, G.M., and Reiser, M.B. (2014). Wide-field feedback neurons dynamically tune early visual processing. *Neuron* 82, 887–895.

**Current Biology, Volume 27**

**Supplemental Information**

**The Temporal Tuning of the *Drosophila*  
Motion Detectors Is Determined  
by the Dynamics of Their Input Elements**

**Alexander Arenz, Michael S. Drews, Florian G. Richter, Georg Ammer, and Alexander Borst**

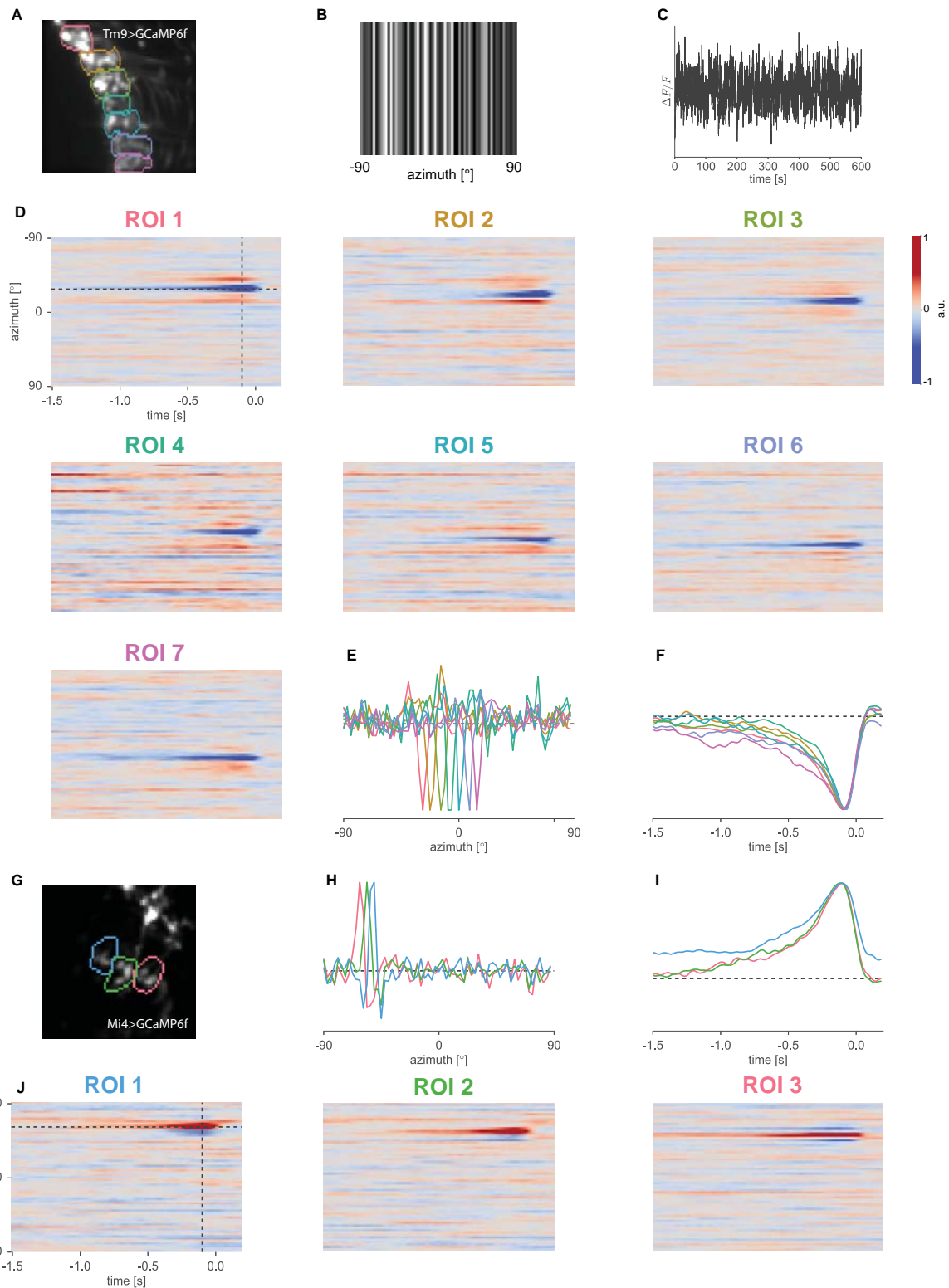


**Figure S1. Related to Figure 2. Example acquisition of spatiotemporal receptive fields via stochastic stimulation and reverse correlation of calcium signals for the neurons Tm9 and Mi4.**

(A) 2-photon image from a fly expressing GCaMP6f in Tm9 axon terminals in the lobula. Highlighted in color are seven manually drawn regions of interest (ROIs) around individual terminals from neighboring columns.

(B) Snapshot of one frame of the one-dimensional horizontal noise stimulus.

(C) Calcium trace from a single ROI in response to 10 minutes of white noise stimulation.

(D) Spatiotemporal receptive fields obtained by reverse correlation of the calcium signals in each ROI with the stimulus.

(E) Cross-sections through the receptive fields along the space axis reflecting the retinotopic organisation of the lobula.

(F) Cross-sections through the receptive fields along the temporal axis revealing the low-pass characteristics of Tm9.

(G-J) Same for Mi4.

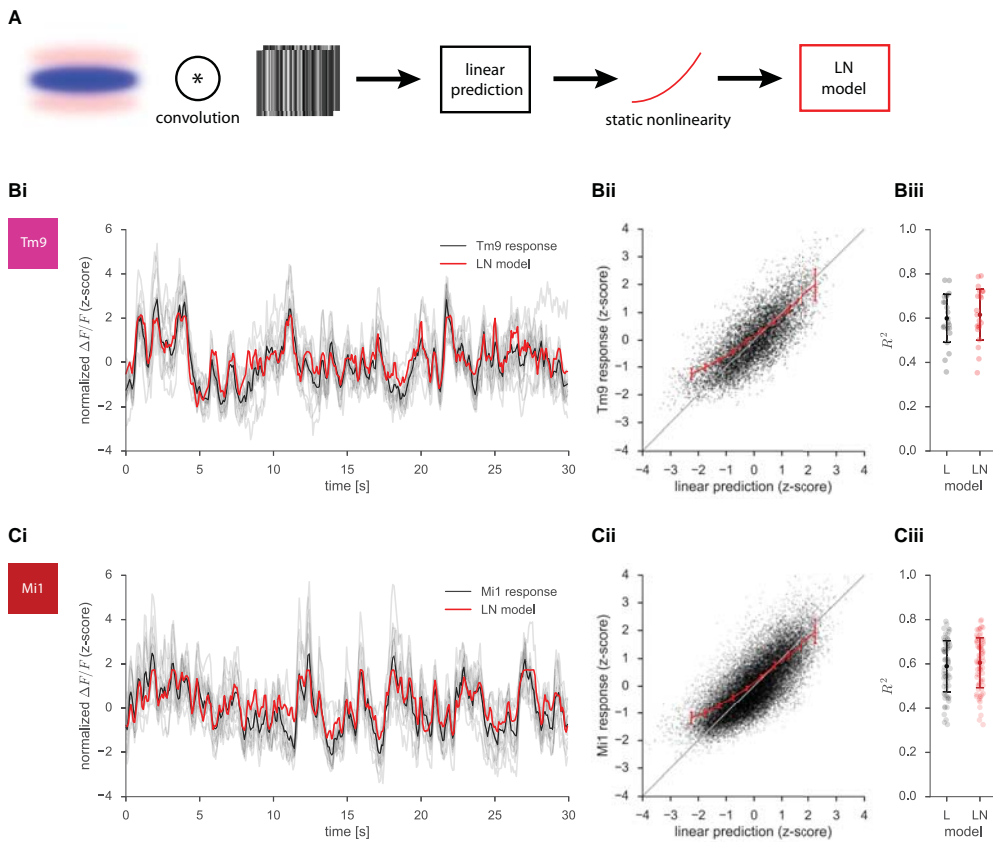


**Figure S2. Related to Figure 2. Prediction of calcium responses in Tm9 and Mi1 terminals from the linear spatiotemporal receptive fields.**

(A) Schematic of the model. The linear prediction of individual axon terminal responses (of Tm9 or Mi1) to a white noise stimulus is given by the convolution of the stimulus with the respective spatio-temporal receptive field of the cell. A linear-nonlinear model (LN) is built by remapping the output of the linear prediction with a static nonlinearity.

(Bi) Actual response of an exemplary Tm9 axon terminal (black) and the prediction of the LN model (red). (Bii) Scatter plot of the linear prediction against the actual response for all cells recorded. The static nonlinearity (red) is obtained by averaging the point cloud within discrete bins along the x-axis for each axon terminal. (Biii) Coefficient of determination for the linear model (L, black) and the linear-nonlinear model (LN, red). The linear model prediction alone accounted for 60% and the LN model for 62% of the response variance. Circles represent measurements of individual terminals, the bar shows the standard deviation and the mean among all cells measured ( $N = 4$ ,  $n = 22$ ).

(C) Same as in (B), but for Mi1 ( $N = 4$ ,  $n = 78$ ). The L model alone accounted for 59% and the LN model for 61% of the response variance.

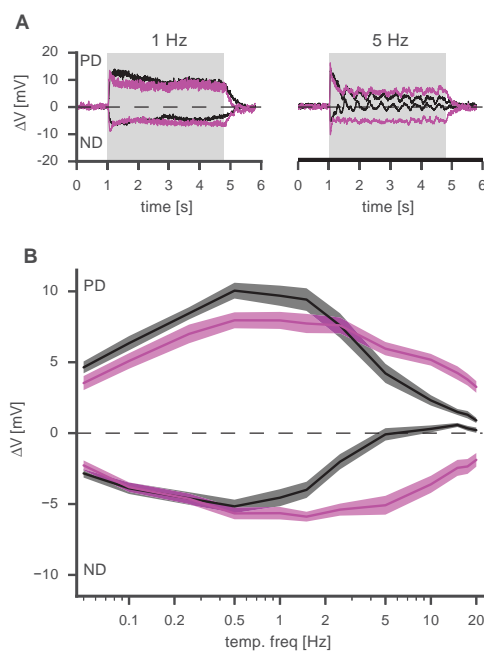


**Figure S3. Related to Figure 3. Temporal frequency tunings of lobula plate tangential cells change with the application of the octopamine agonist CDM.**

(A) Voltage responses of HS and VS tangential cells in the lobula plate (population average,  $N = 15$  flies,  $n=15$  cells) to square-wave gratings moving in the preferred or null direction in control (black) and after application of CDM (magenta) for gratings moving at a temporal frequency of 1 Hz (left) or 5 Hz (right). The period of motion of the grating is indicated by the grey-shaded region.

(B) Average voltage responses over the stimulation period for square-wave gratings at different temporal frequencies. Responses, measured as average voltage deflections over the whole stimulus period, peaked at 0.5 Hz in both the preferred (as maximum average depolarization) and null (as maximum average hyperpolarization) direction. Application of the octopamine agonist chlordimeform (CDM; magenta) at a final concentration of 20  $\mu$ M resulted in increased responses to higher temporal frequencies from 2-20 Hz.

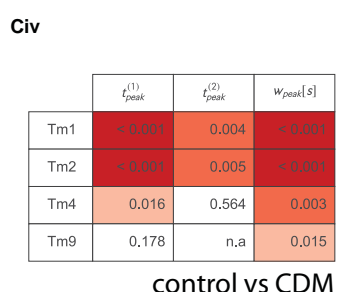
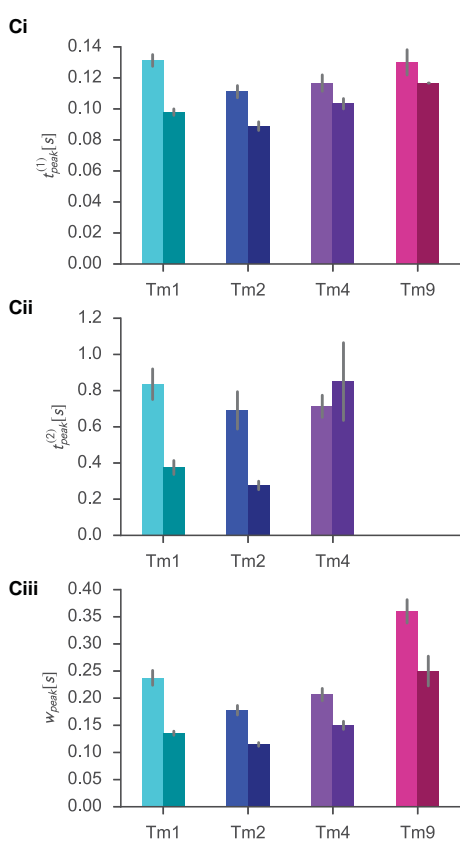
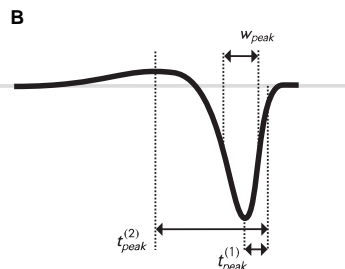
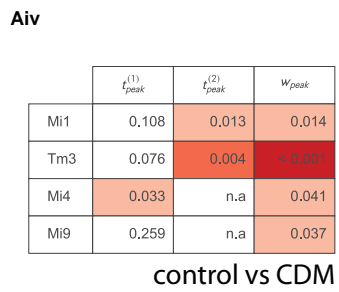
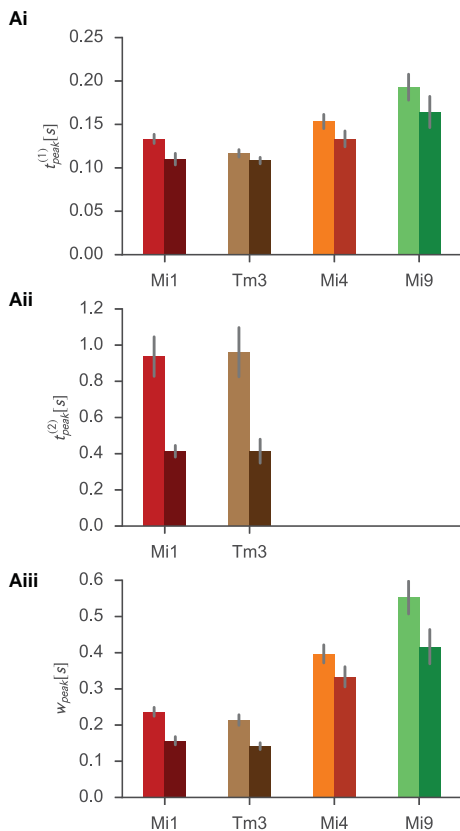


**Figure S4. Related to Figure 2 and 4. Analysis of the temporal filters of the inputs to T4 and T5.**

(A) T4 inputs. We quantified the shape of the temporal filters, as well as their change after application of CDM, by three measures (B): the time-to-peak for the first peak ( $t_{\text{peak}}^{(1)}$ , (Ai)) and, for the biphasic filter kernels of band-pass filters, to the second peak ( $t_{\text{peak}}^{(2)}$ , (Aii)), as well as the full-width at half-maximum for the first peak ( $w_{\text{peak}}$ , (Aiii)) of the temporal kernel. Measurements after application of CDM are presented in a darker color shade (right bars) than for the control condition (left bars) of the respective cell. Statistical comparisons between control and CDM condition (based on a paired t-test) are shown in (Aiv), highlighted in red color when statistical significance is observed (with a gradient in the red nuance from light to dark red indicating p values of  $p < 0.05$ ,  $p < 0.01$  and  $p < 0.001$ ).

(C) Same, for T5 inputs.

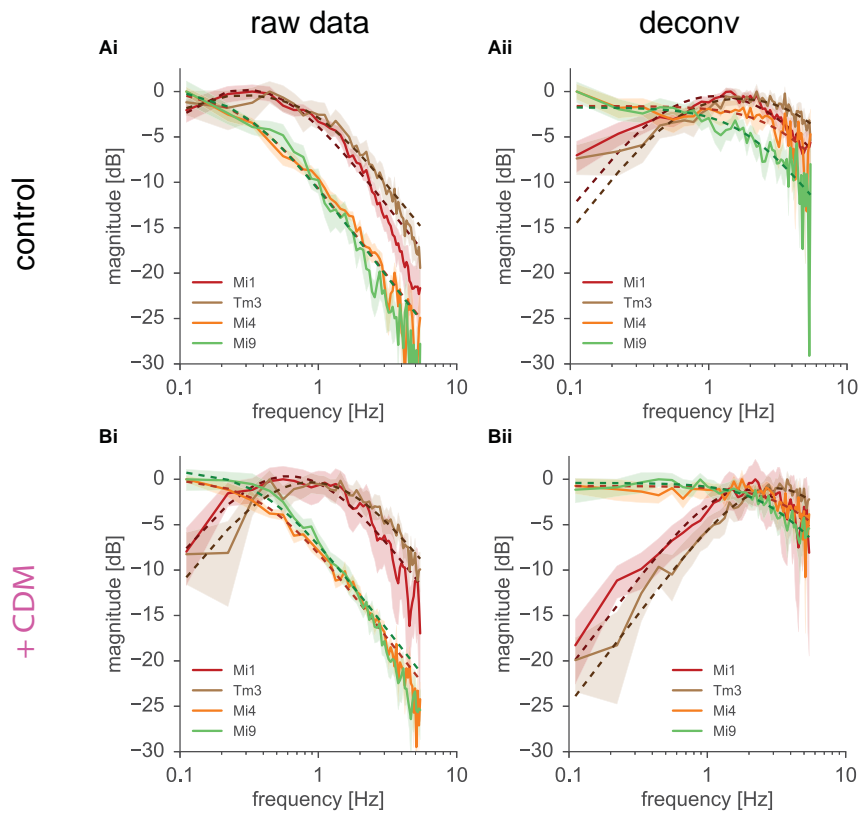


**Figure S5. Related to Figure 5. Model fitting on the frequency spectra of the ON pathway elements.**

(Ai) Frequency spectrum derived from calcium imaging experiments for the ON pathway columnar neurons Mi1, Tm3, Mi4, Mi9. (Aii) Frequency spectrum after deconvolution with a low-pass filter representing the dynamics of the calcium indicator GCaMP6f. Dashed lines represent the fitted frequency responses of 1st order band-pass or low-pass filters.

(Bi, Bii) Like (Ai, Aii), for the spectra determined from the recordings after application of CDM.

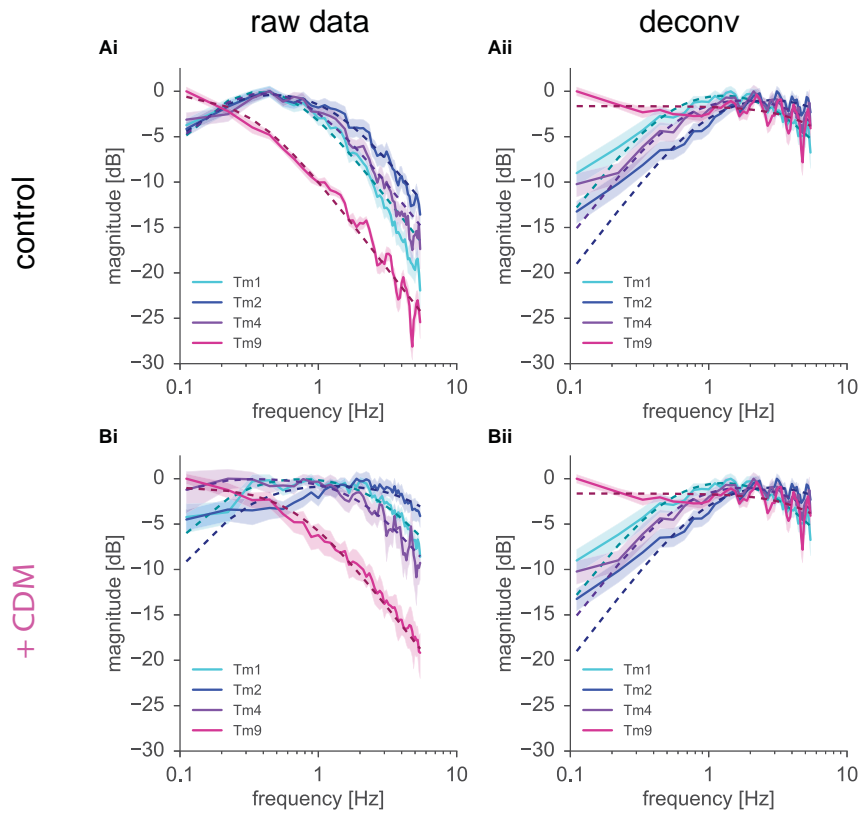


**Figure S6. Related to Figure 5. Model fitting on the temporal filter frequency spectra of the OFF pathway elements.**

(Ai) Measured frequency spectra based on calcium imaging experiments for the OFF pathway elements Tm1, Tm2, Tm4 and Tm9. (Aii) Frequency spectra after deconvolution with a filter describing the dynamics of the calcium indicator. Dashed lines represent the fitted frequency responses of 1st order band-pass or low-pass filters.

(Bi, Bii) Same as (Ai, Aii), after application of CDM.

	Mi1		Tm3		Mi4		Tm9	
	control	+ CDM						
$A_{\text{raw}}$	1.271	1.314	0.996	1.204	1.007	1.000	0.982	1.060
$t_{\text{H},\text{raw}}$	1.078 s	0.445 s	1.769 s	0.340 s	-	-	-	-
$t_{\text{L},\text{raw}}$	0.266 s	0.143 s	0.158 s	0.086 s	0.519 s	0.370 s	0.546 s	0.373 s
$R_s^2$	0.975	0.942	0.971	0.925	0.984	0.990	0.982	0.987
$A_{\text{deconv}}$	1.146	1.643	1.035	2.034	0.831	0.906	0.789	0.940
$t_{\text{H},\text{deconv}}$	0.318 s	0.075 s	0.260 s	0.044 s	-	-	-	-
$t_{\text{L},\text{deconv}}$	0.054 s	0.075 s	0.027 s	0.044 s	0.038 s	0.028 s	0.077 s	0.043 s
$R^2_{\text{t,deconv}}$	0.872	0.851	0.768	0.955	0.666	0.643	0.832	0.906
$A_{\text{sur}}/A_{\text{cen}}$	0.022	0.028	0.000	0.000	0.132	0.093	0.063	0.043
$\text{FWHM}_{\text{cen}}$	6.81 °	7.09 °	11.91 °	12.40 °	6.47 °	6.49 °	6.37 °	6.37 °
$\text{FWHM}_{\text{sur}}$	28.81 °	19.86 °	-	-	16.14 °	20.02 °	23.98 °	28.08 °
$R_s^2$	0.995	0.990	0.985	0.984	0.987	0.989	0.980	0.992

**Table S1. Related to Figure 2 and 4. Spatio-temporal response properties of T4 input cells.**  
 Numerical parameters derived from the model fits to the temporal and the spatial components of the spatio-temporal receptive fields obtained from reverse correlation for the ON-pathway neurons.

	Tm1		Tm2		Tm4		Tm9	
	control	+ CDM						
$A_{\text{raw}}$	1.419	1.072	1.068	0.933	1.218	0.990	0.961	0.890
$t_{\text{Hf, raw}}$	0.632 s	0.754 s	0.962 s	0.558 s	0.788 s	2.210 s		
$t_{\text{Ip, raw}}$	0.271 s	0.051 s	0.113 s	0.020 s	0.186 s	0.070 s	0.462 s	0.220 s
$R^2_{\text{t, raw}}$	0.978	0.901	0.979	0.564	0.972	0.930	0.985	0.981
$A_{\text{deconv}}$	1.117	2.217	1.038	2.657	1.018	1.002	0.827	0.836
$t_{\text{Hf, deconv}}$	0.296 s	0.032 s	0.153 s	0.018 s	0.249 s	0.086 s		
$t_{\text{Ip, deconv}}$	0.044 s	0.032 s	0.014 s	0.018 s	0.024 s	0.015 s	0.017 s	0.008 s
$R^2_{\text{t, deconv}}$	0.895	0.974	0.893	0.990	0.807	0.880	0.273	0.226
$A_{\text{sur}}/A_{\text{cen}}$	0.040	0.029	0.035	0.026	0.054	0.005	0.046	0.071
$\text{FWHM}_{\text{cen}}$	8.12 °	7.34 °	7.93 °	7.23 °	11.45 °	10.10 °	6.92 °	6.53 °
$\text{FWHM}_{\text{sur}}$	27.14 °	20.46 °	30.52 °	23.01 °	34.62 °	72.03 °	23.78 °	21.74 °
$R^2_s$	0.997	0.995	0.994	0.991	0.992	0.988	0.995	0.995

**Table S2. Related to Figure 2 and 4. Spatio-temporal response properties of T5 input cells.**  
 Numerical parameters derived from the model fits to the temporal and the spatial components of the spatio-temporal receptive fields obtained from reverse correlation for the OFF-pathway neurons.

## Supplemental Experimental Procedures

### Flies/preparation

Flies were raised and kept on standard cornmeal-agar medium on a 12 hour light/12 hour dark cycle at 25°C and 60% humidity. For patch-clamp recordings from tangential cells, Canton S flies were used. For calcium imaging experiments, the genetically-encoded calcium indicators GCaMP6f or GCaMP6m [S1] were expressed using the Gal4/UAS- or LexA/lexAop-system in cell-type specific driver lines, resulting in the following genotypes:

Short name	Genotype
Mi1>GC6f	<i>w<sup>-</sup>; R19F01-AD/UAS-GCaMP6f; R71D01-DBD/UAS-GCaMP6f</i>
Tm3>GC6f	<i>w<sup>-</sup>; UAS-GCaMP6f; R13E12-Gal4</i>
Mi4>GC6f	<i>w<sup>-</sup>; R48A07-AD/UAS-GCaMP6f; R13F11-DBD/UAS-GCaMP6f</i>
Mi9>GC6f	<i>w<sup>-</sup>; R48A07-AD/UAS-GCaMP6f; VT046779-DBD/UAS-GCaMP6f</i>
Tm1>GC6f	<i>w<sup>-</sup>; UAS-GCaMP6f; VT12717-Gal4</i>
Tm2>GC6f	<i>w<sup>-</sup>; UAS-GCaMP6f; VT12282-Gal4</i>
Tm4>GC6f	<i>w<sup>-</sup>; UAS-GCaMP6f; R35H01-Gal4</i>
Tm9>GC6f	<i>w<sup>-</sup>; UAS-GCaMP6f; VT65303-Gal4</i>
T4/T5>GC6m	<i>w<sup>-</sup>; Sp/CyO ; VT50384-lexA, lexAop-GCaMP6m/TM6b</i>

The transgenic fly lines driving split-Gal4 expression in the medulla neurons Mi1, Mi4 and Mi9, respectively, were generated and will be described in [S2] (with the Mi1 driver line corresponding to their transgenic fly line SS00809, Mi4 to SS01019, and Mi9 to SS02432).

For electrophysiological and calcium imaging experiments, flies were prepared as previously described [S3, S4]. Briefly, flies were anaesthetized on ice or with CO<sub>2</sub>, fixed with their backs, legs and wings to a Plexiglas holder with the back of the head exposed to a recording chamber filled with fly external solution. The cuticula at the back of the head on one side was cut away with a fine hypodermic needle and removed together with muscles and air sacks covering the underlying optic lobe. To gain access to tangential cells for electrophysiological recordings, the neurolemma covering the brain was partially digested by applying 0.5mg/ml collagenase IV (Gibco) with a glass electrode to the brain until the tangential cell somata were exposed. Where indicated, the octopamine agonist chlordimeform (CDM, Sigma Aldrich) was added as a 2mM stock solution (in external solution) directly to the bath to yield a final concentration of 20 μM. Diffusion was allowed for 15 min before recordings recommenced.

**Patch-clamp recordings** from vertical and horizontal system tangential cells were performed as previously described [S4].

### 2-Photon calcium imaging

Calcium imaging was performed on custom-built 2-photon microscopes as previously described [S3] controlled with the ScanImage software in Matlab [S5]. Acquisition rates were between 3.8 and 15 Hz, image resolution between 64x64 and 128x128 pixels. Before starting the acquisition, we verified that the receptive fields of the cells were located on the stimulus arena by showing a search stimulus consisting of moving gratings.

## Visual stimulation

For the study of visual responses of lobula plate tangential cells and T4/T5 neurons, visual stimuli were presented on an **LED arena**, based on a design by [S6], covering approximately 180° in azimuth and 90° in elevation. Stimuli covered the whole extent of the arena and were presented at full contrast. Square-wave gratings had a spatial wavelength of 24°, and moved with velocities of 1.2-480°/s in the preferred and null direction, corresponding to temporal frequencies ranging from 0.05 to 20°/s. Single stimulation periods of moving gratings lasted for 3.8 s, separated by periods of 5 s where the grating remained stationary. For the edge velocity tuning, bright or dark edges of full contrast were presented, moving at velocities of 3 to 300 °/s in the preferred (up) and null direction (down) of T4c/T5c neurons, separated by 6 s. All stimuli were presented in a pseudo-random order with 3-5 repetitions per stimulus.

The spatio-temporal response properties of the Mi and Tm columnar input elements were determined on a custom-built **projector-based arena** that allowed for greater stimulus flexibility. Stimuli were projected with 2 commercial micro-projectors (TI DLP Lightcrafter 3000) onto the back of an opaque cylindrical screen covering 180° in azimuth and 105° in elevation of the fly's visual field. The projectors were programmed to use only the green LED (OSRAM L CG H9RN) which emits light between 500nm to 600nm wavelength. This increased the refresh rate from 60 to 180 Hz (at 8 bit color depth). To prevent overlap between the spectra of the GCaMP signal and the arena light, we placed two long-pass filters (Thorlabs FEL0550 and FGL550) in front of each projector restricting the stimulus light to wavelengths above 550nm. A band-pass filter in front of the photomultiplier (Brightline 520/35) allowed only the portion of the light within the GCaMP emission spectrum to be detected. Additional shielding of stray light from the arena with black foil effectively suppressed any leak of the arena light into the photomultiplier signal. The maximum luminance achieved by our stimulation system is  $276 \pm 48 \text{ cd/m}^2$ . For all stimuli used here, we set the medium brightness to a 8-bit grayscale value of 50, which corresponds to a medium luminance of  $55 \pm 11 \text{ cd/m}^2$ .

Stimuli were rendered using a custom written software in Python 2.7. To account for the curvature of the arena screen, our software pre-distorts the generated images such that the projected image appears as a regular grating on the screen. For that, the software takes advantage of functions from Panda3D, a framework for 3D rendering for Python.

## Gaussian noise stimulus

To generate the horizontal white noise stimulus, we partitioned the cylindrical screen into 64 bars, so that each bar covered an angle of approximately 2.8° in azimuth. For each bar, samples were drawn at a frame rate of 60 Hz from a Gaussian distribution, so that the standard deviation was at 25% contrast around a mean intensity value of 50 on the 8-bit grayscale of the display devices. We then filtered the random samples for each bar with a Gaussian filter with a standard deviation of 5 Hz in the frequency domain which leads to a stimulus auto-correlation function that is a Gaussian with approximately 45ms standard deviation. Since the calcium indicator dynamics of GCaMP and the data acquisition frame rate (12 Hz in this case) place a lower bound on the temporal precision of the signal we can extract from calcium imaging experiments, we restricted the frequency content of the stimulus in this way to the relevant domain. The whole stimulus sequence was 10 minutes long and was exported as a video file in H.264 format with lossless compression. For the vertical noise the same stimulus was rotated by 90° and scaled such that 54 bars covered the height of the screen, accounting for the aspect ratio of the screen being approximately 1.2.

## Data acquisition and analysis

Data analysis was performed offline using custom-written routines in Matlab and Python 2.7 (with the SciPy and OpenCV-Python Libraries).

For the **electrophysiological experiments**, baseline-subtracted voltage responses of tangential cells were averaged across trials, and the response to gratings was quantified as the average voltage over the whole period of the respective stimulus presentation. Preferred direction was front-to-back for HS and down for VS cells, null direction the corresponding opposite direction. For Suppl. Figure S3 voltage responses over the individual stimuli were averaged across all cells.

**Calcium imaging:** Images were automatically registered using vertical and horizontal translations to correct for the movement of the brain. Fluorescence changes ( $\Delta F/F$  values) were then calculated by dividing every registered frame by the average of the registered first 5 images of the recording. Regions of interest (ROIs) were selected on the average raw image by hand: in layer 10 of the medulla for the ON, in the lobula for the OFF pathway elements, outlining single terminals. For T4 and T5 neurons, ROIs were routinely chosen in the lobula plate, encompassing small regions with single to few axon terminals, or selected to cover single neurites between medulla or lobula and lobula plate. For Figure 3D&E, ROIs were drawn in the medulla for T4 and in the lobula for T5 neurons to separate those 2 cell types. Averaging the fluorescence change over this ROI in space resulted in a  $\Delta F/F$  time course. Neuronal responses were quantified as the maximum  $\Delta F/F$  value over the stimulation period plus the subsequent 0.5 s, subtracted by the average of the baseline period covering the 2 frames before the respective stimulus onset. To average across cells/ROIs, responses were first normalized to the maximum response of each ROI to the corresponding stimulus set. For edges, normalization was performed separately to ON and OFF stimuli to take any selection bias for T4 or T5 cells within the ROI into account.

## White noise reverse-correlation

For the input elements, spatio-temporal receptive fields were calculated following standard reverse-correlation methods (Figure S1) [S7, S8]. First, the mean value was subtracted from the raw signals of single ROIs by using a low-pass filtered version of the signal (Gaussian filter with 120 seconds standard deviation) as a baseline for a  $\Delta F/F$ -like representation of the signal. This effectively removed slow baseline fluctuations caused by bleaching and very slow changes in the average calcium level from the signals.

We then calculated the stimulus-response reverse correlation function

$$K(x, \tau) = \int_0^T dt S(x, t - \tau) \cdot R(t)$$

where S denotes the stimulus and R the response of the neuron.

The resulting spatiotemporal fields were normalized in z-score and as a quality control only receptive fields with peak amplitudes above 10 standard deviations from the mean were taken for further analysis (for Mi9 the threshold was lowered to 7). Cross-sections through the receptive fields along the space axis were fit with a Gaussian function to determine the position of the peak.

Since one imaging frame is built up continuously over one sample time, ROIs lying at different y-coordinates in the image will in fact be imaged at slightly different times. Since the stimulus is presented at a higher frame rate of 60 Hz, this leads to a notable peak shift between the impulse responses of different ROIs. We corrected for this by translating the spatiotemporal receptive field of each ROI by a) the time difference between the start of a frame and the effective sampling point estimated by the y-coordinate of the center of mass of the respective ROI and b) the start time of the white noise stimulus within the very first frame acquired during stimulation.

Spatio-temporal receptive fields resulting from different ROIs (that were retinotopically shifted) were then centered about each other to generate a mean receptive field. To ensure receptive fields of input elements were fully covered, cells with a receptive field center less than 10 pixels (28°) from the edge of the arena were excluded.

### **Frozen noise**

Filter kernels were validated by testing their ability to predict the neuronal responses from the stimulus. For this, neurons were again stimulated with a white-noise stimulus, only this time part of the stimulus consisted of 15 repetitions (each 30 seconds long) of a white-noise sequence ('frozen noise') to eliminate noise in the neuronal responses. As above, spatio-temporal filter kernels were then reconstructed from responses to single repetition stimulus sequences (20 minutes long). Analogously to above, only receptive fields with a peak higher than 20 standard deviations were included for further analysis. Subsequently the averaged response during the held-out test portion of the stimulus was predicted for each recorded cell individually. Linear predictions were obtained by convolution of the spatio-temporal filter kernels with the frozen noise stimulus along the time axis. Filter kernels were thresholded versions of the spatio-temporal receptive fields (all values below 5% of the peak amplitude as well as regions further away than 15° from the receptive field center were set to zero). Both, the predicted response trace and the actual mean response to the frozen noise stimulus, were normalized in z-score in order to make different cells with varying calcium indicator expression levels and therefore different absolute signal values comparable. The static nonlinearity for the LN model was estimated for each cell by averaging all values from the actual mean response corresponding to values of the predicted response within bins of size 0.5 from -2.5 to +2.5 z-score (see scatter plots Bii and Cii in Suppl. Figure S2). Prediction accuracy of the linear filter was assessed through the correlation of the predicted versus actual response of the neuron [S9].

### **Spatial receptive field model**

The one-dimensional spatial receptive fields (Figure 2 E-H and K-N, top and right) are cross-sections through the peak of the spatiotemporal receptive fields along the space axis and are averaged over the 12 samples (200ms) around the peak. For almost all columnar neurons measured we found a small-field, antagonistic center-surround organization of the spatial receptive field using both the horizontal and the vertical white noise stimulus.

Mathematically, receptive fields of this kind can be described as a difference of Gaussians

$$RF_{1D}(\varphi) = e^{-\frac{\varphi^2}{2\sigma_{cen}^2}} - A_{rel} \cdot e^{-\frac{\varphi^2}{2\sigma_{sur}^2}}$$

without loss of generality for the horizontal one-dimensional receptive field along the azimuth  $\varphi$ . Here,  $\sigma_{cen}$  and  $\sigma_{sur}$  are the standard deviations of center and surround, respectively, and  $A_{rel} = A_{sur}/A_{cen}$  denotes the relative strength of the surround in relation to the amplitude of the center Gaussian (which is normalized to 1).

To reconstruct a two-dimensional receptive field from the measured one-dimensional projections, we chose the same mathematical approach as above, only in 2D:

$$RF_{2D}(\varphi, \vartheta) = e^{-\frac{(\varphi^2 + \vartheta^2)}{2\sigma_{cen}^2}} - A_{rel} \cdot e^{-\frac{(\varphi^2 + \vartheta^2)}{2\sigma_{sur}^2}}$$

For simplicity, throughout the analysis we used the small-angle approximation  $\tan \vartheta \approx \vartheta$  for the vertical axis or the elevation  $\vartheta$  even if receptive fields span angles larger than  $5^\circ$ . Thus, we neglected perspective distortions induced by the arena screen not being spherical, but cylindrical. Accounting for additional distortions induced by the relative displacement of the fly's body in relation to the elevation of the receptive field on the arena would require even more detailed mathematical description, yet we did not observe any severe irregularities in the spatial receptive fields.

It is important to note that receptive field estimation via a one-dimensional stimulus as performed here yields in fact a projection of the underlying two-dimensional spatial receptive field:

$$RF_{1D}(\varphi) = \int_{-\infty}^{\infty} RF_{2D}(\varphi, \vartheta) d\vartheta$$

Hence, we fitted the above function  $RF_{2D}(\varphi, \vartheta)$  such that its projections along the horizontal and vertical axis would agree with the given one-dimensional receptive field projections measured via reverse correlation. The fitting procedure was implemented using standard least-square algorithms (SciPy 0.16.1). The resulting values for  $A_{rel}$ ,  $\sigma_{cen}$  and  $\sigma_{sur}$  and the corresponding coefficients of the fit are given in Table S1 and S2 for each neuron type.

### Temporal filter model

The time-reversed impulse responses shown in Figure 2&4 are cross-sections through the center of the spatiotemporal receptive fields along the time axis and are averaged over the three center pixels. For the frequency domain representations in Figure 2&4, impulse responses were Fourier-transformed, averaged, and the resulting amplitude spectrum (absolute value) was divided by the power spectrum of the stimulus for frequencies below 5.5 Hz (below the Nyquist frequency). This is equivalent to deconvolving the impulse response with the stimulus auto-correlation and thereby correcting for non-white input signals [S7]. All frequency-space-representations are plotted on a double logarithmic scale expressing all signal gains in decibel according to convention in filter theory.

The complicated relationships between calcium, calcium indicator, voltage and neurotransmitter release of a cell render it impossible to precisely characterize each of these aspects having access to only the calcium indicator fluorescence as a read-out. However, we can assume under certain conditions that the calcium indicator itself essentially acts as a simple low-pass filter on the calcium signal [S10], which is a kind of distortion that we are able to correct for by applying deconvolution.

GCaMP6f is designed to have especially fast kinetics. However, we can find decay constants in the order of several hundreds milliseconds that vary depending on the system under observation [S1]. As an approximation we chose a time constant of 350 ms for a plausible low-pass filter that distorted the calcium signals in our system, which lies in the range of reported decay constants for GCaMP6f [S1, S11].

We corrected the frequency domain representations of the temporal filters of all cells by dividing the spectra with the frequency response of a 1<sup>st</sup> order low-pass filter with this time constant. Since this was restricted to frequencies below the Nyquist frequency, we did not have to apply additional techniques to avoid the impact of poor signal-to-noise ratios at higher frequencies.

For quantitative description and further simulations, we sought to describe the response characteristic of each cell under each condition with a simplified model that catches the main properties. For that, we fitted simple 1<sup>st</sup> order filters to the corrected frequency responses of all cells. We did this separately for each condition, i.e. for control and CDM condition and for the raw filters (corrected by the stimulus power spectrum only) and the deconvolved filters (corrected by the GCaMP filter) respectively.

In particular, we approximated Mi1, Tm3, Tm1, Tm2 and Tm4 as band-pass filters and fitted a band-pass model consisting of a 1<sup>st</sup> order high-pass and a 1<sup>st</sup> order low-pass filter to the frequency responses (Figures S5, S6). The band-pass model was parametrized by a multiplicative amplitude and the two time constants of the filters. Parameters were optimized using a standard implementation of the Levenberg-Marquardt algorithm (SciPy). Similarly, Mi4, Mi9 and Tm9 frequency responses were fit using a 1<sup>st</sup> order low-pass filter model.

## Computational modeling

Neural simulations (Figure 5 and 6) were based on a motion detector that combines preferred-direction enhancement and null-direction suppression, resembling a hybrid of a Hassenstein-Reichardt half-detector and a Barlow-Levick detector, as suggested in [S12].

Stimuli were simulated in a 2-dimensional space covering 90° in both azimuth and elevation with 1° resolution. Each hypothetical motion (half-)detector had three neighboring input lines (termed A, B and C) which were offset by 5° from each other along the horizontal axis (for simplicity). Each input line consisted of a spatial and a temporal filter that was applied to the stimulus before further processing. The spatial filter was modeled as a 2D convolution with a Mexican hat filter kernel using the above definition (see “Spatial receptive field model”) and the fitted parameters from table S1 and S2. The temporal filter consisted of either a 1<sup>st</sup> order band-pass or as a 1<sup>st</sup> order low-pass filter with the time constants from the table correspondingly. Subsequent rectification simulated the polarity selectivity of the input lines to the downstream motion detector. To implement the nonlinear interaction between the three input lines in the most simplified, we modelled the nonlinear action as  $A \cdot B / (C + 0.1)$  involving only one free parameter to avoid division by zero. 270 of these elementary motion detectors were arranged on a 2-dimensional grid, separated by 5° from each other.

To evaluate the performance and tuning of the simulated detectors across stimulus frequencies, we measured the mean response of the simulated (half-)detectors to moving gratings at different speeds. Vertically oriented square wave gratings of 24° wavelength were swept over the detector array with 50 different velocities corresponding to 50 different contrast frequencies

logarithmically spaced between 0.01 Hz and 20 Hz. The gratings moved for 5s to the right followed by a pause of 0.5s and 5s of motion in the opposite direction. The time step for all simulations was 10 ms. The direction of the stimulus that elicited the strongest response across all frequencies was termed the preferred direction (PD) of the respective motion detector. Consequently, the other direction was the null direction (ND).

The direction selectivity of the resulting tuning curve was evaluated by defining a direction selectivity index (DSI)

$$DSI = \frac{\sum PD - \sum ND}{\sum PD + \sum ND}$$

where the sum goes over all frequencies simulated. This definition produces DSI values between 0 and 1, where 1 means perfect, and 0 means no direction selectivity. Secondly, the optimal frequency  $f_{opt}$  was defined as the stimulus frequency that elicited the strongest response in PD direction.

The above measure only quantifies the response difference between the two opposing directions of motion along the main axis of the detector. However, it cannot distinguish between detectors that differ in their response properties to intermediate directions of motion. Hence, we additionally assessed the directional tuning specificity of each detector by measuring its response to differently oriented moving gratings. We stimulated the model with square wave gratings of 24° wavelength, rotated by different angles from 0° to 360° in steps of 30°, and measured the mean response of the detector array at the optimal frequency  $f_{opt}$ , as determined above. From the corresponding simulated responses, the direction selectivity was quantified as the length of the normalized response vector:

$$L_{dir} = \left| \frac{\sum_{\varphi} \vec{v}(\varphi)}{\sum_{\varphi} |\vec{v}(\varphi)|} \right|$$

where  $\vec{v}(\varphi)$  is a vector proportionally scaled with the mean detector response and pointing in the corresponding stimulus direction of motion given by the rotation angle  $\varphi$  of the stimulus. This quantity  $L_{dir}$  has been suggested as a robust measure of direction selectivity that includes both relative response magnitude and tuning width of a direction selective neuron [S13].

For the bar plots in Figure 5B&E (right column) the simulations were repeated also for all possible implementations of a two-arm detector whose nonlinear interaction was either modelled as  $A \cdot B$  for a classical Hassenstein-Reichardt-(half-)detector or as  $B/(C + 0.1)$  for a Barlow-Levick-detector.

All simulations were performed using Python 2.7.

## Statistics

Throughout this article, values are reported as mean  $\pm$  standard error (SEM). In order to quantify the significance of the effect of CDM application on the temporal response characteristics of the medulla cells, we defined three different measures for the impulse responses: a) the time to the first peak  $t_{peak}^{(1)}$  is the time between the onset of the impulse response (defined as the time when it has reached 15% of its maximum value) and the time when it has reached its maximum value; b) the time to the second peak  $t_{peak}^{(2)}$  is similarly defined as the time between the onset of the impulse response and the peak of the subsequent undershoot or overshoot, which is defined only for the band-pass filters; c) lastly, we defined a peak width  $w_{peak}$  as the width of the first

peak at half maximum. We quantified these values for each fly and tested the change between control and CDM condition for significance using a paired t-test.

### Supplemental References

- S1. Chen, T.-W., Wardill, T. J., Sun, Y., Pulver, S. R., Renninger, S. L., Baohan, A., Schreiter, E. R., Kerr, R. A., Orger, M. B., Jayaraman, V., et al. (2013). Ultrasensitive fluorescent proteins for imaging neuronal activity. *Nature* **499**, 295–300.
- S2. Strother, J. A., Wu, S.-T., Wong, A. M., Nern, A., Rogers, E. M., Le, J. Q., Rubin, G. M., and Reiser, M. B. The emergence of directional selectivity in the visual motion pathway of *Drosophila*. *Neuron* *in press*.
- S3. Maisak, M. S., Haag, J., Ammer, G., Serbe, E., Meier, M., Leonhardt, A., Schilling, T., Bahl, A., Rubin, G. M., Nern, A., et al. (2013). A directional tuning map of *Drosophila* elementary motion detectors. *Nature* **500**, 212–216.
- S4. Ammer, G., Leonhardt, A., Bahl, A., Dickson, B. J., and Borst, A. (2015). Functional specialization of neural input elements to the *Drosophila* ON motion detector. *Curr Biol* **25**, 2247–2253.
- S5. Pologruto, T. A., Sabatini, B. L., and Svoboda, K. (2003). ScanImage: flexible software for operating laser scanning microscopes. *BioMed Eng OnLine* **2**, 13.
- S6. Reiser, M. B., and Dickinson, M. H. (2008). A modular display system for insect behavioral neuroscience. *J Neurosci Methods* **167**, 127–139.
- S7. French, A. S. (1976). Practical nonlinear system analysis by Wiener kernel estimation in the frequency domain. *Biol Cybern* **24**, 111–119.
- S8. Dayan, P., and Abbott, L. F. (2005). *Theoretical Neuroscience*. MIT Press.
- S9. Clark, D. A., Bursztyn, L., Horowitz, M. A., Schnitzer, M. J., and Clandinin, T. R. (2011). Defining the computational structure of the motion detector in *Drosophila*. *Neuron* **70**, 1165–1177.
- S10. Borst, A., and Abarbanel, H. D. I. (2007). Relating a calcium indicator signal to the unperturbed calcium concentration time-course. *Theor Biol Med Model* **4**, 7.
- S11. Schnell, B., Weir, P. T., Roth, E., Fairhall, A. L., and Dickinson, M. H. (2014). Cellular mechanisms for integral feedback in visually guided behavior. *Proc Natl Acad Sci USA* **111**, 5700–5705.
- S12. Haag, J., Arenz, A., Serbe, E., Gabbiani, F., and Borst, A. (2016). Complementary mechanisms create direction selectivity in the fly. *eLife* **5**:e17421.
- S13. Mazurek, M., Kager, M., and Van Hooser, S. D. (2014). Robust quantification of orientation selectivity and direction selectivity. *Front Neural Circuits* **8**, 92.



## Manuscript IV

### Asymmetry of *Drosophila* ON and OFF Motion Detectors Enhances Real-World Velocity Estimation

Aljoscha Leonhardt\*, **Georg Ammer\***, Matthias Meier, Etienne Serbe, Armin Bahl, and Alexander Borst

\* equal contribution

#### Author Contributions

A.L., **G.A.** and A. Borst designed the study. A.L. performed behavioral experiments, associated data analysis and all modeling work. **G.A.**, M.M. and E.S. performed electrophysiological experiments. **G.A.** performed calcium imaging. A.L. and **G.A.** analyzed physiological data. A. Bahl designed the behavioral apparatuses and performed behavioral experiments. A.L. wrote the manuscript with help from all of the authors.

**Nature Neuroscience** 19, 706-715. doi: 10.1038/nn.4262.



# Asymmetry of *Drosophila* ON and OFF motion detectors enhances real-world velocity estimation

Aljoscha Leonhardt<sup>1,3</sup>, Georg Ammer<sup>1,3</sup>, Matthias Meier<sup>1</sup>, Etienne Serbe<sup>1</sup>, Armin Bahl<sup>1,2</sup> & Alexander Borst<sup>1</sup>

The reliable estimation of motion across varied surroundings represents a survival-critical task for sighted animals. How neural circuits have adapted to the particular demands of natural environments, however, is not well understood. We explored this question in the visual system of *Drosophila melanogaster*. Here, as in many mammalian retinas, motion is computed in parallel streams for brightness increments (ON) and decrements (OFF). When genetically isolated, ON and OFF pathways proved equally capable of accurately matching walking responses to realistic motion. To our surprise, detailed characterization of their functional tuning properties through *in vivo* calcium imaging and electrophysiology revealed stark differences in temporal tuning between ON and OFF channels. We trained an *in silico* motion estimation model on natural scenes and discovered that our optimized detector exhibited differences similar to those of the biological system. Thus, functional ON-OFF asymmetries in fly visual circuitry may reflect ON-OFF asymmetries in natural environments.

Motion cues resulting from movement through space constitute an important source of information about the external world, supporting course stabilization, navigation or tracking of landmarks<sup>1</sup>. Biological motion detectors have evolved in environments of astounding complexity. Visual landscapes from which animals derive such cues are cluttered and produce rapidly fluctuating signals. Exploiting a priori knowledge about scene features is therefore critical for organisms to reliably extract the spatiotemporal correlations that indicate motion. Basic statistical properties such as the shape of power spectra are known to be conserved between natural scenes<sup>2–4</sup>. Higher order features such as textures, edges or contrast distributions yield additional cues and exhibit consistent statistics across visual environments. Examples of neural adaptation to natural scene statistics abound, operating at various levels of visual processing hierarchies<sup>5–7</sup>.

Segregated processing of positive (ON) and negative (OFF) changes in sensory magnitude is a common trait among modalities ranging from olfaction to motion detection in the insect and mammalian visual systems<sup>1,8,9</sup>. Splitting time-varying signals into two streams, covering opposite directions of change, is thought to confer various advantages to sensory circuits. For instance, ON-OFF systems maximize information transfer when resources are constrained<sup>8</sup>. In the case of motion detection, the ON-OFF split may drastically simplify the biophysical implementation of operations such as sign-correct multiplication<sup>10,11</sup>.

Luminance distributions in real-world environments are heavily asymmetric with regard to positive and negative contrast<sup>2,12</sup>. Visual systems take this into account: in the mammalian retina, for example, more ganglion cells are dedicated to processing negative than positive spatial contrast, consistent with naturally encountered skewness<sup>13</sup>. Theoretical studies on motion detection have proposed that, in ON-OFF asymmetric environments, higher order correlations carry valuable

information about scene motion<sup>14</sup>. Indeed, flies and humans alike appear to be capable of extracting higher order cues<sup>12,15</sup>, suggesting that both apply this strategy for motion estimation. However, little is known about the neural mechanism by which either visual system gains access to higher order correlations.

As a result of the availability of powerful genetic tools and extensive connectomic<sup>16,17</sup> as well as functional<sup>18–24</sup> characterizations, knowledge about the neural substrate of *Drosophila* motion detectors has grown exponentially in recent years<sup>9</sup>. Briefly, signals impinging on the photoreceptors are split into two polarity-specific channels, with one processing brightness increases (from L1 to T4 via at least Mi1 and Tm3) and the other processing brightness decreases (from L2, L3 and L4 to T5 via Tm1, Tm2, Tm4 and Tm9). Local ON and OFF motion signals are then extracted on the dendrites of T4 and T5, respectively, in a manner that is well explained by the Hassenstein-Reichardt correlation model<sup>9,11,21</sup>. Large tangential cells in the lobula plate pool these signals and influence behavioral output<sup>1,9,25,26</sup>.

Given the ON-OFF asymmetries encountered in natural environments, we set out to determine how the specific features of natural scenes have shaped ON and OFF motion detectors in the fly visual system. In contradistinction to previous studies, we were able to directly assess the behavioral performance of neural pathways by isolating them genetically. We found that asymmetries of natural environments had direct correspondence in tuning asymmetries of the fly motion detection system.

## RESULTS

### ON and OFF motion detectors reliably estimate velocity

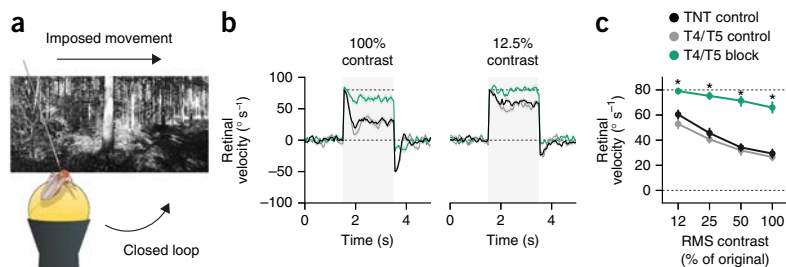
Flies react to visual wide-field motion by turning with the environment<sup>1,19,27</sup>. During navigation, this optomotor response stabilizes the animal's course in the face of external perturbations or internal noise.

<sup>1</sup>Max Planck Institute of Neurobiology, Martinsried, Germany. <sup>2</sup>Present address: Department of Molecular and Cell Biology, Harvard University, Cambridge, Massachusetts, USA. <sup>3</sup>These authors contributed equally to this work. Correspondence should be addressed to A.L. (leonhardt@neuro.mpg.de).

Received 19 November 2015; accepted 29 January 2016; published online 29 February 2016; corrected online 7 March 2016 (details online); doi:10.1038/nn.4262

**Figure 1** Flies stabilize their path in naturalistic environments using a combination of ON and OFF motion detectors. (a) Illustration of behavioral setup. Tethered flies walk in a virtual closed-loop environment. During certain time periods, their trajectories are perturbed externally. (b) Path stabilization under different contrast conditions. Retinal velocity describes environment rotation relative to the fly's eye. During epochs shaded in gray, a constant rotation bias of  $80^\circ \text{ s}^{-1}$  was added. Upper dashed line indicates imposed velocity. Control flies (TNT control,  $N = 19$ ;

T4/T5 control in gray,  $N = 12$ ) reduced the imposed retinal velocity effectively whereas T4/T5 block flies (in green,  $N = 13$ ) did not. Left, unmodified image contrast. Right, artificial reduction of root-mean-square (RMS) contrast to 12.5% of initial value. Exact genotypes are listed in **Supplementary Table 1**. (c) Quantification of stabilization performance across contrasts. Retinal velocity was averaged between 2 and 3 s. Dashed lines correspond to zero and full correction of the perturbation. Shaded areas around traces and vertical bars signify bootstrapped 68% confidence intervals around the mean. Asterisks indicate significant differences of block flies from both genotype controls after Bonferroni-corrected two-tailed  $t$  tests (\* $P < 0.05$ ); exact test statistics are reported in **Supplementary Table 2**.



Any deviation from a straight path results in retinal flow that is counteracted by matching direction and, ideally, velocity of perceived drift through locomotion. Responses of behaving fruit flies and wide-field motion-sensitive neurons to simplified motion stimuli such as sinusoidal gratings have been studied extensively<sup>27,28</sup>. Tethered flying flies placed in such artificial environments do indeed correct for externally applied biases<sup>29</sup>. However, flies generally solve this problem in vastly more complex environments. So far, nothing is known about the quantitative extent of their ability to perform path stabilization in naturalistic contexts.

We addressed this question by allowing tethered flies to stabilize their walking trajectories in virtual environments. To cover many possible surroundings, we generated a library of panoramic images spanning the entire visual field of the fly. Randomly selected images were projected onto a virtual cylinder whose orientation was controlled in closed loop through the angular trajectory of flies walking on an air-suspended ball (Fig. 1a). In addition, we superimposed fixed-velocity rotations and recorded the relative motion between the fly and its environment. Our approach therefore simulated translation-free walking through a distant visual scene in the presence of external course perturbations. As expected, control flies actively reduced retinal slip speed by rotating in the direction of and with similar velocity as their visual environment (Fig. 1b). A combination of neural, motor and setup-intrinsic delays resulted in characteristic over- and undershoots on the order of hundreds of milliseconds, trailing both onset and offset of the motion bias. Notably, control flies rarely achieved a retinal velocity of zero, which would indicate full compensation of the involuntary rotation.

Although combined synaptic silencing of cell types T4 and T5 abolishes behavioral and electrophysiological sensitivity to grating motion<sup>27,30</sup>, it is unclear whether naturalistic stimuli can provide additional cues exploited by secondary circuits. When we used Gal4-controlled<sup>31</sup> expression of the light chain of tetanus toxin<sup>32</sup> (TNT) to genetically disrupt synaptic output of all T4 and T5 cells, which are known to implement local motion detection<sup>21,27,30</sup>, we discovered a marked impairment of stabilization performance. This was the case across the full range of artificially reduced image contrasts tested (Fig. 1b,c). The effect did not stem from gross motor defects; the flies' walking speed was at control level (Supplementary Fig. 1). Contrast reductions also negatively affected the stabilization ability of control flies. This replicated a previously described property of motion-sensitive lobula plate tangential cells in a behavioral setting: response gain of these cells is diminished for natural images artificially reduced in contrast<sup>33</sup>. In summary, we found that flies actively

stabilized their path in complex visual scenes and that T4 and T5 cells were necessary neural elements for this feedback behavior.

Previous work confirmed that T4 and T5 cells are predominantly sensitive to motion defined by luminance increases and decreases, respectively<sup>21</sup>. Full-field motion of naturalistic scenes, especially at large viewing distances and in cluttered environments, creates a rich gamut of both ON and OFF motion. Arrays of ON or OFF detectors may therefore be equally capable of reporting the direction and velocity of realistic global motion. However, nothing is known about the individual contributions of ON and OFF detectors to velocity estimation in such contexts. Moreover, the transformation from stimulus velocity to response strength for all read-outs of the fly motion system is highly sensitive to geometrical features of the stimulus: the fly motion detector is generally not a pure speedometer<sup>1,9</sup>. Even though most gain regimes would eventually lead to stabilization, the optomotor response should ideally match true retinal velocity to correct the fly's course quickly and efficiently<sup>29</sup>. Indeed, tangential cells exhibit a linearized and reliable velocity-response curve when stimulated with natural images as opposed to periodic stimuli such as gratings<sup>33</sup>. We sought to test whether this is reflected by optomotor behavior.

To this end, we assessed *Drosophila*'s behavioral ability to track scene velocity in open loop (Fig. 2a). Velocity-response curves were stochastically probed by presenting randomly chosen images moving at constant velocities drawn from a Gaussian distribution on each individual trial. Estimation performance was then defined as the linear correlation between environment rotation and average turning response of the fly. A correlation coefficient of  $r = 1.0$  indicates a perfectly reliable linear mapping of global motion onto behavioral response across all scenes, as would be required of a functional speedometer. Following visual stimulation, flies responded with robust turning responses that increased until stimulus offset and decayed right after (Supplementary Fig. 2). To our surprise, control flies performed the velocity estimation task exceedingly well (Fig. 2b). For our image set, individual flies reached correlation coefficients above 0.8 across hundreds of trials. Not all behavioral complexity was captured by the linear model: trials with turning responses close to  $0^\circ \text{ s}^{-1}$ , for instance, were rare (Fig. 2b). However, several effects suggested that our simplified measure was indeed valid. First, as anticipated, flies with disrupted T4 and T5 activity exhibited correlation coefficients and response gain close to zero (Fig. 2c–e). Second, the correlation coefficients of control flies were heavily decreased by the reduction of image contrast (Fig. 2d). This reflected increasing task difficulty at the lower end of the contrast spectrum. Third,

**Figure 2** ON and OFF channels are equally capable of estimating the velocity of natural scenes. (a) Sketch of experimental approach. Flies were subjected to a set of natural images rotating at random velocities drawn from a Gaussian distribution (s.d. =  $50^\circ \text{ s}^{-1}$ ) in open loop. (b) Velocity estimation performance of control flies. Each dot represents the average rotational response for one trial at full contrast. Trials were pooled across flies of all control groups ( $n = 1,936$  trials from  $N = 13$  TNT control flies,  $n = 1,879/N = 12$  for T4/T5 control,  $n = 2,070/N = 13$  for T4 control,  $n = 1,331/N = 12$  for T5 control); the linear fit is for illustrative purposes only. The shaded curve to the right shows a kernel density estimate of rotational responses. (c) Velocity estimation performance of block flies, displayed as in b ( $n = 1,755/N = 11$  for T4/T5 block,  $n = 1,976/N = 12$  for T4 block,  $n = 1,778/N = 12$  for T5 block). (d) Quantification of velocity estimation performance across artificially modified image contrasts. Performance was measured as the Pearson correlation between environment rotation and integrated response. Although T4/T5 block flies were strongly impaired at all contrasts, silencing T4 or T5 individually had no measurable effect on estimation performance. (e) Quantification of response gain across contrast range. Gain was measured as the slope of a linear regression model mapping environmental rotation onto rotational response. Vertical bars signify bootstrapped 68% confidence intervals around the mean. Asterisks indicate significant differences for block flies from both Gal4 and UAS controls after Bonferroni-corrected two-tailed *t* tests (\* $P < 0.05$ ); exact test statistics are reported in **Supplementary Table 3**.

we once again found a contrast-dependent decrease of response gain as determined by the slope of a linear fit (Fig. 2e). It should be noted that these gain values depend on the choice of averaging window. For this reason, and because control systems tend to overcompensate in the absence of feedback, large gain values in open loop do not necessarily entail full compensation in closed loop (Fig. 1c).

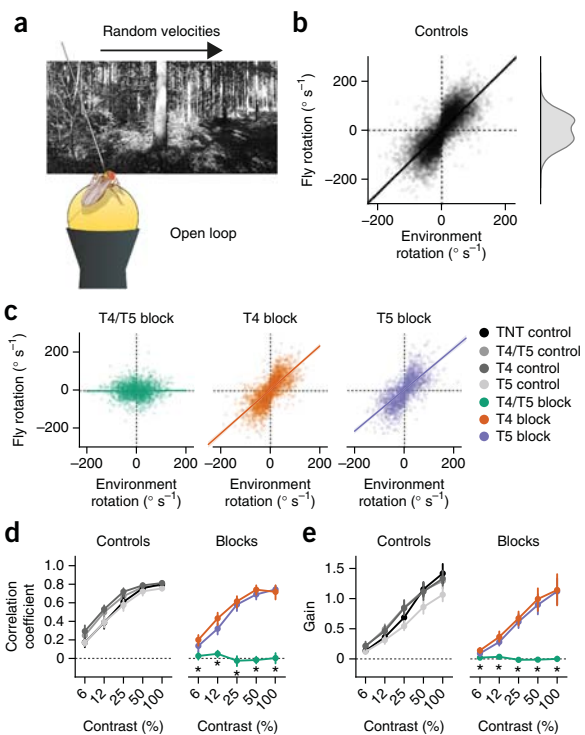
To determine potentially differential contributions of ON and OFF detectors to velocity estimation in naturalistic contexts, we then silenced only T4 or T5 using TNT. In a previous study using the same lines<sup>21</sup>, we found that blocking T4 or T5 led to a strongly reduced ability to detect bright or dark edges, respectively, at both the electrophysiological and behavioral level. In stark contrast to these effects, we found no impairment of velocity estimation for our naturalistic image set. Correlation coefficients for both T4 block and T5 block flies were not substantially different from control groups, even at low contrast levels (Fig. 2c,d and **Supplementary Fig. 2**). Finally, we alternatively quantified estimation performance as the root-mean-square error of a Bayesian estimator trained on the behavioral data, the results of which supported similar conclusions (**Supplementary Fig. 3**).

Taken together, we found that combined silencing of T4 and T5 completely abolished flies' ability to track the velocity of global motion in naturalistic scenes. Notably, ON and OFF channels appeared to be redundant for this task. Either was sufficient to recapitulate naturalistic behavior.

#### Tuning properties of ON and OFF channels are asymmetric

Given that ON and OFF channels seemed equally capable of performing reliable velocity estimation across various visual scenes, it is plausible to assume that they share temporal tuning properties. Previous studies reported comparable temporal frequency optima for sinusoidal gratings<sup>21</sup>. Calcium imaging, however, lacks the temporal resolution required for a precise characterization of pathway kinetics. Moreover, considering the polarity specialization of T4 and T5, we sought to characterize the channels using pure ON or OFF stimuli as opposed to sinusoidal gratings defined equally by brightness increments and decrements.

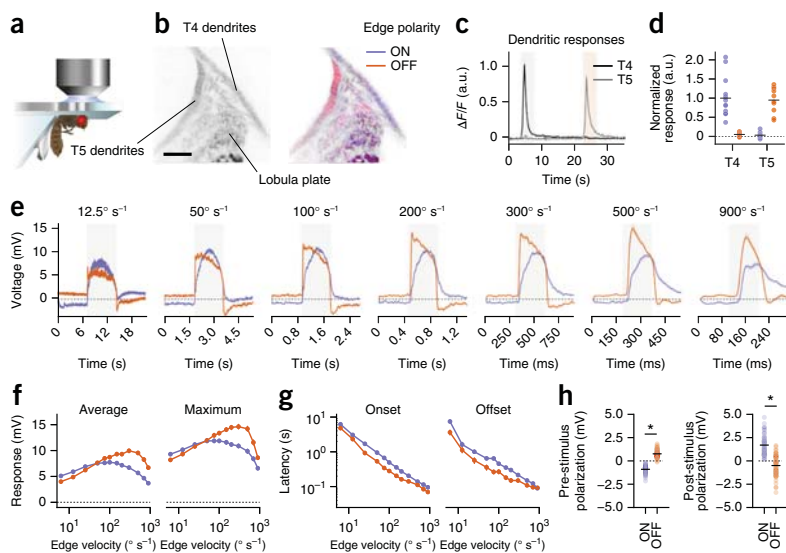
First, we confirmed that T4 and T5 respond exclusively to bright and dark edges, respectively. The T4 driver line used for imaging



in a previous study<sup>21</sup> showed marginal coexpression in T5 cells; the converse applied to the T5 driver line. Our earlier work had revealed minor sensitivity for OFF edges in T4 cells as well as small responses for ON edges in T5 cells, measured in the confines of the lobula plate, where both cell types intermingle. We speculated that this was a result of either Gal4 coexpression or actual physiological crosstalk between ON and OFF circuitry. Moreover, a physiological characterization of T4 input elements suggests that T4 should only be mildly selective for ON motion<sup>24</sup>. To conclusively decide between the alternatives, we performed two-photon calcium imaging using a combined T4 and T5 line in conjunction with the calcium reporter GCaMP6f<sup>34</sup> (Fig. 3a). Separation of T4 and T5 signals was then achieved by restricting the region of interest to the cells' dendrites in the medulla or lobula, respectively (Fig. 3b). Dendrites showed strong calcium increases following visual edge stimulation that were perfectly polarity specific (Fig. 3c,d). This allowed us to characterize the temporal tuning properties of T4 and T5 by means of highly time-resolved electrophysiological recordings from downstream cells.

We determined velocity tuning curves for ON and OFF edges moving at speeds spanning two orders of magnitude by recording from the large-field motion-sensitive cells of the horizontal and vertical systems<sup>9,28</sup> in the lobula plate. These cells are the primary recipients of feedforward ON and OFF signals, receiving direct input from T4 and T5 for stimuli moving in preferred direction and indirect inhibitory input via lobula plate interneurons for null direction motion<sup>30,35</sup>. Cells depolarized when stimulated with ON or OFF edge motion along their preferred direction. Unexpectedly, tuning curves as well as general kinetics differed substantially between ON and OFF (Fig. 3e). Both channels showed increasing response strength up to a certain velocity, after which responses fell off (Fig. 3f). For ON edges, however, this peak was located at approximately  $100^\circ \text{ s}^{-1}$ , whereas OFF responses reached their maximum at edge velocities of  $\sim 300^\circ \text{ s}^{-1}$ . This held true

**Figure 3** Physiological characterization of ON and OFF channels reveals tuning asymmetries. (a) Schematic of preparation used for two-photon calcium imaging and patch-clamp recordings from lobula plate tangential cells (LPTCs). (b) Left, two-photon image of GCaMP6f expression in T4 and T5 cells. Scale bar represents 10  $\mu$ m. Right, representative T4 and T5 activity during ON (blue) or OFF (red) edge stimulation overlaid onto left-hand image. Activity was confined to T4 or T5 dendrites, depending on edge polarity. (c) Relative fluorescence ( $\Delta F/F$ ) across time for regions of interest centered on either T4 (black,  $N = 14$ ) or T5 (gray,  $N = 10$ ) dendrites. (d) Quantification of responses as averages over edge presentation period indicated by shaded areas in c. (e) Average responses of LPTCs for ON and OFF edges moving at a range of velocities in preferred direction. Time axes are scaled differently. Shaded area indicates edge presentation and covers visual field traversal (90°) at the specified velocity. Vertical and horizontal system cells from wild-type flies were pooled ( $n = 70$  from  $N = 43$  flies). (f) Velocity tuning curves for ON and OFF edges based on either average or maximum response during full stimulation period. (g) Response kinetics for ON and OFF edges moving at a range of velocities. (h) Static properties averaged across velocities. Dots represent individual observations and black bars indicate group averages. Vertical bars and shaded areas signify bootstrapped 68% confidence intervals around the mean. Asterisks indicate significant differences between ON and OFF after two-tailed  $t$  tests (\* $P < 0.05$ ). Exact test statistics are reported in **Supplementary Table 4**.



regardless of whether we quantified average or maximum voltage. Moreover, both onset and offset latencies were larger for ON edges than for OFF edges across the full range of velocities tested (Fig. 3g). We also observed a constant polarization that closely reflected surround luminance (Fig. 3h); for instance, the field illumination preceding the onset of an OFF edge led to steady-state depolarization of the cell, which gave way to hyperpolarization after the dark edge had traveled through the fly's visual field (Fig. 3e). In a second set of experiments, we examined whether such differential pre-stimulus polarization could explain the observed ON-OFF asymmetries. Flies were presented with edges starting from an intermediate background luminance that was equal for both polarities (Supplementary Fig. 4a). Notably, edge velocity tuning curves were not affected by this alteration, whereas differences in onset kinetics vanished (Supplementary Fig. 4b,c). This suggests that luminance adaptation has a strong effect on the dynamics of tangential cell responses, but does not influence temporal tuning.

In summary, we observed strongly differential velocity tuning for ON and OFF pathways, with the former responding maximally to slower velocities than the latter. To determine whether the observed tuning differences are behaviorally relevant, we performed balanced motion experiments on walking flies. Multiple resetting ON and OFF edges distributed across the visual field moved simultaneously in opposite directions over several seconds<sup>19,21,23</sup> (Fig. 4a). This was done for a large velocity range and offered a behavioral read-out of the weighting between ON and OFF pathways. Here, a turning tendency of zero implies equal ON and OFF responses. Consistent with electrophysiological results, we found that the balance between ON and OFF responses was clearly modulated by edge velocity (Fig. 4b). At low speeds, ON responses dominated the overall turning behavior and control flies continuously rotated in the direction of bright edges (Fig. 4c). At higher velocities, this turning tendency was reversed, indicating dominant OFF responses. ON and OFF were only completely in balance at an edge velocity of around 80° s<sup>-1</sup>. To test whether these imbalances also occur at the transient time scales dominating walking behavior,

we then shortened the stimulus duration to 500, 250 or 100 ms. These opposing edge pulses produced robust responses whose amplitude diminished with decreasing stimulus length. Notably, all tuning curves had shapes that were comparable to the steady-state condition (Supplementary Fig. 5).

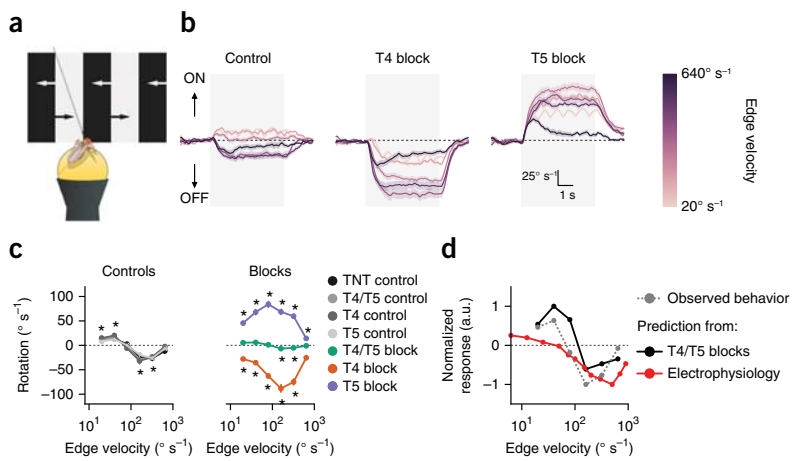
We also performed blocking experiments using this assay (Fig. 4c). Removing T4 and T5 from the circuit resulted in abolished turning tendencies across all velocities. For individual blocks, we recovered effects whose general direction had been described before<sup>21</sup>: T4 block flies always rotated in the direction of OFF edges and T5 block flies consistently followed motion of ON edges (Fig. 4b). Notably, these block effects were most pronounced at different velocities. For T4 block flies, the curve peaked at 160° s<sup>-1</sup>. For T5 block flies, the maximum was found at 80° s<sup>-1</sup>. This roughly confirmed the edge tuning curves from tangential cell recordings (Fig. 3f) under the assumption that each individual block was reasonably complete, leaving only one pathway intact. From this, we generated linear predictions for wild-type behavior. *Post hoc* tuning curves were calculated by either subtracting edge tuning curves measured as average voltage or summing the behavioral curves of T4 block and T5 block flies (Fig. 4d). Both models successfully predicted response signs and approximate zero crossing of control flies, corroborating the notion that tangential cells combine T4 and T5 signals in an approximately linear regime and then control turning behavior directly.

Despite their comparable performance during naturalistic velocity estimation, the ON and OFF pathways represented by T4 and T5 are tuned to different velocity regimes at both the electrophysiological and behavioral level. We next explored whether this tuning asymmetry is critical for their estimation fidelity.

#### Optimized detectors are ON-OFF asymmetric

The *Drosophila* motion detection system is well described by a two-quadrant ON-OFF detector: the combination of two motion detectors, one processing only ON signals akin to the physiological T4 channel and one processing only OFF signals akin to the physiological

**Figure 4** Asymmetry between ON and OFF channels persists at the behavioral level. (a) Schematic drawing of balanced motion stimulus with ON and OFF edges simultaneously moving into opposite directions at various velocities. (b) Rotational responses for TNT control flies as well as T4 and T5 block flies. Trace color indicates velocity of edges. Positive responses are syndirectional with ON edge motion; negative responses follow OFF edge motion. Gray-shaded area denotes epoch during which edges were moving. T4 and T5 block flies are consistently biased away from the disrupted polarity. For control flies, the dominant polarity changes with velocity. (c) Quantification of turning responses averaged over stimulation period (3 to 7 s;  $N = 12$  for TNT control,  $N = 12$  for T4/T5 control,  $N = 12$  for T4 control,  $N = 13$  for T5 control,  $N = 12$  for T4/T5 block,  $N = 15$  for T4 block,  $N = 14$  for T5 block). For controls, asterisks indicate responses that are significantly different from zero ( $*P < 0.05$ ). For block genotypes, asterisks indicate significant differences from both corresponding Gal4 and UAS controls (Bonferroni-corrected  $t$  tests,  $*P < 0.05$ ). (d) Comparison of observed control tuning curves (gray) with tuning curves linearly predicted from either the sum of behavioral T4 block and T5 block tuning curves (black) or the difference between electrophysiologically determined ON and OFF tuning curves (red; Fig. 3). Vertical bars and shaded areas surrounding traces signify bootstrapped 68% confidence intervals around the mean. Exact test statistics are reported in Supplementary Table 5.



T5 channel<sup>10</sup>. Each subunit then computes motion according to the well-established Hassenstein-Reichardt correlation model based on the multiplication of differentially filtered, spatially separated signals<sup>11</sup>. Counter-intuitively, such models are capable of explaining complex phenomena such as the reverse-phi effect observed for motion accompanied by contrast reversals<sup>10,19,36</sup>. Critical for this is the inclusion of a weighted tonic signal (DC component) in addition to the high-pass signal modeling processing in lamina monopolar cells. Parameters for the model are generally chosen such that the ON and OFF subunits of the detector remain symmetric<sup>10,19</sup>. Our results concerning edge velocity tuning, however, speak in favor of asymmetric tuning. Moreover, work on natural scenes has repeatedly shown that realistic environments are strongly asymmetric with regard to ON and OFF<sup>2,12,13</sup>. What does an ON-OFF detector look like that is tuned to naturalistic environments?

Various estimation objectives may be prioritized, depending on the given task<sup>29,37</sup>. For this study, we operationalized detector fitness analogously to previous studies<sup>12</sup> and equivalently to our own behavioral experiments as the linear correlation between the velocity of a rigidly translating natural image and time-averaged detector output. Given that Hassenstein-Reichardt detectors directly explain many aspects of fly optomotor behavior<sup>1,9</sup>, and considering that flies achieve extremely high correlation values in the corresponding experimental setting (Fig. 2), this seemed to be a sensible target for the model. We optimized by exhaustively scanning the parameter space spanned by low-pass filter time constant and DC component of simplified ON and OFF detectors (Fig. 5a). This was done in a cross-validated manner. We chose a small set of parameters for optimization in which ON-OFF asymmetries had been observed previously. Our own results on edge tuning (Fig. 3e,f) indicated that there were large temporal tuning differences between ON and OFF pathways. Physiological characterization of medulla interneurons Mi1 and Tm3 for T4 as well as Tm1 and Tm2 for T5 has revealed distinct differences with regard to the strength of DC signals present at the input of motion detectors<sup>24</sup>. Thus, we looked for combinations of low-pass filter time constants and DC weightings that would maximize velocity estimation performance of isolated ON and OFF detectors for a large

set of natural scenes from the van Hateren image database<sup>6</sup>. Velocities were drawn from a Gaussian distribution whose width was based on turning speed distributions determined in our closed-loop experiments. Optimized parameters were modulated in physiologically plausible ranges; all other settings were chosen based on previous modeling work<sup>10</sup> and not tuned for any particular result.

The resulting fitness landscape as a function of low-pass time constant and DC component was smooth and strongly asymmetric with respect to ON and OFF (Fig. 5b). Indeed, when we extracted the parameter sets that maximized fitness for independent ON and OFF detectors, we found that optimal settings were ON-OFF asymmetric with respect to both parameters (Fig. 5c). Specifically, the best time constants for ON detectors were larger than those achieving maximum correlation for OFF detectors. The best DC weights had higher values for ON detectors than for OFF detectors and opposite signs (Fig. 5c).

To ascertain whether parameter asymmetry improved velocity estimation over that achieved by symmetric models, we compared equally weighted combinations of independently optimized ON and OFF detectors to optimized detectors that were constrained to be symmetric. The cross-validated performance improvement was small but significant ( $t(98) = 4.08$ ,  $P < 0.001$ ), suggesting that detector asymmetry is an advantageous strategy (Fig. 5d). The differences between ON and OFF parameters of optimal asymmetric models were substantial (Fig. 5e). We therefore looked for functional disparities between the average optimized models. Simulated temporal frequency tuning curves for sinusoidal gratings were highly similar, with slightly shifted response optima (Fig. 5f). The asymmetric and the symmetric model also produced comparable output for a dynamically moving grating (Fig. 5g). When we simulated edge velocity tuning curves as we had measured experimentally (Figs. 3 and 4), the symmetric model exhibited identical tuning for ON and OFF edges, as was expected from identical temporal parameters. Our asymmetric model, however, correctly replicated the shift between optima for ON and OFF edges with the detector being tuned to higher OFF than ON edge velocities (Fig. 5h). In addition, the asymmetric model predicted a difference in overall strength between ON and

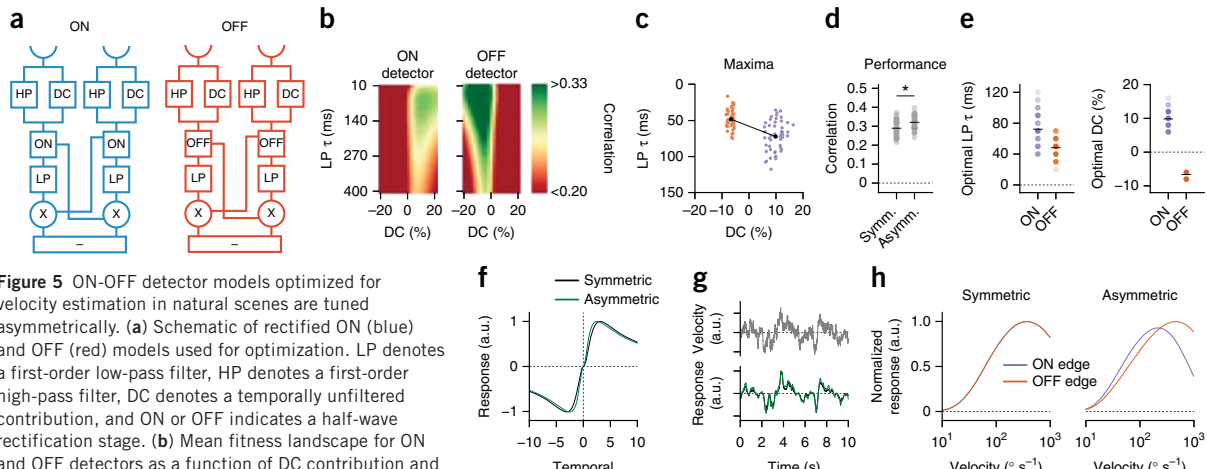


**Figure 5** ON-OFF detector models optimized for velocity estimation in natural scenes are tuned asymmetrically. **(a)** Schematic of rectified ON (blue) and OFF (red) models used for optimization. LP denotes a first-order low-pass filter, HP denotes a first-order high-pass filter, DC denotes a temporally unfiltered contribution, and ON or OFF indicates a half-wave rectification stage. **(b)** Mean fitness landscape for ON and OFF detectors as a function of DC contribution and low-pass filter time constant  $\tau$ . Analogously to behavior (Fig. 2d), estimation performance was measured as the Pearson correlation between input velocity and average detector output. **(c)** Distribution of optimized parameters. Each dot represents the best parameter set found for either ON (blue) or OFF (red) detectors on a given training image set ( $N = 50$  folds; points are jittered for clarity). Black dots mark the center of the ON and OFF parameter clouds. **(d)** Cross-validated performance of detectors. Optimal ON and OFF detectors are linearly combined (asymmetric detectors), tested on images not seen during training and compared with ON-OFF detectors optimized under the additional constraint of ON-OFF symmetry. The difference was significant after a two-tailed  $t$  test ( $N = 50/50$ ,  $t(98) = 4.08$ ,  $*P < 0.001$ ). **(e)** Comparison of parameters for asymmetric detectors from **c**. **(f)** Temporal tuning of optimized symmetric and asymmetric detector. **(g)** Responses of optimized symmetric and asymmetric detector to a sinusoidal grating drifting with Gaussian velocity profile. **(h)** Simulated ON and OFF edge velocity tuning curves (with peaks for the asymmetric model at  $230$  and  $480^\circ \text{s}^{-1}$ , respectively). Dots represent individual results and black bars indicate group averages.

OFF edge responses (Fig. 3f) even though subunits were summed at equal gain. The modeled edge optima occurred at higher velocities than those we had determined experimentally. As optimized parameters for the detectors depended on the s.d. of the distribution from which test velocities were drawn, their absolute scale was

somewhat arbitrary; conditional on behavioral state, turning speed distributions may differ substantially. The direction of the asymmetry, however, was consistent with experimental findings.

We then determined natural image features necessary for asymmetries to appear in tuned ON-OFF detectors. To this end, we repeated the optimization procedure for image sets in which we had manipulated specific statistical properties. First, for the unaltered set, the best asymmetric ON and OFF detectors showed large differences for both low-pass time constant, as well as absolute DC level (Fig. 6a). Second, we randomized the phase structure of every image, thereby removing all higher level features such as textures or edges, as well as making scenes largely ON-OFF symmetric<sup>13</sup>, while retaining the typical power spectrum of natural scenes. Here, the asymmetry of time constants disappeared (Fig. 6b). Third, we artificially reinstated the natural luminance distribution in phase-randomized images (Fig. 6c). This manipulation rescued the time constant asymmetry, suggesting that a skewed luminance distribution is the critical constraint forcing filter

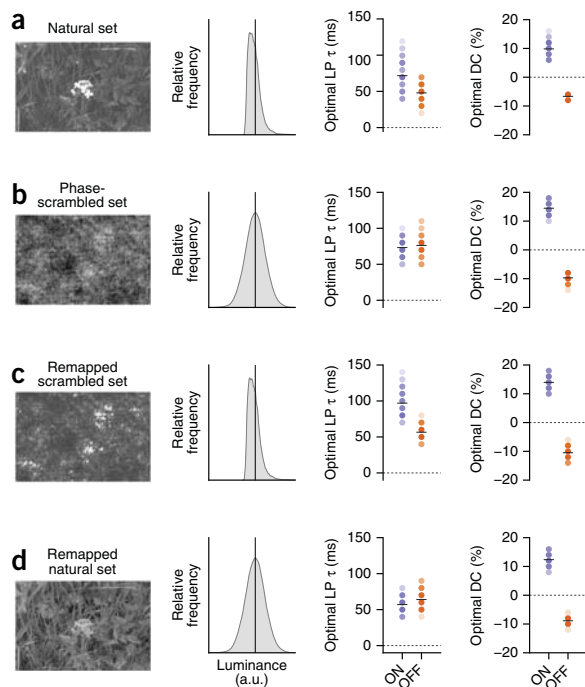
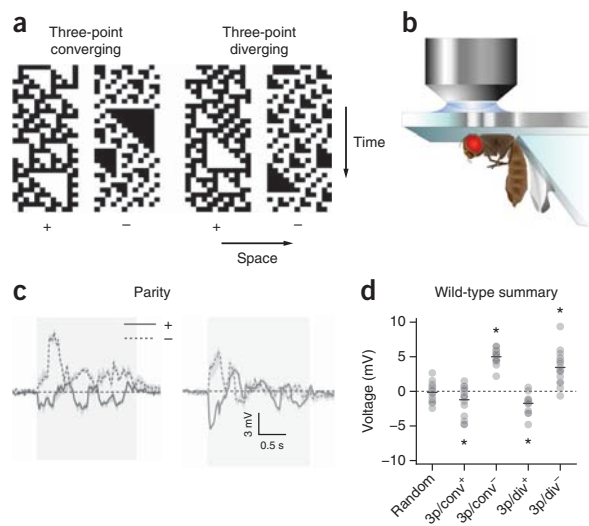


**Figure 6** Luminance asymmetry in natural scenes is critically responsible for asymmetry of ON-OFF parameters in optimized motion detector. **(a-d)** Left, example picture from image set used for optimization. Middle, kernel density estimate of pixel luminance distribution for example picture. The vertical line indicates average image luminance. Right-hand panels, optimized parameters for ON (blue) and OFF (red) detector trained on corresponding image set. **(a)** Unmodified image set used for earlier optimizations (Fig. 5). **(b)** Phase-scrambled image set in which the phase structure of each image was replaced by that of a random image, effectively rendering the luminance distribution symmetric. **(c)** Luminance-remapped image set in which the luminance distribution of natural images was remapped onto phase-scrambled images. **(d)** Luminance-remapped image set in which the luminance distribution of phase-scrambled images was remapped onto natural images. Dots represent individual observations and black bars indicate group averages ( $N = 50$  cross-validations for all image sets). No significance tests were performed in this figure.

**Figure 7** LPTCs are sensitive to higher order correlation stimuli. (a) Space-time plots of glider stimuli used to probe LPTC sensitivity to triple correlations. (b) Schematic drawing of *in vivo* electrophysiology preparation and setup. (c) Average responses to full-field three-point glider stimulation of pooled vertical and horizontal system cells ( $n = 16$  cells from  $N = 12$  flies). Gray shaded area shows duration of stimulus presentation. Shaded areas surrounding traces signify bootstrapped 68% confidence intervals around the mean. (d) Quantification of integrated responses (averaged over the first second of stimulus presentation); “3p/conv” or “3p/div” indicate three-point converging or diverging glider orientation, respectively, and superscript the stimulus parity. All recordings were done in wild-type Canton S flies. Depicted responses are the difference between glider presentation in preferred and null direction. Dots represent individual observations and black bars show group averages. Asterisks indicate significant differences from zero after two-tailed  $t$  tests ( $^*P < 0.05$ ); exact test statistics are reported in **Supplementary Table 6**.

properties to diverge between ON and OFF channels. Finally, replacing the skewed luminance distribution of natural images with a symmetric one again abolished the temporal tuning differences (Fig. 6d). Notably, the DC asymmetry did not depend on higher order statistics of the stimulus. This particular tuning difference may be advantageous for ON-OFF detectors regardless of image statistics.

Taken together, our optimization findings demonstrate that, in realistic environments, the ON and OFF channels of motion detectors that were optimal under our criterion were tuned asymmetrically. The specific parameters that best estimated motion in natural scenes reproduced tuning properties of the biological fly motion detector we determined experimentally. At no point did we use our previous experimental findings as a constraint during optimization; the procedure arrived at this specific asymmetry independently.



#### Higher-order motion sensitivity derives from ON-OFF asymmetry

Theoretical considerations indicate that spatiotemporal correlations of orders higher than two become informative indicators of visual motion in environments that are ON-OFF asymmetric<sup>14</sup>. Hassenstein-Reichardt detectors exclusively capture two-point correlations. Experimental work, however, confirmed that *Drosophila* responds to triple correlations<sup>12</sup>. This suggests that such correlations are either computed explicitly by secondary circuits or implicitly extracted by detectors that treat ON and OFF motion differentially. We assessed whether an asymmetric detector can account for *Drosophila*'s sensitivity to higher order motion.

First, we tested whether tangential cells respond to higher order motion cues given that these neurons receive their primary direction-selective input from T4 and T5 (ref. 30). We made use of previously characterized three-point glider stimuli<sup>12,15</sup> (Fig. 7a), which enforce the mean sign of correlations across three spatiotemporal points. They have four possible forms: converging or diverging, depending on their spatiotemporal orientation, and either positive or negative parity. Notably, they are guaranteed to contain on average zero

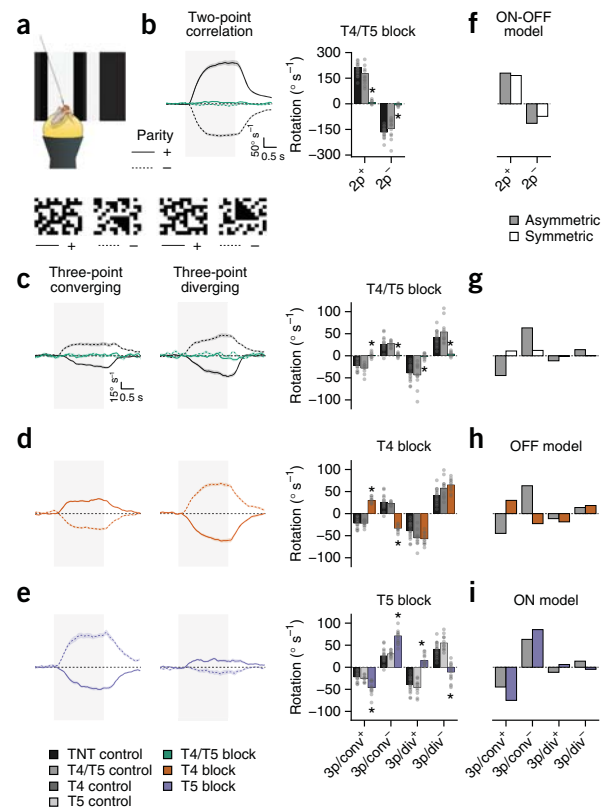


**Figure 8** Behavioral sensitivity to higher order correlations depends on T4 and T5 and is predicted by an asymmetric ON-OFF model. (a) Illustration of behavioral experiment. (b) Two-point glider responses. Left, average response traces for two-point glider stimuli. Right, rotational responses for two-point gliders representing phi and reverse-phi motion are abolished in T4/T5 block flies. (c) Control flies respond to three-point gliders in a specific pattern. Blocking T4 and T5 in conjunction eliminates these responses completely. (d,e) Silencing T4 or T5 modulates responses by reversing rotation for converging or diverging gliders, respectively. (f) Asymmetric and symmetric models account for two-point glider responses. (g) Only the asymmetric model correctly predicts three-point glider responses of control flies. (h,i) Simulating individual T4 and T5 blocks in the asymmetric ON-OFF model by setting the gain for either ON (red) or OFF (blue) channel to zero replicates the behavioral effects. Shaded areas surrounding traces signify bootstrapped 68% confidence intervals around the mean. Dots represent individual flies and bars show group averages. Asterisks indicate significant differences of block flies from both Gal4 and UAS controls after Bonferroni-corrected two-tailed  $t$  tests ( $N = 18$  for TNT control,  $N = 12$  for T4/T5 control,  $N = 12$  for T4 control,  $N = 12$  for T5 control,  $N = 14$  for T4/T5 block,  $N = 13$  for T4 block,  $N = 17$  for T5 block;  $^*P < 0.05$ ). Exact test statistics are reported in **Supplementary Table 7**.

directed two-point correlations, allowing the isolated characterization of responses to higher order motion. When we recorded from tangential cells of both the horizontal and vertical system (Fig. 7b), they responded to single instantiations of three-point gliders with complex dynamics (Fig. 7c). Their time-averaged voltage signals replicated the response pattern observed for behaving flies<sup>12</sup> (Fig. 7d). Given that fly locomotion is thought to reflect integrated tangential cell responses<sup>26</sup>, the combination of T4 and T5 thus appeared to be sufficient for higher order motion sensitivity.

We then examined the necessity of T4 and T5 for three-point glider responses. Tethered walking flies were presented with a complete set of two-point and three-point gliders (Fig. 8a). Next, we silenced T4 and T5 in isolation as well as simultaneously. For control flies, turning responses to two-point correlations were as expected for standard phi and reverse-phi stimuli: flies turned strongly in the direction of positive correlations (positive glider parity) and reversed this tendency for negative correlations (negative glider parity; Fig. 8b). Blocking T4 and T5 in conjunction completely abolished sensitivity to all two-point gliders. This is, to the best of our knowledge, the first demonstration that reverse-phi motion, defined by spatiotemporal anti-correlations, depends on the combined activity of ON and OFF motion detectors<sup>10,19,36</sup>. We then replicated the previously reported behavioral response pattern for three-point gliders<sup>12</sup>. Flies in which both T4 and T5 were silenced failed to respond to any of the higher order motion stimuli, indicating that T4 and T5 are also necessary for motion detection beyond two-point correlations (Fig. 8c). Blocking T4 or T5 in isolation had no effect on two-point responses (Supplementary Fig. 6a–c). We were, however, surprised to find that isolated T4 or T5 blocks resulted in particular three-point glider phenotypes. Silencing the ON pathway specifically reversed the flies' turning tendency for converging gliders while slightly boosting diverging glider responses (Fig. 8d). For OFF block flies, the opposite pattern emerged (Fig. 8e).

Finally, we probed our symmetric and asymmetric detector models for higher order motion sensitivity. Both produced comparable two-point glider responses (Fig. 8f). For three-point gliders, both detectors generated nonzero output, but only the asymmetric model qualitatively matched the pattern we observed in our electrophysiological experiments as well as in walking flies (Fig. 8g). Notably, when evaluating detector responses to individual glider instantiations, we found complex and strongly fluctuating responses that resembled tangential cell responses (Supplementary Fig. 6d,g). Responses became smooth and regular only after integration of many repetitions (Fig. 7 and Supplementary Fig. 6e,f,h,i). We then simulated T4 or T5 silencing by setting ON or OFF gain to zero. These models reliably predicted the specific response reversals (Fig. 8h,i) observed in behavior (Fig. 8d,e). We therefore posit that T4 and T5 are capable of extracting triple correlations on their own. ON and OFF edges have been found to contain a particular combination of triple correlations<sup>12</sup>. The reverse also held: three-point gliders elicited strong signals of opposite sign in pure ON or OFF detectors (Fig. 8d,e,h,i). Only if the pathways were perfectly symmetric did these responses cancel out. If they were asymmetric, as in our optimized detector or the *Drosophila* visual system, then residual responses remained. Our optimized models correctly predicted the sign and relative magnitude of these effects, suggesting that the asymmetries we found *in silico* track the asymmetries of the biological system.

## DISCUSSION

We studied the roles of ON and OFF motion pathways for velocity estimation in natural scenes. *Drosophila* stabilized their walking trajectories in a closed-loop virtual environment whose statistics

resembled those of natural scenes. Genetically silencing cells T4 and T5 rendered flies unable to perform this path correction. In an open-loop setting, flies reliably tracked whole-field motion of naturalistic images. Interrupting the activity of ON or OFF pathways did not affect this capability, suggesting that the two channels subserve redundant functions in information-rich natural scenes. In physiological and behavioral experiments, we found that ON and OFF motion estimators exhibit diverging temporal tuning. When we optimized the estimation performance of an ON-OFF motion detector, we obtained asymmetric models whose temporal tuning properties resembled those found for the biological system. This suggests that *Drosophila* motion detectors are tailored to an ON-OFF asymmetric visual world, with each channel covering the most informative temporal range. In a final set of experiments and without specific tuning of the model, we found that *Drosophila*'s sensitivity to certain types of higher order motion has a straightforward explanation in this framework of differentially tuned pathways.

One could interpret the shifted tuning ranges of T4 and T5 as a solution for maximizing information transfer by avoiding coding redundancy. However, for the asymmetric detector, pathways were optimized independently, forcing both to adequately encode the input velocity distribution. We therefore favor the interpretation that features reliably indicating scene velocity operate on time scales that differ between ON and OFF signals. The skewed luminance distribution of real images (Fig. 6a) offers an intuition for this notion: ON signals are dominated by infrequent and large positive deflections, whereas OFF signals are generally smaller and more regular. As neither RC filters nor lamina cells act as perfect differentiators, these differences plausibly persist at later levels of motion detection, where they may be exploited by appropriately tuned mechanisms<sup>13</sup>. Notably, detector performance was generally better for OFF detectors than for ON detectors (Fig. 5b), possibly reflecting the sparseness of informative ON signals.

During conditioning of detector parameters on natural images, we also optimized the weight of the tonic DC signal. We found nonzero optima for both pathways, as postulated in previous studies on reverse-phi responses<sup>10</sup>. Electrophysiologically, ON pathway interneurons Mi1 and Tm3 did indeed show static responses to absolute brightness levels with the amplitude ratio between high-pass and DC signal qualitatively matching our findings<sup>24</sup>. In contrast to our prediction, OFF intermediaries Tm1 and Tm2 did not exhibit inverted tonic signals. However, other cells presynaptic to T5 still await characterization<sup>17</sup>. How DC signals can be reconciled with our demonstration that T4 and T5 responses are fully polarity specific remains unclear. In particular, theoretical considerations on the basis of the response properties of Mi1 and Tm3 predict sensitivity to OFF edges for T4 (ref. 24). This is not borne out by our experiments (Fig. 3).

Theoretical studies have proposed that responding to higher order correlations allows motion detectors to exploit natural ON-OFF asymmetries<sup>12,14</sup>. The asymmetry between ON and OFF pathways reported here does indeed confer sensitivity to triple correlations. Only under the assumption that ON and OFF steps are processed equally do spurious two-point correlations vanish. However, whether *Drosophila*'s higher order motion responses are an epiphenomenon of detector asymmetries or whether detector asymmetry represents a way of accessing higher order correlations is up for debate. Moreover, it remains to be seen whether the findings at hand generalize to other forms of higher order motion perceived by *Drosophila*<sup>38</sup>.

Our previous characterization of cell types T4 and T5 revealed only minor differences in temporal frequency tuning for gratings<sup>21</sup>. It is currently not well understood how physiological tuning curves for edges and gratings relate to each other. Given the drastically different

## ARTICLES

kinetics of the two stimuli, large ON-OFF differences for one may lead to only small ON-OFF differences for the other. In addition, we suggest that edges provide a better approximation of visual kinetics in the real world than artificial gratings that are periodic as well as constant in mean luminance, contrast and geometry. Moreover, measurements from tangential cells in behaving flies have indicated grating response optima that are shifted toward higher frequencies compared with quiescence<sup>26,39,40</sup>. How this state dependency translates to the tuning for edge velocity is unclear. Indeed, our linear prediction of opposing edge responses from physiological edge tuning underestimates the true crossing point between ON and OFF dominance (Fig. 4d). A shift toward higher preferred velocities, as observed for grating optima, could account for this discrepancy. Notably, our behavioral data demonstrate that basic characteristics of temporal ON-OFF asymmetries are preserved in active flies.

The ON-OFF asymmetry we describe represents one of many examples for the adaptation of sensory systems to the environment in which they evolved<sup>5,6,13,41</sup>. Contrast asymmetries between ON and OFF are a widespread feature shared by most visual niches. It therefore seems probable that the sensory asymmetries found in *Drosophila* are conserved across species. ON-OFF divergence has previously been described for several computations in vertebrate visual systems<sup>42–44</sup>. It will be interesting to examine the effects on optimal tuning exerted by features of the mammalian retina, such as contrast normalization<sup>45</sup>. Finally, motion energy models have been successfully used to explain the psychophysics of motion perception in higher organisms<sup>46</sup>. Given that Hassenstein-Reichardt detectors and motion energy models are generally mathematically equivalent<sup>47</sup>, our optimization results could also emerge for an appropriately rectified ON-OFF motion energy detector.

T4 and T5 are critically involved in behaviors other than the optomotor response. Recently, studies have implicated motion detectors in object fixation<sup>27</sup>, depth perception<sup>48</sup> or looming responses<sup>49</sup>. Given the variety of tasks and resulting visual statistics, optimal tuning needs to be examined under various constraints. Finally, we believe this ecological perspective on biological motion detection could have a decisive role in the continued mapping of the fly visual system. The abundance of information-bearing features in natural visual scenes may necessitate complex filter banks and multi-cell processing stages<sup>17,20,23,50</sup>. Real-world demands will then be critical constraints when assigning function to cells in the *Drosophila* optic lobe.

## METHODS

Methods and any associated references are available in the [online version of the paper](#).

*Note: Any Supplementary Information and Source Data files are available in the online version of the paper.*

## ACKNOWLEDGMENTS

A. Nern and G.M. Rubin (Janelia Research Campus) generated and kindly provided the splitGal4 line targeting T4 and T5. We are grateful for fly work and behavioral experiments performed by R. Kutlesa, C. Theile and W. Essbauer. We thank A. Arenz and A. Mauss for carefully reading the manuscript, T. Schilling for fly illustrations, and all of the members of the Borst laboratory for extensive discussions. The Bernstein Center for Computational Neuroscience Munich supplied computing resources for our simulations. A.L., G.A., M.M., E.S., A. Bahl and A. Borst are members of the Graduate School for Systemic Neurosciences, Munich.

## AUTHOR CONTRIBUTIONS

A.L., G.A. and A. Borst designed the study. A.L. performed behavioral experiments, associated data analysis and all modeling work. G.A., M.M. and E.S. performed electrophysiological experiments. G.A. performed calcium imaging. A.L. and

G.A. analyzed physiological data. A. Bahl designed the behavioral apparatuses and performed behavioral experiments. A.L. wrote the manuscript with help from all of the authors.

## COMPETING FINANCIAL INTERESTS

The authors declare no competing financial interests.

Reprints and permissions information is available online at <http://www.nature.com/reprints/index.html>.

1. Borst, A. Fly visual course control: behavior, algorithms and circuits. *Nat. Rev. Neurosci.* **15**, 590–599 (2014).
2. Ruderman, D.L. & Bialek, W. Statistics of natural images: Scaling in the woods. *Phys. Rev. Lett.* **73**, 814–817 (1994).
3. Simoncelli, E.P. & Olshausen, B.A. Natural image statistics and neural representation. *Annu. Rev. Neurosci.* **24**, 1193–1216 (2001).
4. Field, D.J. Relations between the statistics of natural images and the response properties of cortical cells. *J. Opt. Soc. Am. A* **4**, 2379–2394 (1987).
5. Laughlin, S. A simple coding procedure enhances a neuron's information capacity. *Z. Naturforsch. C* **36**, 910–912 (1981).
6. van Hateren, J.H. & van der Schaaf, A. Independent component filters of natural images compared with simple cells in primary visual cortex. *Proc. Biol. Sci.* **265**, 359–366 (1998).
7. Yu, Y., Schmid, A.M. & Victor, J.D. Visual processing of informative multipoint correlations arises primarily in V2. *eLife* **4**, e06604 (2015).
8. Gjorgjieva, J., Sompolinsky, H. & Meister, M. Benefits of pathway splitting in sensory coding. *J. Neurosci.* **34**, 12127–12144 (2014).
9. Borst, A. & Helmstaedter, M. Common circuit design in fly and mammalian motion vision. *Nat. Neurosci.* **18**, 1067–1076 (2015).
10. Eichner, H., Joesch, M., Schnell, B., Reiff, D.F. & Borst, A. Internal structure of the fly elementary motion detector. *Neuron* **70**, 1155–1164 (2011).
11. Hassenstein, B. & Reichardt, W. Systemtheoretische Analyse der Zeit-, Reihenfolgen- und Vorzeichenabschätzung bei der Bewegungsperzeption des Rüsselkäfers *Chlorophanus*. *Z. Naturforsch. B* **11**, 513–524 (1956).
12. Clark, D.A. *et al.* Flies and humans share a motion estimation strategy that exploits natural scene statistics. *Nat. Neurosci.* **17**, 296–303 (2014).
13. Ratliff, C.P., Borghuis, B.G., Kao, Y.-H., Sterling, P. & Balasubramanian, V. Retina is structured to process an excess of darkness in natural scenes. *Proc. Natl. Acad. Sci. USA* **107**, 17368–17373 (2010).
14. Fitzgerald, J.E., Katsov, A.Y., Clandinin, T.R. & Schnitzer, M.J. Symmetries in stimulus statistics shape the form of visual motion estimators. *Proc. Natl. Acad. Sci. USA* **108**, 12909–12914 (2011).
15. Hu, Q. & Victor, J.D. A set of high-order spatiotemporal stimuli that elicit motion and reverse-phi percepts. *J. Vis.* **10**, 9.1–9.16 (2010).
16. Takemura, S.-Y. *et al.* A visual motion detection circuit suggested by *Drosophila* connectomics. *Nature* **500**, 175–181 (2013).
17. Shinomiyka, K. *et al.* Candidate neural substrates for off-edge motion detection in *Drosophila*. *Curr. Biol.* **24**, 1062–1070 (2014).
18. Joesch, M., Schnell, B., Raghu, S.V., Reiff, D.F. & Borst, A. ON and OFF pathways in *Drosophila* motion vision. *Nature* **468**, 300–304 (2010).
19. Clark, D.A., Bursztyn, L., Horowitz, M.A., Schnitzer, M.J. & Clandinin, T.R. Defining the computational structure of the motion detector in *Drosophila*. *Neuron* **70**, 1165–1177 (2011).
20. Silies, M. *et al.* Modular use of peripheral input channels tunes motion-detecting circuitry. *Neuron* **79**, 111–127 (2013).
21. Maisak, M.S. *et al.* A directional tuning map of *Drosophila* elementary motion detectors. *Nature* **500**, 212–216 (2013).
22. Meier, M. *et al.* Neural circuit components of the *Drosophila* OFF motion vision pathway. *Curr. Biol.* **24**, 385–392 (2014).
23. Ammer, G., Leonhardt, A., Bahl, A., Dickson, B.J. & Borst, A. Functional specialization of neural input elements to the *Drosophila* ON motion detector. *Curr. Biol.* **25**, 2247–2253 (2015).
24. Behnia, R., Clark, D.A., Carter, A.G., Clandinin, T.R. & Desplan, C. Processing properties of ON and OFF pathways for *Drosophila* motion detection. *Nature* **512**, 427–430 (2014).
25. Haikala, V., Joesch, M., Borst, A. & Mauss, A.S. Optogenetic control of fly optomotor responses. *J. Neurosci.* **33**, 13927–13934 (2013).
26. Schnell, B., Weir, P.T., Roth, E., Fairhall, A.L. & Dickinson, M.H. Cellular mechanisms for integral feedback in visually guided behavior. *Proc. Natl. Acad. Sci. USA* **111**, 5700–5705 (2014).
27. Bahl, A., Ammer, G., Schilling, T. & Borst, A. Object tracking in motion-blind flies. *Nat. Neurosci.* **16**, 730–738 (2013).
28. Joesch, M., Plett, J., Borst, A. & Reiff, D.F. Response properties of motion-sensitive visual interneurons in the lobula plate of *Drosophila melanogaster*. *Curr. Biol.* **18**, 368–374 (2008).
29. Warzecha, A.-K. & Egelhaaf, M. Intrinsic properties of biological motion detectors prevent the optomotor control system from getting unstable. *Phil. Trans. R. Soc. Lond. B* **351**, 1579–1591 (1996).
30. Schnell, B., Raghu, S.V., Nern, A. & Borst, A. Columnar cells necessary for motion responses of wide-field visual interneurons in *Drosophila*. *J. Comp. Physiol. A Neuroethol. Sens. Neural Behav. Physiol.* **198**, 389–395 (2012).

31. Brand, A.H. & Perrimon, N. Targeted gene expression as a means of altering cell fates and generating dominant phenotypes. *Development* **118**, 401–415 (1993).
32. Sweeney, S.T., Broadie, K., Keane, J., Niemann, H. & O’Kane, C.J. Targeted expression of tetanus toxin light chain in *Drosophila* specifically eliminates synaptic transmission and causes behavioral defects. *Neuron* **14**, 341–351 (1995).
33. Straw, A.D., Rainsford, T. & O’Carroll, D.C. Contrast sensitivity of insect motion detectors to natural images. *J. Vis.* **8**, 32.1–32.9 (2008).
34. Chen, T.-W. *et al.* Ultrasensitive fluorescent proteins for imaging neuronal activity. *Nature* **499**, 295–300 (2013).
35. Mauss, A.S. *et al.* Neural circuit to integrate opposing motions in the visual field. *Cell* **162**, 351–362 (2015).
36. Tuthill, J.C., Chiappe, M.E. & Reiser, M.B. Neural correlates of illusory motion perception in *Drosophila*. *Proc. Natl. Acad. Sci. USA* **108**, 9685–9690 (2011).
37. Dror, R.O., O’Carroll, D.C. & Laughlin, S.B. Accuracy of velocity estimation by Reichardt correlators. *J. Opt. Soc. Am. A Opt. Image Sci. Vis.* **18**, 241–252 (2001).
38. Theobald, J.C., Duistermars, B.J., Ringach, D.L. & Frye, M.A. Flies see second-order motion. *Curr. Biol.* **18**, R464–R465 (2008).
39. Jung, S.N., Borst, A. & Haag, J. Flight activity alters velocity tuning of fly motion-sensitive neurons. *J. Neurosci.* **31**, 9231–9237 (2011).
40. Chiappe, M.E., Seelig, J.D., Reiser, M.B. & Jayaraman, V. Walking modulates speed sensitivity in *Drosophila* motion vision. *Curr. Biol.* **20**, 1470–1475 (2010).
41. Dyakova, O., Lee, Y.-J., Longden, K.D., Kiselev, V.G. & Nordström, K. A higher order visual neuron tuned to the spatial amplitude spectra of natural scenes. *Nat. Commun.* **6**, 8522 (2015).
42. Komban, S.J. *et al.* Neuronal and perceptual differences in the temporal processing of darks and lights. *Neuron* **82**, 224–234 (2014).
43. Chichilnisky, E.J. & Kalmar, R.S. Functional asymmetries in ON and OFF ganglion cells of primate retina. *J. Neurosci.* **22**, 2737–2747 (2002).
44. Pandarinath, C., Victor, J.D. & Nirenberg, S. Symmetry breakdown in the ON and OFF pathways of the retina at night: functional implications. *J. Neurosci.* **30**, 10006–10014 (2010).
45. Carandini, M. & Heeger, D.J. Normalization as a canonical neural computation. *Nat. Rev. Neurosci.* **13**, 51–62 (2012).
46. Adelson, E.H. & Bergen, J.R. Spatiotemporal energy models for the perception of motion. *J. Opt. Soc. Am. A* **2**, 284–299 (1985).
47. van Santen, J.P. & Sperling, G. Elaborated Reichardt detectors. *J. Opt. Soc. Am. A* **2**, 300–321 (1985).
48. Schwegmann, A., Lindemann, J.P. & Egelhaaf, M. Depth information in natural environments derived from optic flow by insect motion detection system: a model analysis. *Front. Comput. Neurosci.* **8**, 83 (2014).
49. Schilling, T. & Borst, A. Local motion detectors are required for the computation of expansion flow-fields. *Biol. Open* **4**, 1105–1108 (2015).
50. Burge, J. & Geisler, W.S. Optimal speed estimation in natural image movies predicts human performance. *Nat. Commun.* **6**, 7900 (2015).

## ONLINE METHODS

**Fly strains and genetics.** We raised *Drosophila melanogaster* on cornmeal-agar medium under standard conditions (60% humidity, 18 °C for behavioral and 25 °C for physiology experiments, 12-h light/12-h dark schedule) for the full duration of their developmental cycle. Female flies were used in all experiments. For physiological experiments, we selected flies 5–20 h post-eclosion. Flies in behavioral experiments were 1–3 d old. Behavioral experiments targeting T4 or T5 used the following driver lines, as described previously<sup>21</sup>: T4-Gal4 (VT37588) and T5-Gal4 (R42H07). When targeting T4 and T5 simultaneously, we employed a new, highly specific driver line: T4/T5-splitGal4 (R59E08-AD; R42F06-DBD), kindly provided to us by A. Nern and G.M. Rubin at Janelia Research Campus. For visualization of expression patterns (Supplementary Fig. 1), we crossed driver lines to UAS-mCD8GFP reporter flies. For experiments, Gal4 flies were then crossed to either wild type Canton S flies or UAS-TNT-E flies resulting in Gal4 control or block flies, respectively. Crossing UAS-TNT-E flies to Canton S flies generated UAS control flies. For calcium imaging, we combined two different Gal4 lines (VT25965 and VT37588) that in conjunction expressed at comparable levels in T4 and T5. These were crossed to UAS-GCaMP6f<sup>34</sup> flies. Genotypes derived from these crossings and their aliases as used throughout the text are listed in the supplementary material (Supplementary Table 1).

**Immunohistochemistry.** Antibody stainings (Supplementary Fig. 1) were performed as described previously<sup>51</sup>. We used the following antibodies and dilutions. Primary antibodies: rabbit anti-GFP (Torri Pines, TP401, 1:2,000), mouse anti-nc82 (DSHB, AB\_2314866, 1:25); secondary antibodies: goat anti-rabbit 488 (Invitrogen, A-11008, 1:500), goat anti-mouse 633 (Invitrogen, A-21053, 1:500). Imaging was performed on a SP5 confocal microscope (Leica) at a resolution of 1,024 × 1,024. Images were processed in ImageJ 1.46f (US National Institutes of Health). Single z-slices are shown for horizontal views.

**Behavioral experiments.** We performed behavioral experiments as described previously<sup>21,23,27</sup>. Briefly, tethered flies were placed on an air-suspended polyurethane ball in a virtual environment consisting of three computer screens covering a substantial part of the animal's visual field (approximately 270° in azimuth and 120° in elevation). Experiments were run on six set-ups in parallel; two of them displayed visual stimuli at 120 Hz and the remaining four at 144 Hz with all screens calibrated to display at comparable contrast and brightness. We never observed any differences in behavior between refresh rates. All stimuli were rendered in real-time using the graphics engine Panda3D, allowing visual feedback based on flies' instantaneous walking behavior. Due to high pixel density on all computer screens, stimulus pixel size was well below the resolution limit of *Drosophila*. The immediate surround of the ball was temperature-controlled by means of a closed-loop thermoregulation system. Each experiment used the same temperature protocol: Temperature was kept at 25 °C for the first 5 min and then linearly raised to 34 °C within 10 min.

All behavioral experiments ran for 60–90 min and comprised 50–60 repeated trials, except for open-loop velocity estimation experiments (Fig. 2) that lasted 280 trials. In each trial, we randomized stimulus presentation order. Movement of the ball was tracked at 4 kHz and down-sampled to 20 Hz for offline analysis. For each fly, we manually selected a continuous range of 100–200 (Fig. 2) or 25 trials (other experiments) based on the following criteria: First, the temperature was at a constant 34 °C. Second, the average forward walking speed of the fly was above 0.3 cm s<sup>-1</sup>, indicating healthy locomotion and visual responsiveness. Third, the average turning tendency of the fly was stable and close to 0° s<sup>-1</sup>. These criteria excluded approximately 20% of all flies we measured. During analysis, we averaged traces across trials, resulting in a single walking trace per fly per experimental condition. Where applicable (Figs. 1, 4 and 8, and Supplementary Fig. 5), we then subtracted responses to mirror-symmetric stimulus presentations to minimize the impact of small rotational biases in turning behavior. Traces were filtered using a first-order low-pass filter ( $\tau = 100$  ms). In open-loop experiments (Fig. 2), we generated a regression model for each fly that mapped rotation of the environment to the turning response of the fly (averaged over 1 s after stimulus onset) using least-squares fitting. Response gain was then defined as the slope of this model. The intercepts clustered around 0° s<sup>-1</sup>, indicating trajectories that were on average straight. For additional analysis (Supplementary Fig. 3), we constructed Bayesian decoders that minimize the squared error of their estimates. This was done on a fly-by-fly basis. We first split the data set consisting of pairs of image

velocity and turning response as for the correlation analysis (Fig. 2) into training and test sets at a ratio of 3:1, approximated the posterior distribution through application of Bayes' rule to the joint probability generated from appropriate histograms, and estimated image velocity as the expected value of the posterior for a given response. Finally, we assessed decoding performance of resulting mapping functions by calculating the root-mean-square error after application to the test set. The behavioral data analysis pipeline was implemented in Python 2.7 using pandas 15.1, NumPy 1.6, SciPy 0.15, matplotlib 1.3 and Numba 0.18.

**Electrophysiology.** Electrophysiological *in vivo* patch-clamp recordings from lobula plate tangential cells closely followed previously described protocols<sup>21,22,28</sup>. Recordings were low-pass filtered with a cut-off frequency of 3 kHz and digitized at 10 kHz. Data acquisition was based on Matlab R2011A (MathWorks). We identified cell types based on their response profile when stimulated with moving gratings. In addition, cells were dye-filled and anatomically verified whenever possible.

We visually stimulated flies using a custom-built LED arena spanning approximately 180° in azimuth and 90° in elevation of the fly's visual field with a spatial resolution of 1.5° per individual LED. The LED refresh rate was in the kHz range; stimulus images were then updated with up to 600 Hz. Maximum luminance was 80 cd m<sup>-2</sup>. During offline data analysis, recorded traces were down-sampled to 2 kHz and averaged across 2–5 trials per cell. We randomized the order of stimulus presentation within trials. Cells that did not respond reliably to grating stimulation were excluded from further analysis. Before we extracted response maxima and minima for edge responses (Fig. 3), electrophysiological traces were filtered with a second-order Savitzky-Golay kernel that was 40 samples wide. The electrophysiological data analysis pipeline was implemented in Python 2.7 using pandas 15.1, NumPy 1.6, matplotlib 1.3 and Numba 0.18.

**Calcium imaging.** We employed a custom-built two-photon laser scanning microscope as described previously<sup>21,22</sup>. We prepared flies analogously to electrophysiology experiments. Images were recorded at a resolution of 256 × 128 pixels and a frame rate of 3.74 Hz. Raw images were then converted into relative fluorescence change ( $\Delta F/F$ ) series by using the mean of three frames before stimulation onset as a baseline. For summary images, the resulting images were averaged across time; for time-resolved traces, we defined relevant regions of interest and collapsed signals within the defined borders by averaging across pixels. We used the LED arena described above for visual stimulation. Data acquisition and analysis were performed in Matlab R2011a (MathWorks) using ScanImage 3.8.

**Image sets.** Two image sets were used throughout the study. First, for all behavioral experiments involving natural images, we generated a small library of 60 panoramic images spanning approximately 360° in azimuth using a consumer-grade camera (iPhone 5s; Apple). The resolution of each image was 10,800 × 2,460 pixels. Images were taken in various natural environments covering different visual statistics: woods (30%), open rural spaces (30%), urban landscapes (20%), and laboratories (20%). We used raw images without processing or calibration and converted them to gray scale by averaging across color channels. Critical image statistics such as RMS contrast (that is, the s.d. of pixel values), luminance distribution, and power spectrum were comparable to other scientific image libraries. Second, for all *in silico* experiments, we made use of calibrated images from the van Hateren natural image database<sup>6</sup>. No image category was excluded and we performed no further sorting, yielding 4,167 images at a resolution of 1,536 × 1,024 pixels. One pixel corresponded to one arc minute of visual angle. We normalized the set through subtraction of and division by the mean pixel value for each image<sup>12,45</sup>. Kernel density estimates (Figs. 2 and 6) were generated using a routine in the SciPy library. Gaussian kernels were used, and we determined bandwidth via Silverman's rule.

We scaled the contrast of our in-house image set by subtracting the image's mean luminance, applying the specified multiplicative factor, and then adding the initial mean luminance (Figs. 1 and 2). Phase-scrambling of the van Hateren image set was achieved by performing a Fourier transform, replacing the phase spectrum with that of a Gaussian random image of equal mean luminance, and finally recovering the phase-randomized image via the inverse Fourier transform (Fig. 6b). The luminance-remapped scrambled set was generated by replacing each pixel value of a phase-randomized image with the value corresponding to

the same luminance-ordered rank in the original image (Fig. 6c). Analogously, we generated the luminance-remapped natural set by drawing pixel values from the corresponding phase-scrambled image (Fig. 6d).

**Visual stimuli.** On every trial of the closed-loop course stabilization experiment (Fig. 1), a random image was chosen from our in-house image library and projected onto a virtual cylinder surrounding the fly. In order to cover the visual field without significant distortion, the panorama was mirrored across the fly's elevation axis. Each trial lasted 5 s. The rotational component of the walking trajectory was used as a feedback signal for the azimuthal orientation of the virtual cylinder, effectively giving flies control over their angular orientation relative to the environment. Feedback gain was set to unity. Between 1.5 s and 3.5 s, we additionally rotated the virtual environment at a constant  $80^\circ \text{ s}^{-1}$  in clockwise or counter-clockwise direction. Contrast was scaled in accordance with the procedure described above to 12.5%, 25%, 50% and 100% of the original RMS value.

For open-loop velocity estimation experiments (Fig. 2), images were chosen and projected as above while feedback gain was set to zero. On each trial, a random velocity was drawn from a Gaussian distribution centered at  $0^\circ \text{ s}^{-1}$  with a s.d. of  $50^\circ \text{ s}^{-1}$ . Trials lasted 3.5 s. Between 1.5 s and 2 s, the virtual environment rotated with the constant velocity drawn earlier. The border where the image on the cylinder wrapped around was placed such that it remained in the back of the fly on most trials. Here, we added the 6% contrast condition.

We used single bright and dark edges for characterizing the physiological response properties of ON and OFF channels (Fig. 3). During electrophysiology experiments, we presented edges moving at 12 constant velocities across two orders of magnitude ( $6.25, 12.5, 25, 50, 75, 100, 150, 200, 300, 500, 700$  and  $900^\circ \text{ s}^{-1}$ ). When recording from vertical system or horizontal system cells, edges traveled along the vertical or horizontal axis, respectively, and in the preferred direction of the cell. Edges used during calcium imaging always moved at  $25^\circ \text{ s}^{-1}$  and either downwards or from front to back (no differences in the two directions were observed). Physiology stimuli (Fig. 3) had a Michelson contrast of 100%, starting from either a dark (ON) or bright (OFF) background. For additional experiments (Supplementary Fig. 4), edges started from an equal background luminance of  $10.7 \text{ cd m}^{-2}$ . As the stimulation device only allowed discrete steps, ON edges then had a contrast of 76% and OFF edges a contrast of 100%.

The behavioral balanced motion stimulus resembled previous iterations<sup>19,21,23</sup>. Briefly, we presented flies with a stationary square wave grating that had an initial spatial wavelength of  $45^\circ$  and Michelson contrast of 50%. Each individual trial lasted 9 s. Between 2 s and 7 s, bright and dark edges moved in opposite directions at the same velocity. In contradistinction to previous experiments, we reset the stimulus to the initial state after edges had traversed  $20^\circ$  of visual angle, allowing us to keep stimulus duration fixed regardless of edge velocity. After each reset, we applied a random phase shift in order to minimize the effect of initial grating position relative to the fly. This was done for six velocities ( $20, 40, 80, 160, 320$  and  $640^\circ \text{ s}^{-1}$ ) in clockwise and counter-clockwise direction. Pulse experiments (Supplementary Fig. 5) were performed analogously, with edge movement being limited to the indicated duration (500 ms, 250 ms or 100 ms).

Glider experiments (Figs. 7 and 8) were performed as described previously<sup>12</sup>. Briefly, the visual field was divided into vertical stripes that had an azimuthal extent of  $6^\circ$  (behavior) or  $4.5^\circ$  (electrophysiology). Each bar could either be dark or bright; Michelson contrast for these experiments was 50% (behavior) or 100% (electrophysiology). Initial bars were seeded with a random binary pattern. Depending on the glider, bars were then updated according to the corresponding deterministic rule. The glider update frequency was either 24 Hz (behavior) or 10 Hz (electrophysiology). For electrophysiological experiments, we used a single pre-generated glider sequence. Here, preferred direction was defined as the update direction that would depolarize cells for two-point gliders.

**Modeling.** The ON-OFF detector used in this study (Figs. 5, 6 and 8) was derived from a previously published two-quadrant model<sup>10</sup>. Briefly, we modeled photoreceptor signals as time series with a resolution of 10 ms (for optimization experiments) or 1 ms (for other experiments) per step. Lamina processing was then approximated as the linear sum of a high-pass-filtered signal (first-order RC filter with  $\tau = 250$  ms) and an unfiltered tonic component (DC) with variable weight. This was followed by a half-wave rectification step. For the pure ON detector, signals were rectified with the threshold set to exactly zero. For the pure OFF detector, the signal was inverted and then rectified with the threshold set to exactly

zero. Further processing was identical for both: The signal was first-order low-pass filtered with variable time constant  $\tau$  and then multiplied with an unfiltered signal from the other spatial location. This was done twice in a mirror-symmetrical fashion, followed by subtraction, yielding a fully opponent direction-selective signal. For the full ON-OFF detector, an ON detector and an OFF detector were summed with equal weight. Unlike previous versions<sup>10</sup>, our simplified detector did not make use of shifted rectification thresholds or unequally weighted detector halves. Outside of natural image experiments, stimuli were rendered at a spatial resolution of  $0.1^\circ$ . We modeled the spatial acceptance profile of photoreceptors as Gaussians with a half-width at maximum of  $5^\circ$ . The symmetric detectors (Figs. 5 and 8) had, by definition, zero DC component and identical filter time constants for the ON and the OFF channel as determined by the optimization procedure. The asymmetric detector had DC components and time constants that were allowed to differ between ON and OFF during optimization.

The detector characterization (Fig. 5) depicts results from a combination of 20 detectors separated by  $6.5^\circ$ . The spatial wavelength of all gratings was  $20^\circ$  with velocity being defined by temporal frequency. Simulations for grating and edge tunings ran for 10 s each; output was averaged across detectors and time. For the velocity profile (Fig. 5g), we used a time series drawn from a Gaussian distribution with s.d. =  $20^\circ \text{ s}^{-1}$  that was first-order low-pass filtered with  $\tau = 500$  ms. Units were discarded for display purposes. Modeled edge stimuli lasted for 15 s, with movement starting after 2 s. The starting condition was fixed at 1.0 and followed by a jump to 1.2 for ON edges or 0.8 for OFF edges. Detector output was averaged for the duration of edge motion, which depended on velocity. We simulated 50 velocities on a logarithmic scale from  $10^\circ \text{ s}^{-1}$  to  $1,000^\circ \text{ s}^{-1}$ . Glider stimuli (Fig. 8) were rendered as idealized signals mapping 21 virtual stripes to the 21 virtual photoreceptors of an array of 20 detectors, without any spatial overlap. The array was seeded with a random combination of binary dark and bright values (arbitrarily defined as 1.0 and 3.0, respectively) and then updated according to previously described rules<sup>12</sup> at a frequency of 5 Hz. Glider simulations ran for 5 s each and were averaged across 500 instantiations and time (Fig. 8f-i). We approximated compressive characteristics of the visuo-motor transformation by multiplying two-point and three-point responses with slightly different gain values ( $2,500^\circ \text{ s}^{-1}$  and  $3,500^\circ \text{ s}^{-1}$ , respectively) when translating detector output into turning tendency. All simulations were implemented in Python 2.7 using NumPy 1.6 and Numba 0.18.

**Detector optimization.** Optimization of detector models was based on an exhaustive cross-validated search on a two-dimensional parameter grid. We generated 50 random training-to-test splits from the 4,167 images of the van Hateren data set with a training-to-test ratio of 4:1. All images received a luminance bias of 3.0 and were clipped at zero in order to ensure that only positive signals arrived at detector inputs while keeping mean values constant. The optimization procedure was then performed independently for each training fold.

We scanned a parameter space comprising  $40 \times 21$  combinations of low-pass time constants (from 10 to 400 ms in 10-ms steps) and DC contribution (from  $-20\%$  to  $+20\%$  in 2% steps). For each parameter set, three detectors with the corresponding parameter settings were simulated: a pure ON detector, a pure OFF detector, and a symmetric ON-OFF detector where ON and OFF channels used the same parameters. Fitness of a given detector was determined as follows, based on previous studies<sup>12</sup> and analogously to behavioral experiments (Fig. 2): on each iteration, we drew a random image from the training set and a random velocity from a Gaussian distribution centered at zero with s.d. =  $25^\circ \text{ s}^{-1}$ . We then generated two time series corresponding to a simulated pair of photoreceptors separated by  $6.5^\circ$  traveling across the horizontal middle row of the image at the constant velocity drawn before and for a duration of 1,000 ms. The signals were fed into each of the three detectors. Detector output was averaged across time. We repeated this procedure 50,000 times per parameter set. Detector fitness was then defined as the Pearson correlation between input velocity and average detector output. During testing, we assembled two detectors per test set. The optimal symmetric detector was the best-performing detector constrained to use equal ON and OFF settings and zero DC. The optimal asymmetric detector was the linear combination of the best performing ON detector and the best performing OFF detector. The performance of both was then evaluated on the corresponding test set; here, detector evaluations were repeated 100,000 times. This was done for the natural, phase-scrambled and luminance-remapped image sets.

We implemented the optimization procedure in Python 2.7 using NumPy 1.6, SciPy 0.15, Numba 0.18, and IPython 3.0. Parallel operations were distributed across 128 CPUs on a Beowulf cluster consisting of eight physical machines.

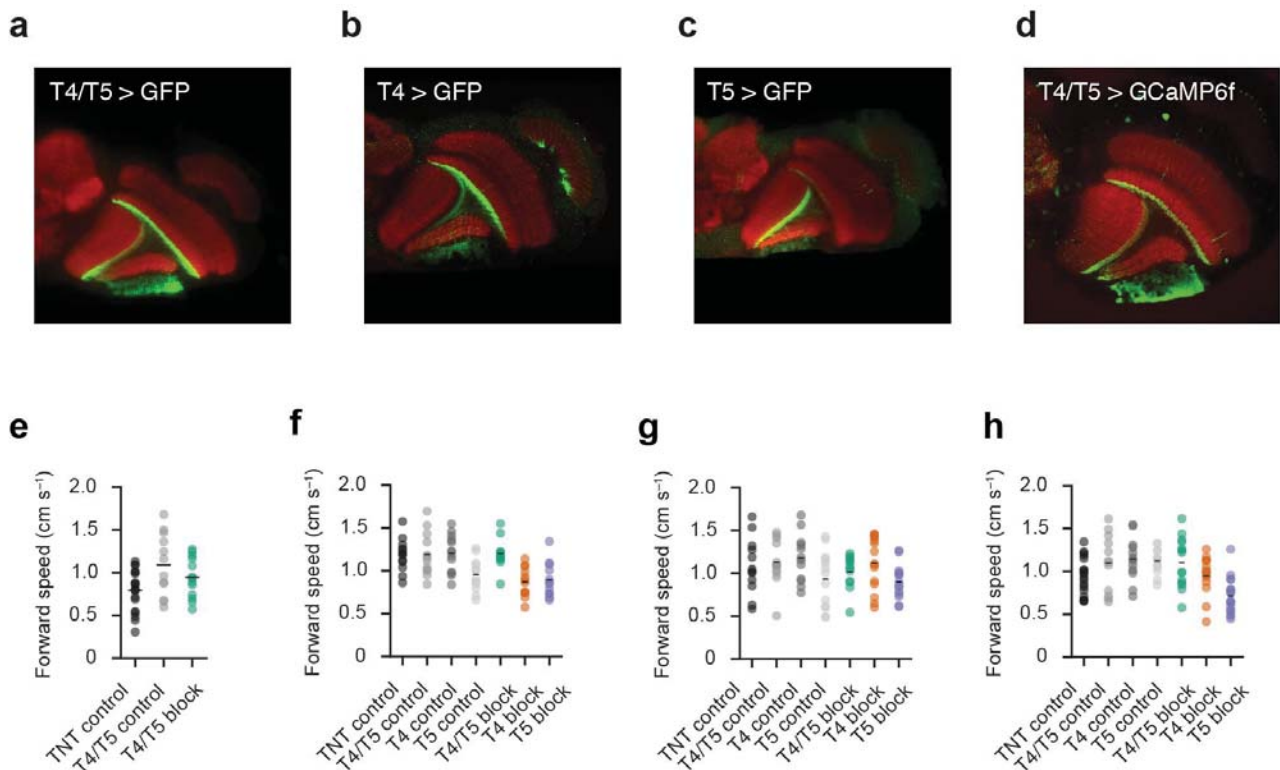
**Code availability.** Python and Matlab code used throughout analysis, modeling, and optimization is available upon request to the authors.

**Statistics.** All statistical tests were two-tailed Student's *t* tests at a significance level of 0.05, assuming unequal variance unless stated otherwise. Where necessary, conservative Bonferroni correction was applied in order to correct for multiple hypothesis testing. Normality of data was confirmed visually and not formally tested. We did not predetermine sample sizes using statistical tests, but numbers

are in line with established work<sup>12,20,21,23,27</sup>. Our confidence intervals were computed according to a bootstrapping procedure based on 1,000 re-samplings of the data set. We did not differentiate levels of significance; only single asterisks are used regardless of *P* value. Statistical procedures were used as implemented in SciPy 0.15. All experiments and data analysis were performed without blinding to conditions or genotypes.

A **Supplementary Methods Checklist** is available.

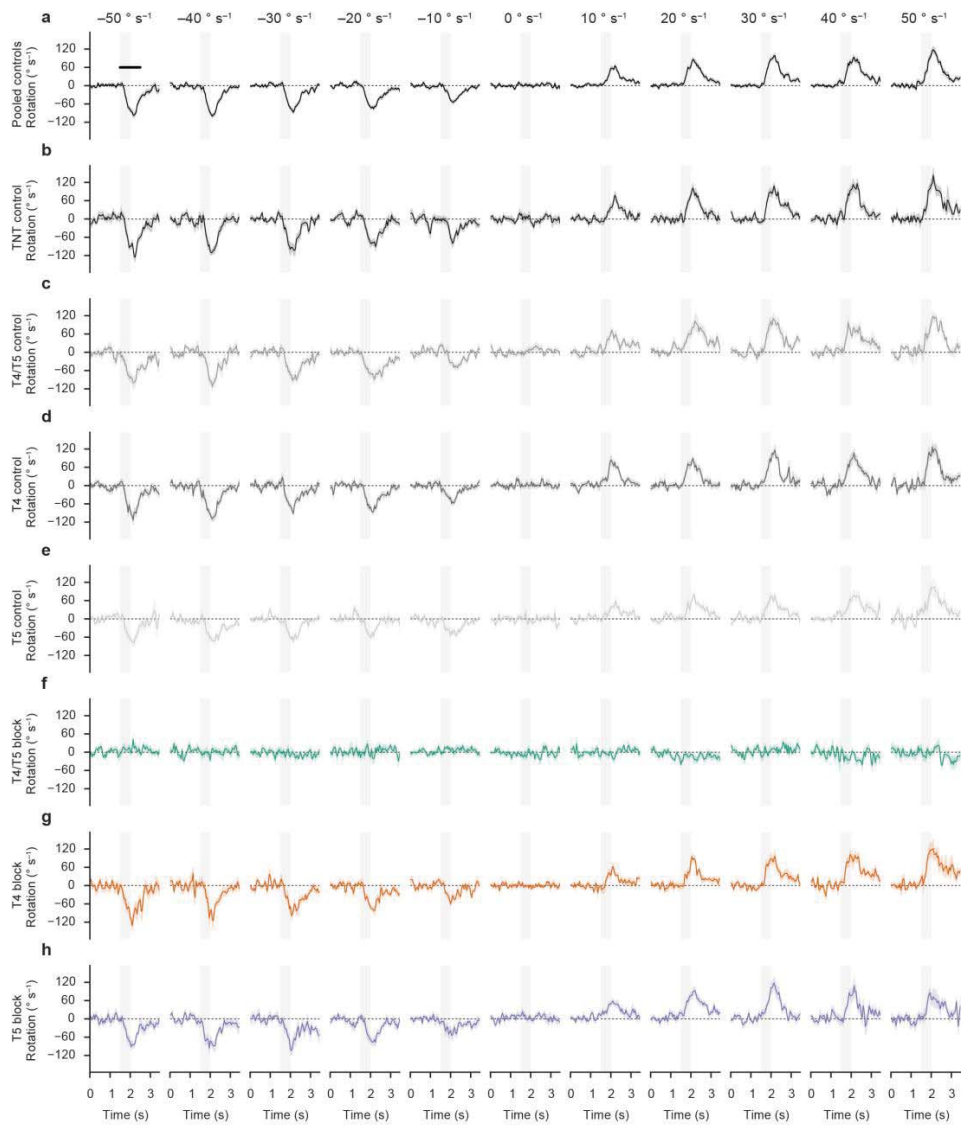
51. Yu, J.Y., Kanai, M.I., Demir, E., Jefferis, G.S.X.E. & Dickson, B.J. Cellular organization of the neural circuit that drives *Drosophila* courtship behavior. *Curr. Biol.* **20**, 1602–1614 (2010).



Supplementary Figure 1

**Auxiliary data for Gal4 lines used throughout the study.**

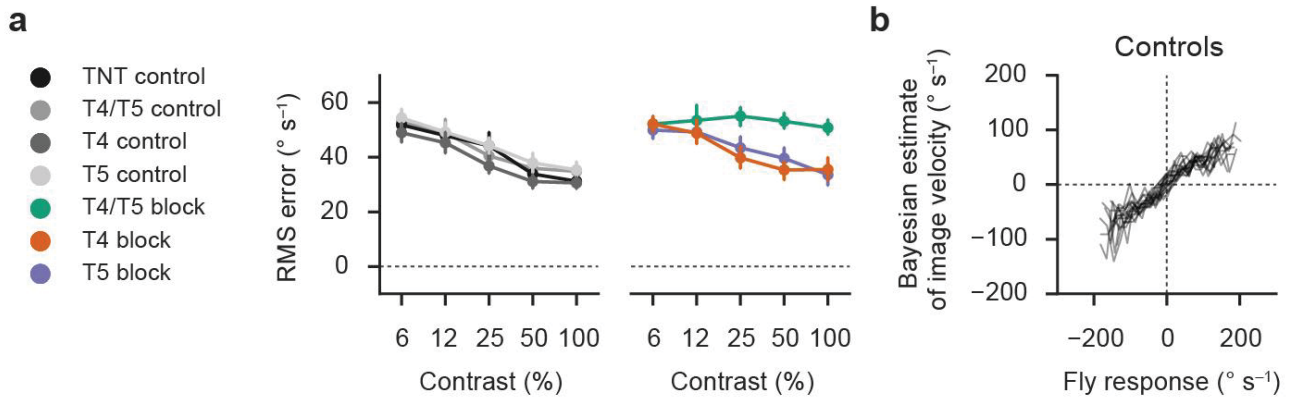
**(a-d)** UAS-mCD8GFP or UAS-GCaMP6f were driven by Gal4 driver lines used throughout the text and visualized using confocal images of the optic lobe. **(a)** GFP expression of splitGal4 line labeling T4 and T5. **(b)** GFP expression of Gal4 line labeling T4. **(c)** GFP expression of Gal4 line labeling T5. **(d)** GCaMP6f expression of combined Gal4 line labeling T4 and T5. See Online Methods for Gal4 line names and details of the immunohistochemistry procedures. **(e-h)** Locomotor integrity for each behavioral experiment was quantified as the mean forward velocity across conditions, with values close to control level indicating a general ability to respond to visual stimuli. **(e)** Walking speeds for closed-loop experiments (Fig. 1). **(f)** Walking speeds for open-loop experiments (Fig. 2). **(g)** Walking speeds for opposing edge experiments (Fig. 4). **(h)** Walking speeds for glider experiments (Fig. 8). Dots represent individual flies. Black bars mark the group mean for each genotype.



Supplementary Figure 2

**Walking traces for open-loop velocity estimation experiment.**

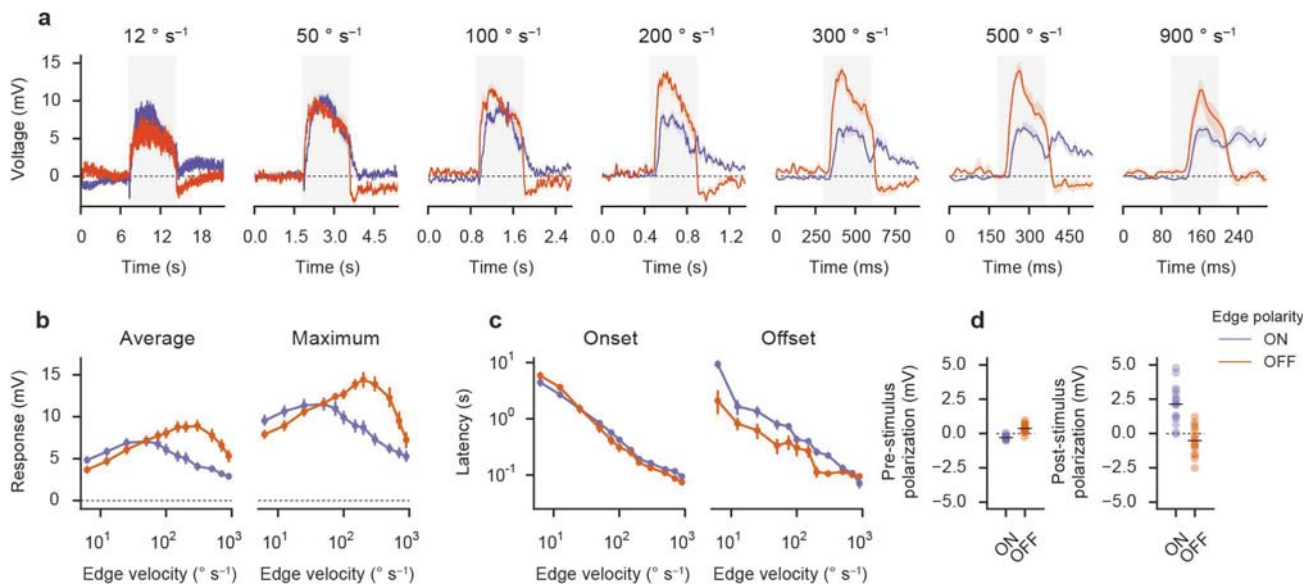
Binned response traces for all genotypes used throughout the stochastic open loop velocity estimation experiment (Fig. 2). In order to generate velocity-specific traces, stimulus velocities were sorted into bins spanning  $5^{\circ} \text{ s}^{-1}$  centered about the value indicated above each column. The corresponding traces were then averaged for each fly. Shaded areas indicate the bootstrapped 68% confidence interval across flies ( $N$  as in main figure; Fig. 2). Nota bene, traces were not low-pass filtered and the sampling base for each fly decreases with distance from zero velocity due to the stimulus distribution. The black line in the top leftmost panel indicates the period over which we averaged in order to generate responses for main experiment (Fig. 2). See Online Methods for details. (a) Responses for pooled controls as in main experiment (Fig. 2b). (b-h) Responses for individual genotypes.



Supplementary Figure 3

**Bayesian analysis of open-loop behavioral data.**

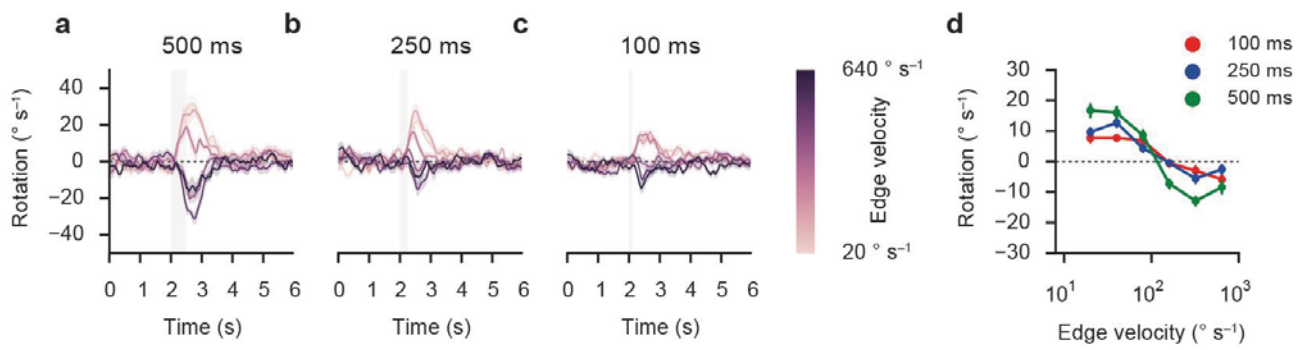
Using open-loop behavioral data (Fig. 2), we generated Bayesian decoders according to the procedure outlined in the Online Methods. For details about quantification and subject numbers, refer to main experiment (Fig. 2). (a) Mapping error across image contrast values, quantified as the root-mean-square error after application to the test data set. With higher contrasts, the quality of the estimate improves; this resembles results based on linear correlation. For T4/T5 block flies, the error stays flat. T4 or T5 block cannot be distinguished from wild-type behavior. (b) Visualization of resulting mapping functions, transforming fly responses into Bayesian estimates of input image velocity. Each line corresponds to a single fly. No significance tests were performed.



Supplementary Figure 4

**Physiological edge velocity tuning for fixed starting luminance.**

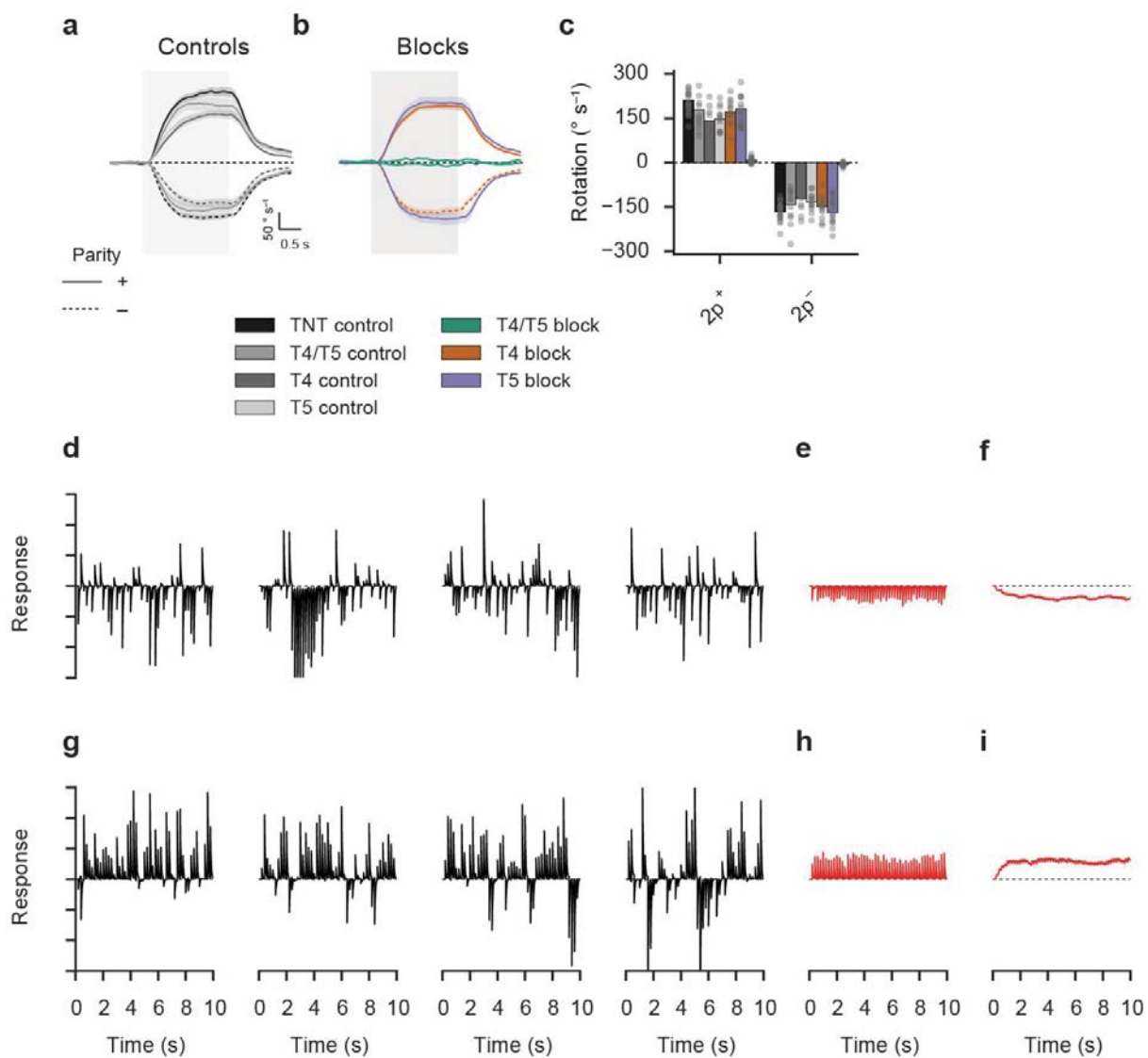
Lobula plate tangential cell responses to ON and OFF edges for equalized initial mean luminance ( $N=16$  by pooling 12 vertical system/4 horizontal system cells). See legend of main experiment (Fig. 3) as well as Online Methods for details. (a) Response traces for edges moving at various velocities. Note that the timescale depends on edge velocity. (b) Quantification of velocity tuning. (c) Quantification of response dynamics (with latency being defined as the time to maximal response during stimulation for onset or time to minimal response after stimulation for offset). (d) Quantification of polarization before and after stimulus presentation. No significance tests were performed.



Supplementary Figure 5

**Opposing edge responses for varying stimulus durations.**

Presentation and quantification are analogous to main experiment (Fig. 4; see Online Methods and associated legend for details). Depicted flies were T4/T5 control flies. (a-c) Turning responses for edge pulses of 500 ms ( $N=12$ ), 250 ms ( $N=12$ ), and 100 ms ( $N=14$ ) duration, respectively. (d) Quantification of turning responses.



Supplementary Figure 6

**Extended data for higher-order motion experiments and simulations.**

**(a-c)** T4 block flies and T5 block flies show 2-point glider responses at control level. **(a)** Control responses for 2-point gliders of positive or negative parity. **(b)** Block fly responses. **(c)** Summary of average turning tendency. Shaded area indicates stimulation period (see Online Methods and legend of main experiment for details; **Fig. 8**). **(d-i)** Time- and instantiation-resolved output of the asymmetric detector for converging 3-point gliders. Black traces are arbitrarily scaled detector responses for five random starting conditions of the pattern. **(d)** Single traces for positive parity. **(e)** Average time-resolved output for positive parity across 100 instantiations of the stimulus. **(f)** Low-pass filtered trace from **e** (first order with time constant of 500 ms followed by multiplicative scaling with a factor of four, approximating the behavioral response). **(g)** Single traces for negative parity. **(h)** Average time-resolved output for negative parity across 100 instantiations of the stimulus. **(i)** Low-pass filtered and scaled trace from **h** (procedure as in **f**).

**Supplementary Table 1**

<b>Alias</b>	<b>Genotype</b>	<b>Experiments</b>
<b>T4/T5 block</b>	$w^+/w^-$ ; UAS-TNT-E/Gal4-R59E08-AD; +/Gal4-R42F06	Figs. 1, 2, 4, 8, S1, S2, S3, S6
<b>T4/T5 imaging</b>	$w^-$ ; UAS-GCaMP6f; Gal4-VT25965/Gal4-VT37588	Fig. 3, S1
<b>T4 block</b>	$w^+/w^-$ ; UAS-TNT-E/+; +/Gal4-VT37588	Figs. 2, 4, 8, S1, S2, S3, S6
<b>T5 block</b>	$w^+/w^-$ ; UAS-TNT-E/+; +/Gal4-R42H07	Figs. 2, 4, 8, S1, S2, S3, S6
<b>TNT control</b>	$w^+/w^-$ ; UAS-TNT-E/+; +/+	Figs. 1, 2, 4, 8, S1, S2, S3, S6
<b>T4/T5 control</b>	$w^+/w^-$ ; +/Gal4-R59E08-AD; +/Gal4-R42F06	Figs. 1, 2, 4, 8, S1, S2, S3, S5, S6
<b>T4 control</b>	$w^+/w^-$ ; +/+; +/Gal4-VT37588	Figs. 2, 4, 8, S1, S2, S3, S6
<b>T5 control</b>	$w^+/w^-$ ; +/+; +/Gal4-R42H07	Figs. 2, 4, 8, S1, S2, S3, S6
<b>Colony S</b>	$w^+$ ; +/+; +/+	Figs. 3, 7, S4

Supplementary Table 2

12.5% contrast			25% contrast		
Genotype		T4/T5 block (n=13)	Genotype		T4/T5 block (n=13)
UAS control	n	19	UAS control	n	19
	t	9.27		t	12.2
	p	2.83e-10		p	3.89e-13
Gal4 control	n	12	Gal4 control	n	12
	t	11.2		t	16.4
	p	1.35e-9		p	3.75e-14

50% contrast			100% contrast		
Genotype		T4/T5 block (n=13)	Genotype		T4/T5 block (n=13)
UAS control	n	19	UAS control	n	19
	t	14.4		t	12.9
	p	4.55e-13		p	3.56e-12
Gal4 control	n	12	Gal4 control	n	12
	t	13.7		t	13.9
	p	1.47e-12		p	3.36e-12

**Extended statistics for Fig. 1.** For each contrast condition, we determined significance by comparing the block group to both control groups (UAS control and Gal4 control) using a two-tailed Student's *t* test. Blocks were declared significantly different if and only if both control groups were significantly different at a level of 0.05. For multiple comparisons, Bonferroni correction was applied. Red fields indicate significant differences after Bonferroni correction. The number indicated by *n* is the number of individual flies.

**Supplementary Table 3**

		Correlation coefficient (Fig. 2d)			Gain (Fig. 2e)					
		Genotype	T4/T5 block (n=11)	T4 block (n=12)	T5 block (n=12)	Genotype	T4/T5 block (n=11)	T4 block (n=12)	T5 block (n=12)	
c = 6.25%	UAS control	n	12	12	12	UAS control	n	12	12	
		t	-3.98	0.673	-0.862		t	-4.13	0.175	-1.34
		p	7.06e-4	0.508	0.398		p	5.41e-4	0.863	0.193
	Gal4 control	n	12	13	12	Gal4 control	n	12	13	12
		t	-6.20	-1.95	-0.923		t	-5.99	-1.81	-0.987
		p	3.89e-6	0.0631	0.368		p	1.15e-5	0.0853	0.336
c = 12.5%	UAS control	n	12	12	12	UAS control	n	12	12	12
		t	-9.15	0.968	-1.49		t	-8.66	0.0732	-1.58
		p	4.05e-8	0.344	0.150		p	5.01e-7	0.942	0.129
	Gal4 control	n	12	13	12	Gal4 control	n	12	13	12
		t	-14.7	-2.38	-1.57		t	-10.5	-1.55	-0.614
		p	2.86e-12	0.0277	0.130		p	9.04e-8	0.136	0.546
c = 25%	UAS control	n	12	12	12	UAS control	n	12	12	12
		t	-13.2	0.108	-0.545		t	-11.3	-0.161	-0.828
		p	2.50e-11	0.915	0.591		p	4.18e-8	0.874	0.417
	Gal4 control	n	12	13	12	Gal4 control	n	12	13	12
		t	-19.1	-2.53	0.0875		t	-14.4	-1.82	0.969
		p	7.56e-14	0.0198	0.931		p	2.00e-9	0.0810	0.344
c = 50%	UAS control	n	12	12	12	UAS control	n	12	12	12
		t	-31.5	-0.499	-2.02		t	-19.3	-1.38	-2.35
		p	1.42e-17	0.624	0.0608		p	1.53e-10	0.185	0.0300
	Gal4 control	n	12	13	12	Gal4 control	n	12	13	12
		t	-28.2	-1.49	-0.832		t	-17.3	-0.927	0.328
		p	4.00e-18	0.156	0.415		p	7.31e-10	0.364	0.747
c = 100%	UAS control	n	12	12	12	UAS control	n	12	12	12
		t	-24.0	-1.89	-2.25		t	-16.0	-1.68	-2.00
		p	4.04e-13	0.0803	0.0362		p	1.42e-9	0.110	0.0596
	Gal4 control	n	12	13	12	Gal4 control	n	12	13	12
		t	-22.3	-2.17	-0.458		t	-19.2	-1.23	0.404
		p	6.25e-14	0.0495	0.652		p	4.77e-11	0.235	0.692

**Extended statistics for Fig. 2.** Test details were as in Supplementary Table 2. c denotes contrast. Red fields indicate significant differences after Bonferroni correction. The number indicated by n is the number of individual flies.

**Supplementary Table 4**

Feature		Mean (n=70)	Maximum (n=70)	Onset latency (n=70)	Offset latency (n=70)	Pre-stimulus polarization (n=70)	Post-stimulus polarization (n=70)
ON vs. OFF	t	-7.30	-5.50	5.18	5.63	-17.2	11.1
	p	3.76e-10	6.13e-7	2.13e-6	3.63e-7	1.12e-26	6.10e-17

**Extended statistics for Fig. 3.** We compared response features between ON and OFF edge presentation. Responses were always averaged across velocities and then tested using two-tailed Student's *t* tests at a significance level of 0.05. Red fields indicate significant differences. The number indicated by *n* is the number of individual cells pooled from vertical and horizontal system cells.

Supplementary Table 5

		Difference from zero				Difference from control			
		TNT control (n=12)	T4/T5 control (n=13)	T4 control (n=12)	T5 control (n=13)	T4/T5 block (n=12)		T4 block (n=15)	T5 block (n=14)
versus 0		t	6.36	6.64	5.57	4.90	n	12	12
		p	5.34e-5	2.39e-5	1.67e-4	3.65e-4	t	-2.66	-14.9
$v = 20^{\circ}/s$									
$v = 40^{\circ}/s$									
$v = 80^{\circ}/s$									
$v = 160^{\circ}/s$									
$v = 320^{\circ}/s$									
$v = 640^{\circ}/s$									

**Extended statistics for Fig. 4.** For each velocity condition, we determined significance by comparing control groups to zero or block groups to both corresponding control groups (UAS control and Gal4 control) using a two-tailed Student's t test. Blocks were declared significantly different if and only if both control groups were significantly different at a significance level of 0.05. v denotes velocity. For multiple comparisons, Bonferroni correction was applied. Red fields indicate significant differences after Bonferroni correction. The number indicated by n is the number of individual flies.

**Supplementary Table 6**

Stimulus		Random (n=16)	3p/conv/+( n=16)	3p/conv/-( n=16)	3p/div/+( n=16)	3p/div/-( n=16)
versus 0	t	-0.426	-2.33	18.4	-5.44	5.73
	p	0.676	0.0341	1.02e-11	6.89e-5	3.98e-5

**Extended statistics for Fig. 7.** We compared glider voltage responses to zero. Responses were tested using two-tailed Student's *t* tests at a significance level of 0.05. Red fields indicate significant differences. The number indicated by *n* is the number of individual cells pooled across cells from the horizontal and vertical systems.

**Supplementary Table 7**

		Positive parity			Negative parity					
		Genotype	T4/T5 block (n=14)	T4 block (n=13)	T5 block (n=17)	Genotype	T4/T5 block (n=14)	T4 block (n=13)	T5 block (n=17)	
2-point	UAS control	n	18	18	18	Gal4 control	n	18	18	18
		t	-16.2	-2.41	-1.33		t	21.3	1.29	-0.169
		p	2.17e-12	0.0228	0.194		p	1.43e-14	0.211	0.867
	Gal4 control	n	12	12	12		n	12	12	12
		t	-7.93	1.82	1.54		t	8.08	-1.79	-1.91
		p	5.91e-6	0.0814	0.136		p	5.28e-6	0.0869	0.0679
3-point/conv.	UAS control	n	18	18	18	Gal4 control	n	18	18	18
		t	7.82	16.7	-5.85		t	-6.44	-14.0	6.83
		p	2.73e-8	4.72e-16	1.85e-6		p	3.12e-6	1.30e-13	2.01e-7
	Gal4 control	n	12	12	12		n	12	12	12
		t	8.57	19.3	-5.49		t	-12.4	-23.7	7.00
		p	2.56e-7	2.39e-15	1.11e-5		p	4.45e-10	1.88e-15	1.00e-6
3-point/div.	UAS control	n	18	18	18	Gal4 control	n	18	18	18
		t	8.58	-3.34	10.8		t	-9.25	4.52	-8.51
		p	2.83e-8	2.32e-3	8.68e-12		p	8.57e-9	1.01e-4	1.36e-9
	Gal4 control	n	12	12	12		n	12	12	12
		t	5.36	-0.354	11.4		t	-6.82	0.991	-9.76
		p	1.85e-4	0.727	7.10e-10		p	2.12e-5	0.335	3.33e-10

**Extended statistics for Fig. 8.** Test details were as in Supplementary Table 2. Red fields indicate significant differences after Bonferroni correction. The number indicated by n is the number of individual flies.

## Manuscript V

### Object Tracking in Motion-Blind Flies

Armin Bahl, **Georg Ammer**, Tabea Schilling, and Alexander Borst

#### Author Contributions

A. Bahl set up the locomotion recorder and the stimulus display, and wrote the software for reading the behavioral output and displaying the stimulus. A. Bahl and T.S. performed all of the behavioral experiments and evaluated the data. **G.A.** performed the electrophysiological recordings and analyzed the data. A. Bahl and A. Borst designed the study. A. Borst carried out the modeling work. A. Borst and A. Bahl wrote the manuscript with the help of the other authors.

**Nature Neuroscience** 16, 730-738. doi: 10.1038/nn.3386.



# Object tracking in motion-blind flies

Armin Bahl, Georg Ammer, Tabea Schilling & Alexander Borst

Different visual features of an object, such as its position and direction of motion, are important elements for animal orientation, but the neural circuits extracting them are generally not well understood. We analyzed this problem in *Drosophila*, focusing on two well-studied behaviors known as optomotor response and fixation response. In the neural circuit controlling the optomotor response, columnar T4 and T5 cells are thought to be crucial. We found that blocking T4 and T5 cells resulted in a complete loss of the optomotor response. Nevertheless, these flies were still able to fixate a black bar, although at a reduced performance level. Further analysis revealed that flies in which T4 and T5 cells were blocked possess an intact position circuit that is implemented in parallel to the motion circuit; the optomotor response is exclusively controlled by the motion circuit, whereas the fixation response is supported by both the position and the motion circuit.

Optomotor and fixation responses of flies have been studied extensively. Experiments on tethered *Drosophila* walking or flying inside a rotating drum revealed a strong and persistent optomotor response along the direction of the rotating drum<sup>1–3</sup> (open loop). The effect of large-field stimuli on visual course control can also be seen in free flight, where the structure of the flight path of *Drosophila* depends on the visual pattern of the surrounding environment<sup>4</sup>. When the pattern is rotating, the fly's behavior exhibits distinct, circular flight paths around the center of the arena<sup>5</sup>. Fixation behavior was first observed in tethered flying house flies in which the fly's torque was fed back into a servo motor controlling the position of a black bar<sup>6,7</sup> (closed loop). Under these conditions, flies keep the bar in front of them most of the time. Moreover, it was shown that bar fixation interacts with the expansion avoidance reaction of *Drosophila* when presented with translatory full-field optic flow<sup>8</sup>. Fixation behavior has also been studied in freely walking and flying *Drosophila*<sup>9–12</sup>. On the basis of their different dynamics and spatial sensitivity, the optomotor and fixation responses were proposed to represent the output of different visual processing pathways<sup>13</sup>. Similar conclusions were drawn from experiments in which the tangential cells of the lobula plate were either genetically or surgically removed<sup>14–17</sup>, or in mutants with reduced optic lobes<sup>18</sup>; in general, flies seem to be impaired more strongly in their response to large-field rotating patterns than in their reaction to single, moving bars. However, none of the techniques used provided a sufficiently high resolution to make any definitive statements about the involvement of individual cell types of the fly optic lobe in one or the other pathway.

To dissect the neural circuits underlying the optomotor and fixation responses, we built on recent progress in our understanding of the visual processing stream<sup>19</sup> leading from the photoreceptors R1–6 via lamina and medulla to directionally selective motion responses in the lobula plate tangential cells (LPTCs; Fig. 1a). Recording from LPTCs via whole-cell patch<sup>20,21</sup> combined with selective blockade of individual columnar cells revealed that lamina cells L1 and L2 provide the main input to the motion detection circuit, functionally

segregating into an ON and an OFF pathway, respectively<sup>22,23</sup>. The L1 and L2 pathways, which have been described anatomically<sup>24,25</sup>, converge again on the dendrites of the tangential cells in the lobula plate via T4 and T5 cells; blocking the synaptic output from T4 and T5 cells completely abolishes the motion response in tangential cells, but leaves some residual response to full-field flicker<sup>26</sup>. To test the behavioral performance of these flies, we used a procedure in which a tethered fly walks on a small sphere supported by an air stream<sup>2,27</sup>. A computer reads the movement of the sphere, controls the visual stimulus presented to the fly and adjusts the ambient temperature. Moreover, we used the *Gal4-UAS* system<sup>28</sup> to genetically express a temperature-sensitive allele of *shibire*<sup>29</sup> in a small subset of neurons in the fly brain. This permitted a selective shut down of the desired part of the neuronal circuit during the experiment by switching from the permissive temperature for *shibire<sup>ts</sup>* (25 °C) to its restrictive one (34 °C).

## RESULTS

### Optomotor and fixation response

We tested the optomotor and fixation response of flies in which *shibire<sup>ts</sup>* was expressed in T4 and T5 cells (T4/T5 block flies). As the behavior of flies turned out to be highly dependent on temperature (Supplementary Fig. 1), all of our control experiments were carried out with flies of a different genotype using the same temperature protocol. For controls, we used flies with two different genotypes: flies that carried the *shibire<sup>ts</sup>* effector allele, but no *Gal4* driver gene (*shibire<sup>ts</sup>* control), and flies that carried the *Gal4* driver gene, but no *shibire<sup>ts</sup>* effector gene (T4/T5 control). We examined the temperature dependency of the block: T4/T5 block flies behaved similar to control flies at 25 °C, as well as when the temperature was slowly elevated to 34 °C. However, clear differences emerged approximately 5 min after reaching 34 °C (Supplementary Fig. 1). To exclude any motor deficits in T4/T5 block flies, we analyzed their general walking and turning activity, which were not different from those of control flies (Supplementary Fig. 2).

Max Planck Institute of Neurobiology, Martinsried, Germany. Correspondence should be addressed to A. Bahl (bahl@neuro.mpg.de) or A. Borst (borst@neuro.mpg.de).

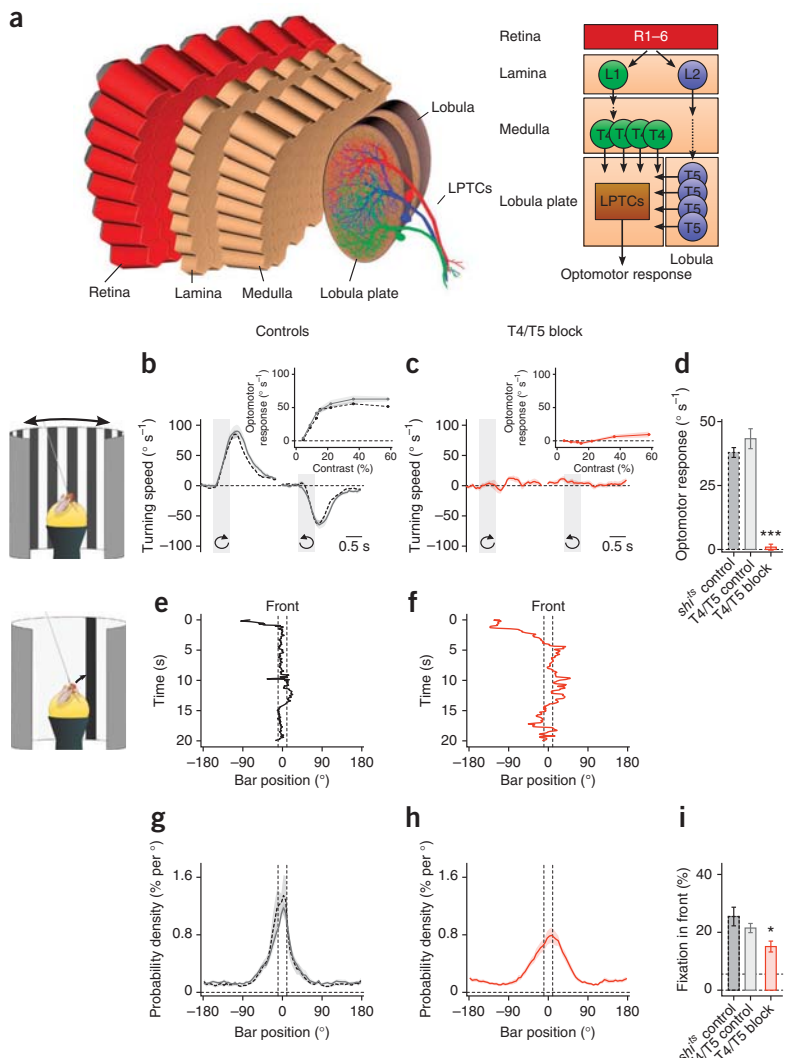
Received 6 February; accepted 28 March; published online 28 April 2013; doi:10.1038/nn.3386

**Figure 1** Optomotor response and fixation response of control and T4/T5 block flies. **(a)** Schematic of the fly's optic lobe. In each lamina column, photoreceptors R1–6 synapse onto lamina cells L1 and L2, forming parallel pathways for motion detection. The output signals of both pathways converge via T4 and T5 cells on the dendrites of LPTCs. **(b,c)** Turning speed of control (*sh<sup>ts</sup>* control (dashed black line) and T4/T5 control (solid gray line); **b**) and T4/T5 block (solid red line; **c**) flies in response to clockwise and counterclockwise rotation of a grating pattern (contrast = 22%, gray shaded areas; 20 trials per fly,  $n = 10$  flies per group). Inset, optomotor response as function of grating contrast (clockwise minus counterclockwise rotation response divided by 2; averaged in 1 s after stimulus onset). **(d)** Average optomotor response (average over contrasts). \*\*\* $P < 0.001$ , two-sided  $t$  test compared with both control groups. The response of the T4/T5 block group was not significantly different from zero ( $P = 0.47$ , two-sided  $t$  test). **(e,f)** Bar position over time during closed-loop fixation (single trial of one *sh<sup>ts</sup>* control fly **e**), single trial for one T4/T5 block fly **f**). Vertical dashed lines indicate the frontal area ( $\pm 10^\circ$ ). **(g,h)** Average probability density as function of bar position for control (40 trials per fly,  $n = 10$  flies per group; **g**) and T4/T5 block (40 trials per fly,  $n = 12$  flies; **h**) flies. **(i)** Integration of the probability density curves between  $\pm 10^\circ$  gives the percentage of time the bar is held in the frontal visual field (fixation in front). Upper horizontal dashed line represents the chance level (5.6%, no fixation). \* $P < 0.05$ , two-sided  $t$  test compared with both control groups. The value of the T4/T5 block group was significantly different from chance ( $P < 0.001$ , two-sided  $t$  test). All data represent mean  $\pm$  s.e.m.

We first confronted the flies with a large-field grating moving clockwise and counterclockwise (Fig. 1b–d). Both types of control flies exhibited a strong and reliable optomotor response over a wide range of pattern contrasts (Fig. 1b,d). Instead, T4/T5 block flies no longer followed the motion of the panorama, no matter how high the pattern contrast (Fig. 1c,d). We next performed closed-loop fixation experiments and coupled the flies' turning tendency to the position of a single black bar such that whenever the fly turned into one direction, the bar moved into the other (Fig. 1e–i). Control flies robustly moved the bar to the front and kept it there (Fig. 1e,g,i). When we tested the flies in which the output from T4 and T5 cells was blocked, we were surprised that they were still clearly able to fixate the bar, although with a somewhat broader position distribution than control flies (Fig. 1f,h,i). Taken together, these results indicate that T4 and T5 cells are a necessary part of the neural circuit controlling the optomotor response to large-field motion, but are not needed for fixation behavior.

#### Dissection of motion and position system

Does that mean that fixation behavior relies on a separate set of motion-sensitive neurons tuned specifically to small moving objects, or does fixation behavior rely on a purely position-dependent system that is insensitive to motion? To tease apart the response to the



direction and the response to the position of a moving bar, we used a classical approach<sup>30</sup> and moved a single bar in open loop around the fly, first in a clockwise and then in a counterclockwise direction, and measured both responses ( $R_{\text{cw}}$  and  $R_{\text{ccw}}$  respectively) as a function of bar position ( $\Psi$ )<sup>31</sup>.

Assuming that the turning response  $R$  of the fly to the rotating bar reflects a superposition of a position system  $P$  and a motion system  $M$  (with  $v = d\Psi/dt$  denoting the angular velocity of the bar), we can write

$$R = P(\Psi, v) + M(\Psi, v)$$

For the two directions of bar rotations, we obtain

$$R_{\text{cw}} = P(\Psi, v) + M(\Psi, v)$$

$$R_{\text{ccw}} = P(\Psi, -v) + M(\Psi, -v)$$

To simplify these equations, two classical assumptions can be made<sup>30</sup>. First, the position system is velocity independent ( $P(\Psi, v) = P(\Psi)$ ). Second, the motion system is linear in  $v$  ( $M(\Psi, v) = M(\Psi) \cdot v$ ). Following

**Figure 2** Open-loop analysis of the fixation response. (a,b) Responses of control (a) and T4/T5 block (b) flies to a single black bar moving clockwise (thicker lines) and counterclockwise around the fly. Responses are plotted as a function of the azimuth position of the bar; that is, during counterclockwise rotation, time progresses from right to left. (c,d) Summation of the clockwise and counterclockwise responses divided by 2 revealed the position-dependent response component,  $P(\Psi)$ , of control (c) and T4/T5 block (d) flies. (e) The position response (the integral of the curve  $P(0^\circ < \Psi < 180^\circ)$  minus the integral of  $P(-180^\circ < \Psi < 0^\circ)$  divided by 2). The response of the T4/T5 block group was significantly greater than zero ( $P < 0.001$ , two-sided  $t$  test). (f,g) Subtraction of the clockwise and counterclockwise responses divided by 2 yielded the motion-dependent response component,  $M(\Psi) \cdot v$ , of control (f) and T4/T5 block (g) flies (a positive value indicates a tendency to turn with the stimulus). (h) The motion response (the integral of the curve  $M(0^\circ < \Psi < 180^\circ) \cdot v$  plus the integral of  $M(-180^\circ < \Psi < 0^\circ) \cdot v$  divided by 2). The response of the T4/T5 block group was not significantly different than zero ( $P = 0.06$ , two-sided  $t$  test). All data represent mean  $\pm$  s.e.m.; 35 trials per fly,  $n = 10, 11$  and 14 flies per group (shif<sup>ts</sup> control, dashed black lines; T4/T5 control, solid gray lines; T4/T5 block, solid red lines). \*\*\* $P < 0.001$ , two-sided  $t$  test compared with both control groups.

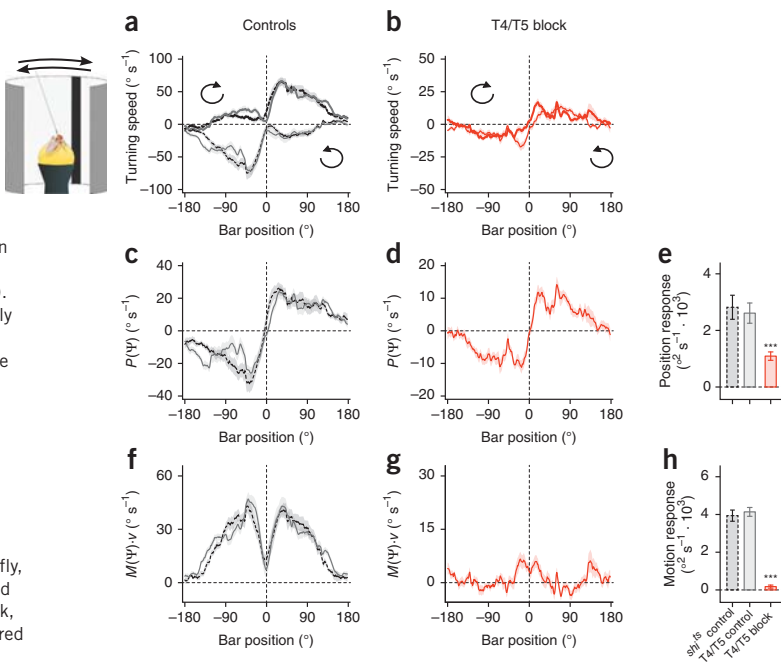
these assumptions, the position system as well as the motion system can be recovered

$$P(\Psi) = (R_{\text{cw}} + R_{\text{ccw}})/2$$

$$M(\Psi) \cdot v = (R_{\text{cw}} - R_{\text{ccw}})/2$$

We performed such experiments on control and T4/T5 block flies (Fig. 2). With a starting position behind the flies, control flies followed the direction of motion of the bar, turning clockwise (+) during clockwise motion and counterclockwise (−) during counterclockwise motion (Fig. 2a), which is slightly different from what has been measured in flying *Drosophila* under similar conditions<sup>8</sup>. According to the formal decomposition outlined above, we recovered a position-dependent response component,  $P(\Psi)$  (Fig. 2c,e), and a motion-dependent response component,  $M(\Psi)$  (Fig. 2f,h). The responses of T4/T5 block flies to such stimuli were markedly different from those of control flies; in general, T4/T5 block fly responses had smaller amplitudes and were almost identical for both directions of bar motion (Fig. 2b). Decomposing the reaction into the position- and motion-dependent components revealed that the response of these flies to the position of the bar,  $P(\Psi)$ , was still present, although reduced in amplitude (Fig. 2d,e). However, the response to the motion of the moving bar,  $M(\Psi) \cdot v$ , was completely abolished (Fig. 2g,h). We conclude that T4/T5 block flies are blind to the motion of a single bar, but can still detect its position. Thus, the ability of motion-blind flies to fixate a bar in closed loop (Fig. 1f,h,i) is a result of the remaining position response.

What is the visual cue used by the position system that allows the detection of bar position: is it mere stationary contrast, its temporal change or its local motion? To address these questions, we presented control flies with an appearing black bar (10° width) at +90° azimuth which stayed there for 4 s before disappearing again (Fig. 3). The time during which the bar appeared and disappeared amounted to 0.5 s approximating the local luminance change when a black bar (width = 10° and  $v = 20^\circ \text{ s}^{-1}$ ) moves into a 10°-wide window and, after 4 s, moves



out again. Control flies exhibited a strong, but transient, response toward the position at which the bar was appearing as well as where it was disappearing, but, during the stationary phase of the bar, no response was detectable (Fig. 3a). We then determined the response values as function of bar position. In control flies, the shape of the resulting response functions (Fig. 3c,i) looked similar to  $P(\Psi)$  as obtained in the previous experiment (Fig. 2c,d). We next repeated the experiments on T4/T5 block flies. Like control flies, T4/T5 block flies responded transiently to both the appearance as well as to the disappearance of the bar, but not when the bar was stationary (Fig. 3b). Moreover, the shape of the position-dependent response functions was almost identical to the ones of control flies (Fig. 3d,g,j). We conclude that the position system is insensitive to a stationary image but uses the change of luminance over time as its input signal<sup>32</sup>. Furthermore, the position system is not affected by blocking the output of T4 and T5 cells.

#### Turning responses to local motion and luminance changes

We observed a clear reduction of the performance of T4/T5 block flies compared to controls when we characterized their position response under closed-loop fixation conditions (Fig. 1e-i) and when we used a rotating bar (Fig. 2). However when we used local luminance changes, we found no difference between T4/T5 block and control flies (Fig. 3). This discrepancy suggests that the detection of motion somehow enhances the fly's response toward the position of the bar. We considered two possible mechanisms. First, the motion and position system may not be fully separable on the neuronal level. In this case, local motion might directly modify the position system to enhance the position response. Second, the motion system may have a stronger response to front-to-back than back-to-front motion. In the behaving fly, this would lead to a stronger compensation of bar motion away from the front, thereby improving fixation<sup>33</sup>. In both cases, T4/T5 block flies would no longer be able to detect the motion of the bar and their position response would be reduced. Furthermore, both arguments indicate that our assumptions (Fig. 2), which were adopted from classical experiments<sup>30</sup>, might not be fully correct.

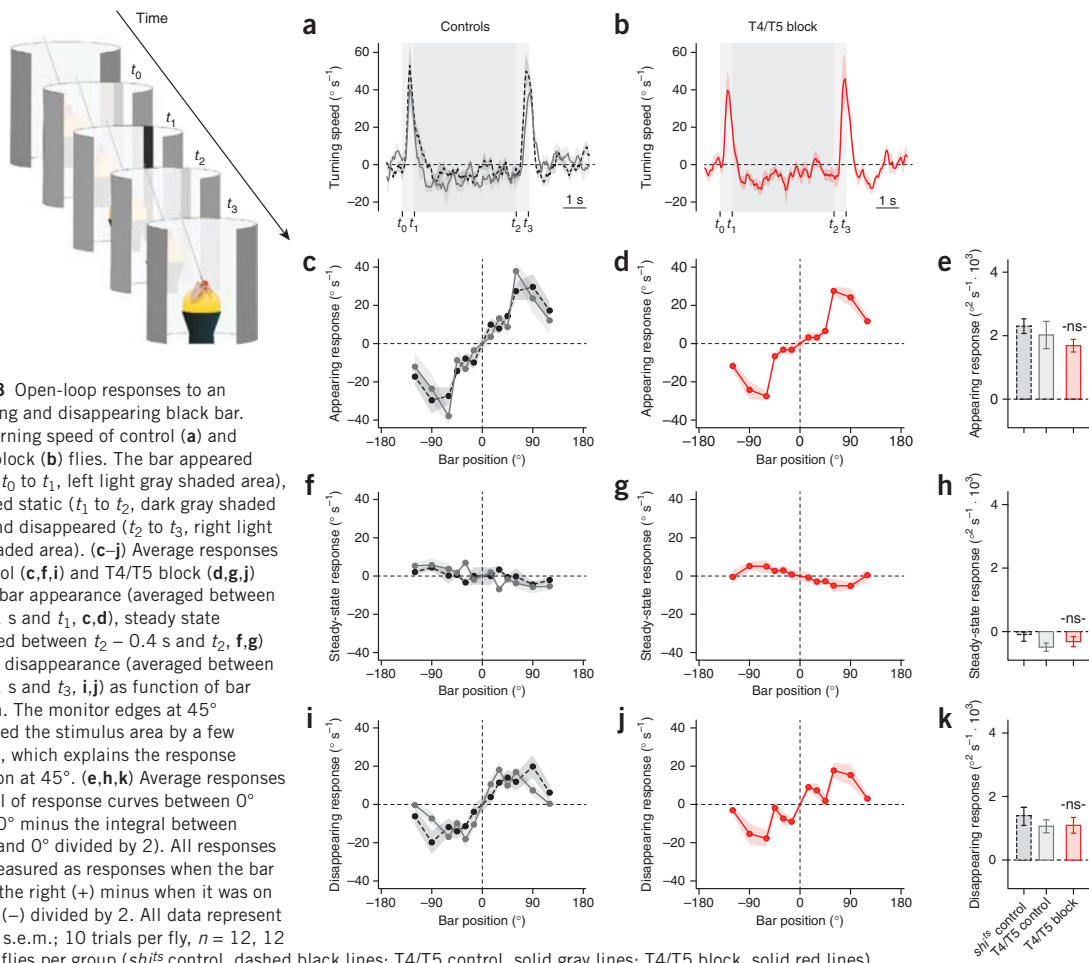


**Figure 3** Open-loop responses to an appearing and disappearing black bar. **(a,b)** Turning speed of control **(a)** and T4/T5 block **(b)** flies. The bar appeared at 90° ( $t_0$  to  $t_1$ , left light gray shaded area), remained static ( $t_1$  to  $t_2$ , dark gray shaded area) and disappeared ( $t_2$  to  $t_3$ , right light gray shaded area). **(c–j)** Average responses of control **(c,f,i)** and T4/T5 block **(d,g,j)** flies to bar appearance (averaged between  $t_0 + 0.1$  s and  $t_1$ , **c,d**), steady state (averaged between  $t_2 - 0.4$  s and  $t_2$ , **f,g**) and bar disappearance (averaged between  $t_2 + 0.1$  s and  $t_3$ , **i,j**) as function of bar position. The monitor edges at 45° decreased the stimulus area by a few degrees, which explains the response reduction at 45°. **(e,h,k)** Average responses (integral of response curves between 0° and 120° minus the integral between -120° and 0° divided by 2). All responses were measured as responses when the bar was on the right (+) minus when it was on the left (-) divided by 2. All data represent mean  $\pm$  s.e.m.; 10 trials per fly,  $n = 12, 12$  and 16 flies per group (*shifts* control, dashed black lines; T4/T5 control, solid gray lines; T4/T5 block, solid red lines). ns indicates not significant,  $P \geq 0.05$ , two-sided *t* test compared with both control groups. Responses of T4/T5 block flies at 45° were not significantly different to control responses ( $P \geq 0.05$ ; two-sided *t* test compared with both control groups). Responses of *shifts* control and T4/T5 block flies during steady state were not significantly different from zero, but the response of T4/T5 control flies was ( $P = 0.37, 0.11, 0.02$ , respectively; two-sided *t* test).

To test these ideas, we investigated the turning responses to local front-to-back motion, back-to-front motion and luminance changes in isolation (Fig. 4). We created a virtual environment consisting of a gray cylinder with a 10° window at two azimuthal positions (either  $\Psi = 30^\circ$  or  $\Psi = 60^\circ$ ). Outside, a 10° black bar rotates at  $40^\circ \text{ s}^{-1}$  around the cylinder. Whenever the bar passes the window, it briefly allows the fly's motion system to detect the direction of bar motion (either front to back or back to front), inducing a turning tendency ( $M_{\text{FTB}}$  and  $M_{\text{BTF}}$ ) in the same direction. Moreover, when the bar passes through the window, it produces local luminance changes such that luminance first decreases and then increases again. This change in luminance is detected by the fly's position system, leading to an additional turning tendency toward that position ( $P_{\text{FTB}}$  and  $P_{\text{BTF}}$ ). Thus, the turning response to local front-to-back and back-to-front motion can be described as the sum of both turning tendencies.

$$R_{\text{FTB}} = M_{\text{FTB}} + P_{\text{FTB}}$$

$$R_{\text{BTF}} = M_{\text{BTF}} + P_{\text{BTF}}$$

To tease apart the different response components, we need the response of the position system alone. We approximated the local

luminance change when the rotating bar passes the window with a non-moving stimulus. The whole window starts at background luminance, darkens and then brightens again. This stimulus should only activate the position system, resulting in a turning tendency toward the position of the local luminance change ( $R_L = P_L$ ).

When measuring the turning response of control flies to the three different stimulus conditions, all turning responses were found to be different. The response to the front-to-back stimulus ( $R_{\text{FTB}}$ ) was positive and large in amplitude (Fig. 4a,c), the response to the back-to-front stimulus ( $R_{\text{BTF}}$ ) was biphasic and weak (Fig. 4d,f), and the response to local luminance changes ( $R_L$ ) was positive and weak (Fig. 4g,i). In contrast, the responses of T4/T5 block flies to front-to-back motion, back-to-front motion and local luminance changes were all identical (Fig. 4b,e,h,j). We found no differences in the responses to local luminance changes of controls and T4/T5 block flies (Fig. 4i), which is consistent with our earlier observations (Fig. 3). Taken together, these results indicate that the position system only detects changes in local luminance and that local motion does not influence its response properties. Thus,

$$R_L = P_L = P_{\text{FTB}} = P_{\text{BTF}}$$

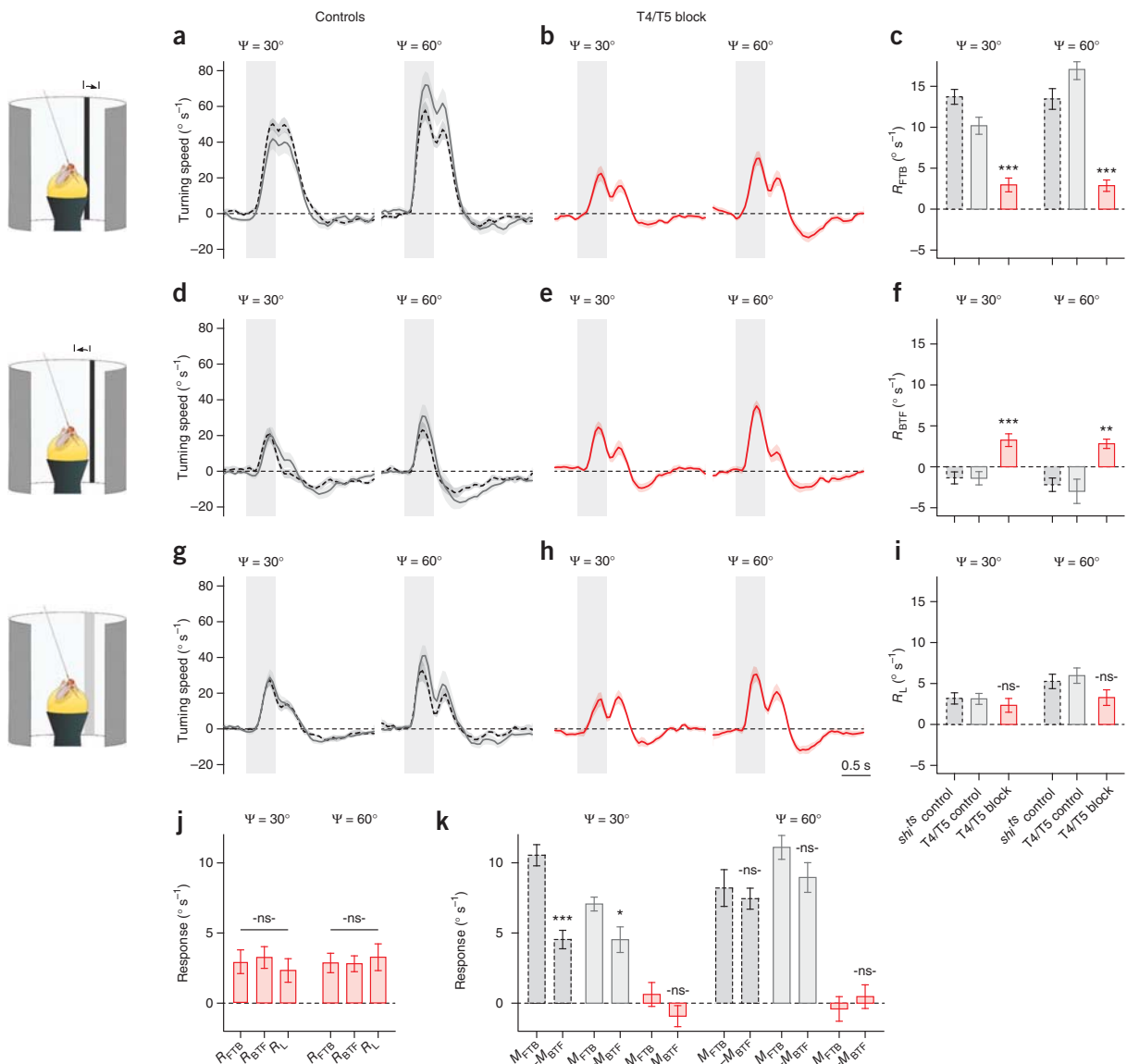


**Figure 4** Open-loop responses to local bar motion and to local luminance changes. **(a–i)** Turning responses of control **(a,d,g)** and T4/T5 block **(b,e,h)** flies to local front-to-back motion **(a,b)**, local back-to-front motion **(d,e)** and local luminance changes **(g,h)** at  $\Psi = 30^\circ$  and  $\Psi = 60^\circ$  (gray shaded areas). The corresponding average turning responses are shown in **c, f** and **i** ( $R_{FTB}$ ,  $R_{BTF}$  and  $R_L$ , respectively; averaged between  $t = 0.1$  s and  $t = 2.1$  s after stimulus onset). **(j)** Comparison of responses to the different stimuli of T4/T5 block flies. **(k)** Comparison of isolated motion responses ( $M_{FTB} = R_{FTB} - R_L$  and  $M_{BTF} = R_{BTF} - R_L$ ). Motion responses of T4/T5 block flies were not significantly different from zero ( $P \geq 0.05$ , two-sided  $t$  test). All responses were measured as the response with the bar at  $\Psi = +30^\circ$  or  $\Psi = +60^\circ$  minus the response with the bar at  $\Psi = -30^\circ$  or  $\Psi = -60^\circ$ , respectively, divided by 2. All data represent mean  $\pm$  s.e.m.; 60 trials per fly of  $n = 10$ , 12 and 11 flies (at  $\Psi = 30^\circ$ ) and of  $n = 10$ , 11 and 11 flies (at  $\Psi = 60^\circ$ ) per group (*sh<sup>1/2</sup>* control, dashed black lines; T4/T5 control, solid gray lines; T4/T5 block, solid red lines). ns indicates not significant ( $P \geq 0.05$ ),  $^*P < 0.05$ ,  $^{**}P < 0.01$  and  $^{***}P < 0.001$ ; two-sided  $t$ -test compared with both controls **(c,f,i)** or comparing  $M_{FTB}$  to  $-M_{BTF}$  within the groups **(k)**; one-way ANOVA in **j**.

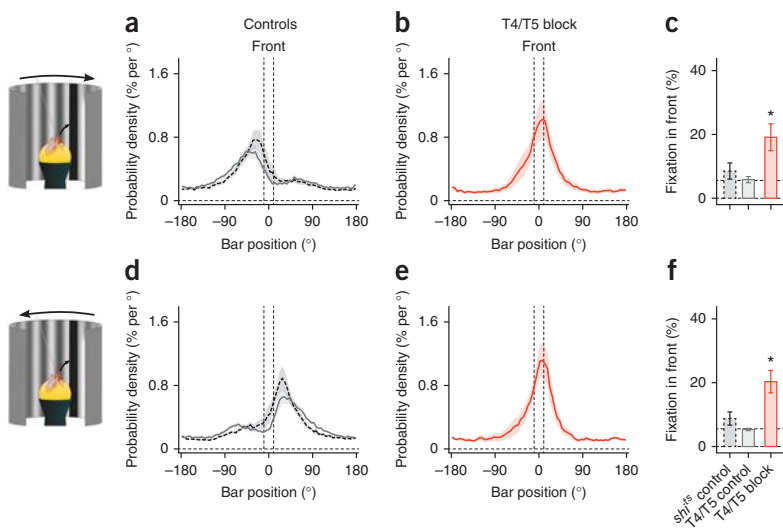
This finding allowed us to isolate the responses of the motion system to front-to-back and back-to-front stimulation.

$$M_{FTB} = R_{FTB} - R_L$$

$$M_{BTF} = R_{BTF} - R_L$$

Analyzing the data of control flies in this way revealed a strong asymmetry in the motion system for the frontal part of the visual field ( $\Psi = 30^\circ$ ), where its response to front-to-back was approximately twice as strong as that to back-to-front motion (Fig. 4k). In the lateral part ( $\Psi = 60^\circ$ ), we observed a similar tendency (Fig. 4k). This finding implies that  $M(\Psi, v) \neq -M(\Psi, -v)$  and suggests that it is

**Figure 5** Closed-loop fixation response during open-loop background motion. (a–f) Fixation responses of control (a,d) and T4/T5 block (b,e) flies during clockwise (a,b) and counterclockwise (d,e) rotation of the sine-grating. The ability to keep the bar in front is shown in c and f (same measure as in Fig. 1i). Upper horizontal dashed lines represent the chance level (5.6%, no fixation). All data represent mean  $\pm$  s.e.m.; 30 trials of  $n = 11$ , 9 and 9 flies per group ( $sh^{\text{hs}}$  control, dashed black lines; T4/T5 control, solid gray lines; T4/T5 block, solid red lines). \* $P < 0.05$ , two-sided  $t$  test compared with both controls.



necessary to omit the classical assumption of velocity linearity of the motion system<sup>30</sup>. Consequently, we revised the interpretation of  $P(\Psi)$  obtained in the previous experiment with the rotating bar (Fig. 2). Thus,  $P(\Psi)$  actually overestimates the response of the pure position system ( $P_L$ ) in control flies.

$$\begin{aligned} P(\Psi)^{\text{controls}} &= (R_{\text{cw}} + R_{\text{ccw}})/2 \\ &= (M(\Psi, \nu) + M(\Psi, -\nu) + 2 \cdot P_L)/2 \\ &> P_L \end{aligned}$$

On the other hand, for T4/T5 block flies, the motion responses were zero (Figs. 2h and 4k). Under these conditions,  $P(\Psi)$  corresponds to the response of the position system alone ( $P_L$ ).

$$\begin{aligned} P(\Psi)^{\text{T4/T5 block}} &= (R_{\text{cw}} + R_{\text{ccw}})/2 \\ &= (M(\Psi, \nu) + M(\Psi, -\nu) + 2 \cdot P_L)/2 \\ &= P_L \end{aligned}$$

Taken together, these results indicate that the visual pathways of the motion and position system are indeed separable at the neuronal level. However, fixation is shaped by an interaction of both systems at the level of behavior.

#### Object tracking with background motion

Do both control systems also superimpose when the fly encounters a more natural situation where it has to track an object while the whole background is in motion? To answer this question, we fed back the fly's turning tendency on the position of the black bar, as in the usual fixation procedure (closed loop), and displayed a large-field sine-grating rotating in one or the other direction without giving the fly control over it (open loop) (Fig. 5). If both responses superimpose at the level of the fly's turning tendency, the large field stimulus should create a permanent offset, leading to a shift of the position where the fly fixates the bar.

We tested whether the presence of the sine-grating alone would alter the fixation response. To our surprise, the fixation response clearly improved for both control and T4/T5 block flies when the background was a static sine-grating (Supplementary Fig. 3), although the grating had the same average luminance as the uniformly gray background used in previous fixation experiments (Fig. 1e–i). This indicates that the fixation response is modulated by the spatial properties of the background, yet the detailed mechanism of this effect remains unknown.

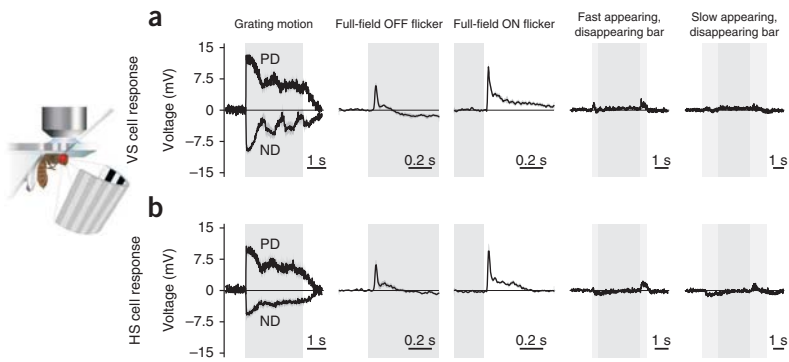
With the sine-grating background moving clockwise or counterclockwise, control flies were still able to fixate the bar, but the peak of the position histogram was shifted in the direction opposite to the direction of the moving large-field stimulus (Fig. 5a,d). The motion system produced a tendency to turn in the direction of the moving background, whereas the position system induced turning toward the position of the bar. When the bar was shifted opposite to the direction of background motion, both responses summed to zero. Under the same conditions, T4/T5 block flies did not shift the fixation peak, but rather kept the bar in front of them, regardless of whether the large-field stimulus was moving clockwise or counterclockwise (Fig. 5b,e). These results suggest a superposition of the large-field motion system and the position system at the level of behavioral output, as has been proposed<sup>30</sup>.

#### Electrophysiology in horizontal and vertical system cells

In our behavioral experiments, we found that a turning response could be elicited by local luminance changes and that this response was not changed when blocking T4 and T5 cell output (Figs. 3 and 4). In electrophysiological recordings from LPTCs sensitive to horizontal and vertical motion (horizontal and vertical system cells, respectively), the response to full-field flicker is only moderately reduced when T4 and T5 cell output is blocked<sup>26</sup>, indicating that horizontal system and vertical system cells receive additional input from an unidentified flicker pathway. To investigate whether horizontal system or vertical system cells use this information to mediate the position response, we performed electrophysiological recordings from horizontal system and vertical system cells in the immobilized fly (Fig. 6). We presented gratings moving in different directions, full-field OFF and ON flicker, as well as appearing and disappearing black bars at different positions along the azimuth. Vertical system cells responded strongly in a direction-selective manner to vertical motion (Fig. 6a), whereas horizontal system cells responded most strongly to horizontal motion (Fig. 6b). Both cell types also responded strongly to full-field OFF and ON flicker. However, cellular responses to appearing and disappearing vertical bars were orders of magnitude weaker. Moreover, horizontal system cells slightly hyperpolarized when the black bar appeared, but depolarized when it disappeared.

These recordings conflict with the behavioral responses that we observed in several ways. First, flies robustly turned toward the

**Figure 6** *In vivo* electrophysiological recordings from vertical system (VS) and horizontal system (HS) cells in the immobilized fly. (a,b) Voltage traces obtained from vertical system (a) and horizontal system cells (b) while presenting vertical (a) or horizontal (b) grating motion into the preferred direction (PD) and the null direction (ND) of the cell, full-field OFF and ON flicker, and a vertical dark bar that appeared and disappeared (fast or slow in 0.5 s or 1.5 s, respectively) at  $\Psi = 30^\circ$  in the front of the fly (responses at  $\Psi = 60^\circ$  and  $\Psi = 90^\circ$  were similar in amplitude; data not shown). All data represent mean  $\pm$  s.e.m. obtained from  $n = 8$  vertical system cells and  $n = 6$  horizontal system cells from wild-type Canton S flies.



location of an appearing and a disappearing black bar, and this position response was on the same order of magnitude as the optomotor response to full-field grating motion (Figs. 1b and 3a). Second, assuming that horizontal system and vertical system cells convey position information, we would not expect the fly to remain capable of tracking objects when the background is moving (Fig. 5); the tiny

voltage responses to local luminance changes would vanish in the much stronger voltage response to the background motion. These discrepancies between electrophysiological responses of horizontal system and vertical system cells and behavioral responses render it unlikely that horizontal system and vertical system cells are part of the fly's position circuit.

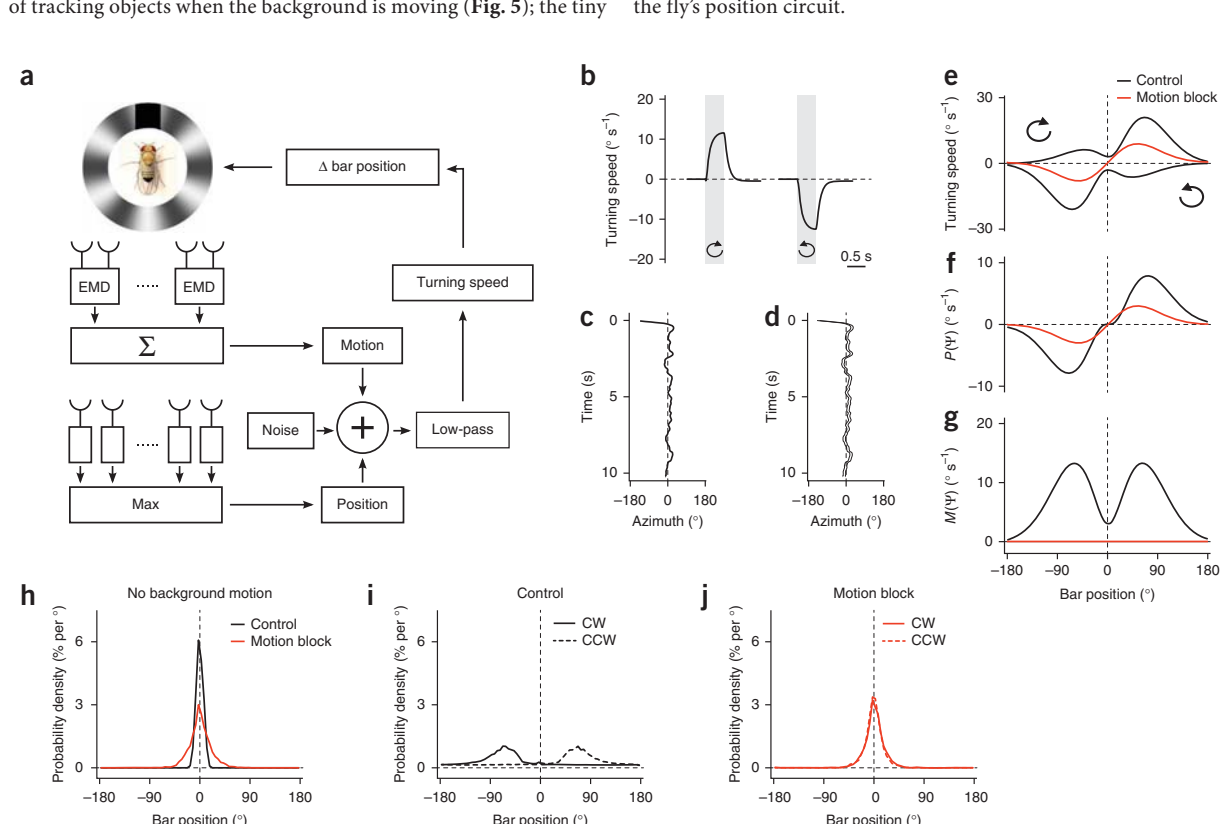


**Figure 7** Model simulations of the fly's course control system. (a) Outline of the model. The visual scene was analyzed in parallel by a motion and a position system. Their output signals, plus noise, were summed and low-pass filtered to yield the fly's turning speed. To simulate closed-loop fixation behavior, this signal was used to control the bar position. (b) Turning responses of the model to full-field clockwise and counterclockwise grating rotation. (c,d) Bar position over time (c) and the resulting activity pattern of the array of position detectors (d) during a single run of closed-loop fixation. (e) Model responses to a bar rotating in open-loop clockwise, followed by counterclockwise. (f) Position component,  $P(\Psi)$  (calculated by summing the two responses obtained in e and dividing them by 2). (g) Motion component,  $M(\Psi)$  (calculated by subtracting the two responses obtained in e and dividing by 2). (h) Probability density as function of bar position obtained from 20 runs of closed-loop bar fixation. (i,j) Closed-loop fixation behavior during superimposed open-loop background sine-grating motion (solid lines,  $10^\circ \text{ s}^{-1}$  clockwise (CW) rotation of the grating; dashed lines,  $-10^\circ \text{ s}^{-1}$  counterclockwise (CCW) rotation of the grating). Model responses were calculated with an intact motion system (black lines) and with the gain of the motion system set to zero (red lines).

## Modeling

Our results suggest the existence of two course control systems operating in parallel. Can such a system track a single object effectively and quantitatively account for the observed behavior of the flies? To address this question, we modeled the two course control systems and tested them under the conditions that were used in the experiments (Fig. 7). We implemented the large-field motion system as an array of elementary motion detectors of the Reichardt type<sup>34</sup> weighted by a spatial sensitivity profile similar to  $M(\Psi)$ , as obtained in the experiments (Fig. 2f), and with a 50% stronger weight on front-to-back than on back-to-front motion, as we observed (Fig. 4k). The output signals of all motion detectors were summated. The position system was modeled as an array of squared high-pass filters. From the array, the location of the maximum response was extracted at each time point. The response amplitude toward this position was determined from a spatial sensitivity profile similar to the experimentally determined one (Fig. 2c,d). Both signals were multiplied by a gain factor, added together with white noise and low-pass filtered to obtain a turning signal. This could either be interpreted as the output signal under open-loop conditions or fed back into the bar position when simulating closed-loop fixation behavior (Fig. 7a).

Stimulating the model with grating motion under open-loop conditions resulted in a syndirectional optomotor response (Fig. 7b). When tested under closed-loop conditions, the model revealed a pronounced fixation behavior, bringing and keeping the bar in a frontal position (Fig. 7c,h). Comparing the bar position (Fig. 7c) with the output of the squared high-pass filters over time (Fig. 7d) revealed the effective detection of bar position. Moving the bar in open loop, first clockwise, then counterclockwise, led to a response profile that was consistent with the respective experimental data (Fig. 7e). We added and subtracted both responses to reveal the position-dependent and motion-dependent components ( $P(\Psi)$  and  $M(\Psi)$ , respectively) and obtained similar profiles as in our experiments (Fig. 7f,g). We then tested the system for closed-loop fixation during open-loop background grating motion. As seen in the experiments, the maximum of the fixation histograms moved opposite to the direction of the drifting grating and the histograms became broader (Fig. 7i).

We then tested the model with the gain of the large-field motion system set to zero, simulating the blockage of T4 and T5 cell output; the model was still able to keep the bar in front, yet with a broader distribution (Fig. 7h). When the model was presented with the clockwise and counterclockwise rotating bar, the responses were identical for both directions of bar motion and only depended on the bar's position (Fig. 7e). Moreover, the resulting position-dependent response function,  $P(\Psi)$ , was reduced in amplitude compared with the control (Fig. 7f). Finally, in the case of closed-loop fixation with background motion, the model kept the bar in front, no matter the direction in which the background was moving (Fig. 7j). In summary, all of the effects that we observed in the experiments were reproduced by the model with one set of parameters.

## DISCUSSION

Behavioral and electrophysiological studies in larger fly species have proposed that fixation behavior is mediated by a special class of lobula plate neurons that are selective for small moving objects<sup>35–38</sup>. These cells are thought to receive retinotopic input from the same set of columnar, motion-sensitive neurons as the large field-sensitive tangential cells. Their selectivity for small moving objects arises from additional inhibition that they receive from other large-field neurons of the lobula plate<sup>39–41</sup>. In contrast, we found that transgenic *Drosophila* in which the T4 and T5 cells were blocked were

still able to fixate and track individual objects, even though their lobula plate tangential cells were motion blind and flies consequently did not show an optomotor response<sup>26</sup>. Our genetic and behavioral experiments revealed a control system that is purely sensitive to the position of the object and not to the direction in which it is moving, with the exact same spatial sensitivity profile as that revealed by the mathematical examination of behavioral results in wild-type houseflies performed many years ago<sup>30</sup>. Although the reduction in fixation strength observed in T4/T5 block flies might, at first sight, be interpreted as a partial overlap between the motion and the position circuit at the neuronal level, our analysis indicates that this is not the case; as a result of its asymmetry with respect to the direction of motion (front to back as compared to back to front), the motion circuit contributes to the fixation response at the behavioral level, but is separate from the position circuit at the neuronal level. An asymmetry in turning was also observed in the responses to rotating stripes<sup>8,30</sup> (Fig. 2), but, from these findings, one cannot conclude that the response of the motion circuit is asymmetrical. Even a perfectly symmetrical motion response, combined with the position response, would lead to the very same behavior. Our investigation of the two response components revealed that the asymmetrical turning response has two sources: a turning response to the position of the rotating bar and an asymmetrical motion response to its direction of motion. The powerful genetic tools available in *Drosophila*<sup>42</sup> will allow the future identification of the specific neural components of the position circuit.

## METHODS

Methods and any associated references are available in the online version of the paper.

*Note: Supplementary information is available in the online version of the paper.*

## ACKNOWLEDGMENTS

We wish to thank G. Rubin and A. Nern for providing the T4/T5 cell-specific driver line *R42F06-Gal4* and V. Jayaraman for advice on setting up the locomotion recorder. We are also grateful to J. Haag, A. Mauss, A. Arenz and A. Leonhardt for many helpful discussions and critically reading the manuscript, S. Prech for help with the design of the Peltier temperature control system, C. Theile for fly work, and F. Foerstner for reconstructing the three horizontal system cells shown in Figure 1a. A. Bahl and A. Borst are members of the Bernstein Center for Computational Neuroscience and the Graduate School of Systemic Neurosciences.

## AUTHOR CONTRIBUTIONS

A. Bahl set up the locomotion recorder and the stimulus display, and wrote the software for reading the behavioral output and displaying the stimulus. A. Bahl and T.S. performed all of the behavioral experiments and evaluated the data. G.A. performed the electrophysiological recordings and analyzed the data. A. Bahl and A. Borst designed the study. A. Borst carried out the modeling work. A. Borst and A. Bahl wrote the manuscript with the help of the other authors.

## COMPETING FINANCIAL INTERESTS

The authors declare no competing financial interests.

Reprints and permissions information is available online at <http://www.nature.com/reprints/index.html>.

1. Götz, K.G. Optomotorische Untersuchung des visuellen Systems einiger Augenmutanten der Fruchtfliege *Drosophila*. *Kybernetik* **2**, 77–92 (1964).
2. Buchner, E. Elementary movement detectors in an insect visual system. *Biol. Cybern.* **24**, 85–101 (1976).
3. Blondeau, J. & Heisenberg, M. The three-dimensional optomotor torque system of *Drosophila melanogaster*. Studies on wild type and the mutant optomotor blind H31. *J. Comp. Physiol. A* **145**, 321–329 (1982).
4. Tammero, L.F. & Dickinson, M.H. The influence of visual landscape on the free flight behavior of the fruit fly *Drosophila melanogaster*. *J. Exp. Biol.* **205**, 327–343 (2002).

## ARTICLES

5. Mronz, M. & Lehmann, F.-O. The free-flight response of *Drosophila* to motion of the visual environment. *J. Exp. Biol.* **211**, 2026–2045 (2008).
6. Reichardt, W. & Wenking, H. Optical detection and fixation of objects by fixed flying flies. *Naturwissenschaften* **56**, 424–425 (1969).
7. Heisenberg, M. & Wolf, R. *Vision in Drosophila: Genetics of Microbehavior* (Springer-Verlag, Berlin, 1984).
8. Reiser, M.B. & Dickinson, M.H. *Drosophila* fly straight by fixating objects in the face of expanding optic flow. *J. Exp. Biol.* **213**, 1771–1781 (2010).
9. Rister, J. *et al.* Dissection of the peripheral motion channel in the visual system of *Drosophila melanogaster*. *Neuron* **56**, 155–170 (2007).
10. Götz, K.G. Visual guidance in *Drosophila*. In *Development and Neurobiology of Drosophila* (eds. Siddiqi, O., Babu, P., Hall, M.L. & Hall, J.C.) 391–407 (Plenum Press, New York, 1980).
11. Strauss, R. & Pichler, J. Persistence of orientation toward a temporarily invisible landmark in *Drosophila melanogaster*. *J. Comp. Physiol. A* **182**, 411–423 (1998).
12. Maimon, G., Straw, A.D. & Dickinson, M.H. A simple vision-based algorithm for decision making in flying *Drosophila*. *Curr. Biol.* **18**, 464–470 (2008).
13. Aptekar, J.W., Shoemaker, P.A. & Frye, M.A. Figure tracking by flies is supported by parallel visual streams. *Curr. Biol.* **22**, 482–487 (2012).
14. Heisenberg, M., Wonneberger, R. & Wolf, R. Optomotor-blind (H31): a *Drosophila* mutant of the lobula plate giant neurons. *J. Comp. Physiol. A* **124**, 287–296 (1978).
15. Geiger, G. & Nässel, D.R. Visual orientation behavior of flies after selective laser beam ablation of interneurons. *Nature* **293**, 398–399 (1981).
16. Hausen, K. & Wehrhahn, C. Neural circuits mediating visual flight control in flies. II. Separation of two control systems by microsurgical brain lesions. *J. Neurosci.* **10**, 351–360 (1990).
17. Bausenwein, B., Wolf, R. & Heisenberg, M. Genetic dissection of optomotor behavior in *Drosophila melanogaster*. Studies on wild-type and the mutant optomotor-blind (H31). *J. Neurogenet.* **3**, 87–109 (1986).
18. Wolf, R. & Heisenberg, M. Visual orientation in motion-blind flies is an operant behavior. *Nature* **323**, 154–156 (1986).
19. Meinertzhagen, I.A. & O’Neil, S.D. Synaptic organization of columnar elements in the lamina of the wild type in *Drosophila melanogaster*. *J. Comp. Neurol.* **305**, 232–263 (1991).
20. Joesch, M., Plett, J., Borst, A. & Reiff, D.F. Response properties of motion-sensitive visual interneurons in the lobula plate of *Drosophila melanogaster*. *Curr. Biol.* **18**, 368–374 (2008).
21. Schnell, B. *et al.* Processing of horizontal optic flow in three visual interneurons of the *Drosophila* brain. *J. Neurophysiol.* **103**, 1646–1657 (2010).
22. Joesch, M., Schnell, B., Raghu, S.V., Reiff, D.F. & Borst, A. ON and OFF pathways in *Drosophila* motion vision. *Nature* **468**, 300–304 (2010).
23. Eichner, H., Joesch, M., Schnell, B., Reiff, D.F. & Borst, A. Internal structure of the fly elementary motion detector. *Neuron* **70**, 1155–1164 (2011).
24. Bausenwein, B. & Fischbach, K. Activity labeling patterns in the medulla of *Drosophila melanogaster* caused by motion stimuli. *Cell Tissue Res.* **270**, 25–35 (1992).
25. Bausenwein, B., Dittrich, A.P. & Fischbach, K.F. The optic lobe of *Drosophila melanogaster*. II. Sorting of retinotopic pathways in the medulla. *Cell Tissue Res.* **267**, 17–28 (1992).
26. Schnell, B., Raghu, S.V., Nern, A. & Borst, A. Columnar cells necessary for motion responses of wide-field visual interneurons in *Drosophila*. *J. Comp. Physiol. A* **198**, 389–395 (2012).
27. Seelig, J.D. *et al.* Two-photon calcium imaging from head-fixed *Drosophila* during optomotor walking behavior. *Nat. Methods* **7**, 535–540 (2010).
28. Brand, A.H. & Perrimon, N. Targeted gene expression as a means of altering cell fates and generating dominant phenotypes. *Development* **118**, 401–415 (1993).
29. Kitamoto, T. Conditional modification of behavior in *Drosophila* by targeted expression of a temperature-sensitive *shibire* allele in defined neurons. *J. Neurobiol.* **47**, 81–92 (2001).
30. Poggio, T. & Reichardt, W. A theory of the pattern induced flight orientation of the fly *Musca domestica*. *Kybernetik* **12**, 185–203 (1973).
31. Wehrhahn, C. Flight torque and lift responses of the housefly (*Musca domestica*) to a single stripe moving in different parts of the visual field. *Biol. Cybern.* **29**, 237–247 (1978).
32. Pick, B. Visual flicker induces orientation behavior in the fly *Musca*. *Z. Naturforsch. C* **29c**, 310–312 (1974).
33. Wehrhahn, C. Fast and slow flight torque responses in flies and their possible role in visual orientation behavior. *Biol. Cybern.* **40**, 213–221 (1981).
34. Reichardt, W. Evaluation of optical motion information by movement detectors. *J. Comp. Physiol. A* **161**, 533–547 (1987).
35. Reichardt, W. & Poggio, T.A. Figure-ground discrimination by relative movement in the visual system of the fly. Part I: Experimental Results. *Biol. Cybern.* **35**, 81–100 (1979).
36. Egelhaaf, M. On the neuronal basis of figure-ground discrimination by relative motion in the visual system of the fly. I. Behavioral constraints imposed on the neuronal network and the role of the optomotor system. *Biol. Cybern.* **52**, 123–140 (1985).
37. Egelhaaf, M. On the neuronal basis of figure-ground discrimination by relative motion in the visual system of the fly. II. Figure-detection cells, a new class of visual interneurons. *Biol. Cybern.* **52**, 195–209 (1985).
38. Liang, P., Heitwerth, J., Kern, R., Kurtz, R. & Egelhaaf, M. Object representation and distance encoding in three-dimensional environments by a neural circuit in the visual system of the blowfly. *J. Neurophysiol.* **107**, 3446–3457 (2012).
39. Egelhaaf, M. On the neuronal basis of figure-ground discrimination by relative motion in the visual system of the fly. III. Possible input circuitries and behavioral significance of the FD cells. *Biol. Cybern.* **52**, 267–280 (1985).
40. Warzecha, A.K., Borst, A. & Egelhaaf, M. Photo-ablation of single neurons in the fly visual system reveals neural circuit for the detection of small moving objects. *Neurosci. Lett.* **141**, 119–122 (1992).
41. Cuntz, H., Haag, J. & Borst, A. Neural image processing by dendritic networks. *Proc. Natl. Acad. Sci. USA* **100**, 11082–11085 (2003).
42. Borst, A. *Drosophila*’s view on insect vision. *Curr. Biol.* **19**, R36–R47 (2009).

## ONLINE METHODS

**Behavioral experiments.** The locomotion recorder<sup>2,27</sup> consisted of an air-suspended sphere floating in a bowl-shaped sphere holder. The sphere had a diameter of 6 mm and a weight of 40 mg; it was made from polyurethane foam and coated with polyurethane spray (spheres were kindly provided by V. Jayaraman, Janelia Farm). The airflow is adjusted to  $\sim 0.7$  l min<sup>-1</sup> by a rotary vane pump (G6/01-K-EB9L Gardner Denver Thomas GmbH) such that the sphere rotated freely in the holder, but did not jump out. A high-power infrared LED (800 nm, JET series, 90 mW, Roithner Electronics) was located in the back to illuminate the fly and the sphere surface. Two optical tracking sensors were equipped with lens and aperture systems to focus two 1-mm<sup>2</sup> equatorial spots (at  $\pm 30^\circ$ ) on the sphere at a distance 15 cm behind the fly. The tracking data were processed in a custom-designed circuit<sup>27</sup> at 4 kHz internally, read out via a USB interface and processed by a computer at  $\sim 200$  Hz. This allowed real-time calculation of the instantaneous rotation axis of the sphere. A third camera (GRAS-20S4M-C, Point Grey Research) was located in the back, which is essential for proper positioning of the fly and allowed real-time observation and video recording of the fly during experiments. The bottom of the sphere holder was surrounded by an open plastic funnel connected to a metal fan with an aluminum tube. A self-designed Peltier controlling system read out the temperature of a thermometer placed just below the sphere and controlled the fan temperature such that the air temperature around the fly was regulated precisely ( $\pm 0.1$  °C). In all experiments, the temperature started at the permissive temperature level for *shibire<sup>ts</sup>* (25 °C) and was raised linearly to the restrictive temperature of 34 °C in 10–20 min. Three 120-Hz LCD screens (Samsung 2233 RZ) were vertically arranged and formed a U-shaped visual arena (31 × 31 × 47 cm) with the fly in the center. We removed the monitor covers to minimize the borders between the screens in the corners of the arena and glued thin sheets of parchment paper onto the screens to scatter and evenly distribute the emitted light. The visual arena had a luminance ranging from 0–131 cd m<sup>-2</sup> and covered almost the whole visual field of the fly (horizontal,  $\pm 135^\circ$ ; vertical,  $\pm 57^\circ$ ; resolution < 0.1°). The three LCD screens were controlled via NVIDIA 3D Vision Surround Technology on Windows 7 64 bit, allowing a synchronized update of the screens at 120 frames per s. For visual stimulation, we use Panda3D, an open-source gaming engine, and Python 2.7, which simultaneously controlled the frame rendering in Panda3D, read out the tracking data and temperature, and streamed data to the hard disk.

Time-position plots for the visual stimuli are illustrated in **Supplementary Figure 4** for all experiments. The large-field open-loop optomotor stimulus (**Fig. 1b–d** and **Supplementary Fig. 4a,b**) consisted of a striped grating ( $\lambda = 20^\circ$ ) rotating clockwise (+) or counterclockwise (−) at a velocity of 20 ° s<sup>-1</sup> for 0.5 s. Seven contrasts were tested. The dark stripes always had a luminance value of 27 cd m<sup>-2</sup>, whereas the luminance values of the brighter stripes ranged from 30–104 cd m<sup>-2</sup>, resulting in contrast values between 4 and 58%, measured as  $(I_{\max} - I_{\min}) / (I_{\max} + I_{\min})$ . In the open- and closed-loop fixation experiments, we showed a single black bar (10° wide, 114° high, 9 cd m<sup>-2</sup>) on a gray background (58 cd m<sup>-2</sup>). In the first set of open-loop fixation experiments (**Fig. 2** and **Supplementary Fig. 4d,e**), the bar started in the back and rotated at velocities of  $\pm 18^\circ$  s<sup>-1</sup> around the fly. In another set of experiments (**Fig. 3** and **Supplementary Fig. 4f**), the bar did not move, but slowly appeared (in 0.5 s), remained static for 4 s and disappeared (in 0.5 s) at well-defined locations ( $\pm 120^\circ, \pm 90^\circ, \pm 60^\circ, \pm 45^\circ, \pm 30^\circ$  and  $\pm 15^\circ$ ). In another experiment (**Fig. 4** and **Supplementary Fig. 4g–i**), we chose two locations ( $\Psi = 30^\circ$  and  $\Psi = 60^\circ$ ) to show local motion (front to back and back to front) and local luminance change. Here, the local luminance change dynamics were chosen such that they approximated the luminance change when the local motion was shown. In the case of closed-loop fixation, the bar was placed at a random position (between  $-180^\circ$  and  $+180^\circ$ ) around the fly before each trial and the fly was then given 20 s control of the angular position of that bar ( $\Delta\text{bar} = -\text{fly turning}$ , updated approximately every 9 ms). This was done either in front of a gray background (**Fig. 1e–i** and **Supplementary Figs. 3a–c** and **4c**) or a large-field sine-grating ( $\lambda = 30^\circ$ , the luminance values of the pattern were between 27 and 104 cd m<sup>-2</sup>). The sine-grating was either static (**Supplementary Figs. 3d–f** and **4j**) or rotated at  $\pm 15^\circ$  s<sup>-1</sup> (**Fig. 5** and **Supplementary Fig. 4k,l**).

Flies were raised on standard cornmeal-agar medium at 18 °C and 60% humidity throughout development on a 12-h light, 12-h dark cycle. We used *shibire<sup>ts</sup>* control flies (*w<sup>+</sup>; +; +/UAS-shibire<sup>ts</sup>*), T4/T5 control flies (*w<sup>+</sup>/w<sup>-</sup>; +; R42F06-Gal4/+*) and T4/T5 block flies (*w<sup>+</sup>/w<sup>-</sup>; +; R42F06-Gal4/UAS-shibire<sup>ts</sup>*). The T4 and T5 cell-specific driver line *R42F06-Gal4* was kindly provided by A. Nern and G. Rubin

(Janelia Farm) and was generated<sup>43</sup> using a 4.0-kb DNA fragment of the *bab2* gene amplified from genomic DNA with primers CGGCTGATCCAACAAAGGATG CACC and CTCAGTAGCCGCACCTTGTTCT. The *shibire<sup>ts</sup>* effector has multiple insertions on the third chromosome. We used wild-type Canton S flies for the control crosses. Only female flies aged 2–10 d were used in experiments. Flies were taken from 18 °C just before the experiment and immediately cold anesthetized. The head, thorax and wings were glued to a needle using near-ultraviolet bonding glue (Sinfony Opaque Dentin) and strong blue LED light (440 nm, dental curing light, New Woodpecker).

For each fly, the experiment lasted approximately 50 min and was split into 50–200 trials depending on the length and the number of visual stimuli. Stimuli in one trial were presented in random order. For data analysis, we chose a range of trials (same for control and T4/T5 block flies per experiment) during which the temperature was constant at 34 °C and during which flies had a constant average turning and walking speed. The experimental raw data were first downsampled (interpolated from 120 to 20 Hz). Turning speed traces were then determined by taking the average over trials and low-pass filtering the resulting trace ( $\tau = 0.1$  s in all experiments, except those shown in **Fig. 2**, where  $\tau = 0.4$  s). Probability density functions of bar position were calculated separately for each trial with a bin size of 5° and then averaged over trials and flies. The measure 'fixation in front' was determined by integrating the probability density function of one trial between  $-10^\circ$  and  $10^\circ$ , which resulted in a percentage value for how probable it was to find the bar in that area during that trial. These values were then averaged over trials and flies. Flies were excluded from data analysis when the average walking speed during the whole experiment was below 0.1 cm s<sup>-1</sup>, indicating severe walking problems, or (only in closed-loop fixation experiments with static background) when the average turning speed was either larger than  $+10^\circ$  s<sup>-1</sup> or smaller than  $-10^\circ$  s<sup>-1</sup>, indicating an asymmetry in walking behavior that led to a substantially reduced fixation performance. All data analysis was performed in Python 2.7 using NumPy and SciPy on Mac OSX 10.8.

*P* values were obtained using different statistical tests. To test the hypothesis that a group had a certain mean, we performed a two-sided *t* test. When two groups were compared (**Fig. 4k**), we performed a two-sided *t* test. When T4/T5 block flies were compared with *shibire<sup>ts</sup>* control and T4/T5 control flies, we performed a two-sided *t* test comparing each control with the block flies and chose the larger *P* value. When three groups were compared (**Fig. 4j**), we performed a one-way ANOVA. We used approximately the same sample size (smallest  $n = 9$  flies, largest  $n = 16$  flies) per group and experiment, which permitted a statistical comparison between the different experiments. This sample size was considered as sufficiently large because the optomotor response of T4/T5 block flies shown in **Figure 1b–d** was highly significantly reduced at  $n = 10$  flies ( $P < 0.001$ , two-sided *t* test compared with both controls). See **Supplementary Statistics** for a detailed list of group sizes, statistical tests and *P* values.

**Electrophysiology.** Patch-clamp recordings were performed as described previously<sup>20</sup> with minor modifications. All electrophysiological experiments were performed with female wild-type Canton S flies 6–24 h post-eclosion. Flies were raised on standard cornmeal-agar medium and kept at 25 °C and 60% humidity on a 12-h dark/light cycle.

Flies were anesthetized on ice and immobilized on a plexiglas holder with wax. The head was bent downwards and fixed by waxing the proboscis to the thorax. The fly was then inserted into an opening cut into a piece of aluminum foil mounted in a recording chamber. A part of the posterior side of the head cuticle and the muscle that covers the cell bodies of LPTCs was removed with fine forceps. Extracellular saline (103 mM NaCl, 3 mM KCl, 5 mM TES, 10 mM trehalose, 10 mM glucose, 7 mM sucrose, 26 mM NaHCO<sub>3</sub>, 1 mM NaH<sub>2</sub>PO<sub>4</sub>, 1.5 mM CaCl<sub>2</sub> and 4 mM MgCl<sub>2</sub>, pH 7.3, 280 mOsm) was bubbled with 95% O<sub>2</sub> and 5% CO<sub>2</sub> and continuously perfused over the preparation. The brain of the fly was visualized with an upright microscope (AxioTech Vario 100, Zeiss) equipped with a 40× water-immersion objective (LumPlanFL, NA 0.8, Olympus) and an Hg-light source (HXP-120, Visitron Systems). For contrast enhancement, we used two polarization filters that were slightly shifted with respect to their polarization plane. The health of the flies was checked regularly by monitoring periodic movements of the brain. A glass electrode filled with collagenase (Collagenase IV, Gibco, 0.5 mg ml<sup>-1</sup> in extracellular saline) was used to weaken the perineural sheath and expose the somata of LPTCs.

Somata of vertical system and horizontal system cells were patched with a glass electrode (6–9 MΩ) filled with internal solution (140 mM potassium aspartate, 10 mM HEPES, 4 mM Mg-ATP, 0.5 mM Na-GTP, 1 mM EGTA, 1 mM KCl and 0.03 mM Alexa 568–hydrazide sodium, pH 7.26, 265 mOsm). All recordings were performed in current-clamp bridge mode with an NPI BA-1S amplifier (NPI electronics), low-pass filtered at 3 kHz and digitized at 10 kHz. Data acquisition was performed with Matlab (version R2011a, MathWorks). Cells had an average resting membrane potential of  $-51.6 \pm 0.7$  mV (corrected for a liquid junction potential of 12 mV) and an average input resistance of  $204.5 \pm 16.7$  MΩ. Cell types were identified on the basis of their typical response profiles to moving gratings. In addition, fluorescence images of each cell were taken after the recording with a CCD camera (Spot Pursuit, Visitron Systems) to verify their identity.

Visual stimuli were presented on a custom-built LED arena that subtended 170° in azimuth and 85° in elevation with a resolution of approximately 1.4° per LED. The arena allowed refresh rates of up to 600 Hz and had a maximum luminance of 80 cd m<sup>-2</sup>. Motion stimuli consisted of square-wave gratings with a wavelength of 20° moving at 1 Hz. Stimuli lasted for 3 s with an interstimulus interval of 5 s and were repeated three times. For bar flicker stimuli, the arena background was set to full luminance. After 1.5 s, a dark bar that had a width of 10° and was centered at 30°, 60° or 90° along the azimuth appeared. The contrast of that bar was increased linearly to a maximum of 66% over 0.5 s or 1.5 s. After an interval of 3 s, the dark bar disappeared again in the same time period. Bar flicker stimuli were presented five times. For full-field flicker stimuli, the arena was stepped to full luminance for 3 s and then back to zero again for 3 s. Full-field flicker stimuli were presented ten times per cell.

Data analysis was performed with Matlab (version R2011b, MathWorks) using custom-written scripts. For all stimuli, we averaged voltage traces over sweeps and calculated the mean and s.e.m. over cells. The baseline membrane potential was calculated by averaging over a period of 500 ms preceding the stimulus onset and subtracted from the responses. For horizontal system cells, we pooled responses of all three horizontal system cell types. To properly match the receptive field of vertical system cells<sup>20</sup>, we averaged the responses of vertical system cells with frontal receptive fields (VS1–VS3) to obtain the responses to the appearing and disappearing bar at 30° and 60°. Responses of vertical system cells with lateral receptive fields (VS5–6) were averaged to determine the responses at 90°.

**Modeling.** Visual patterns were modeled as one-dimensional luminance functions at a spatial resolution of 0.01° and a temporal resolution of 1 ms. They were covered by 360 elementary motion detectors of the Reichardt type<sup>34</sup>. Briefly, the luminance value at one location was low-pass filtered (first-order, 20-ms time constant) and subsequently multiplied with the instantaneous value derived from the neighboring location, separated by 1° of visual angle. This was done

twice in a mirror-symmetrical fashion, and the output signals of both operations were subtracted. All elementary motion detectors were weighted according to the  $M(\Psi)$  sensitivity profile and subsequently summated. In each hemisphere, motion detection subunits tuned to back-to-front motion were given half the response amplitude of those tuned to front-to-back motion. The visual pattern was also viewed by an array of 360 position detectors. These were modeled as high-pass filters (first-order, 10-ms time constant), the outputs of which were squared. From this array, the location of the maximum was determined. If this maximum was below a certain threshold, the location decayed back to zero with a 20-ms time constant. The output of the position system was calculated as the value of the  $P(\Psi)$  function at this location. The  $M(\Psi)$  and  $P(\Psi)$  functions were approximated in the following way, with  $Z(\Psi)$  describing the shape of their profiles,  $g_P$  being the gain factor of the position system (= 3) and  $g_M$  being the gain factor of the motion system (= 5).

$$\begin{aligned} Z(\Psi) &= -\frac{d}{d\Psi} e^{-(\Psi/75)^2} \\ P(\Psi) &= g_P \cdot Z(\Psi) \\ M(\Psi) &= g_M \cdot |Z(\Psi)| \end{aligned}$$

$M(\Psi)$  was subsequently smoothed by a box filter of 20° width. As a noise function we used Gaussian white noise that was filtered by a first-order low-pass filter with 100-ms time constant and multiplied with a noise-gain factor ( $g_N = 15$ ). The sum of noise, motion and position system was then fed through a first-order low-pass filter with 100-ms time-constant to result in the turning speed. In closed-loop simulations, the turning speed was used to update the bar position each millisecond.

$$\text{bar position}(t+1) = \text{bar position}(t) - 0.1 \cdot \text{turning speed}(t)$$

Fixation histograms were obtained from 20 simulation runs, each 30 s long. At the beginning of each run, the bar was positioned in front of the fly. As large field pattern, we used a sine-grating with a spatial wavelength of 22.5°, a mean luminance of 0.5 and a contrast of 1. When activated, it moved at 10° s<sup>-1</sup>, resulting in a temporal frequency of 0.44 Hz. The black bar was simulated as zero luminance from -5° to +5° around the bar location, replacing the luminance value of either the grating or the one of a uniform background of luminance value 1. The model was simulated in IDL (Exelis) on 64-bit Windows 7.

43. Pfeiffer, B.D. *et al.* Tools for neuroanatomy and neurogenetics in *Drosophila*. *Proc. Natl. Acad. Sci. USA* **105**, 9715–9720 (2008).

## Object Tracking in Motion-Blind Flies

Armin Bahl, Georg Ammer, Tabea Schilling and Alexander Borst\*

Max-Planck-Institute of Neurobiology, Am Klopferspitz 18, 82152 Martinsried, Germany

\* Corresponding author: [borst@neuro.mpg.de](mailto:borst@neuro.mpg.de)

### Supplemental Material

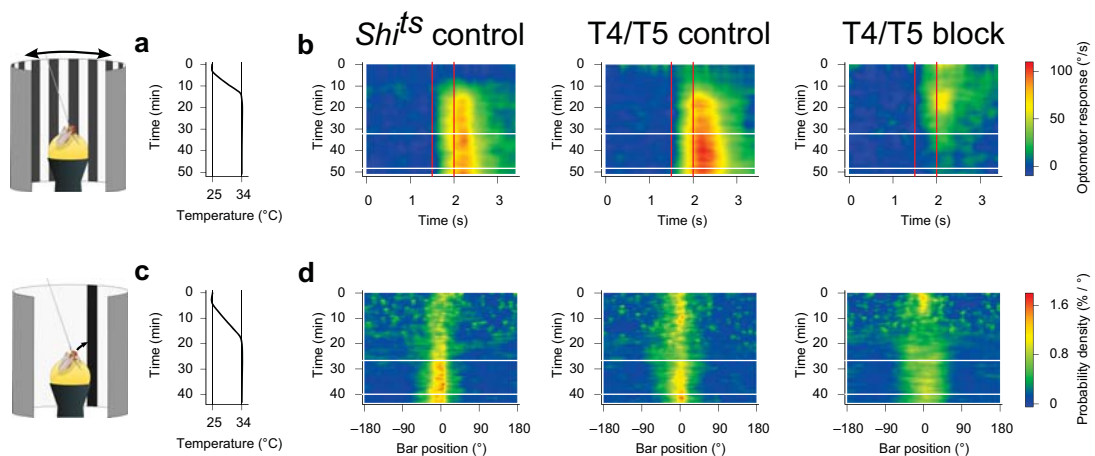


**Fig. S1** Temperature control data for the optomotor response and fixation response. **a** Temperature protocol during the full-field grating motion experiment (Fig. 1b-d). The temperature around the fly starts at 25 °C and rises slowly to 34 °C within 10 minutes. **b** The optomotor response – defined as the turning speed in response to clockwise motion minus the turning speed in response to counterclockwise motion divided by two – as a function of stimulus time (x-axis) and overall experimental time (y-axis) for the three groups. Red vertical lines illustrate the time points when grating motion starts and ends. White horizontal lines indicate the time span during which the trials were used for detailed data analysis (Fig. 1). **c** Temperature protocol for closed-loop bar fixation (Fig. 1e-i). **d** Probability density of bar positions (x-axis) as function of overall experimental time (y-axis). All data represent mean of  $N = 10,10,10$  (b) and  $N = 10,10,12$  (d) flies per group (left to right). Same flies as in Fig. 1.

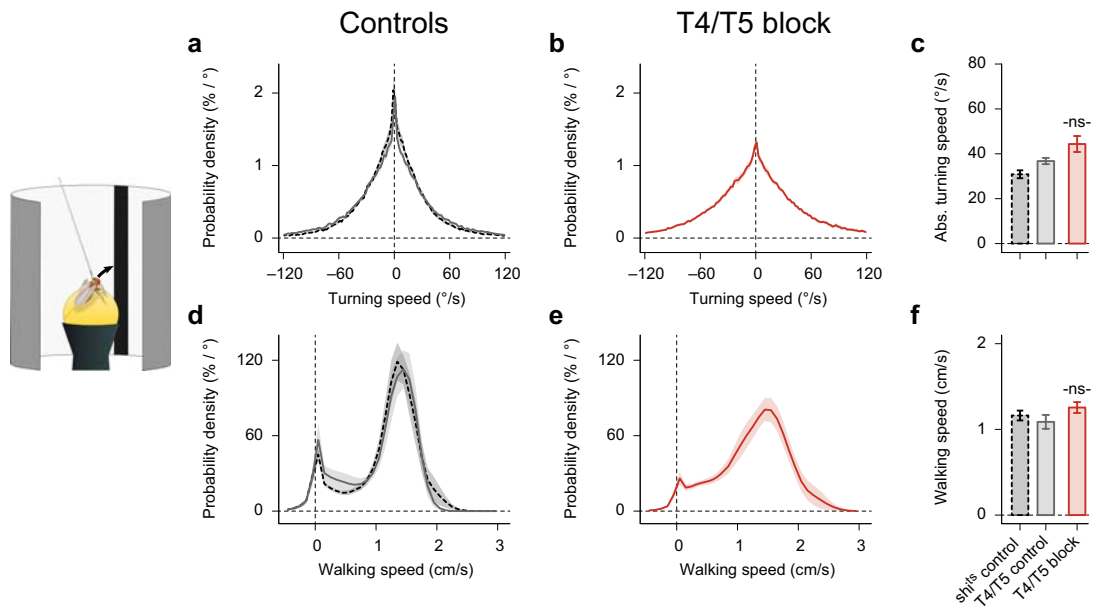


**Fig. S2** Walking and turning speed of control and T4/T5 block flies during closed-loop fixation. **a** Probability density functions for turning speed (bin size = 2 °/s) of control flies. **d** Probability density functions for walking speeds (bin size = 0.1 cm/s) of control flies. **b,e** Same as in (a,d), but obtained from flies in which the output from T4 and T5 cells was blocked. **c** Average absolute turning speed. **f** Average walking speed. All data represent mean  $\pm$  SEM; 40 trials per fly of  $N = 11, 9, 9$  flies per group (*shi<sup>ts</sup>* control, dashed black lines; T4/T5 control, solid gray lines; T4/T5 block, solid red lines).  $^{ns}p \geq 0.05$ ; two-sided t-test comparing to both controls. Same flies as in Fig. 1e-i.

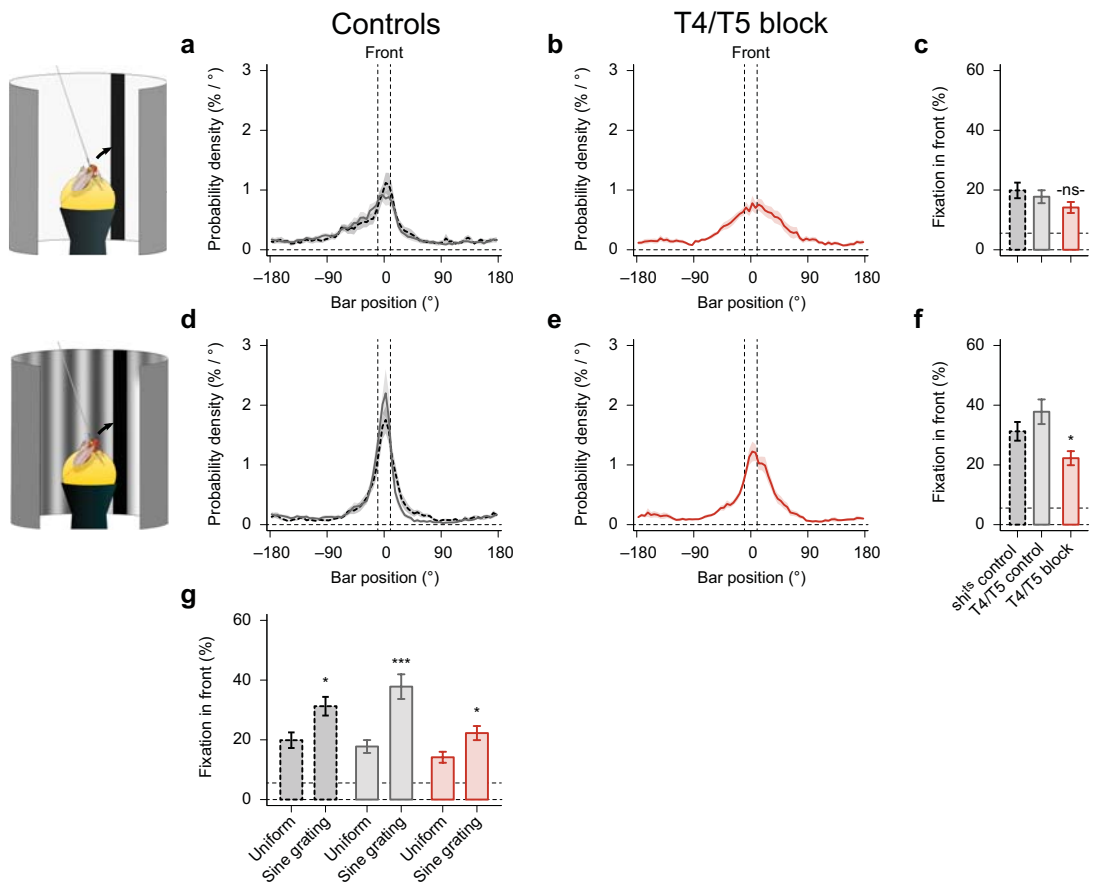


**Fig. S3** The fixation response improves with a static background pattern. **a,d** Average probability density as function of bar position for the two controls when the background is gray (a) and when it is a static sine-grating pattern with the same average luminance (d). **b,e** Same as in (a,d) but for flies in which the output of T4/T5 cells was blocked. **c,f** Ability to keep the stripe in the frontal field (same measure as in Fig. 1i) when the background is gray (c) or when it is a static sine-grating background (f). **g** Comparison of the ability to keep the bar in the frontal field between uniform and sine-grating background for all groups. Upper horizontal dashed lines in (c,f,g) indicate the chance level (= 5.6 %; no fixation). All data represent mean  $\pm$  SEM; 15 trials per fly of  $N = 10, 10, 9$  flies per group (*shi<sup>ts</sup>* control, dashed black lines; T4/T5 control, solid gray lines; T4/T5 block, solid red lines).  $^{*ns-}p \geq 0.05$ ,  $*p < 0.05$ ,  $^{***}p < 0.001$ ; two-sided t-test comparing to both controls (c,f) or comparing uniform to sine-grating within the groups (g).

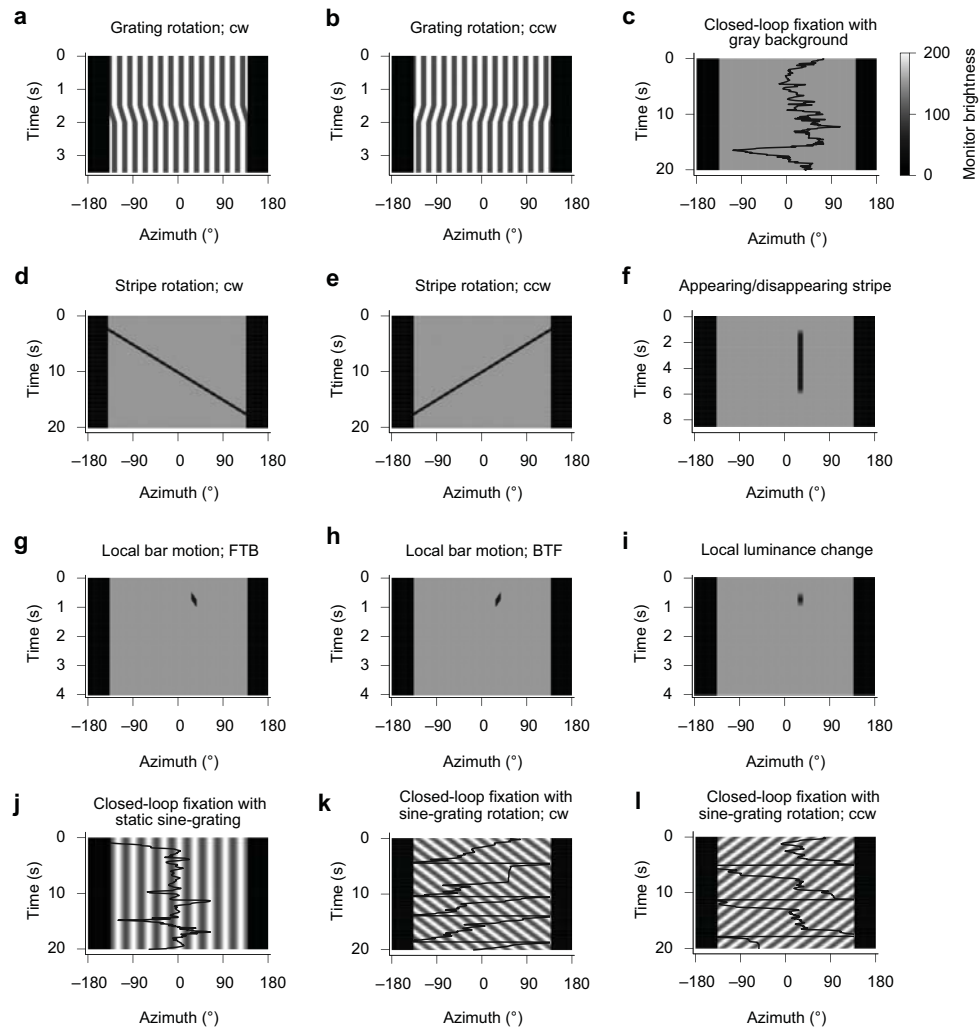


**Fig. S4** Position-time plots of all visual stimuli in all experiments. **a,b** Full-field grating moving clockwise (cw) or counterclockwise (ccw). **c** Closed-loop fixation of a black bar on an uniformly gray background. **d,e** Rotating black bar (cw, ccw). **f** Slowly appearing and disappearing black bar at  $\Psi = +60^\circ$  (other locations were  $\pm 15^\circ$ ,  $\pm 30^\circ$ ,  $\pm 45^\circ$ ,  $-60^\circ$ ,  $\pm 90^\circ$ ,  $\pm 120^\circ$ ). **g,h** A localized black bar moves front-to-back (g) and back-to-front (h) at  $\Psi = +60^\circ$  (other locations were  $\Psi = \pm 30^\circ$ ,  $\Psi = -60^\circ$ ). **i** Approximation of the local luminance dynamics in (g,h). **j** Closed-loop fixation of a black bar on a static sine-grating with the same average brightness as in (c). **k,l** Closed-loop bar fixation during background motion (cw, ccw, respectively); the black traces in (c,j-l) are experimental example traces of bar position for a single trial of a *shi<sup>ts</sup>* control fly. Monitor position  $0^\circ$  is directly in front of the fly. The black areas indicate the region of no visual stimulation behind the fly ( $-180^\circ < x < -135^\circ$  and  $+135^\circ < x < +180^\circ$  in azimuth).

### Detailed statistics (list of group sizes, statistical tests and p-values)

The degree of significance was given as follows: not significant (-ns-) when  $p \geq 0.05$ ; \* when  $p < 0.05$ ; \*\* when  $p < 0.01$ ; \*\*\* when  $p < 0.001$ .

#### Figure 1

##### Fig. 1d

20 trials per fly;  $N^{shi\ control} = 10$  flies,  $N^{T4/T5\ control} = 10$  flies,  $N^{T4/T5\ block} = 10$  flies.

$Shi^{ts}$  control  $\leftrightarrow$  T4/T5 control:  $p = 0.254$ ,  $t = -1.177$  (two-sided t-test)

$Shi^{ts}$  control  $\leftrightarrow$  T4/T5 block:  $p < 0.001$ ,  $t = 15.663$  (two-sided t-test)

T4/T5 control  $\leftrightarrow$  T4/T5 block:  $p < 0.001$ ,  $t = 9.882$  (two-sided t-test)

T4/T5 block  $\leftrightarrow$  zero:  $p = 0.473$ ,  $t = 0.749$  (two-sided t-test)

##### Fig. 1i

40 trials per fly;  $N^{shi\ control} = 10$  flies,  $N^{T4/T5\ control} = 10$  flies,  $N^{T4/T5\ block} = 12$  flies.

$Shi^{ts}$  control  $\leftrightarrow$  T4/T5 control:  $p = 0.307$ ,  $t = 1.052$  (two-sided t-test)

$Shi^{ts}$  control  $\leftrightarrow$  T4/T5 block:  $p = 0.012$ ,  $t = 2.759$  (two-sided t-test)

T4/T5 control  $\leftrightarrow$  T4/T5 block:  $p = 0.025$ ,  $t = 2.427$  (two-sided t-test)

T4/T5 block  $\leftrightarrow$  chance:  $p < 0.001$ ,  $t = 5.862$  (two-sided t-test)

#### Figure 2

35 trials per fly;  $N^{shi\ control} = 10$  flies,  $N^{T4/T5\ control} = 11$  flies,  $N^{T4/T5\ block} = 14$  flies.

##### Fig. 2e

$Shi^{ts}$  control  $\leftrightarrow$  T4/T5 control:  $p = 0.725$ ,  $t = 0.356$  (two-sided t-test)

$Shi^{ts}$  control  $\leftrightarrow$  T4/T5 block:  $p < 0.001$ ,  $t = 4.136$  (two-sided t-test)

T4/T5 control  $\leftrightarrow$  T4/T5 block:  $p < 0.001$ ,  $t = 4.068$  (two-sided t-test)

T4/T5 block  $\leftrightarrow$  zero:  $p < 0.001$ ,  $t = 7.086$  (two-sided t-test)

##### Fig. 2h

$Shi^{ts}$  control  $\leftrightarrow$  T4/T5 control:  $p = 0.618$ ,  $t = 0.507$  (two-sided t-test)

$Shi^{ts}$  control  $\leftrightarrow$  T4/T5 block:  $p < 0.001$ ,  $t = 13.408$  (two-sided t-test)

T4/T5 control  $\leftrightarrow$  T4/T5 block:  $p < 0.001$ ,  $t = 16.735$  (two-sided t-test)

T4/T5 block  $\leftrightarrow$  zero:  $p = 0.056$ ,  $t = 2.098$  (two-sided t-test)

#### Figure 3

10 trials per fly;  $N^{shi\ control} = 12$  flies,  $N^{T4/T5\ control} = 12$  flies,  $N^{T4/T5\ block} = 16$  flies. Half of each group was used to measure responses at positions  $\pm 15^\circ$ ,  $\pm 60^\circ$ ,  $\pm 120^\circ$ , the other half at  $\pm 30^\circ$ ,  $\pm 45^\circ$ ,  $\pm 90^\circ$ .

##### Fig. 3e

$Shi^{ts}$  control  $\leftrightarrow$  T4/T5 control:  $p = 0.611$ ,  $t = 0.524$  (two-sided t-test)

$Shi^{ts}$  control  $\leftrightarrow$  T4/T5 block:  $p = 0.086$ ,  $t = 1.872$  (two-sided t-test)

T4/T5 control  $\leftrightarrow$  T4/T5 block:  $p = 0.489$ ,  $t = 0.713$  (two-sided t-test)

##### Fig. 3h

$Shi^{ts}$  control  $\leftrightarrow$  T4/T5 control:  $p = 0.151$ ,  $t = 1.553$  (two-sided t-test)

*Shi<sup>ts</sup>* control  $\leftrightarrow$  T4/T5 block: **p = 0.527, t = 0.650** (two-sided t-test)  
 T4/T5 control  $\leftrightarrow$  T4/T5 block: **p = 0.465, t = -0.753** (two-sided t-test)  
*Shi<sup>ts</sup>* control  $\leftrightarrow$  zero: **p = 0.368, t = -0.990** (two-sided t-test)  
 T4/T5 control  $\leftrightarrow$  zero: **p = 0.018, t = -3.451** (two-sided t-test)  
 T4/T5 block  $\leftrightarrow$  zero: **p = 0.107, t = -1.851** (two-sided t-test)

#### Fig. 3i,j

At 45°:

*Shi<sup>ts</sup>* control  $\leftrightarrow$  T4/T5 block: **p = 0.054, t = 2.137** (two-sided t-test)  
 T4/T5 control  $\leftrightarrow$  T4/T5 block: **p = 0.155, t = 1.517** (two-sided t-test)

#### Fig. 3k

*Shi<sup>ts</sup>* control  $\leftrightarrow$  T4/T5 control: **p = 0.407, t = 0.865** (two-sided t-test)  
*Shi<sup>ts</sup>* control  $\leftrightarrow$  T4/T5 block: **p = 0.470, t = 0.745** (two-sided t-test)  
 T4/T5 control  $\leftrightarrow$  T4/T5 block: **p = 0.939, t = -0.077** (two-sided t-test)

#### Figure 4

60 trials per fly; At  $\Psi = 30^\circ$ :  $N^{shi\ control} = 10$  flies,  $N^{T4/T5\ control} = 12$  flies,  $N^{T4/T5\ block} = 11$  flies. At  $\Psi = 60^\circ$ : Additional  $N^{shi\ control} = 10$  flies,  $N^{T4/T5\ control} = 11$  flies,  $N^{T4/T5\ block} = 11$  flies.

#### Fig. 4c

At 30°

*Shi<sup>ts</sup>* control  $\leftrightarrow$  T4/T5 control: **p = 0.027, t = 2.390** (two-sided t-test)  
*Shi<sup>ts</sup>* control  $\leftrightarrow$  T4/T5 block: **p < 0.001, t = 8.262** (two-sided t-test)  
 T4/T5 control  $\leftrightarrow$  T4/T5 block: **p < 0.001, t = 5.103** (two-sided t-test)

At 60°:

*Shi<sup>ts</sup>* control  $\leftrightarrow$  T4/T5 control: **p = 0.067, t = -1.939** (two-sided t-test)  
*Shi<sup>ts</sup>* control  $\leftrightarrow$  T4/T5 block: **p < 0.001, t = 7.148** (two-sided t-test)  
 T4/T5 control  $\leftrightarrow$  T4/T5 block: **p < 0.001, t = 9.596** (two-sided t-test)

#### Fig. 4f

At 30°

*Shi<sup>ts</sup>* control  $\leftrightarrow$  T4/T5 control: **p = 0.969, t = 0.039** (two-sided t-test)  
*Shi<sup>ts</sup>* control  $\leftrightarrow$  T4/T5 block: **p < 0.001, t = -4.101** (two-sided t-test)  
 T4/T5 control  $\leftrightarrow$  T4/T5 block: **p < 0.001, t = -3.962** (two-sided t-test)

At 60°:

*Shi<sup>ts</sup>* control  $\leftrightarrow$  T4/T5 control: **p = 0.666, t = 0.438** (two-sided t-test)  
*Shi<sup>ts</sup>* control  $\leftrightarrow$  T4/T5 block: **p < 0.001, t = -4.842** (two-sided t-test)  
 T4/T5 control  $\leftrightarrow$  T4/T5 block: **p = 0.002, t = -3.488** (two-sided t-test)

#### Fig. 4i

At 30°

*Shi<sup>ts</sup>* control  $\leftrightarrow$  T4/T5 control: **p = 0.955, t = 0.057** (two-sided t-test)  
*Shi<sup>ts</sup>* control  $\leftrightarrow$  T4/T5 block: **p = 0.471, t = 0.736** (two-sided t-test)  
 T4/T5 control  $\leftrightarrow$  T4/T5 block: **p = 0.485, t = 0.711** (two-sided t-test)

At 60°:

*Shi<sup>ts</sup>* control  $\leftrightarrow$  T4/T5 control: **p = 0.609, t = -0.518** (two-sided t-test)

*Shi<sup>ts</sup>* control  $\leftrightarrow$  T4/T5 block: **p = 0.165, t = 1.443** (two-sided t-test)  
 T4/T5 control  $\leftrightarrow$  T4/T5 block: **p = 0.069, t = 1.916** (two-sided t-test)

**Fig. 4j**

At 30°

$R_{FTB} \leftrightarrow R_{BTF} \leftrightarrow R_L$  (T4/T5 block): **p = 0.742, F = 0.300** (one-way ANOVA)

At 60°

$R_{FTB} \leftrightarrow R_{BTF} \leftrightarrow R_L$  (T4/T5 block): **p = 0.902, F = 0.103** (one-way ANOVA)

**Fig. 4k**

At 30°

$M_{FTB} \leftrightarrow -M_{BTF}$  (*shi<sup>ts</sup>* control): **p < 0.001, t = 5.696** (two-sided t-test)

$M_{FTB} \leftrightarrow -M_{BTF}$  (T4/T5 control): **p = 0.028, t = 2.346** (two-sided t-test)

$M_{FTB} \leftrightarrow -M_{BTF}$  (T4/T5 block): **p = 0.209, t = 1.299** (two-sided t-test)

$M_{FTB} \leftrightarrow$  zero (T4/T5 block): **p = 0.447, t = 0.790** (two-sided t-test)

$M_{BTF} \leftrightarrow$  zero (T4/T5 block): **p = 0.325, t = -1.035** (two-sided t-test)

At 60°

$M_{FTB} \leftrightarrow -M_{BTF}$  (*shi<sup>ts</sup>* control): **p = 0.639, t = 0.476** (two-sided t-test)

$M_{FTB} \leftrightarrow -M_{BTF}$  (T4/T5 control): **p = 0.147, t = 1.508** (two-sided t-test)

$M_{FTB} \leftrightarrow -M_{BTF}$  (T4/T5 block): **p = 0.499, t = -0.687** (two-sided t-test)

$M_{FTB} \leftrightarrow$  zero (T4/T5 block): **p = 0.653, t = -0.463** (two-sided t-test)

$M_{BTF} \leftrightarrow$  zero (T4/T5 block): **p = 0.622, t = 0.508** (two-sided t-test)

**Figure 5**

30 trials per fly;  $N^{shi\ control} = 11$  flies,  $N^{T4/T5\ control} = 9$  flies,  $N^{T4/T5\ block} = 9$  flies.

**Fig. 5c**

*Shi<sup>ts</sup>* control  $\leftrightarrow$  T4/T5 control: **p = 0.394, t = 0.874** (two-sided t-test)

*Shi<sup>ts</sup>* control  $\leftrightarrow$  T4/T5 block: **p = 0.047, t = -2.127** (two-sided t-test)

T4/T5 control  $\leftrightarrow$  T4/T5 block: **p = 0.010, t = -2.908** (two-sided t-test)

**Fig. 5f**

*Shi<sup>ts</sup>* control  $\leftrightarrow$  T4/T5 control: **p = 0.176, t = 1.410** (two-sided t-test)

*Shi<sup>ts</sup>* control  $\leftrightarrow$  T4/T5 block: **p = 0.012, t = -2.797** (two-sided t-test)

T4/T5 control  $\leftrightarrow$  T4/T5 block: **p = 0.001, t = -3.999** (two-sided t-test)

**Figure S1**

**Fig. S1b**

$N^{shi\ control} = 10$  flies,  $N^{T4/T5\ control} = 10$  flies,  $N^{T4/T5\ block} = 10$  flies. Same flies as in Fig. 1b-d.

**Fig. S1d**

$N^{shi\ control} = 10$  flies,  $N^{T4/T5\ control} = 10$  flies,  $N^{T4/T5\ block} = 12$  flies. Same flies as in Fig. 1e-i.

**Figure S2**

40 trials per fly;  $N^{shi\ control} = 10$  flies,  $N^{T4/T5\ control} = 10$  flies,  $N^{T4/T5\ block} = 12$  flies. Same flies as in Fig. 1e-i.

**Fig. S2c**

$Shi^{ts}$  control  $\leftrightarrow$  T4/T5 control: **p = 0.023, t = -2.490** (two-sided t-test)  
 $Shi^{ts}$  control  $\leftrightarrow$  T4/T5 block: **p = 0.006, t = -3.049** (two-sided t-test)  
T4/T5 control  $\leftrightarrow$  T4/T5 block: **p = 0.095, t = -1.767** (two-sided t-test)

**Fig. S2f**

$Shi^{ts}$  control  $\leftrightarrow$  T4/T5 control: **p = 0.486, t = 0.710** (two-sided t-test)  
 $Shi^{ts}$  control  $\leftrightarrow$  T4/T5 block: **p = 0.319, t = -1.021** (two-sided t-test)  
T4/T5 control  $\leftrightarrow$  T4/T5 block: **p = 0.131, t = -1.575** (two-sided t-test)

**Figure S3**

15 trials per fly;  $N^{shi \text{ control}} = 10$  flies  $N^{T4/T5 \text{ control}} = 10$  flies,  $N^{T4/T5 \text{ block}} = 9$  flies.

**Fig. S3c**

$Shi^{ts}$  control  $\leftrightarrow$  T4/T5 control: **p = 0.561, t = 0.591** (two-sided t-test)  
 $Shi^{ts}$  control  $\leftrightarrow$  T4/T5 block: **p = 0.115, t = 1.659** (two-sided t-test)  
T4/T5 control  $\leftrightarrow$  T4/T5 block: **p = 0.252, t = 1.186** (two-sided t-test)

**Fig. S3f**

$Shi^{ts}$  control  $\leftrightarrow$  T4/T5 control: **p = 0.246, t = -1.200** (two-sided t-test)  
 $Shi^{ts}$  control  $\leftrightarrow$  T4/T5 block: **p = 0.047, t = 2.136** (two-sided t-test)  
T4/T5 control  $\leftrightarrow$  T4/T5 block: **p = 0.008, t = 3.004** (two-sided t-test)

**Fig. S3g**

Uniform  $\leftrightarrow$  Sine grating ( $shi^{ts}$  control): **p = 0.016, t = -2.651** (two-sided t-test)  
Uniform  $\leftrightarrow$  Sine grating (T4/T5 control): **p < 0.001, t = -4.079** (two-sided t-test)  
Uniform  $\leftrightarrow$  Sine grating (T4/T5 block): **p = 0.021, t = -2.553** (two-sided t-test)

## Manuscript VI

### Neural Mechanisms for *Drosophila* Contrast Vision

Armin Bahl, Etienne Serbe, Matthias Meier, **Georg Ammer**, and Alexander Borst

#### Author Contributions

A.Ba. and A.Bo. designed the study. E.S. and M.M. performed electrophysiological recordings. **G.A.** provided the Mi1, Tm3, and Mi1/Tm3-Gal4 lines and did the immunostainings. A.Ba. built the behavioral setup, programmed the visual stimuli, performed the behavioral experiments, and analyzed the data. A.Ba. wrote the paper with help from the other authors.

**Neuron** 88, 1240-1252. doi:10.1016/j.neuron.2015.11.004

## Neural Mechanisms for *Drosophila* Contrast Vision

### Highlights

- Flies are susceptible to contrast illusions in the same way as human observers
- Contrast and motion computations are carried out in parallel pathways
- Medulla cells Mi1 and Tm3 form a center-surround antagonism for contrast computation
- Signals from the motion and contrast pathways converge again in the lobula plate

### Authors

Armin Bahl, Etienne Serbe, Matthias Meier, Georg Ammer, Alexander Borst

### Correspondence

arminbahl@fas.harvard.edu

### In Brief

Bahl et al. employ optical illusions in behavioral experiments in *Drosophila* to investigate mechanisms and neuronal correlates of spatial contrast computation. They find that spatial contrast and motion cues are computed largely in parallel and that both pathways eventually converge.



Bahl et al., 2015, Neuron 88, 1240–1252  
December 16, 2015 ©2015 Elsevier Inc.  
<http://dx.doi.org/10.1016/j.neuron.2015.11.004>

CellPress

# Neural Mechanisms for *Drosophila* Contrast Vision

Armin Bahl,<sup>1,2,\*</sup> Etienne Serbe,<sup>1</sup> Matthias Meier,<sup>1</sup> Georg Ammer,<sup>1</sup> and Alexander Borst<sup>1</sup>

<sup>1</sup>Max Planck Institute of Neurobiology, Am Klopferspitz 18, 82152 Martinsried, Germany

<sup>2</sup>Present address: Department of Molecular and Cell Biology, Harvard University, 16 Divinity Avenue, Cambridge, MA 02138, USA

\*Correspondence: [arminbahl@fas.harvard.edu](mailto:arminbahl@fas.harvard.edu)

<http://dx.doi.org/10.1016/j.neuron.2015.11.004>

## SUMMARY

Spatial contrast, the difference in adjacent luminance values, provides information about objects, textures, and motion and supports diverse visual behaviors. Contrast computation is therefore an essential element of visual processing. The underlying mechanisms, however, are poorly understood. In human psychophysics, contrast illusions are means to explore such computations, but humans offer limited experimental access. Via behavioral experiments in *Drosophila*, we find that flies are also susceptible to contrast illusions. Using genetic silencing techniques, electrophysiology, and modeling, we systematically dissect the mechanisms and neuronal correlates underlying the behavior. Our results indicate that spatial contrast computation involves lateral inhibition within the same pathway that computes motion of luminance increments (ON pathway). Yet motion-blind flies, in which we silenced downstream motion-sensitive neurons needed for optomotor behavior, have fully intact contrast responses. In conclusion, spatial contrast and motion cues are first computed by overlapping neuronal circuits which subsequently feed into parallel visual processing streams.

## INTRODUCTION

Computation of spatial contrast, the local difference in adjacent luminance values, allows animals to distinguish between figure and ground, to detect edges, and to visually adapt to the dynamic range of the current visual scene. Despite the importance of such computations for a wide range of visual behaviors, the mechanisms underlying spatial contrast computation are not well-understood in any organism. Optical illusions elicit visual perceptions that differ from physical reality and can serve as a tool in psychophysical experiments to explore how the brain computes. For example, when a gray bar of uniform luminance is embedded in a gradient background, humans perceive a brightness gradient within the bar, which indicates that human brightness estimation is based on relative rather than absolute luminance (Adelson, 2000). Such illusions are static and require the experimental subject to report its perception. Hence, they are difficult to use in other species. Motion illusions, however, often elicit behavioral responses and can be transferred to sim-

ple model organisms (Bülthoff and Götz, 1979; Eichner et al., 2011; Tuthill et al., 2011). A motion illusion based on spatial contrast computation, the contrast motion illusion, has recently been described in human psychophysics (Shapiro and Hamburger, 2007). Here, several dark stripes are embedded in a gradient background which is dark on the left and bright on the right end. When all stripes brighten simultaneously, humans report illusory motion to the right (see Movie S1 available online). The contrast motion illusion is thought to rest on similar principles as another type of contrast illusion known as the single-field contrast asynchrony illusion (Shapiro et al., 2004): A single stripe is embedded in a dark or in a bright background. When an identical sinusoidal luminance change is applied to the stripe, humans report that the modulations are out of phase for the different background conditions (Movie S2). This indicates that humans perceive temporal variations of spatial contrast rather than luminance. Responses to such contrast stimuli cannot be explained by classical models of motion vision based on spatio-temporal correlation of luminance (Shapiro et al., 2005). Alternatively, it was hypothesized that rectified center-surround filters compute spatial contrast and further integrate such cues in higher visual centers. However, detailed systematic dissections of the computational mechanisms are missing, and very little is known about potential neuronal circuits involved.

In order to investigate visual processing at the cellular level, humans offer limited experimental access. In contrast, other species, such as the fruit fly *Drosophila melanogaster*, provide various tools for such a purpose. *Drosophila* has a set of innate and robust visual behaviors and can be genetically modified. The anatomy and connectivity of the visual system is well-known (Fischbach and Dittrich, 1989; Takemura et al., 2013) and is accessible via electrophysiology (Behnia et al., 2014; Joesch et al., 2008). The visual system is arranged in a retinotopic manner and forms several neuropils for visual processing (Figure 1A). Photoreceptor input from R1–R6 provides direct or indirect signals to lamina neurons L1–L5 (Figures 1B and S1A). Subsequently, L1/L5 and L2/L3/L4 form separate visual pathways specialized for motion computation of luminance increments (ON pathway) and decrements (OFF pathway), respectively (Clark et al., 2011; Eichner et al., 2011; Joesch et al., 2010; 2013; Maisak et al., 2013; Meier et al., 2014; Strother et al., 2014). Connectomics has revealed potential components of both pathways, namely Mi1 and Tm3 within the ON pathway and Tm1, Tm2, Tm4, and Tm9 within the OFF pathway (Shinomiyama et al., 2014; Takemura et al., 2013). Neurons in the two pathways converge onto T4 and T5 neurons (Bausenwein et al., 1992), which are the first direction-selective elements in the fly visual system and which are selective for motion of

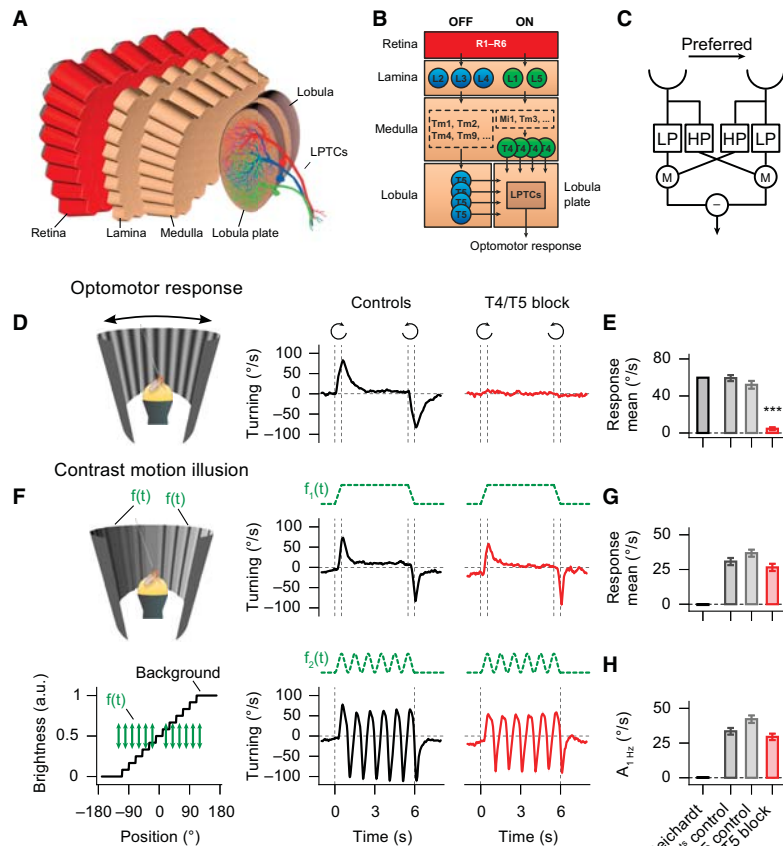


**Figure 1. Control and Motion-blind Flies Respond to Contrast Motion Illusions**

(A and B) Schematic of the fly's optic lobe and its cellular composition within the ON (green) and OFF (blue) pathways.

(C) Hassenstein-Reichardt detector with preferred direction to the right.

(D) Experiment with full-field moving sine-grating. Motion direction and stimulus on- and offset are illustrated by circular arrows and vertical dashed lines.

(E) Quantification of the optomotor response (response to clockwise motion minus that to counterclockwise motion divided by two; averaged between 0.1 and 1.1 s after stimulus onset) of the Hassenstein-Reichardt detector simulation and of the experimental groups.

(F) Contrast motion illusion. Several vertical stripes are embedded in a stepped luminance gradient background (black trace in bottom part) and simultaneously change luminance according to  $f_1(t)$  or  $f_2(t)$  (green arrows and green dashed time traces).

(G) Quantification of the response to the contrast motion illusion with stripe luminance dynamics according to  $f_1(t)$  (response to luminance increment minus that to luminance decrement divided by two; averaged between 0.1–1.1 s after stimulus onset) of the Hassenstein-Reichardt detector simulation and of the experimental groups.

(H) Quantification of the response for luminance dynamics according to  $f_2(t)$  (1 Hz amplitude of the Fourier-transformed response during stimulation) of the Hassenstein-Reichardt detector simulation and of the experimental groups.

Data represent mean ± SEM with  $n = 12$ –13 flies per group.  $p$  values based on a two-sided Welch's  $t$  test, comparing T4/T5 block flies with both control groups (\*\* $p < 0.001$ ;  $p = 0.26$  in G;  $p = 0.25$  in H). Detailed statistics in Table S1A. Hassenstein-Reichardt detector simulation result in black, shibire<sup>ts</sup> flies in dark gray, T4/T5 control flies in light gray and T4/T5 block flies. Raw time traces for control flies (black) in (D) and (F) are pooled from both control groups.

brightness increments and decrements, respectively (Maisak et al., 2013). Mi1 and Tm3 have been proposed to provide temporally different and spatially offset inputs to the T4 dendrite, giving rise to its direction-selectivity (Behnia et al., 2014; Takeamura et al., 2013). Furthermore, Mi1 and Tm3 were recently shown to also be functionally involved in the computation of motion of brightness increments (Ammer et al., 2015). Eventually, T4 and T5 neurons converge onto lobula plate tangential cells (Figures S1B and S1C) and render vertical system cells and horizontal system cells direction-selective for motion along the vertical and horizontal axis, respectively. Genetic silencing of T4 and T5 neurons abolishes direction-selective responses in lobula plate tangential cells (Schnell et al., 2012). Moreover, in behavioral experiments, flies are motion-blind and no longer show an optomotor response (Bahl et al., 2013). Various aspects of fly motion vision can be modeled by the Hassenstein-Reichardt detector (Hassenstein and Reichardt, 1956). In this model, luminance signals from two neighboring ommatidia are differently filtered in time and subsequently multiplied. Subtracting the output of a mirror-symmetric detector subunit leads to fully

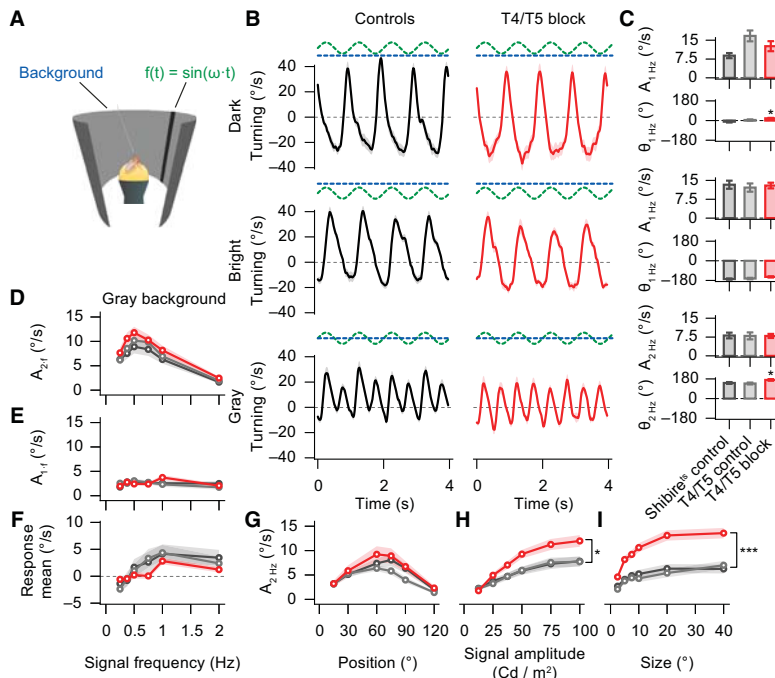
opponent direction-selective responses (Figure 1C). Computation of visual cues other than motion, such as color (Morante and Desplan, 2008) or spatial contrast, are less explored in flies.

In this paper, we employ contrast illusions as a tool to study spatial contrast computation in *Drosophila*. We use tethered flies walking on an air-suspended ball in a virtual environment. Throughout the paper, we measure fly turning speed in response to various kinds of visual stimuli, which allows quantitative comparisons of the behavior and systematic dissections of the underlying computational mechanisms. In order to identify neuronal correlates, we use the GAL4-UAS system (Brand and Perrimon, 1993) to genetically target specific subsets of neurons for silencing synaptic transmission via temperature-sensitive shibire (shibire<sup>ts</sup>) (Kitamoto, 2001; Pfeiffer et al., 2012).

## RESULTS

### Flies Respond to Contrast Motion Illusions

In a first set of control experiments, we tested behavioral performance to full-field sine-grating motion (Figure 1D). As expected,



control flies responded with a robust optomotor response, a behavior predicted by the Hassenstein-Reichardt detector (Figures 1D and 1E). Next, we tested the contrast motion illusion as used in human psychophysics (Shapiro and Hamburger, 2007) (Figure 1F): several stripes are embedded in a stepped luminance gradient. We applied identical luminance dynamics to the stripes. The stimulus is designed such that luminance change is symmetric around the fly and, therefore, potential directed turning responses toward luminance change average out. Moreover, the local stripe environment is symmetric in luminance, and hence pairwise local comparisons, as performed by the Hassenstein-Reichardt detector, cancel out as well. We tested two luminance dynamics for the stripes: first, stripe luminance increased, remained bright for a few seconds, and then decreased again. Second, stripe luminance oscillated sinusoidally at 1 Hz. As expected, the Hassenstein-Reichardt detector predicted no turning response for both stimuli (Figures 1G and 1H). However, control flies robustly responded to the contrast motion illusion: when the background was dark on the left and bright on the right end, a luminance increase elicited turning to the right and a luminance decrease turning to the left. For the 1 Hz luminance oscillations, control flies responded with a robust 1 Hz oscillatory turning response. Notably, response strengths were similar to those observed for the optomotor response, and turning directions matched the direction of illusory motion reported by human observers (Shapiro and Hamburger, 2007).

Since the observed responses to the contrast motion illusion cannot be explained by the Hassenstein-Reichardt detector,

we developed two alternative hypotheses which could explain the result. First, the behavior might be a side effect of potentially unexplored interactions within the motion pathway. Second, it might be controlled by an independent visual pathway dedicated to the computation of spatial contrast. In order to test both hypotheses, we used a driver line which selectively labels T4 and T5 neurons, allowing us to silence synaptic transmission from these cells via *shibire*<sup>ts</sup>. T4/T5 block flies are completely motion-blind and lack an optomotor response (Bahl et al., 2013) (Figures 1D and 1E). Yet, when we tested the contrast motion illusion, such flies responded with exactly the same magnitude and direction as control flies (Figures 1F–1H). In conclusion, spatial contrast and motion computations seem to be carried out in parallel visual pathways.

#### Flies Respond to Single-Field Contrast Asynchronies

In order to gain a better understanding of the computational mechanisms underlying spatial contrast computation in the fly brain, we further investigated behavioral responses to another type of contrast illusion known as the single-field contrast asynchrony illusion (Shapiro et al., 2004). In particular, this stimulus allows us to investigate whether flies respond to signed or unsigned (absolute) spatial contrast, which is not possible with the global contrast motion illusion. We presented flies with a single vertical stripe in the right visual field and modulated the stripe luminance sinusoidally at 1 Hz (Figure 2A). Such a stimulus contains two components, flicker of luminance and flicker of relative spatial luminance (spatial contrast flicker). The luminance flicker

**Figure 2. Control and Motion-Blind Flies Respond to Single-Field Contrast Asynchrony Illusions**

(A) A single nonmoving vertical stripe on the right side of the fly flickers sinusoidally in luminance with frequency  $\omega$  on a uniform background. (B) Responses for 1 Hz stripe flicker (identical in all conditions; green dashed lines) on three different backgrounds (dark, bright, and gray; blue dashed lines). (C) Quantification of amplitude  $A$  and phase  $\Theta$  of the 1 Hz or 2 Hz response components. (D–F) Quantification of the response amplitudes (2-f and 1-f components) and the response mean to stripes flickering at different frequencies on a gray background. (G–I) Quantification of 2 Hz amplitude response components to a 1 Hz flickering stripe on a gray background when varying stripe position, signal amplitude, or size. All stimuli lasted for 10 s, the last 9 s were analyzed. Only the last 4 s are illustrated in (B). Data represent mean  $\pm$  SEM with  $n = 12$ –14 flies per group.  $p$  values based on a two-sided Welch's  $t$  test, comparing T4/T5 block flies with both control groups (\* $p < 0.05$ ; \*\* $p < 0.001$ ;  $p = 0.18$ , 0.69, and 0.99 for response amplitudes for the different background conditions, respectively, and  $p = 0.10$  for response phase for the bright background in C). Detailed statistics in Table S1B. *Shibire*<sup>ts</sup> flies in dark gray, T4/T5 control flies in light gray, T4/T5 block flies in red. Raw time traces for control flies (black) in (B) are pooled from both control groups.

dynamics remain independent of background light levels but the spatial contrast flicker is background-dependent. To explore responses to spatial contrast flicker, we varied background light levels. When the stripe was presented against a dark background, control and T4/T5 block flies responded with 1 Hz turning speed oscillations of large amplitude with the same phase as the stimulus (Figures 2B and 2C). In contrast, when the stripe was presented against a bright background, control and T4/T5 block flies still responded with 1 Hz turning speed oscillations but responses were shifted in phase by 180°. Interestingly, an intermediate gray background led to 2 Hz turning speed oscillations, following the 2 Hz absolute spatial contrast dynamics of the flickering stripe. In summary, the observed behaviors rely on the computation of unsigned spatial contrast and are largely independent of T4 and T5 neurons, both in terms of amplitude and phase. These findings provide further evidence that spatial contrast computations are carried out in a T4/T5-independent visual circuit.

We further characterized the response oscillation amplitude to different parameters of a flickering stripe on a gray background (Figures 2D–2I). We first varied stimulus frequency. For all tested frequencies, control and T4/T5 block flies responded with turning speed oscillations of the frequency of the spatial contrast flicker (2·f component of the response), with the strongest response for 0.5 Hz signals (Figure 2D). The 1·f response component, corresponding to the luminance dynamics, however was small (Figure 2E) and response averages over time were close to zero (Figure 2F). The latter result is in contrast to previous findings which suggested that flickering stripes elicit strong directed turning toward the stimulus (Bahl et al., 2013; Pick, 1974). We further characterized responses as function of azimuthal position, signal amplitude, and size. For both control and T4/T5 block flies, responses were strongest for stripes located at ~70° (Figure 2G), became stronger with increasing signal amplitude (Figure 2H), and increased for stripe sizes up to 20°, after which the response saturated (Figure 2I).

The amount of luminance flicker increases with stripe size. Spatial contrast flicker however only occurs at the boundary of the flickering stripe and remains independent of size once the stripe exceeds the receptive field of the underlying neuronal elements. Interestingly, T4/T5 block flies responded stronger than control flies for large signal amplitudes and for large stripe sizes (Figures 2H and 2I). This suggests that luminance flicker, analyzed via T4/T5 cells, can reduce the responsiveness of the circuit performing spatial contrast computation.

#### Receptive Field Properties of Spatial Contrast Computation

In further experiments, we wanted to better characterize the spatial receptive field properties of the contrast response. To this end, we used counterphase flicker (Movie S3) which provide contrast flicker covering a large extent of the visual field. Such stimuli do not contain any net-motion and the average luminance in the area of stimulation remains constant. Hence, counterphase flicker allow characterization of the contrast system in isolation. We presented stimuli within a unilateral circular window on the right side of the fly and varied spatial frequency and orientation (Figure 3A).

As a control experiment, we first characterized responses to moving sine-gratings. As expected, control flies turned right and left for front-to-back and back-to-front motion, respectively, with comparable absolute amplitudes (Figure 3B). When we tested different spatial frequencies, motion responses in control flies decreased for high spatial frequencies and even inverted for spatial frequencies larger than 0.1 cycles per degree ( $\lambda = 10^\circ$ ) but no tuning was apparent for low spatial frequencies (Figures 3C and 3E). The response reduction and inversion for high spatial frequencies is due to the resolution of the *Drosophila* eye (~5°) (Götz, 1964). Next, we presented grating motion along different axes and quantified direction-selectivity (Figures 3D and 3E). As expected, control flies were able to discriminate motion direction well and did not respond with horizontal turning to motion along the vertical axis. Irrespective of spatial frequency or direction, T4/T5 block flies did not respond to any of the motion stimuli (Figures 3B–3E).

We next tested counterphase flicker. The luminance at each point was modulated at 1 Hz, resulting in a 2 Hz modulation of the absolute spatial contrast (Movie S3). If flies follow changes in absolute spatial contrast, they should respond with a 2 Hz oscillation in turning speed. Indeed, this was the case for both control and T4/T5 block flies (Figure 3F). Quantification of the response to different spatial frequencies revealed a clear tuning peak at a spatial frequency of 0.5 cycles per degree ( $\lambda = 20^\circ$ ) (Figures 3G and 3I). Such band-pass properties are reminiscent of a spatial antagonism involving center-surround receptive fields, which indicates that lateral inhibition is involved in the computation of spatial contrast. In order to characterize the receptive field isotropy of the contrast system, we quantified turning responses to differently oriented counterphase flicker (Figures 3H and 3I). We found that responses of control and T4/T5 block flies were strongly orientation-tuned. Interestingly, counterphase flicker along the vertical axis also elicited small responses and the orientation tuning curves were shifted by ~30°. This shift corresponds to a 30° backward-tilted pattern and is probably due to the position of the flies which walk slightly upward on the ball.

Responses to orientations perpendicular to the preferred orientation were almost zero for control flies but still present in T4/T5 block flies. It is known that counterphase flicker elicits depolarization in T4/T5 neurons (Maisak et al., 2013). T4 and T5 cells then target lobula plate tangential cells as well as lobula plate intrinsic inhibitory interneurons (Mauss et al., 2015). If the contrast and motion pathways converge in later processing stages, the latter cells might then actively suppress contrast responses along the vertical axis, improving counterphase flicker orientation tuning in control flies.

In summary, the observed spatial frequency and orientation tuning properties suggest a mechanism for contrast computation which involves lateral inhibition. T4 and T5 neurons are not required for such computations.

#### Identification of Neuronal Elements of Contrast Computation

Having found that unilateral counterphase flicker elicit robust contrast responses, we next used this stimulus to screen for neuronal elements underlying contrast computation. To maximize stimulus strength, we presented a vertically oriented sine-

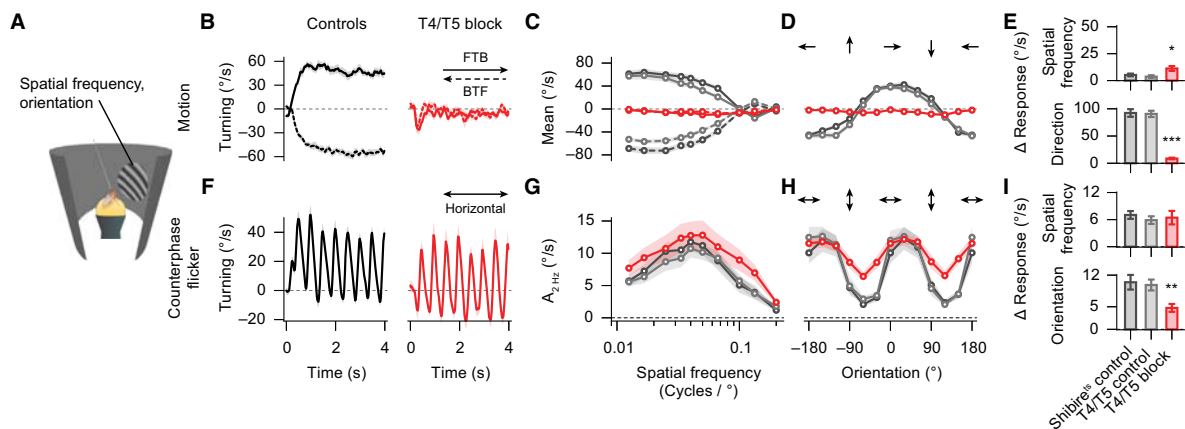


**Figure 3. Characterization of Receptive Field Properties of Motion and Contrast Systems**

(A) A circular window is shown on the right side of the fly in which a sine-grating moves or flickers in counterphase with different spatial frequencies or orientations. (B) Example traces for horizontal front-to-back motion (FTB; solid lines) and back-to-front motion (BTF; dashed lines). (C and D) Spatial frequency and orientation tuning for motion. (E) Quantification of spatial frequency tuning (difference between maximal absolute response and that for the smallest spatial frequency) and direction-selectivity (difference between maximal absolute response and that of motion in the opposite direction). (F) Example traces for the counterphase flicker stimulus. (G and H) Spatial frequency and orientation tuning curves of the 2 Hz response component. (I) Quantification of spatial frequency tuning (difference between maximal absolute response and that for the smallest spatial frequency) and orientation tuning (difference between maximal absolute response and that for counterphase flicker in perpendicular orientation). All stimuli lasted for 10 s, the last 9 s were analyzed, and the first 4 s are illustrated in (B) and (F). Data represent mean  $\pm$  SEM with  $n = 12$ –14 flies per group.  $p$  values based on a two-sided Welch's  $t$  test, comparing T4/T5 block flies with both control groups (\* $p < 0.05$ ; \*\* $p < 0.01$ ; \*\*\* $p < 0.001$ ;  $p = 0.75$  for the spatial frequency tuning in I). Detailed statistics in Table S1C. Shibe<sup>ts</sup> flies in dark gray, T4/T5 control flies in light gray, T4/T5 block flies in red. Raw time traces for control flies (black) in (B) and (F) are pooled from both control groups.

grating in a rectangular window on the right side of the fly. The sine-grating either moved front-to-back or back-to-front along the horizontal axis with a temporal frequency of 1 Hz or it flickered in counterphase, providing a 2 Hz spatial contrast flicker (Figures 4A and 4B). As expected, control flies followed the direction of stimulus motion (Figure 4C) and responded robustly to counterphase flicker with strong 2 Hz oscillatory turning responses (Figure 4D), as previously described (Figures 3B and 3F). We tested ten different Gal4 driver lines, labeling cells in the lamina, medulla, and lobula (Figures S2A and S2B), and quantified optomotor behavior (Figure 4E) and responses to counterphase flicker (Figure 4F) for control and block flies. All flies had a comparable walking speed of around 1 cm/s (Figure S2D).

First, we tested the optomotor response in flies with silenced lamina neurons L1–L5. Surprisingly, we did not find response reductions when blocking L1 or L2. This can be attributed to the fact that the ON or OFF motion pathways receive redundant signals when stimulated with sine-grating motion (Joesch et al., 2010; Silies et al., 2013; Tuthill et al., 2013). Nevertheless, we found small but significant decreases when blocking L3 or L5 and an unexpected mild increase in the response when silencing L4. Next, we quantified responses to the counterphase flicker: Blocking output of L1 led to a strong reduction of the contrast response. Blocking L2, L3, or L5 however showed no significant phenotypes. Notably, silencing L4 almost doubled the response strength, suggesting that L4 not only modulates elements for

motion computation (Meier et al., 2014), but also affects the contrast computation circuit.

These experiments indicated that the ON pathway seems to be the key player for contrast computation. In order to test for its sufficiency, we next silenced the output of L2, L3, and L4 at the same time, abolishing all input channels into the OFF pathway. We did not find a reduction of the contrast response even though further analysis indicated that the triple lamina block is functional (Figure S3). This finding provides evidence that the ON pathway alone can compute spatial contrast.

We next tested medulla interneurons Mi1 and Tm3 which are known to be the major postsynaptic elements to L1 (Takemura et al., 2013). We first tested motion responses: Mi1 block flies showed a mild, but significant, optomotor response reduction. In contrast, using two different driver lines for Tm3, we found that silencing Tm3 output did not alter the response. Blocking the output of Mi1 and Tm3 together, using a driver line which labels both neuron types (revealed by stochastic GFP-labeling; Figures S2A and S2C), led to a strong response reduction of ~50% compared to controls. Because L1-silenced flies did not show such a phenotype, this finding suggests that further lamina input to Mi1 or Tm3 play a role in motion computation, such as L3 (Silies et al., 2013; Takemura et al., 2013). As expected, silencing T4 and T5 neurons abolished optomotor behavior completely (Figures 4C and 4E).

When testing counterphase flicker, Mi1-silenced flies showed a response reduction tendency, and blocking Tm3 output led to

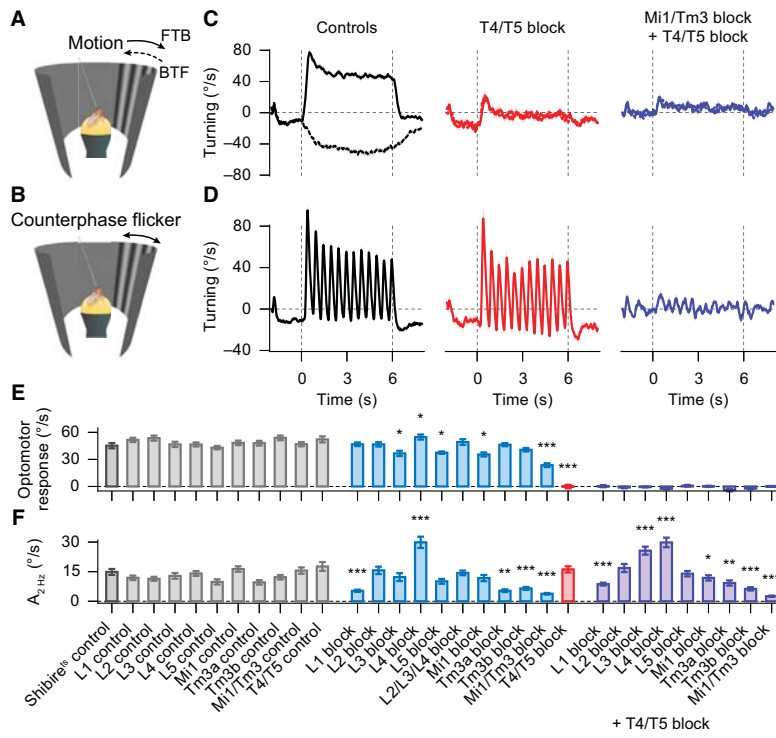


**Figure 4. Mi1 and Tm3 Neurons Are Key Neuronal Elements of Contrast Computation**

(A and B) A vertical oriented sine-grating either moves front-to-back (FTB), back-to-front (BTF; dashed lines), or flickers in counterphase in a rectangular window on the right side of the fly.

(C and D) Example traces of control, T4/T5 block, and combined Mi1/Tm3 block + T4/T5 block flies. Vertical gray dashed lines indicate onset and offset of the stimulus.

(E) Quantification of the optomotor response (response to front-to-back motion minus response to back-to-front motion divided by two; averaged from 2 to 6 s).

(F) Quantification of the response to counterphase flicker (2 Hz response amplitude component of the Fourier-transformed signal from 2 to 6 s).

Data represent mean  $\pm$  SEM with  $n = 14\text{--}19$  flies per group.  $p$  values based on a two-sided Welch's  $t$  test, comparing the group of block flies with respective control groups (for example, L1 block with L1 control and shibire<sup>ts</sup> control; groups with combined lamina or medulla block + T4/T5 block (right side) were compared only to the T4/T5 block group; \* $p < 0.05$ ; \*\* $p < 0.01$ ; \*\*\* $p < 0.001$ ). Detailed statistics in Tables S4 and S5. Expression patterns and list of genotypes in Figures S2A–S2C. Shibire<sup>ts</sup> control flies in dark gray, Gal4 control flies in light gray, lamina and medulla block flies in blue, T4/T5 block flies in red, and combined lamina or medulla block + T4/T5 block flies in violet. Raw time traces for control flies (black) in (C) and (D) are pooled from shibire<sup>ts</sup> control, T4/T5 control, and Mi1/Tm3 control flies. See Figures 1A, 1B, and S1A for schematics of cell types and locations.

a strong response reduction comparable to that found in L1-silenced flies. Since blocking Tm3 left some residual response intact, we tested the combined Mi1/Tm3 block flies and found that responses to counterphase flicker were almost completely abolished in these flies. Yet, when blocking T4/T5, contrast responses remained fully intact (Figures 4D and 4F), as found previously (Figures 3F–3I).

L1, Mi1, and Tm3 are part of the ON pathway for motion vision which converges onto T4 cells (Takemura et al., 2013). In order to determine whether these cells act directly on the contrast response or indirectly through T4, we repeated the screen in a T4/T5 block background. Moreover, working in such a simplified visual circuit makes it easier to interpret a particular phenotype when silencing neurons upstream to T4 and T5. As expected, the optomotor response remained abolished for flies in which lamina or medulla neurons were blocked in addition to T4 and T5 (Figure 4E). When analyzing responses to counterphase flicker, we found that blocking L1 led to a strong response reduction while silencing L3 or L4 increased the response strength, and blocking L2 or L5 did not have a significant effect (Figure 4F). Blocking Mi1 led to a small, but significant, response reduction and blocking Tm3 strongly reduced the response. We also combined the Mi1/Tm3 block with the T4/T5 block and found that such flies no longer responded at all to the counterphase flicker (Figures 4D and 4F). We conclude that medulla interneurons Mi1 and Tm3 act directly on the contrast response, and not via T4/T5, and that the response is modulated by L3 and L4.

Mi1 and Tm3 neurons are thought to provide temporally different and spatially offset signals to the dendrites of T4 neurons for computing motion direction of luminance increments (Behnia et al., 2014; Takemura et al., 2013). The optomotor response reduction we observed when Mi1 and Tm3 were jointly silenced is in agreement with previous findings (Ammer et al., 2015) which indicated an important role of these neurons in fly motion vision. Our data further suggest that Mi1 and Tm3 are also key elements for spatial contrast computation. In addition to targeting T4 neurons, Mi1 and Tm3 project onto yet unidentified neurons which function in parallel to T4 cells. In summary, thus, motion and contrast computations are carried out by shared neuronal circuit elements within the ON pathway and, subsequently, visual processing streams diverge.

#### Mi1 and Tm3 Neurons Form a Center-Surround Antagonism

We found that responses to counterphase flicker were spatial frequency-tuned, which suggested that the underlying neuronal system uses lateral inhibition for contrast computation (Figures 3G and 3I). Taking away lateral inhibition should decrease responses to intermediate spatial frequency but should increase the response strength to large spatial frequencies, in particular to homogeneous field flicker. Such a differential effect allows distinguishing lateral inhibition from localized inhibition as silencing a cell involved in localized inhibition should affect responses to all spatial frequencies equally. Our experiments

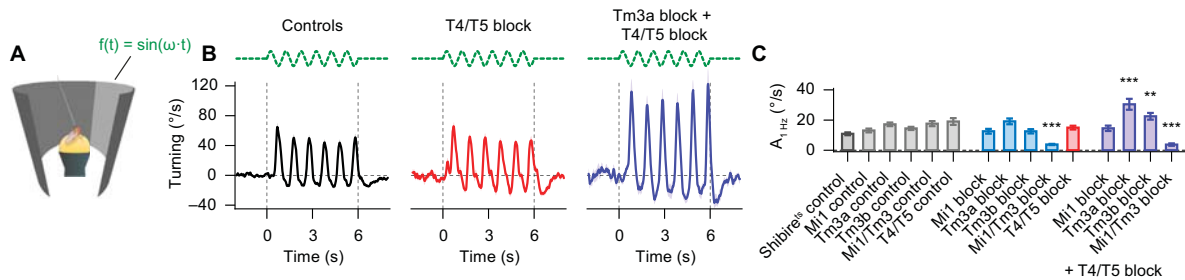


**Figure 5. Tm3 Cells Provide Lateral Inhibition**

(A) A large field sinusoidal 1 Hz luminance flicker (green dashed lines) on a gray background is presented on the right side. (B) Example response traces for control, T4/T5 block and combined Tm3a block + T4/T5 block flies. (C) Response quantification (1 Hz response amplitude component of the Fourier-transformed signal from 2 to 6 s). Data represent mean  $\pm$  SEM with  $n = 14\text{--}19$  flies per group.  $p$  values based on a two-sided Welch's  $t$  test, comparing the group of block flies with respective control groups (groups with combined lamina or medulla block + T4/T5 block were compared only to the T4/T5 block group; \*\* $p < 0.01$ ; \*\*\* $p < 0.001$ ). Detailed statistics in Table S1D. Shibire<sup>ts</sup> control flies in dark gray, Gal4 control flies in light gray, lamina and medulla block flies in blue, T4/T5 block flies in red, and combined lamina or medulla block + T4/T5 block flies in violet. Raw time traces for control flies (black) in (B) are pooled from shibire<sup>ts</sup> control, T4/T5 control, and Tm3a control flies. See Figures 1A, 1B, and S1A for schematics of cell types and locations.

show that silencing Mi1 or Tm3 leads to a reduced responsiveness to counterphase flicker of intermediate spatial frequency ( $\lambda = 20^\circ$ ; Figure 4F). To test for responses to large spatial frequency flicker, we presented flies with a wide 1 Hz homogeneously flickering region on the right side (Figure 5A). We observed that the turning speed of control and T4/T5 block flies followed the luminance dynamics of the stimulus: Flies turned right for luminance decrease and left for luminance increase (Figures 5B and 5C). Blocking Mi1 or Tm3, with intact T4 and T5, had no effect on the behavior, and silencing Mi1 in a T4/T5-blocked background did not change the behavior either. However, silencing Tm3 together with T4 and T5 cells almost doubled the response amplitude. In contrast, blocking Mi1 and Tm3 at the same time abolished responses to field flicker completely (Figure 5C). These findings, together with our previous silencing experiments (Figure 4F), suggest that Mi1 and Tm3 neurons form a center-surround antagonism for the computation of spatial contrast. In this arrangement, Tm3 cells provide lateral inhibition, not localized inhibition.

The fact that the Tm3 block phenotype was only visible when T4 and T5 neurons were additionally silenced suggests an interesting interplay between the motion and contrast circuit: Since Tm3 is connected to T4 (Takemura et al., 2013), Tm3 output likely modulates T4 responses to field flicker. In turn, T4 and T5 output can reduce the responsiveness of the contrast system using mechanisms discussed previously (Figures 2H, 2I, 3H, and 3I). Hence, silencing only Tm3 might show no phenotype in the response to field flicker because an increased flicker sensitivity in the contrast system is compensated by an increased flicker sensitivity in the motion system.

#### Contrast Illusions in Mi1/Tm3-Silenced Flies

Having identified Mi1 and Tm3 as the key players shaping response dynamics to counterphase and homogeneous field flicker (Figures 4 and 5), we wondered whether such flies also show deficits when presented with contrast illusions (Figures 1F–1H and 2). We first stimulated Mi1/Tm3-silenced flies with

full-field sine-grating motion and found a reduction of the opto-motor response (Figures 6A and 6B). The effect was smaller compared to our previous findings (Figure 4E), since we used bilateral motion stimuli here, likely leading to a response saturation. When presenting the contrast motion illusion (Figure 1F) to Mi1/Tm3 block flies, turning responses were completely abolished (Figures 6C and 6D). This finding suggests that the contrast motion illusion is mediated by spatial contrast computations within the ON pathway. Subsequently, neurons postsynaptic to Mi1/Tm3 globally integrate these contrast cues and control behavior.

We also tested Mi1/Tm3 block flies with the single-field contrast asynchrony illusion (compare Figures 2A–2C, 6E, and 6F). The response amplitude to a flickering stripe on a dark background was not different to that of control flies. Yet, when the background was bright or gray, response amplitudes were strongly reduced (Figures 6E and 6F). Moreover, we compared response phases for the dark and bright background condition and found that responses were still in antiphase to one another. However, turning speed oscillations for the two background conditions were shifted in phase by  $\sim 90^\circ$  compared to controls. The same was true for Mi1/Tm3 block flies in a T4/T5 block background (Figure S4).

We also performed spatial frequency tuning experiments in Mi1/Tm3 block flies (Figures 6G and 6H). To our surprise, we found that for low spatial frequencies, control and Mi1/Tm3 block flies showed weak but identical responses to counterphase flicker. Only for intermediate spatial frequencies, control flies had a much stronger contrast response.

These experiments indicated that beside the Mi1/Tm3-dependent local spatial contrast system, another Mi1/Tm3-independent contrast system exists which operates on larger spatial scales, perhaps globally. To directly test this hypothesis, we slightly modified the single-field contrast asynchrony stimulus and now only varied the background luminance locally around the 1 Hz flickering stripe (Figure S5A). The rest of the arena was gray. Hence, the global light levels remain approximately

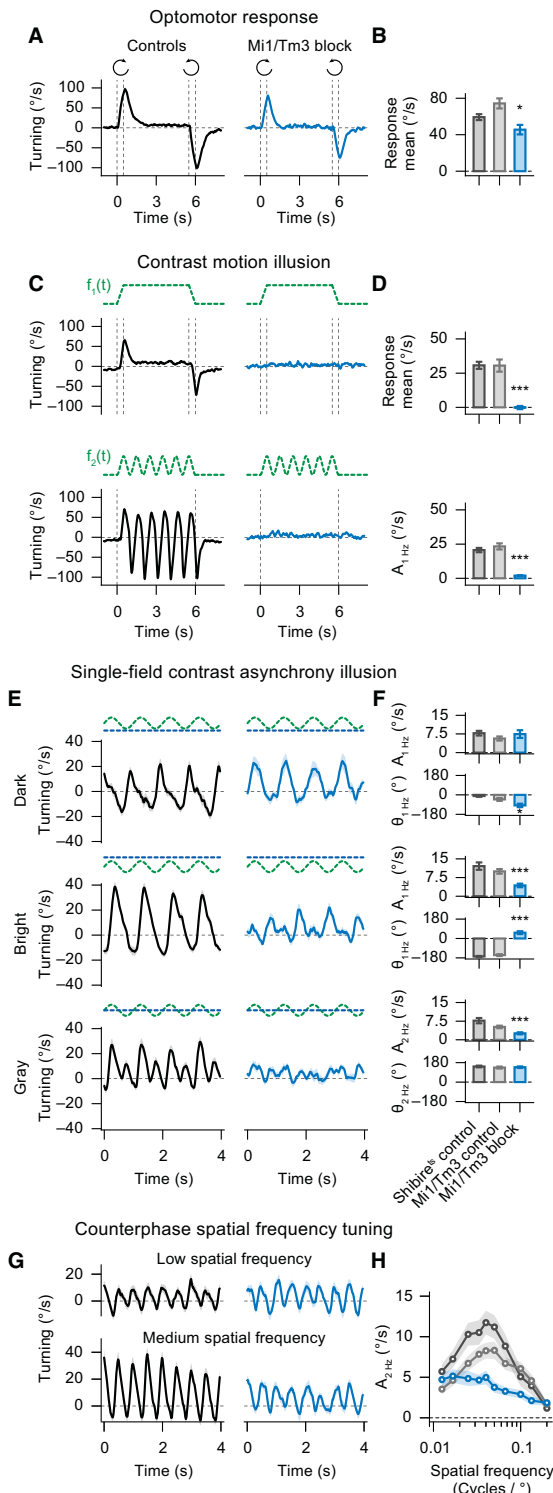


**Figure 6. Mi1/Tm3-Silenced Flies Lack Responses to Contrast Illusions**

(A and B) Responses of control and Mi1/Tm3 block flies to full-field sine-grating motion (= optomotor response) and quantification (see Figures 1D and 1E for comparison).

(C and D) Responses to contrast motion illusions with stripe luminance profiles  $f_1(t)$  and  $f_2(t)$  (green dashed lines) and quantification (see Figures 1F–1H for comparison).

(E and F) Responses to the single-field contrast asynchrony illusion and quantification (see Figures 2A–2C for comparison; green dashed lines represent the sinusoidal luminance modulation of the single vertical stripe, blue dashed lines represent background luminances dark, bright, and gray).

(G and H) Example traces for the counterphase flicker stimulus with low ( $\lambda = 80^\circ$ ) and intermediate ( $\lambda = 25^\circ$ ) spatial frequency and quantification of the 2 Hz response components.

Data represent mean  $\pm$  SEM with  $n = 12$ –13 flies per group.  $p$  values based on a two-sided Welch's  $t$  test, comparing Mi1/Tm3 block flies with both control groups (\* $p < 0.001$ ; \*\* $p < 0.001$ ;  $p = 0.85$  for the amplitude of the 1 Hz response component for the dark background condition, and  $p = 0.78$  for the phase of the 2 Hz response component for the gray background condition in F). Detailed statistics in Table S2A. Shibire<sup>tg</sup> flies in dark gray, Mi1/Tm3 control flies in light gray, Mi1/Tm3 block flies in blue. Raw time traces for control flies (black) in (A), (C), (E), and (G) are pooled from both control groups.

gray for any local background luminance. If a Mi1/Tm3-independent global contrast system exists, Mi1/Tm3 block flies should respond, independently of local background light levels, with a 2 Hz contrast response as the flickering stripe is compared to global gray background light levels. When we tested the new stimulus, control flies behaved as before (compare Figures 2B, 2C, S5B, and S5C), indicating that the local contrast system is the dominating one. Mi1/Tm3 block flies however responded with a weak 2 Hz response that was independent of local background luminance (Figure S5B–S5D), providing evidence for the existence of a global contrast system.

In summary, the observed residual turning responses in Mi1/Tm3-silenced flies (Figures 6E–6H) are likely mediated by another, weaker, subsystem which analyzes spatial contrast on a global scale.

#### Output Elements of the Circuit for Spatial Contrast Computation

Next, we wanted to identify the output elements of the contrast computation circuit. As neurons with major input from both Mi1 and Tm3, other than T4, have not yet been identified (Takemura et al., 2013), we could not proceed further with our strategy of characterizing circuit elements based on their behavioral phenotype when silenced. Since membrane depolarization in lobula plate tangential cells elicits an optomotor response (Haikala et al., 2013), we wondered whether the membrane voltage of these cells might also reflect the contrast responses we observed in the behavioral experiments. In order to test this hypothesis, we performed electrophysiological whole-cell patch clamp recordings from these neurons, stimulated flies with motion and counterphase flicker, and silenced synaptic output of either T4 and T5, or Mi1, Tm3, T4, and T5, as in the behavioral experiments.

When stimulated with motion along the vertical axis of a horizontally oriented sine-grating, lobula plate vertical system cells responded in a direction-selective manner (Figures 7A and 7B).

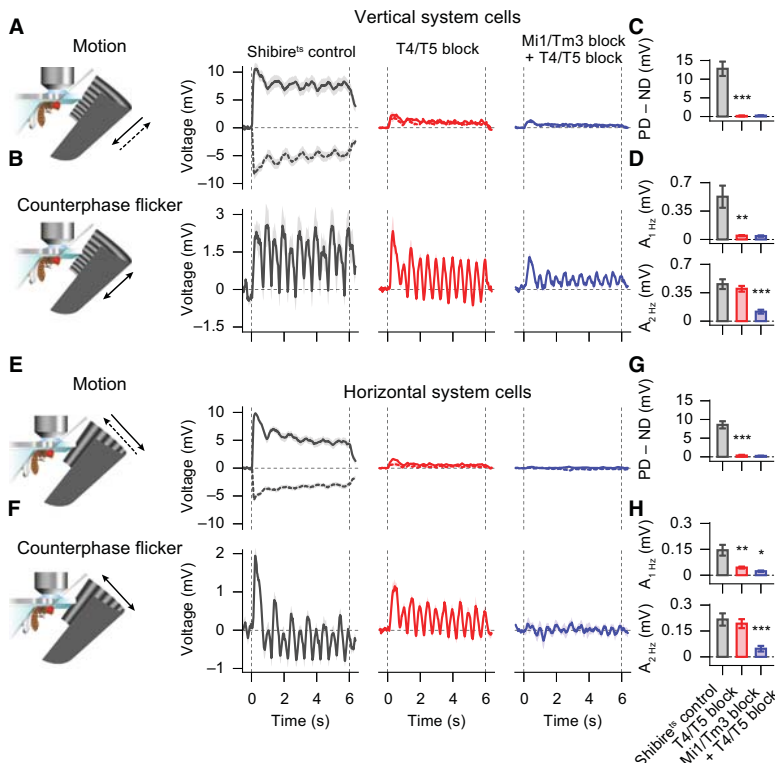


**Figure 7. Lobula Plate Tangential Cell Membrane Voltage Reflects Spatial Contrast Dynamics of Counterphase Flicker**

(A and B) Vertical system cell responses to a horizontally oriented sine-grating moving downward (PD, solid lines), upward (ND, dashed lines), or flickering in counterphase (2 Hz spatial contrast flicker).

(C and D) Quantification of the motion responses (mean of PD-ND) and of the 1 Hz and 2 Hz amplitude components of the Fourier-transformed responses to the counterphase flicker.

(E–H) Same as in (A)–(D), but for a vertically oriented sine-grating which moves along the horizontal axis or flickers in counterphase. Data represent mean  $\pm$  SEM with  $n = 4$ –11 cells per group (of two to eight flies per group), analyzed from 1–6 s after stimulus onset.  $p$  values based on a two-sided Welch's  $t$  test, comparing *shibire<sup>ts</sup>* control flies with T4/T5 block flies and T4/T5 block flies with combined Mi1/Tm3 block + T4/T5 block flies (\* $p < 0.05$ ; \*\* $p < 0.01$ ; \*\*\* $p < 0.001$ ;  $p = 0.42$  and  $p = 0.59$  for the amplitudes of the 2 Hz response component of the T4/T5 block in D and H, respectively). Detailed statistics in Table S2C. *Shibire<sup>ts</sup>* flies in dark gray, T4/T5 block flies in red, combined Mi1/Tm3 block + T4/T5 block flies in violet. See Figures 1A, 1B, and S1 for schematics of cell types and locations.

As expected from previous studies (Schnell et al., 2012), motion responses were completely abolished when blocking T4 and T5. Blocking Mi1 and Tm3 in addition did not change responses further. Next, we stimulated flies with counterphase flicker of the same orientation, providing 1 Hz local luminance flicker and 2 Hz spatial contrast flicker. We observed complex oscillatory voltage dynamics in control flies (Figure 7C) which contained both a 1 Hz and a 2 Hz component (Figure 7D). Hence, vertical system cells integrate both the 1 Hz luminance dynamics of counterphase flicker as well as its 2 Hz spatial contrast dynamics. When we tested T4/T5 block flies, the neurons' voltage dynamics were much simpler: While the 1 Hz component was completely abolished, the 2 Hz response component remained unchanged and when silencing Mi1/Tm3 together with T4/T5, the 2 Hz response component was strongly decreased as well. In further experiments, we also recorded from lobula plate horizontal system cells and presented sine-gratings with vertical orientation (Figure 7E). We obtained essentially the same results as we did in vertical system cells (Figures 7E–7H). Because no motion and contrast responses were detectable in flies with silenced Mi1, Tm3, T4, and T5, we also tested full-field flicker (Figure S6). In these flies, we still found robust voltage responses to such stimuli, indicating that even more visual processing pathways arrive at the lobula plate (Schnell et al., 2012) and that the recorded neurons were functionally intact.

From these experiments, we conclude that lobula plate tangential cells not only collect direction-selective input from

T4 and T5; they also receive signals from another, unidentified, visual pathway which computes spatial contrast. This pathway requires Mi1 and Tm3 to be functional and bypasses T4 and T5. Hence, spatial contrast and motion cues converge in the lobula plate where they shape visuomotor behavior together. Such interactions could also explain the smaller contrast responses in control flies compared to that of T4/T5 block flies which we observed in some of the behavioral experiments (Figures 2H, 2I, 3H, 3I, and 5C).

### Modeling

Our experiments revealed that contrast responses rely on the change of absolute spatial contrast. In particular, when spatial contrast decreases on the right side, flies turn right, when it increases, flies turn left (Figures 2 and 3). Based on these experimental findings, we developed a minimal computational model which could reproduce our results.

Spatial contrast can be computed by taking the difference between adjacent luminance values, i.e., by lateral inhibition,

$$S_{i,\text{rel}} = S_i - 0.5 \cdot (S_{i-1} + S_{i+1}),$$

where  $S_i$  describes signals of an ommatidium at location  $i$ . The change in absolute spatial contrast can then be described by a full-wave rectification followed by a high-pass filter:

$$R_i = -\text{HP}(\text{abs}(S_{i,\text{rel}})).$$

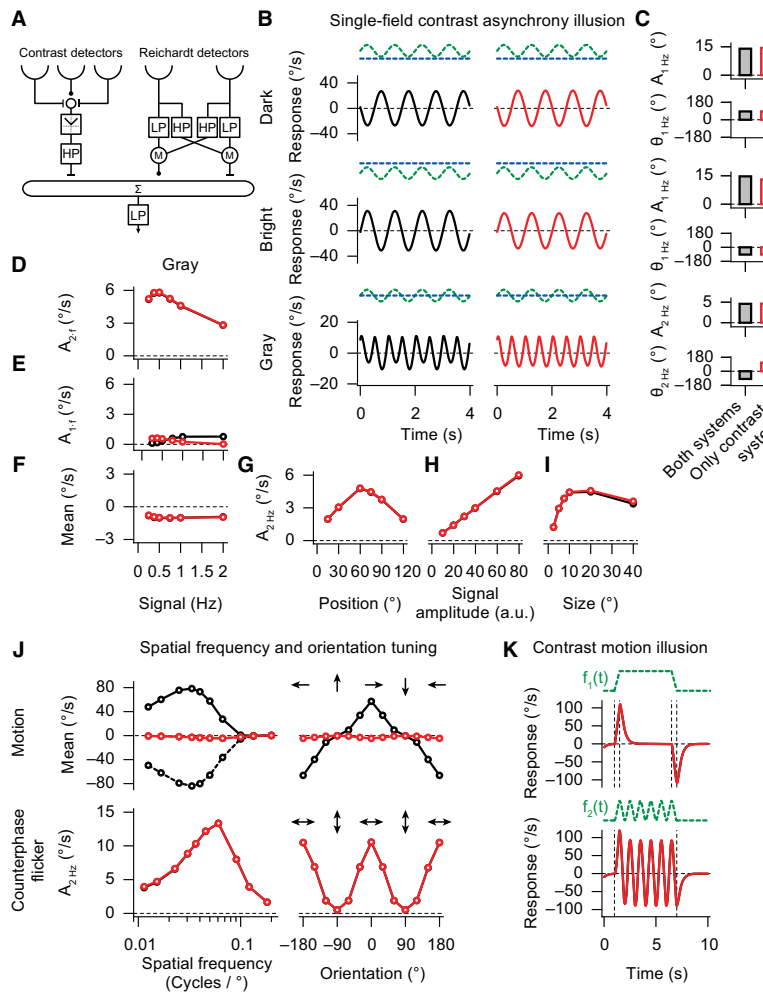


**Figure 8. A Simple Computational Model Reproduces Contrast Responses Observed in the Behavioral Experiments**

(A) Model structure of contrast detectors combined with Hassenstein-Reichardt detectors. We use an array of these detectors, weighted according to the function in Figure 2G.

(B and C) Responses to the single-field contrast asynchrony illusion for different backgrounds (blue dashed lines) and quantification of amplitude  $A$  and phase  $\Theta$  of the 1 Hz and 2 Hz response components (green dashed lines illustrate sinusoidal 1 Hz flicker of the vertical stripe). See Figures 2A–2C for comparison.

(D–I) Responses as a function of stripe flicker frequency, position, signal amplitude, and size (Figure 2D–2I for comparison).

(J) Variation of spatial frequency and orientation of a sine-grating which moves (upper part) or flickers in counterphase (bottom part) in a circular window on the right side. See Figure 3 for comparison.

(K) Responses to the contrast motion illusion for vertical stripe luminance profiles  $f_1(t)$  and  $f_2(t)$ , as in Figures 1F–1H. Black and red traces are simulation results from the complete model (contrast + Hassenstein-Reichardt detectors; corresponds to control flies) and from a model in which motion responses were blocked (only contrast detector; corresponds to T4/T5 block flies), respectively.

This equation can be translated into a simple detector model diagram (Figure 8A). We modeled motion detectors as classical Hassenstein-Reichardt detectors (Hassenstein and Reichardt, 1956). The output of an array of both types of detectors was locally weighted and summated according to the position-dependent function found in our experiments (Figure 2G). A final low-pass filter mimicked the inertia of the motor system. We presented the model with exactly the same visual stimuli as used in the behavioral experiments. We then tested the model under two conditions, the complete model (both systems = simulating control flies) and the model without Hassenstein-Reichardt detectors (only contrast system = simulating T4/T5 block flies).

The model reproduced the antiphase turning response oscillations for the flickering stripe under the dark and bright background conditions, respectively, as well as the frequency doubling when the background was gray (Figures 8B–8D). Moreover, we observed a small 1 Hz component in the response in the complete model (Figures 8B and 8E). The phase and the mean of

the response oscillation were only slightly different compared to those measured experimentally (compare Figures 8C and 2C). Next, we varied the position, the signal amplitude, and the size of the flickering stripe on a gray background. As expected, the model reproduced the position dependency because positional weighting was an intrinsic component of the model construction. Moreover, the model showed a linear dependency on the signal amplitude (Figure 8H), which

is expected from the model structure. Our model also reproduced the other experimental findings which were not used for its design. The model reproduced the shape of the size dependency and even predicted a small reduction for larger sizes under control conditions (compare Figures 8I and 2I). We also probed the spatial receptive field properties of the model (Figure 8J) and obtained very similar results as observed in our experiments (Figure 3). Finally, we presented the contrast motion illusion to our model (Figure 8K): The model faithfully reproduced both the direction and the amplitude of the response for both stripe luminance profiles as seen in our experiments (Figures 1F–1H). The negative arm of the Hassenstein-Reichardt detector was minimally weighted less than the positive arm (Eichner et al., 2011), which is the reason why simulated control flies have slightly different contrast responses to stripe flicker and counterphase flicker than simulated block flies.

In summary, using a single set of parameters, the simple model reproduced our experimental results astonishingly well,

both qualitatively and quantitatively. We conclude that spatial contrast computation in the fly visual system is based on lateral inhibition followed by full-wave rectification and high-pass filtering. The resulting spatial contrast signals are then globally integrated in a similar fashion as local motion cues.

As our experimental findings indicate that Mi1 and Tm3 neurons are required for both spatial contrast computation and for motion vision (Figures 4 and 6), we also wanted to know to what extent a more detailed model, incorporating such a circuit overlap, can account for our results (Figure S7). The detailed model is based on separate pathways for brightness increments (ON pathway) and for brightness decrements (OFF pathway). Within each pathway, motion is computed by independent polarity-specific Hassenstein-Reichardt detectors (Eichner et al., 2011). We extended the ON pathway by a stage for the computation of absolute spatial contrast, as done in the less complex model (Figure 8). Simulation of the model under different conditions (control condition = full model; T4/T5 block = only the contrast system; Mi1/Tm3 block = only the OFF pathway) revealed a qualitative and quantitative match to most of our experimental data. This shows that overlapping circuitry in the ON pathway can account for spatial contrast computation as well as for motion computation.

As suggested by our experiments, apart from computing local spatial contrast, flies also have a system for the computation of spatial contrast on a global scale (Figures 6C–6H and S5). We incorporated such a system in our detailed model by taking signals from photoreceptors minus the global average luminance level followed by full-wave rectification and high-pass filtering (Figure S8). Interestingly, the model now reproduced the residual responses to the single-field contrast asynchrony illusion (compare Figures 6E and 6F with Figures S8B and S8C), the counterphase spatial frequency tuning experiment (compare Figures 6G, 6H, and S8J) and the lack of responses to the contrast motion illusion (compare Figures 6C, 6D, and S8K) under Mi1/Tm3 block conditions (only the OFF pathway and the system for global contrast computation intact). This close agreement between modeling and experiments provides further evidence that a Mi1/Tm3-independent contrast system operating on a larger spatial scale can account for the residual responses seen in Mi1/Tm3 block flies (Figure 6).

## DISCUSSION

In this paper, we studied contrast computation in *Drosophila*. We employed two types of contrast illusions, the contrast motion illusion and the single-field contrast asynchrony illusion, as a tool to explore the underlying circuit mechanisms. Testing the first type of illusion, we found that flies responded with a turning response along the direction of illusory motion as perceived by humans (Shapiro and Hamburger, 2007) (Figures 1F–1H). Moreover, when testing the second type of illusion, flies responded to the flickering spatial contrast rather than to its flickering luminance (Figure 2), a phenomenon which is also observed in human psychophysics (Shapiro et al., 2004). Genetic silencing of the essential elements of motion computation, T4 and T5, left responses to contrast stimuli largely unaffected. This suggested

that spatial contrast and motion computations are implemented in different visual pathways. Further behavioral analysis revealed that lateral inhibition is involved in the computation, resulting in spatial frequency and orientation tuning of contrast responses (Figure 3). Using counterphase flicker as a stimulus which elicits robust responses to spatial contrast change, we identified the lamina neuron L1 and its postsynaptic partners Mi1 and Tm3 to be essential for contrast computation (Figure 4D). Moreover, silencing the output of both Mi1 and Tm3 at the same time, completely abolished responses to the contrast motion illusion and reduced, or even inverted, responses to the single-field contrast asynchrony illusion (Figures 6C–6F). These results held also true when blocking T4 and T5 in combination with Mi1 and Tm3 (Figures 4D and S2).

Notably, connectomics (Takemura et al., 2013) and electrophysiological recordings (Behnia et al., 2014) revealed small receptive fields for Mi1 and larger receptive fields for Tm3. Both neuron types provide spatially offset and temporally different input to the T4 dendrite in order to shape its direction-selectivity (Behnia et al., 2014; Takemura et al., 2013). In agreement with previous silencing experiments (Ammer et al., 2015), our experiments provide further behavioral evidence for an important role of Mi1 and Tm3 in motion vision because Mi1/Tm3-silenced flies show a reduced optomotor response (Figures 4C, 6A, and 6B). We identified Tm3 to be important for lateral inhibition during contrast computation (Figure 5), but lateral inhibition is not apparent in electrophysiological recordings from Tm3 (Behnia et al., 2014). Hence, lateral inhibition ought to be further downstream. Taking these findings and our modeling results (Figure 8) into account, we suggest that Mi1 provides excitatory input and Tm3 surround inhibition to neurons other than T4 in order to compute spatial contrast. We speculate that a similar circuit motif might also be found on the T4 dendrite (Behnia et al., 2014; Takemura et al., 2013), forming the basis for orientation-selective responses described for these cells (Fisher et al., 2015; Maisak et al., 2013).

Using electrophysiological recordings, we found voltage oscillations in lobula plate tangential cells that correlate with the contrast dynamics of counterphase flicker (Figure 7). Blocking T4 and T5 cells left the response intact, but silencing additionally Mi1 and Tm3 neurons abolished the response. Hence, contrast cues converge on the level of the lobula plate, bypassing T4 and T5. Tm3 is known to synapse also in the lobula (Fischbach and Ditttrich, 1989) (Figures S1A, S2A, and S2C), which could be the area where spatial contrast cues are integrated and then transmitted into the lobula plate.

Nevertheless, the identification of a membrane voltage representation of contrast computation does not necessarily imply that lobula plate tangential cells control the behavioral responses we observed. The responses to counterphase flicker might simply be a reflection of other, unidentified, neurons within the highly interconnected network of lobula plate tangential cells (Haag and Borst, 2001, 2002, 2004; Schnell et al., 2010). Moreover, the contrast system might provide signals to neurons in the lobula as well. In order to identify such elements, it will be required to explore further postsynaptic partners of Mi1 and Tm3, and probe the response properties of lobula plate neurons, after silencing such cells.

In conclusion, spatial contrast and motion computation in the fly brain share some of the neuronal circuit elements, pre- and postsynaptic to T4 cells. Such a circuit design suggests that computation of contrast provides important auxiliary signals which assist or further shape direction-selective responses in lobula plate tangential cells. Such cues could, for example, equilibrate motion responses to local variations of contrast, shape motion response to edges or bars (Bahl et al., 2013), improve orientation or spatial frequency tuning, or realize figure-ground discrimination (Egelhaaf, 1985). Our identification of the mechanisms and neuronal elements of spatial contrast computation opens the door for further behavioral, genetic, anatomical, and physiological dissections of these interactions and might help to elucidate the functional relevance of spatial contrast computation, and the associated contrast illusions, in flies and, perhaps, even humans.

#### EXPERIMENTAL PROCEDURES

Behavioral experiments were performed as described previously (Bahl et al., 2013). Briefly, tethered flies were walking on an air-suspended ball in a monitor-based virtual environment. Temperature was precisely controlled. In the electrophysiological experiments, control and block flies were heat-shocked for one hour before the experiments. The recording protocol was as described previously (Joesch et al., 2008). Immunostainings and stochastic flip-outs (Figures S2A and S2C) were performed as previously described (Nern et al., 2015; Yu et al., 2010). For statistical analysis, we use a two-sided Welch's t test throughout the paper. In order to average circular phase angles and to determine their variance, we applied circular operators. Statistical tests were performed between both genetic controls and block flies (shibire<sup>ts</sup> and Gal4 control versus block) and the larger p value determined significance:  $p^* < 0.05$ ,  $p^{**} < 0.01$ , and  $p^{***} < 0.001$ . For the simulations, we used movies of  $360 \times 180$  pixels at 60 Hz as model stimuli which were rendered from cylindrical projections of the same stimuli used in the experiments. Simulations were carried out according to the models shown in Figures 8A, S7A, and S8A. See *Supplemental Experimental Procedures* for detailed methods.

#### SUPPLEMENTAL INFORMATION

Supplemental Information includes eight figures, six tables, three movies, and Supplemental Experimental Procedures and can be found with this article at <http://dx.doi.org/10.1016/j.neuron.2015.11.004>.

#### AUTHOR CONTRIBUTIONS

A.Ba. and A.Bo. designed the study. E.S. and M.M. performed electrophysiological recordings. G.A. provided the Mi1, Tm3, and Mi1/Tm3-Gal4 lines and did the immunostainings. A.Ba. built the behavioral setup, programmed the visual stimuli, performed the behavioral experiments, and analyzed the data. A.Ba. wrote the paper with help from the other authors.

#### ACKNOWLEDGMENTS

We are grateful to Romina Kutlesa and Christian Theile for superb technical assistance with the behavioral experiments and fly work, and to Aljoscha Leonhardt for many valuable discussions. We also wish to thank Aljoscha Nern and Gerald M. Rubin for providing the T4/T5 split-Gal4 line and stochastic flipase, and Aljoscha Leonhardt, Alison Barker, Alexander Arenz, and Anna Schützenberger for critically reading the manuscript.

Received: April 13, 2015

Revised: September 24, 2015

Accepted: October 28, 2015

Published: December 3, 2015

#### REFERENCES

Adelson, E.H. (2000). Lightness perception and lightness illusions. In *The New Cognitive Neurosciences*, Second Edition, M. Gazzaniga, ed. (Cambridge, MA: MIT Press), pp. 339–351.

Ammer, G., Leonhardt, A., Bahl, A., Dickson, B.J., and Borst, A. (2015). Functional specialization of neural input elements to the *Drosophila* ON motion detector. *Curr. Biol.* 25, 2247–2253.

Bahl, A., Ammer, G., Schilling, T., and Borst, A. (2013). Object tracking in motion-blind flies. *Nat. Neurosci.* 16, 730–738.

Bausenwein, B., Dittrich, A.P., and Fischbach, K.F. (1992). The optic lobe of *Drosophila melanogaster*. II. Sorting of retinotopic pathways in the medulla. *Cell Tissue Res.* 267, 17–28.

Behnia, R., Clark, D.A., Carter, A.G., Clandinin, T.R., and Desplan, C. (2014). Processing properties of ON and OFF pathways for *Drosophila* motion detection. *Nature* 512, 427–430.

Brand, A.H., and Perrimon, N. (1993). Targeted gene expression as a means of altering cell fates and generating dominant phenotypes. *Development* 118, 401–415.

Büthhoff, H., and Götz, K.G. (1979). Analogous motion illusion in man and fly. *Nature* 278, 636–638.

Clark, D.A., Bursztyn, L., Horowitz, M.A., Schnitzer, M.J., and Clandinin, T.R. (2011). Defining the computational structure of the motion detector in *Drosophila*. *Neuron* 70, 1165–1177.

Egelhaaf, M. (1985). On the neuronal basis of figure-ground discrimination by relative motion in the visual system of the fly. I. Behavioural constraints imposed on the neuronal network and the role of the optomotor system. *Biol. Cybern.* 52, 123–140.

Eichner, H., Joesch, M., Schnell, B., Reiff, D.F., and Borst, A. (2011). Internal structure of the fly elementary motion detector. *Neuron* 70, 1155–1164.

Fischbach, K.F., and Dittrich, A. (1989). The optic lobe of *Drosophila melanogaster*. I. A Golgi analysis of wild-type structure. *Cell Tissue Res.* 258, 441–475.

Fisher, Y.E., Silies, M., and Clandinin, T.R. (2015). Orientation selectivity sharpens motion detection in *Drosophila*. *Neuron* 88, 390–402.

Götz, K.G. (1964). Optomotorische Untersuchung des visuellen Systems einiger Augenmutanten der Fruchtfliege *Drosophila*. *Kybernetik* 2, 77–92.

Haag, J., and Borst, A. (2001). Recurrent network interactions underlying flow-field selectivity of visual interneurons. *J. Neurosci.* 21, 5685–5692.

Haag, J., and Borst, A. (2002). Dendro-dendrite interactions between motion-sensitive large-field neurons in the fly. *J. Neurosci.* 22, 3227–3233.

Haag, J., and Borst, A. (2004). Neural mechanism underlying complex receptive field properties of motion-sensitive interneurons. *Nat. Neurosci.* 7, 628–634.

Haikala, V., Joesch, M., Borst, A., and Mauss, A.S. (2013). Optogenetic control of fly optomotor responses. *J. Neurosci.* 33, 13927–13934.

Hassenstein, B., and Reichardt, W. (1956). Systemtheoretische Analyse der Zeit, Reihenfolgen und Vorzeichenauswertung bei der Bewegungsperzeption des Rüsselkäfers *Chlorophanus*. *Z. Naturforsch. B* 11, 513–524.

Joesch, M., Plett, J., Borst, A., and Reiff, D.F. (2008). Response properties of motion-sensitive visual interneurons in the lobula plate of *Drosophila melanogaster*. *Curr. Biol.* 18, 368–374.

Joesch, M., Schnell, B., Raghu, S.V., Reiff, D.F., and Borst, A. (2010). ON and OFF pathways in *Drosophila* motion vision. *Nature* 468, 300–304.

Joesch, M., Weber, F., Eichner, H., and Borst, A. (2013). Functional specialization of parallel motion detection circuits in the fly. *J. Neurosci.* 33, 902–905.

Kitamoto, T. (2001). Conditional modification of behavior in *Drosophila* by targeted expression of a temperature-sensitive shibire allele in defined neurons. *J. Neurobiol.* 47, 81–92.

Maisak, M.S., Haag, J., Ammer, G., Serbe, E., Meier, M., Leonhardt, A., Schilling, T., Bahl, A., Rubin, G.M., Nern, A., et al. (2013). A directional tuning map of *Drosophila* elementary motion detectors. *Nature* 500, 212–216.

Mauss, A.S., Pankova, K., Arenz, A., Nern, A., Rubin, G.M., and Borst, A. (2015). Neural circuit to integrate opposing motions in the visual field. *Cell* 162, 351–362.

Meier, M., Serbe, E., Maisak, M.S., Haag, J., Dickson, B.J., and Borst, A. (2014). Neural circuit components of the *Drosophila* OFF motion vision pathway. *Curr. Biol.* 24, 385–392.

Morante, J., and Desplan, C. (2008). The color-vision circuit in the medulla of *Drosophila*. *Curr. Biol.* 18, 553–565.

Nern, A., Pfeiffer, B.D., and Rubin, G.M. (2015). Optimized tools for multicolor stochastic labeling reveal diverse stereotyped cell arrangements in the fly visual system. *Proc. Natl. Acad. Sci. USA* 112, E2967–E2976.

Pfeiffer, B.D., Truman, J.W., and Rubin, G.M. (2012). Using translational enhancers to increase transgene expression in *Drosophila*. *Proc. Natl. Acad. Sci. USA* 109, 6626–6631.

Pick, B. (1974). Visual flicker induces orientation behaviour in the fly *Musca*. *Z. Naturforsch. C* 29, 310–312.

Schnell, B., Joesch, M., Forstner, F., Raghu, S.V., Otsuna, H., Ito, K., Borst, A., and Reiff, D.F. (2010). Processing of horizontal optic flow in three visual interneurons of the *Drosophila* brain. *J. Neurophysiol.* 103, 1646–1657.

Schnell, B., Raghu, S.V., Nern, A., and Borst, A. (2012). Columnar cells necessary for motion responses of wide-field visual interneurons in *Drosophila*. *J. Comp. Physiol. A Neuroethol. Sens. Neural Behav. Physiol.* 198, 389–395.

Shapiro, A.G., and Hamburger, K. (2007). Last but not least. *Perception* 36, 1104–1107.

Shapiro, A.G., D'Antona, A.D., Charles, J.P., Belano, L.A., Smith, J.B., and Shear-Heyman, M. (2004). Induced contrast asynchronies. *J. Vis.* 4, 459–468.

Shapiro, A.G., Charles, J.P., and Shear-Heyman, M. (2005). Visual illusions based on single-field contrast asynchronies. *J. Vis.* 5, 764–782.

Shinomiya, K., Karuppudurai, T., Lin, T.-Y., Lu, Z., Lee, C.-H., and Meierzhagen, I.A. (2014). Candidate neural substrates for off-edge motion detection in *Drosophila*. *Curr. Biol.* 24, 1062–1070.

Silies, M., Gohl, D.M., Fisher, Y.E., Freifeld, L., Clark, D.A., and Clandinin, T.R. (2013). Modular use of peripheral input channels tunes motion-detecting circuitry. *Neuron* 79, 111–127.

Strother, J.A., Nern, A., and Reiser, M.B. (2014). Direct observation of ON and OFF pathways in the *Drosophila* visual system. *Curr. Biol.* 24, 976–983.

Takemura, S.-Y., Bharioke, A., Lu, Z., Nern, A., Vitaladevuni, S., Rivlin, P.K., Katz, W.T., Olbris, D.J., Plaza, S.M., Winston, P., et al. (2013). A visual motion detection circuit suggested by *Drosophila* connectomics. *Nature* 500, 175–181.

Tuthill, J.C., Chiappe, M.E., and Reiser, M.B. (2011). Neural correlates of illusory motion perception in *Drosophila*. *Proc. Natl. Acad. Sci. USA* 108, 9685–9690.

Tuthill, J.C., Nern, A., Holtz, S.L., Rubin, G.M., and Reiser, M.B. (2013). Contributions of the 12 neuron classes in the fly lamina to motion vision. *Neuron* 79, 128–140.

Yu, J.Y., Kanai, M.I., Demir, E., Jefferis, G.S.X.E., and Dickson, B.J. (2010). Cellular organization of the neural circuit that drives *Drosophila* courtship behavior. *Curr. Biol.* 20, 1602–1614.

Neuron, Volume 88

## **Supplemental Information**

### **Neural Mechanisms for *Drosophila* Contrast Vision**

Armin Bahl, Etienne Serbe, Matthias Meier, Georg Ammer, and Alexander Borst

## SUPPLEMENTAL EXPERIMENTAL PROCEDURES

### FLIES

Flies were raised on standard cornmeal-agar medium on a 12h light/12h dark cycle and 60% humidity for the entire period of development. For the first seven days of development, flies were kept at 25 °C and then transferred to 18 °C. In experiments, we only used female flies aged ~1 day. We used the following driver lines: L1-splitGal4 (OK371-AD, ort-C1-3-DBD), L2-Gal4 (21D), L3-Gal4 (VT40568), L4-Gal4 (VT40547), L5-splitGal4 (R21A05-AD; R31H09-DBD), Mi1-Gal4 (VT7747), Tm3a-Gal4 (R12C11), Tm3b-Gal4 (R13E12), Mi1/Tm3-Gal4 (VT0465), T4/T5-splitGal4 (R59E08-AD; R42F06-DBD), T4/T5-Gal4 (R42F06). These lines were either crossed to wild type Canton S flies or to 20xUAS-shibire<sup>ls</sup> flies (Pfeiffer et al., 2012), resulting in the genotypes presented in Figure S2B.

### ELECTROPHYSIOLOGY

The glial sheet was digested locally by application of a stream of 0.5 mg/ml collagenase IV (GIBCO) through a cleaning micropipette (5  $\mu$ m opening) under polarized light contrast. Then, somata of lobula plate tangential cells were whole-cell patched. We identified vertical and horizontal system cells based on their directional tuning properties (control flies), cell body location and resting membrane potential (block flies). For visual stimulation, we used a LED arena covering  $\pm 90^\circ$  in azimuth and  $\pm 48^\circ$  in elevation. Patterns had a spatial wavelength of  $\lambda = 22.5^\circ$  and 100% contrast (maximal luminance 75 cd/m<sup>2</sup>). Recordings were performed at 2 kHz, the signal was then downsampled to 50 Hz and 2–4 trials were averaged per cell. Further analysis was performed as in the behavioral experiments.

### IMMUNOHISTOCHEMISTRY

Primary antibodies used were rabbit polyclonal anti-GFP (1:2000, Torri Pines) and mouse anti-nc82 (1:25, Developmental Studies Hybridoma Bank). We used the following secondary antibodies: goat anti-rabbit Alexa-488 and goat anti-mouse Alexa-633 (both 1:500, Invitrogen). Brains were mounted in Vectashield (Vectalabs) and optically sectioned in the horizontal plane with a Leica SP5 confocal microscope. For documentation, single sections were processed in ImageJ 1.46r (NIH). For stochastic labeling of cells in the VT0465-Gal4 line, we used a weak flippase which sparsely removes an FRT-flanked stop cassette and thereby allows Gal4-driven expression of a GFP reporter (Nern et al., 2015).

### BEHAVIORAL EXPERIMENTS

We used six independent setups (almost identical to those presented in Bahl et al. 2013) for visual stimulation and to record fly locomotion. All monitors were equilibrated in brightness and contrast. We applied the same temperature protocol in all behavioral experiments: Temperature was kept at 25 °C for the first 5 min and then, within 10 min, raised to 34 °C. The sine-grating in Figure 1D had a spatial wavelength of  $\lambda = 20^\circ$ , 60% contrast and moved at a velocity of 20 %/s. In the contrast motion illusion, we used a stepped gradient background (20° wide steps) ranging from luminance 0–100 cd/m<sup>2</sup>. Twelve 5° wide vertical stripes were superimposed within the centers of the background steps. The luminance of these stripes varied from 9–45 cd/m<sup>2</sup> according to the functions illustrated in Figure 1F. In Figures 2A–F and 6E–F, we used a single 10° wide vertical stripe located at 70° in azimuth. The luminance of the stripe varied sinusoidally (1 Hz) from 4–57 cd/m<sup>2</sup>. In Figure 2G–I, only the illustrated parameters were varied, the other parameters were as in Figure 2B (gray background) but in Figure 2I, the stripe was centered at 80° in azimuth. The uniformly dark, bright, and gray backgrounds had luminances of 1.3, 27, and 86 cd/m<sup>2</sup>, respectively. The sine pattern in Figures 3 and 6G,H had a contrast of 60%. Stimuli were shown in a circular window (radius = 40°) positioned at 90° in azimuth and 0° in elevation. Stimuli in Figure 4 were shown within a 70° wide rectangular window located at 90° in azimuth and full elevation. The sine-grating had a spatial wavelength of  $\lambda = 20^\circ$  and 60% contrast. Field flicker (Figure 5) was shown within the same window and varied from 4–57 cd/m<sup>2</sup> in luminance. The rest of the visual field for stimuli in Figures 3, 4 and 5 was gray (27 cd/m<sup>2</sup>). The size of the local background around the flickering stripe in Figure S5 was 30°, the rest of the arena was gray (27 cd/m<sup>2</sup>). Otherwise the stimulus was as in Figure 2A. The spatial phase of all sine-gratings (Figures 1A, 3, 4,

6A) was chosen randomly before each trial. In all behavioral experiments, we additionally presented exact mirror-symmetrical versions of the stimuli.

For each experiment, fly locomotion was sampled for ~90 min at 4 kHz and data was subsequently downsampled to 50 Hz. We then picked a trial range during which the average walking speed in each trial was above 0.5 cm/s. Trials were then averaged. Experiments not having at least 9 of such trials were discarded. Further, responses to all stimuli and to their mirror-symmetrical versions were subtracted from another and divided by two, which removed potential turning biases and improved data quality. Finally, we applied a first order low-pass filter ( $\tau = 40$  ms). The resulting data was then analyzed by averaging or via Fourier transform within a specific time range. In the Fourier-transformed signal, we picked the frequency of interest and calculated its amplitude and phase. For each stimulus, we then averaged these values and calculated the standard error of the mean (s.e.m.) over flies.

## STATISTICS

The Welch's t-test is a variant of Student's t-test and does not require equal variances ([https://en.wikipedia.org/wiki/Welch%27s\\_t-test](https://en.wikipedia.org/wiki/Welch%27s_t-test)). T-values were calculated as

$$t = \frac{\bar{X}_1 - \bar{X}_2}{\sqrt{\frac{s_1^2}{N_1} + \frac{s_2^2}{N_2}}},$$

where  $\bar{X}_i$ ,  $s_i^2$  and  $N_i$  are population mean, variance, and size of group  $i$ , respectively. We used the Welch–Satterthwaite equation to calculate degrees of freedom:

$$df = \frac{\left(\frac{s_1^2}{N_1} + \frac{s_2^2}{N_2}\right)^2}{\frac{s_1^4}{N_1^2 \cdot (N_1 - 1)} + \frac{s_2^4}{N_2^2 \cdot (N_2 - 1)}}.$$

In order to work with circular variables (response phases), we used the following circular operators to calculate mean ( $\bar{\alpha}$ ) and variance ( $s_\alpha^2$ ) of the values:

$$\bar{\alpha} = \arg \left( \sum_{j=1}^N \exp(i \cdot \alpha_j) \right),$$

$$s_\alpha^2 = -2 \cdot \log \left( \frac{1}{N} \cdot \left| \sum_{j=1}^N \exp(i \cdot \alpha_j) \right| \right).$$

To obtain the enumerator in the Welch's t test, we determined the smallest difference of angular means:

$$(\bar{\alpha}_1 - \bar{\alpha}_2 + \pi) \bmod 2\pi - \pi.$$

## MODELING

In the first step, frames were spatially convolved with a 2D Gaussian kernel of isotropic  $\sigma = 1.75^\circ$  and then fed into an array of 90 x 45  $4^\circ$ -spaced input elements. For input elements on the left visual hemisphere, the Hassenstein-Reichardt detector had a mirror-symmetrical structure. All filters in the input stage had the same time constants of  $\tau = 100$  ms. Lateral inhibition in the contrast detector along the horizontal axis was calculated as

$$R_i = S_i - 0.5 \cdot (S_{i-1} + S_{i+1}),$$

where  $S_i$  is the central input element. Output weighting of the contrast detector was 20, of the positive arm of the Hassenstein-Reichardt detector 0.15 and of the negative arm 0.147. Output of all detectors was then summated according to the weighting function

$$w(x) = \exp\left(-\frac{x^2}{2 \cdot 60^2}\right) - 0.9 \cdot \exp\left(-\frac{x^2}{2 \cdot 40^2}\right),$$

approximating the function in [Figure 2G](#), and values along the y-axis were summated. For simplicity, all motion and contrast detectors were weighted with the same function, as done in previous modeling studies ([Bahl et al., 2013](#)). In the left visual hemisphere, output signals were multiplied by  $-1$ . The resulting signal was then low-pass filtered ( $\tau = 300$  ms). All filters were of first-order and implemented according to [https://en.wikipedia.org/wiki/Low-pass\\_filter](https://en.wikipedia.org/wiki/Low-pass_filter) and [https://en.wikipedia.org/wiki/High-pass\\_filter](https://en.wikipedia.org/wiki/High-pass_filter), respectively. The high-pass filter in the input stage take away signal means completely and, for example, reduce a sinusoidal 1 Hz input signal to 50 % in amplitude and produce a phase shift of around  $0.3 \cdot \pi$ .

In the detailed models ([Figures S7](#) and [S8](#)), the DC component was 40% of the photoreceptor signal and the half-wave rectification in the OFF pathway was shifted by  $+80$ . The weight for the spatial contrast detector in the ON pathway was 30, for the positive and negative arms of the Hassenstein-Reichardt detectors 0.1 and 0.098, respectively. The output weight of the global contrast system was either 0 ([Figure S7](#)) or 2 ([Figure S8](#)). All other parameter were as in the less complex model.

The output weights, the DC component and the shift in the OFF rectification (only in the detailed models) were the only free model parameters and were adjusted by hand. Time constants were approximately the same as in previous modeling studies ([Eichner et al., 2011](#)) and were not optimized.

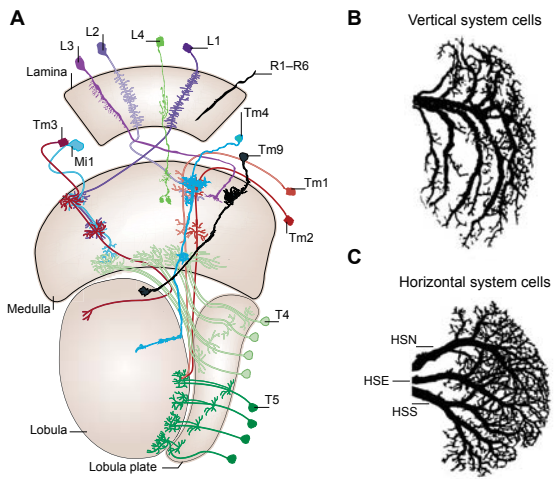


**Figure S1, related to Figure 1. Cellular Schematic of the Fly Optic Lobe and Morphology of Lobula Plate Tangential Cells**

(A) Cellular schematic of the fly optic lobe. See corresponding abstract schematic in [Figure 1A,B](#) for comparison. (B,C) Anatomy of five of the six vertical system cells and of the three horizontal system cells in *Drosophila*. Both cell types reside in the lobula plate and receive input from T4 and T5 neurons. The scheme in (A) was modified from [Borst, 2014](#). The images of lobula plate tangential cells in (B,C) are taken from [Rajashekhar and Shamprasad, 2004](#). Cell sizes not to scale.

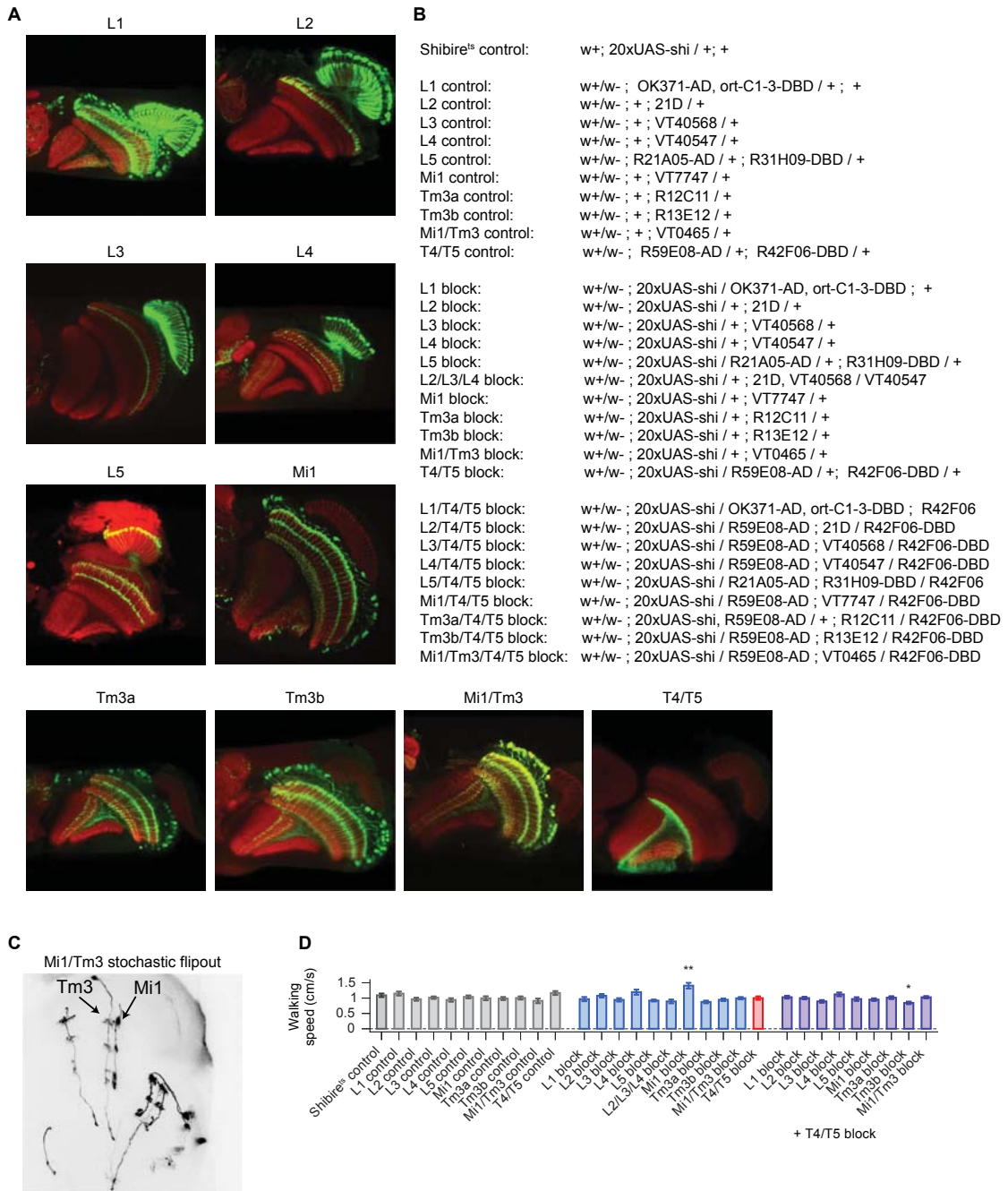


**Figure S2, related to Figures 4, 5, S3, and S4. Expression Patterns, Genotypes, and Walking Speed**

(A) GFP expression pattern of GAL4 driver lines. Horizontal sections of the optic lobe. (B) Genotypes used in the experiments. (C) Stochastic GFP labeling of neurons in the VT0465 Gal4 line. Flipouts of several Mi1 and Tm3 cells are distinguishable. In addition to these cells, we occasionally found weak expression in unidentified Mi and Dm cells. (D) Walking speed (averaged over same trial range as used for quantification of turning speeds and over all stimuli). Data represent mean  $\pm$  s.e.m with  $n = 14$ –19 flies per group. P-values based on a two-sided Welch's t test, comparing the group of block flies with respective control groups (for example, L1 block with L1 control and shibire<sup>ts</sup> control; groups with combined lamina or medulla block + T4/T5 block (right side) were compared only to the T4/T5 block group;  $P^* < 0.05$ ;  $P^{**} < 0.01$ ). Detailed statistics in Table S6. Shibire<sup>ts</sup> control flies in dark gray, Gal4 control flies in light gray, lamina and medulla block flies in blue, T4/T5 block flies in red, and combined lamina or medulla block + T4/T5 block flies in violet.

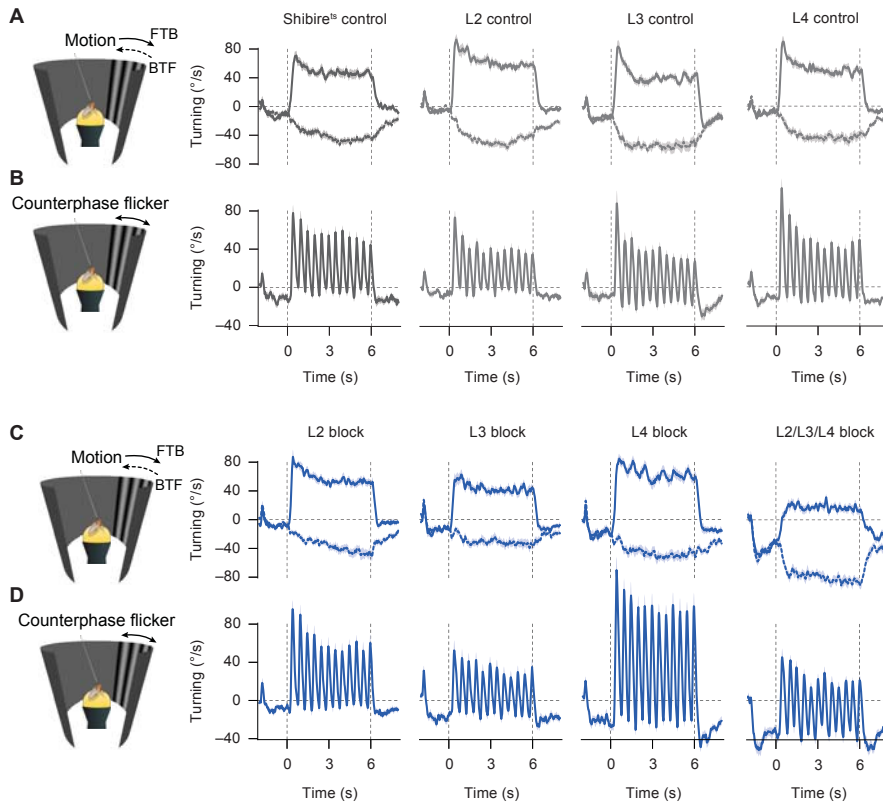


**Figure S3, related to Figure 4. Raw Time Traces for OFF Pathway Lamina Blocks**

(A,B) Responses of control flies to motion and counterphase flicker. (C,D) Responses of L2, L3, L4 and combined L2/L3/L4 block flies to motion and counterphase flicker. L2/L3/L4 block flies strongly turn away from stationary patterns ( $\approx 40$  °/s). For motion and counterphase flicker, all responses were shifted to negative values. This effect was not found in any of the controls or in any of the flies where L2, L3, or L4 cells were blocked independently. Even though we do not understand these dynamics, it shows that the triple lamina block works. For quantification, we calculated the optomotor response by subtracting front-to-back and back-to-front motion responses and by determining the 2 Hz response amplitude to counterphase flicker. Hence, a shift of the traces to negative values is not seen in the quantification in Figure 4E,F. Vertical gray dashed lines indicate on- and offset of the stimulus. Shibire<sup>ts</sup> control flies in dark gray, Gal4 control flies in light gray, lamina block flies in blue. Data represent mean  $\pm$  s.e.m with  $n = 14$ –19 flies per group. Same flies as in Figure 4.

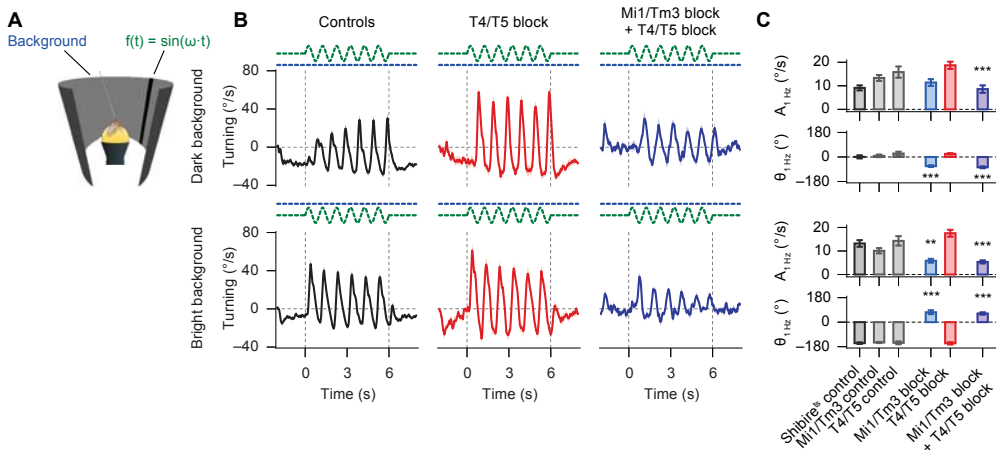


**Figure S4, related to Figure 6. Single-field Contrast Illusion in Mi1/Tm3 Block Flies**

(A) Same as in Figure 2A. (B) Fly turning responses for 1 Hz stripe flicker (identical in the two conditions; green dashed line) on two different backgrounds (dark and bright; blue dashed line). (C) Quantification of response amplitude  $A$  and phase  $\Theta$ . Data represent mean  $\pm$  s.e.m with  $n = 14$ –19 flies per group. Same flies as in Figures 4 and 5. P-values based on a two-sided Welch's t test, comparing the group of block flies with respective control groups (Mi1/Tm3 block with Mi1/Tm3 control and shibire<sup>ts</sup> control; The combined Mi1/Tm3 block + T4/T5 block (right side) was compared only to the T4/T5 block group;  $P^{**} < 0.01$ ;  $P^{***} < 0.001$ ). Detailed statistics in Table S2B. Expression patterns and list of genotypes in Figure S2A–C. Shibire<sup>ts</sup> control flies in dark gray, Gal4 control flies in light gray, Mi1/Tm3 block flies in blue, T4/T5 block flies in red, and combined Mi1/Tm3 block + T4/T5 block flies in violet. Raw time traces for control flies (black) in (C,D) are pooled from shibire<sup>ts</sup> control, T4/T5 control and Mi1/Tm3 control flies.

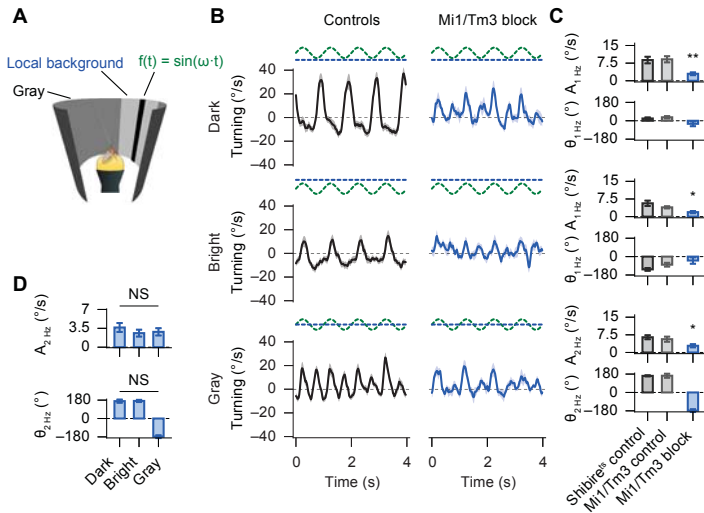


**Figure S5, related to Figure 6. Single-Field Contrast Asynchrony Illusion with Local Background Variation in Mi1/Tm3 Block Flies**

(A) The global background is gray for all conditions. Varied is the local background (dark, bright, and gray; blue dashed line) surrounding the  $\omega = 1$  Hz flickering stripe (identical in all conditions; green dashed line). Compare with stimuli in [Figures 2A](#) and [6E](#) where global background luminance is varied. (B,C) Fly turning responses for the three local background conditions and quantification of response amplitude  $A$  and phase  $\Theta$ . (D) Quantification of the 2 Hz response component for the three local background conditions for Mi1/Tm3 block flies. Data represent mean  $\pm$  s.e.m with  $n = 8$ –12 flies per group. P-values based on a two-sided Welch's t test, comparing Mi1/Tm3 block flies with both control groups ( $P^* < 0.05$ ;  $P^{**} < 0.01$ ). Statistics in (D) was done by pairwise comparing responses between the different conditions. None of these combinations was statistically different. Detailed statistics in [Table S3](#). Shibire<sup>ts</sup> control flies in dark gray, Mi1/Tm3 control flies in light gray, Mi1/Tm3 block flies in blue. Raw time traces for control flies (black) in (B) are pooled from shibire<sup>ts</sup> control and Mi1/Tm3 control flies.

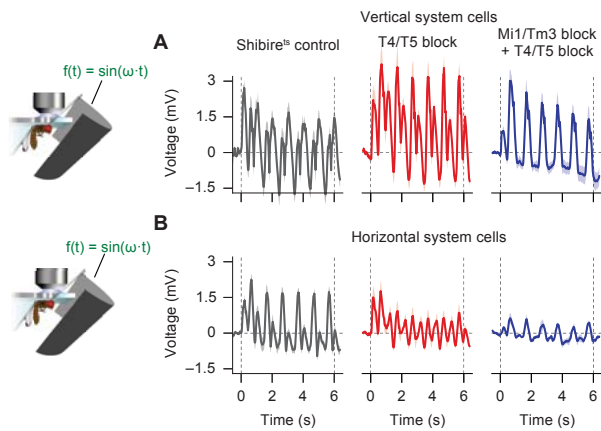


**Figure S6, related to Figure 7. Responses of Lobula Plate Tangential Cells to Full Field Flicker**

(A,B) Responses of vertical system and horizontal system cells to 1 Hz full field flicker. Data represent mean  $\pm$  s.e.m with  $n = 4-11$  cells per group (of 2-8 flies per group). Same flies and cells as in Figure 7. Shibire<sup>ts</sup> flies in dark gray, T4/T5 block flies in red, combined Mi1/Tm3 block + T4/T5 block flies in violet. See Figure S1B,C for illustration of the recorded neurons.

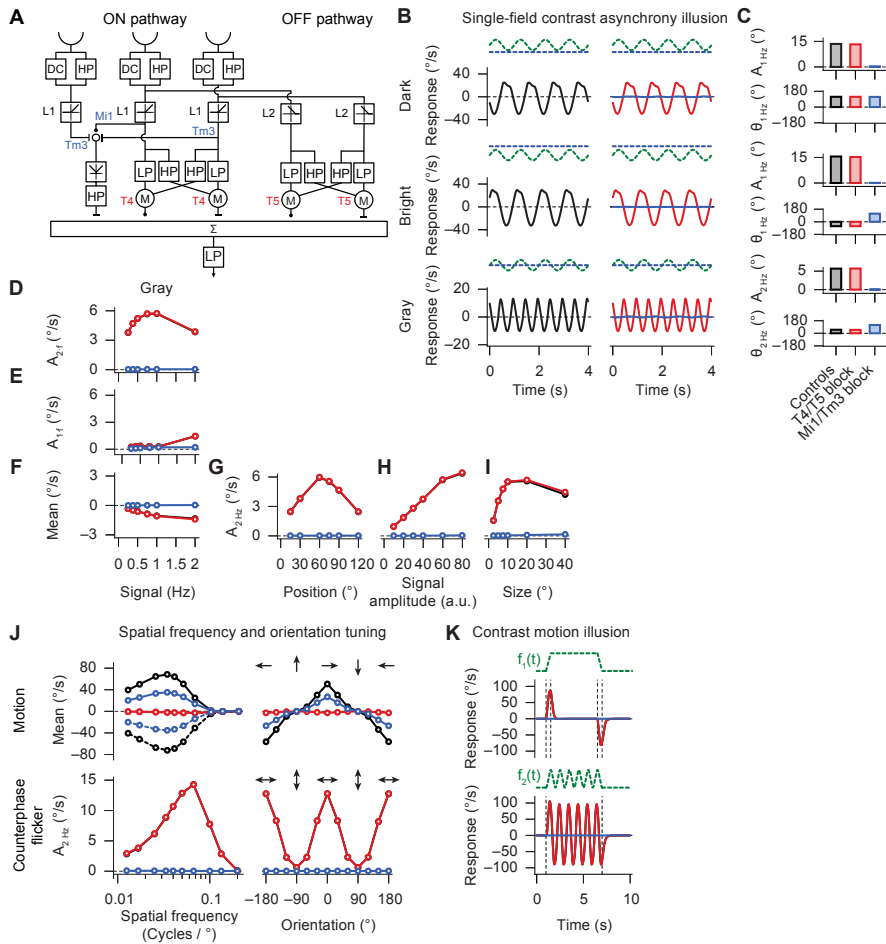


**Figure S7, related to Figure 8. Detailed Model with Contrast Computation within the ON Pathway**

(A) Detailed model with two pathways computing motion from brightness increments (ON pathway) and brightness decrements (OFF pathway). See Eichner et al., 2011. Within the ON pathway, lateral inhibition by Tm3 neurons and central excitation by Mi1 neurons are used to compute local spatial contrast (compare with Figure 8A). T4 and T5 neurons represent the output of the Hassenstein-Reichardt detectors in the two motion pathways. (B,C) Model responses for the single-field contrast asynchrony illusion (same stimulus as in Figures 2A–C and 6E–F) and quantification of amplitude  $A$  and phase  $\Theta$ . (D–I) Quantification of responses to varying signal frequency, position, amplitude, and stripe size. (J) Model responses for motion and counterphase flicker spatial frequency and orientation tuning (same stimulus as in Figure 3). (K) Model responses for the contrast motion illusion (same stimulus as in Figures 1F–H and 6C,D). Control conditions (full model) in black. T4/T5 block (model without Hassenstein-Reichardt detectors) in red. Mi1/Tm3 block (only OFF motion pathway intact) in blue.

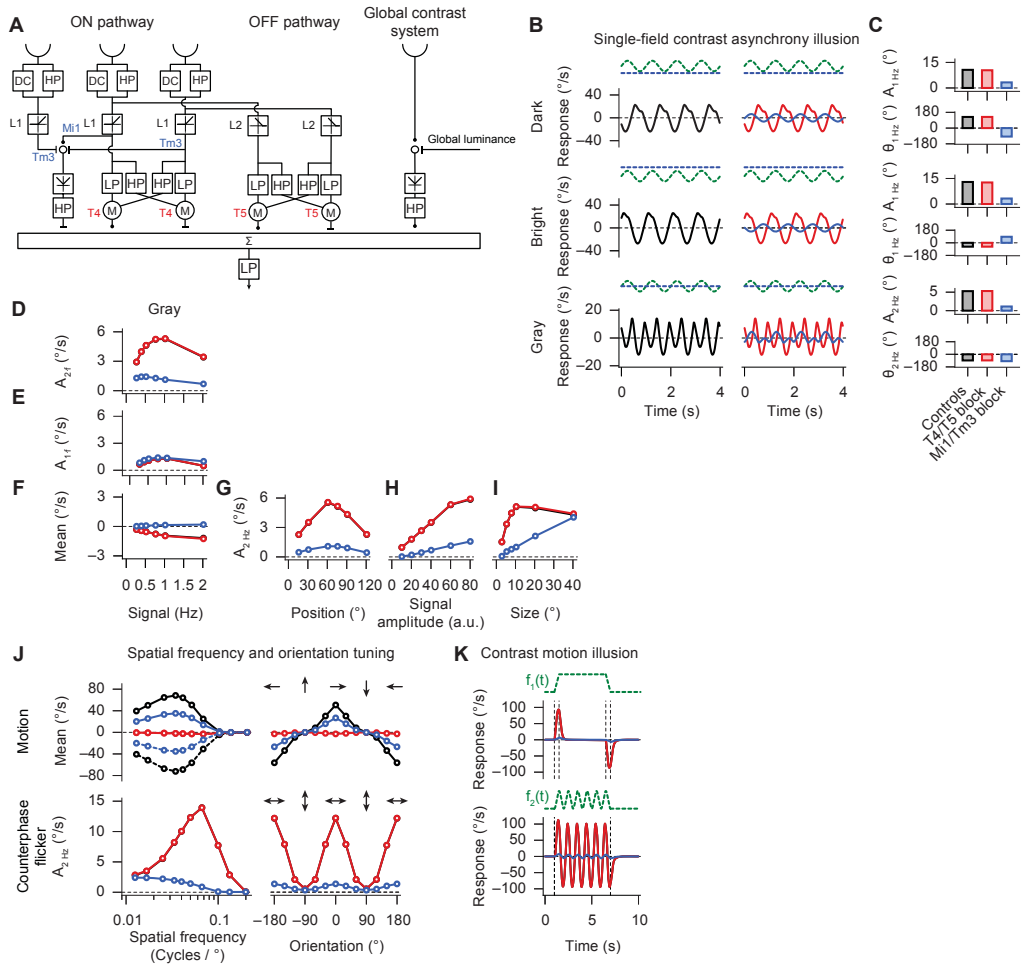


**Figure S8, related to Figure 8. Detailed Model with Local Contrast Computation within the ON Pathway and an Additional Pathway for Global Contrast Computation**

(A–K) Same as in [Figure S7](#) but with an additional pathway for global contrast computation. Control conditions (full model) in black. T4/T5 block (model without Hassenstein-Reichardt detectors) in red. Mi1/Tm3 block (only OFF motion pathway and global contrast pathway intact) in blue.

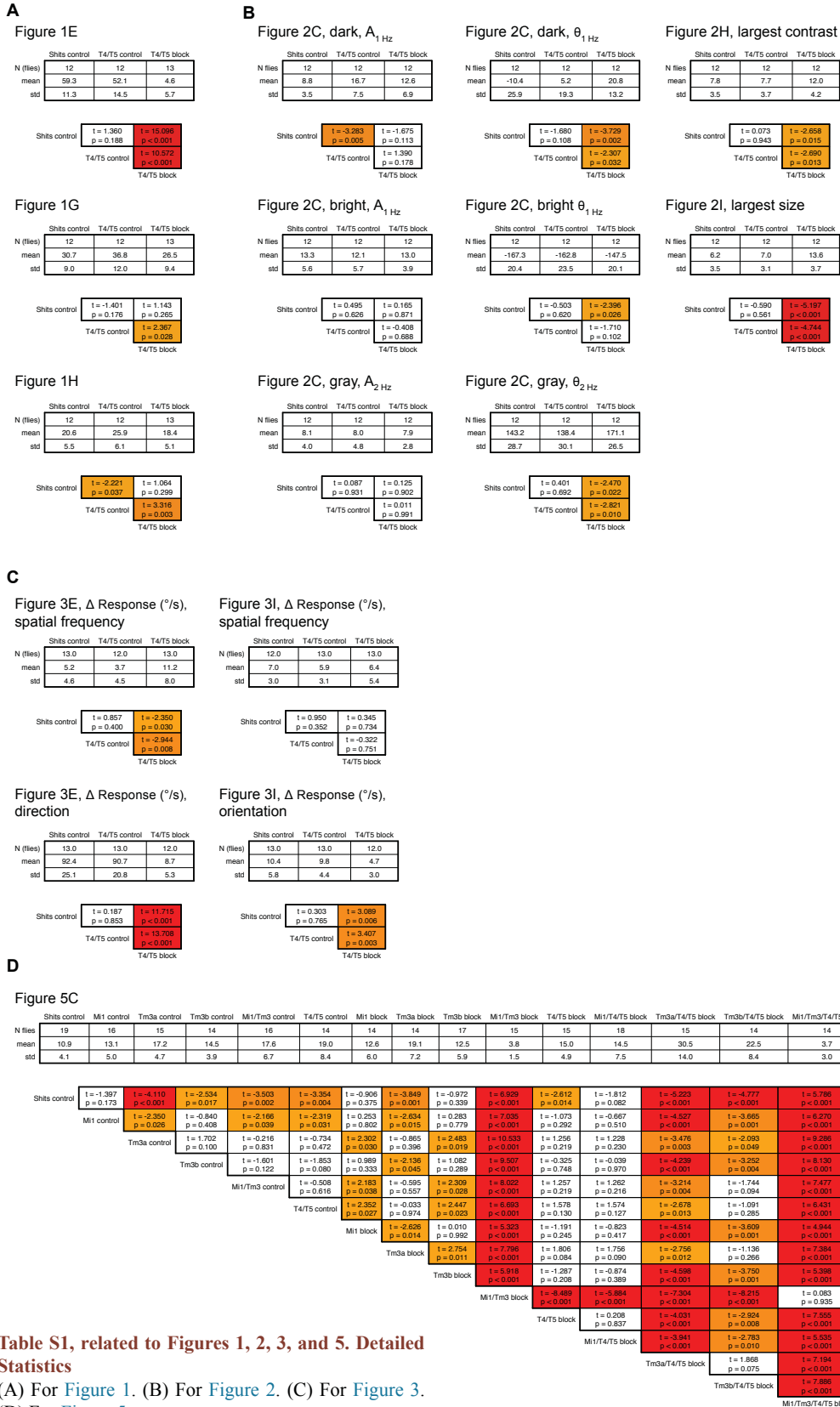


**Table S1, related to Figures 1, 2, 3, and 5. Detailed Statistics**

(A) For Figure 1. (B) For Figure 2. (C) For Figure 3.  
(D) For Figure 5.

**A Figure 6B**

	Shifts control	M1/Tm3 control	M1/Tm3 block
N files	12	12	12
mean	59.3	74.3	45.6
std	11.3	19.1	18.1

Shifts control  $t = -2.348$   
 $p = 0.031$   
M1/Tm3 control  $t = 2.227$   
 $p = 0.039$

M1/Tm3 control  $t = 3.782$   
 $p = 0.001$   
M1/Tm3 block

**Figure 6F,  $A_1$  Hz, dark**

	Shifts control	M1/Tm3 control	M1/Tm3 block
N files	12	12	13
mean	7.8	5.7	7.5
std	3.3	2.8	5.6

Shifts control  $t = 1.711$   
 $p = 0.101$   
M1/Tm3 control  $t = 0.198$   
 $p = 0.845$

M1/Tm3 control  $t = -1.010$   
 $p = 0.326$   
M1/Tm3 block

**Figure 6F,  $\theta_1$  Hz, dark**

	Shifts control	M1/Tm3 control	M1/Tm3 block
N files	12	12	13
mean	-10.5	-42.0	-97.6
std	26.1	46.7	57.0

Shifts control  $t = 2.038$   
 $p = 0.057$   
M1/Tm3 control  $t = 0.969$   
 $p = 0.001$

M1/Tm3 control  $t = 2.874$   
 $p = 0.014$   
M1/Tm3 block

**Figure 6D, response mean**

	Shifts control	M1/Tm3 control	M1/Tm3 block
N files	12	12	12
mean	30.7	30.5	-0.2
std	9.0	14.4	4.1

Shifts control  $t = 0.038$   
 $p = 0.970$   
M1/Tm3 control  $t = 0.020$   
 $p = 0.991$

M1/Tm3 control  $t = 7.122$   
 $p = 0.001$   
M1/Tm3 block

**Figure 6F,  $A_1$  Hz, bright**

	Shifts control	M1/Tm3 control	M1/Tm3 block
N files	12	12	13
mean	12.1	10.0	4.3
std	5.2	3.2	2.6

Shifts control  $t = 1.025$   
 $p = 0.243$   
M1/Tm3 control  $t = 1.407$   
 $p < 0.001$

M1/Tm3 control  $t = 7.122$   
 $p = 0.001$   
M1/Tm3 block

**Figure 6F,  $\theta_1$  Hz, bright**

	Shifts control	M1/Tm3 control	M1/Tm3 block
N files	12	12	13
mean	-167.0	-154.3	54.0
std	18.1	29.5	48.6

Shifts control  $t = -1.287$   
 $p = 0.221$   
M1/Tm3 control  $t = 0.922$   
 $p < 0.001$

M1/Tm3 control  $t = 5.513$   
 $p < 0.001$   
M1/Tm3 block

**Figure 6D,  $A_2$  Hz**

	Shifts control	M1/Tm3 control	M1/Tm3 block
N files	12	12	12
mean	20.6	23.3	2.0
std	5.5	7.7	1.1

Shifts control  $t = 0.986$   
 $p = 0.336$   
M1/Tm3 control  $t = 1.009$   
 $p = 0.001$

M1/Tm3 control  $t = 2.459$   
 $p < 0.001$   
M1/Tm3 block

**Figure 6F,  $A_2$  Hz, gray**

	Shifts control	M1/Tm3 control	M1/Tm3 block
N files	12	12	13
mean	7.7	5.2	2.6
std	3.7	1.8	1.5

Shifts control  $t = 2.139$   
 $p = 0.048$   
M1/Tm3 control  $t = 4.409$   
 $p < 0.001$

M1/Tm3 control  $t = 5.919$   
 $p < 0.001$   
M1/Tm3 block

**Figure 6F,  $\theta_2$  Hz, gray**

	Shifts control	M1/Tm3 control	M1/Tm3 block
N files	12	12	13
mean	144.5	134.5	137.8
std	27.7	31.7	26.3

Shifts control  $t = 0.827$   
 $p = 0.418$   
M1/Tm3 control  $t = 0.618$   
 $p = 0.543$

M1/Tm3 control  $t = 2.287$   
 $p = 0.777$   
M1/Tm3 block

**B****Figure S4C,  $A_1$  Hz, dark**

	Shifts control	M1/Tm3 control	T4/T5 control	M1/Tm3 block	T4/T5 block	M1/Tm3/T4/T5 block
N files	19	16	14	15	15	14
mean	9.1	13.3	15.8	11.4	18.7	8.6
std	6.9	4.6	5.8	5.1	3.6	3.8

Shifts control  $t = -2.585$   
 $p = 0.015$   
M1/Tm3 control  $t = 2.573$   
 $p = 0.019$

M1/Tm3 control  $t = -0.292$   
 $p = 0.365$   
T4/T5 control  $t = -0.928$   
 $p = 0.314$

T4/T5 control  $t = 1.026$   
 $p = 0.125$   
M1/Tm3 block  $t = 1.595$   
 $p = 0.321$

M1/Tm3 block  $t = -1.014$   
 $p = 0.321$   
T4/T5 block  $t = -3.489$   
 $p = 0.002$

T4/T5 block  $t = 0.159$   
 $p = 0.875$   
M1/Tm3/T4/T5 block  $t = 4.572$   
 $p < 0.001$

**Figure S4C,  $A_1$  Hz, bright**

	Shifts control	M1/Tm3 control	T4/T5 control	M1/Tm3 block	T4/T5 block	M1/Tm3/T4/T5 block
N files	19	16	14	15	15	14
mean	13.2	10.1	14.3	5.8	17.5	5.4
std	6.3	6.1	2.7	3.0	6.5	3.7

Shifts control  $t = 1.736$   
 $p = 0.092$   
M1/Tm3 control  $t = -0.835$   
 $p = 0.081$

T4/T5 control  $t = -1.835$   
 $p = 0.001$   
M1/Tm3 block  $t = 3.930$   
 $p = 0.021$

M1/Tm3 block  $t = -0.985$   
 $p < 0.001$   
T4/T5 block  $t = 1.312$   
 $p = 0.202$

T4/T5 block  $t = 0.276$   
 $p = 0.785$   
M1/Tm3/T4/T5 block  $t = 7.988$   
 $p < 0.001$

**Figure S4C,  $\theta_1$  Hz, bright**

	Shifts control	M1/Tm3 control	T4/T5 control	M1/Tm3 block	T4/T5 block	M1/Tm3/T4/T5 block
N files	19	16	14	15	15	14
mean	-154.3	-149.5	-152.0	72.7	-155.7	63.6
std	25.6	16.5	38.4	54.7	32.7	31.7

Shifts control  $t = -0.663$   
 $p = 0.512$   
M1/Tm3 control  $t = -0.229$   
 $p = 0.822$

T4/T5 control  $t = -0.746$   
 $p = 0.001$   
M1/Tm3 block  $t = 0.7746$   
 $p = 0.001$

M1/Tm3 block  $t = -0.276$   
 $p = 0.785$   
T4/T5 block  $t = 10.848$   
 $p < 0.001$

T4/T5 block  $t = 7.988$   
 $p < 0.001$   
M1/Tm3/T4/T5 block  $t = 11.771$   
 $p < 0.001$

**C****Figure 7C**

	Shifts control	T4/T5 block	M1/Tm3 + T4/T5 block
N cells (files)	13 (8)	5 (5)	7 (5)
mean	12.784	0.157	0.25
std	6.934	0.304	0.228

Shifts control  $t = -0.526$   
 $p = 0.602$   
T4/T5 block  $t = 1.409$   
 $p = 0.170$

M1/Tm3 + T4/T5 block  $t = 5.205$   
 $p < 0.001$   
M1/Tm3 + T4/T5 block  $t = -0.578$   
 $p < 0.001$

**Figure 7D,  $A_1$  Hz**

	Shifts control	T4/T5 block	M1/Tm3 + T4/T5 block
N cells (files)	13 (8)	5 (5)	7 (5)
mean	0.527	0.047	0.042
std	0.492	0.016	0.022

Shifts control  $t = 3.515$   
 $p < 0.001$   
T4/T5 block  $t = 3.549$   
 $p < 0.001$

M1/Tm3 + T4/T5 block  $t = 0.449$   
 $p = 0.963$   
M1/Tm3 + T4/T5 block  $t = -11.749$   
 $p = 0.344$

**Figure 7D,  $A_2$  Hz**

	Shifts control	T4/T5 block	M1/Tm3 + T4/T5 block
N cells (files)	13 (8)	5 (5)	7 (5)
mean	0.456	0.399	0.117
std	0.217	0.079	0.064

Shifts control  $t = 0.818$   
 $p = 0.427$   
T4/T5 block  $t = 0.943$   
 $p < 0.001$

M1/Tm3 + T4/T5 block  $t = -6.423$   
 $p < 0.001$   
M1/Tm3 + T4/T5 block  $t = 11.771$   
 $p < 0.001$

**Figure 7G**

	Shifts control	T4/T5 block	M1/Tm3 + T4/T5 block
N cells (files)	11 (6)	8 (6)	4 (3)
mean	8.561	0.351	0.25
std	3.191	0.528	0.146

Shifts control  $t = 8.376$   
 $p < 0.001$   
T4/T5 block  $t = 8.612$   
 $p < 0.001$

M1/Tm3 + T4/T5 block  $t = -0.505$   
 $p = 0.827$   
M1/Tm3 + T4/T5 block  $t = 0.505$   
 $p = 0.827$

**Figure 7H,  $A_1$  Hz**

	Shifts control	T4/T5 block	M1/Tm3 + T4/T5 block
N cells (files)	11 (6)	8 (6)	4 (3)
mean	0.145	0.044	0.023
std	0.103	0.016	0.008

Shifts control  $t = 3.179$   
 $p < 0.001$   
T4/T5 block  $t = 3.875$   
 $p < 0.001$

M1/Tm3 + T4/T5 block  $t = -0.706$   
 $p = 0.214$   
M1/Tm3 + T4/T5 block  $t = 0.706$   
 $p = 0.214$

**Figure 7H,  $A_2$  Hz**

	Shifts control	T4/T5 block	M1/Tm3 + T4/T5 block
N cells (files)	11 (6)	8 (6)	4 (3)
mean	0.217	0.192	0.047
std	0.117	0.074	0.033

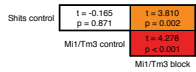
Shifts control  $t = 0.520$   
 $p = 0.590$   
T4/T5 block  $t = 3.442$   
 $p < 0.001$

M1/Tm3 + T4/T5 block  $t = -0.714$   
 $p = 0.201$   
M1/Tm3 + T4/T5 block  $t = 0.714$   
 $p = 0.201$

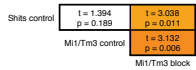
**Table S2, related to Figures 6, S4, and 7. Detailed Statistics**  
(A) For Figure 6. (B) For Figure S4. (C) For Figure 7.

**A** Figure S5C,  $A_1$  Hz<sup>1</sup> dark

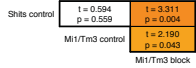
	Shifts control	Mi1/Tm3 control	Mi1/Tm3 block
N files	10	12	8
mean	8.8	9.1	3.0
std	4.5	4.5	1.7

Figure S5C,  $A_1$  Hz<sup>1</sup> bright

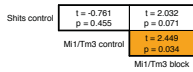
	Shifts control	Mi1/Tm3 control	Mi1/Tm3 block
N files	10	12	8
mean	5.7	3.9	1.9
std	3.6	1.6	1.3

Figure S5C,  $A_2$  Hz<sup>1</sup> gray

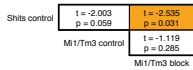
	Shifts control	Mi1/Tm3 control	Mi1/Tm3 block
N files	10	12	8
mean	6.5	5.6	2.8
std	2.7	3.8	1.9

Figure S5C,  $\theta_1$  Hz<sup>1</sup> dark

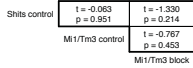
	Shifts control	Mi1/Tm3 control	Mi1/Tm3 block
N files	10	12	8
mean	22.6	34.1	-30.0
std	32.7	38.5	67.1

Figure S5C,  $\theta_1$  Hz<sup>1</sup> bright

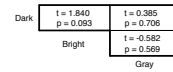
	Shifts control	Mi1/Tm3 control	Mi1/Tm3 block
N files	10	12	8
mean	-125.3	-79.2	-38.3
std	43.0	64.2	89.1

Figure S5C,  $\theta_2$  Hz<sup>1</sup> gray

	Shifts control	Mi1/Tm3 control	Mi1/Tm3 block
N files	10	12	8
mean	162.5	163.8	-177.9
std	18.4	66.1	38.4

Figure S5D,  $A_2$  Hz<sup>1</sup> Mi1/Tm3 block

	Dark	Bright	Gray
N files	8	8	8
mean	3.7	2.7	2.8
std	2.3	1.8	1.9

Figure S5D,  $\theta_2$  Hz<sup>1</sup> Mi1/Tm3 block

	Dark	Bright	Gray
N files	8	8	8
mean	170.1	172.1	-177.9
std	45.0	30.2	38.4

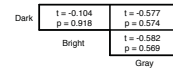
**Table S3, related to Figure S5. Detailed Statistics**  
(A) For Figure S5.

Figure 4E

**Table S4, related to Figure 4. Detailed Statistics (A) For Figure 4E.**

A Figure 4F

**Table S6**, related to Figure S2. Detailed Statistics

(A) For Figure S2D.

#### **SUPPLEMENTAL REFERENCES**

Borst, A. (2014). Fly visual course control: behaviour, algorithms and circuits. *Nat. Rev. Neurosci.* 15, 590–599.

Rajashekhar, K.P., and Shamprasad, V.R. (2004). Golgi analysis of tangential neurons in the lobula plate of *Drosophila melanogaster*. *J. Biosci.* 29, 93–104.

## Manuscript VII

### Preserving Neural Function under Extreme Scaling

Hermann Cuntz, Friedrich Forstner, Bettina Schnell, **Georg Ammer**, Shamprasad Varija Raghu, and Alexander Borst

#### Author Contributions

Conceived and designed the experiments: HC FF AB. Performed the experiments: FF BS **GA** SVR. Analyzed the data: HC FF. Wrote the paper: HC FF BS **GA** SVR AB.

**PLoS One** 8, e71540. doi: 10.1371/journal.pone.0071540.



# Preserving Neural Function under Extreme Scaling

Hermann Cuntz<sup>1,2,3\*</sup>, Friedrich Forstner<sup>1</sup>, Bettina Schnell<sup>1,4</sup>, Georg Ammer<sup>1</sup>, Shamprasad Varija Raghu<sup>1,5</sup>, Alexander Borst<sup>1</sup>

**1** Department of Systems and Computational Neurobiology, Max Planck Institute of Neurobiology, Martinsried, Germany, **2** Institute of Clinical Neuroanatomy, Goethe University, Frankfurt/Main, Germany, **3** Ernst Strüngmann Institute for Neuroscience in Cooperation with Max Planck Society, Frankfurt/Main, Germany, **4** Department of Biology, University of Washington, Seattle, Washington, United States of America, **5** Neuroscience Research Partnership, Biopolis, Singapore

## Abstract

Important brain functions need to be conserved throughout organisms of extremely varying sizes. Here we study the scaling properties of an essential component of computation in the brain: the single neuron. We compare morphology and signal propagation of a uniquely identifiable interneuron, the HS cell, in the blowfly (*Calliphora*) with its exact counterpart in the fruit fly (*Drosophila*) which is about four times smaller in each dimension. Anatomical features of the HS cell scale isometrically and minimise wiring costs but, by themselves, do not scale to preserve the electrotonic behaviour. However, the membrane properties are set to conserve dendritic as well as axonal delays and attenuation as well as dendritic integration of visual information. In conclusion, the electrotonic structure of a neuron, the HS cell in this case, is surprisingly stable over a wide range of morphological scales.

**Citation:** Cuntz H, Forstner F, Schnell B, Ammer G, Raghu SV, et al. (2013) Preserving Neural Function under Extreme Scaling. PLoS ONE 8(8): e71540. doi:10.1371/journal.pone.0071540

**Editor:** Maurice J. Chacron, McGill University, Canada

**Received:** April 26, 2013; **Accepted:** June 28, 2013; **Published:** August 19, 2013

**Copyright:** © 2013 Cuntz et al. This is an open-access article distributed under the terms of the Creative Commons Attribution License, which permits unrestricted use, distribution, and reproduction in any medium, provided the original author and source are credited.

**Funding:** The authors have no funding or support to report.

**Competing Interests:** The authors have declared that no competing interests exist.

\* E-mail: hermann.neuro@gmail.com

## Introduction

Intuition from simple cable theory tells us that smaller neurons should have larger input resistances, faster integration times and be altogether electrically more compact (e.g. [1]). However, the brains of smaller organisms which consist of correspondingly smaller cells (e.g. [2–6]) often implement very much the same computations and functions as their larger counterparts. Since brain tissue is energetically expensive to maintain [7–9] the question arises why brain evolution did not lead to more compact brains even in larger organisms? How does the single neuron cope with the electrotonic changes due to differences in size? Would a neuron compromise material costs that are known to be otherwise instrumental in determining dendrite structure [10–12] to adjust its shape to preserve a particular computation? To address these questions the concept of conservative scaling may be useful (e.g. [3,13]). In such a setting an invariance preserving important electrotonic properties rather than anatomical proportions could result in a conservation of dendritic integration features such as relative conduction delays and non-linear interactions of synaptic currents in the dendrite.

Here, we address these questions in a circuit of the fly visual system for which both the function and the underlying biophysical mechanisms are well understood at the cellular and the network level: Tangential Cells (LPTCs) of the third visual neuropil, the Lobula Plate, form a circuitry involved in optic flow calculations. By pooling of inputs from presynaptic elementary motion detectors and cross-talk between LPTCs they compute large field visual motion features required for the fly's course control [14]. In a number of electrophysiology and modelling studies on *Calliphora* LPTCs, their predominantly passive electrotonic features [15–17] were characterised and linked to their function as large-field signal

integrators: They were shown to average out spatial structure in the motion image [18], to communicate signal features selectively to other LPTCs (e.g. [19,20]) and to compartmentalise the signals between their dendrites and axons [21–23]. More recently, LPTCs have also become amenable to intracellular electrophysiological analysis in *Drosophila* [24,25] revealing surprisingly conserved functionality and visual responses. This opens up the opportunity to compare both electrophysiology and shape of an identified neuron with its exact homolog in two flies of fundamentally different sizes (Figure 1A), with a scaling factor of about four in each dimension. LPTCs are the ideal subject to study the scaling property of one particular neuron since each LPTC is individually identifiable due to the high degree of constancy in receptive field, morphology, location within the Lobula Plate and visual response properties [26,27].

In this study we focus particularly on a subset of LPTCs, the Horizontal System (HS) cells, which respond selectively to horizontal large-field motion. Their membrane potential responds in a graded direction-selective manner, i.e. it depolarises during front-to-back visual motion stimulation and hyperpolarises when stimulated in the opposite direction. Three individual HS cells exist in each of the two optic lobes of the fly brain. They are named according to their position within the Lobula Plate, with HSN (Northern) covering the dorsal, HSE (Equatorial) the intermediate and HSS (Southern) the ventral parts, respectively [26] (Figures 1B and C show the HSN and HSE in *Calliphora* and *Drosophila*, respectively). In the following, we use electrophysiological and morphological data in combination with computational models to quantitatively assess the scaling principles of HS cells in both species.

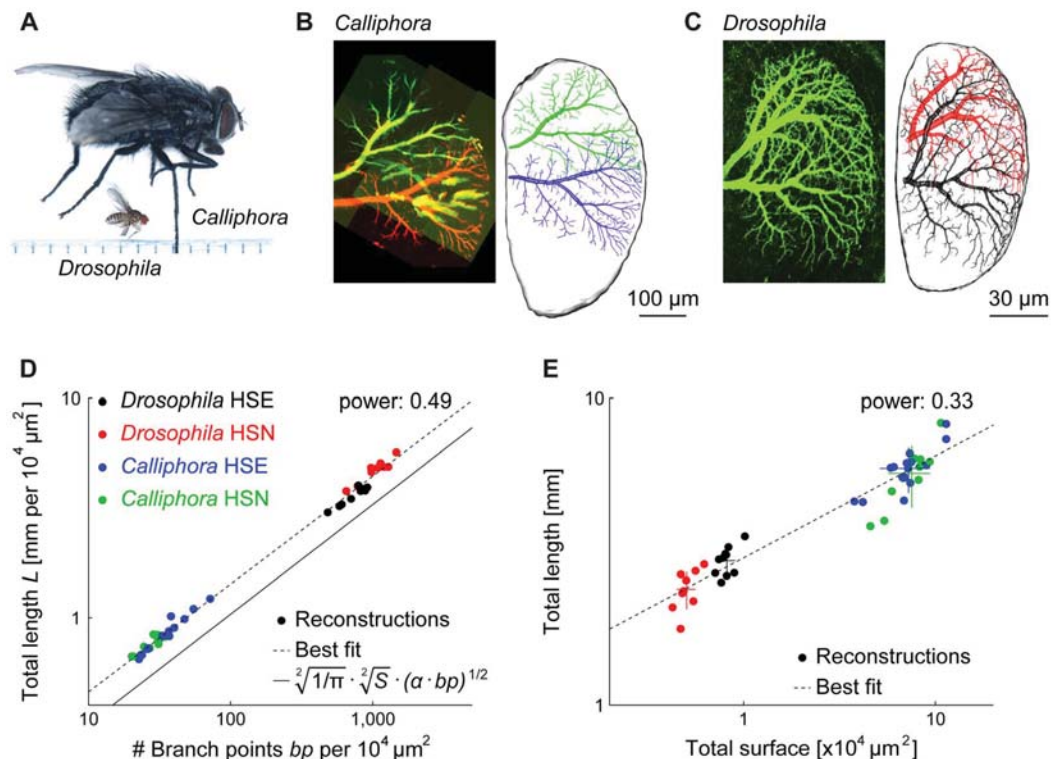


**Figure 1. Morphological analysis of *Drosophila* vs. *Calliphora* HS cell dendrites.** (A) Comparison of size between the blowfly (*Calliphora*) and the fruit fly (*Drosophila*); ruler has mm markings. (B) Superposition of the HSN (green) and the HSE (red) in a Lobula Plate of *Calliphora*. On the right side, a rendering of the full reconstructions of both cells (HSN – green and HSE – blue) within the marked boundaries of the reconstructed Lobula Plate is depicted. (C) Similar setting for the HSN and HSE cells (both are green since they both express GFP) in a brain of *Drosophila* with corresponding reconstructions (HSN – red and HSE – black) to the right. (D) Power law between branch point and total length densities, a power of 1/2 being indicative of optimal wiring for planar dendrites [33]. (E) Absolute scaling between total surface and total length. Crosses indicate population mean and standard deviation.

doi:10.1371/journal.pone.0071540.g001

## Materials and Methods

### Reconstructions and anatomy

*Calliphora* cells were filled intracellularly using sharp electrodes with Alexa 488 [28] for the three dimensional reconstructions. In *Drosophila*, a Gal4 driver (NP0282) driving expression specifically in HSN and HSE in both lobes was used (Figure 1C) [25,29]. Reconstructions of HS dendrites (see overview in Figure S1) were done using custom-made software in Matlab (The Mathworks, Inc.) and exported to our software package that is freely available for download (the TREES toolbox, [www.treestoolbox.org](http://www.treestoolbox.org)) [10,30]. Reconstructions are available on the TREES toolbox

website and at [www.neuro.mpg.de/30330/borst\\_modelfly\\_downloads](http://www.neuro.mpg.de/30330/borst_modelfly_downloads). All further analyses and models were performed using these tools. Reconstruction of the axons was not possible in *Drosophila* HS cells due to co-localisation of other labelled cells in the NP0282 driver line. One axonal reconstruction was obtained using intracellular injection of a fluorescent dye (see below) and was appended to all *Drosophila* dendrites for electrotonic analysis. Combined spanning fields of HSE and HSN cells provided good context clues for the Lobula Plate contours (confirmed with background stains).

### *Drosophila* electrotonic analysis

Whole cell patch-clamp recordings were performed as described previously [24,25]. Briefly, flies were anaesthetized on ice and waxed on a Plexiglas holder. A small window was cut into the cuticle on the backside of the head and a glass electrode filled with collagenase (Collagenase IV, Gibco, 0.5 mg/ml in extracellular saline) was used to weaken the perineural sheath and expose the somata of LPTCs. Somata were approached with a patch electrode (7–10 MΩ resistance, thin wall) filled with intracellular solution (as in [31] containing an additional 30 mM Alexa Fluor 568 hydrazide-Na (A-10441, Molecular Probes) adjusted to pH 7.3). Signals were recorded on a BA-1S Bridge Amplifier (npi electronics, Tamm, Germany), low-pass filtered at 3 kHz, and

**Table 1. Scaling of global anatomical features.**

Size parameters	<i>Calliphora</i>	<i>Drosophila</i>	scale	linear scale
body length (mm)	11	2.6	4.2	4.2
brain volume (mm <sup>3</sup> )	1.22	0.015	81.3	4.3
Lobula Plate area (mm <sup>2</sup> )	0.18	0.009	20.0	4.5

(personal communication, Christoph Kapfer).

doi:10.1371/journal.pone.0071540.t001

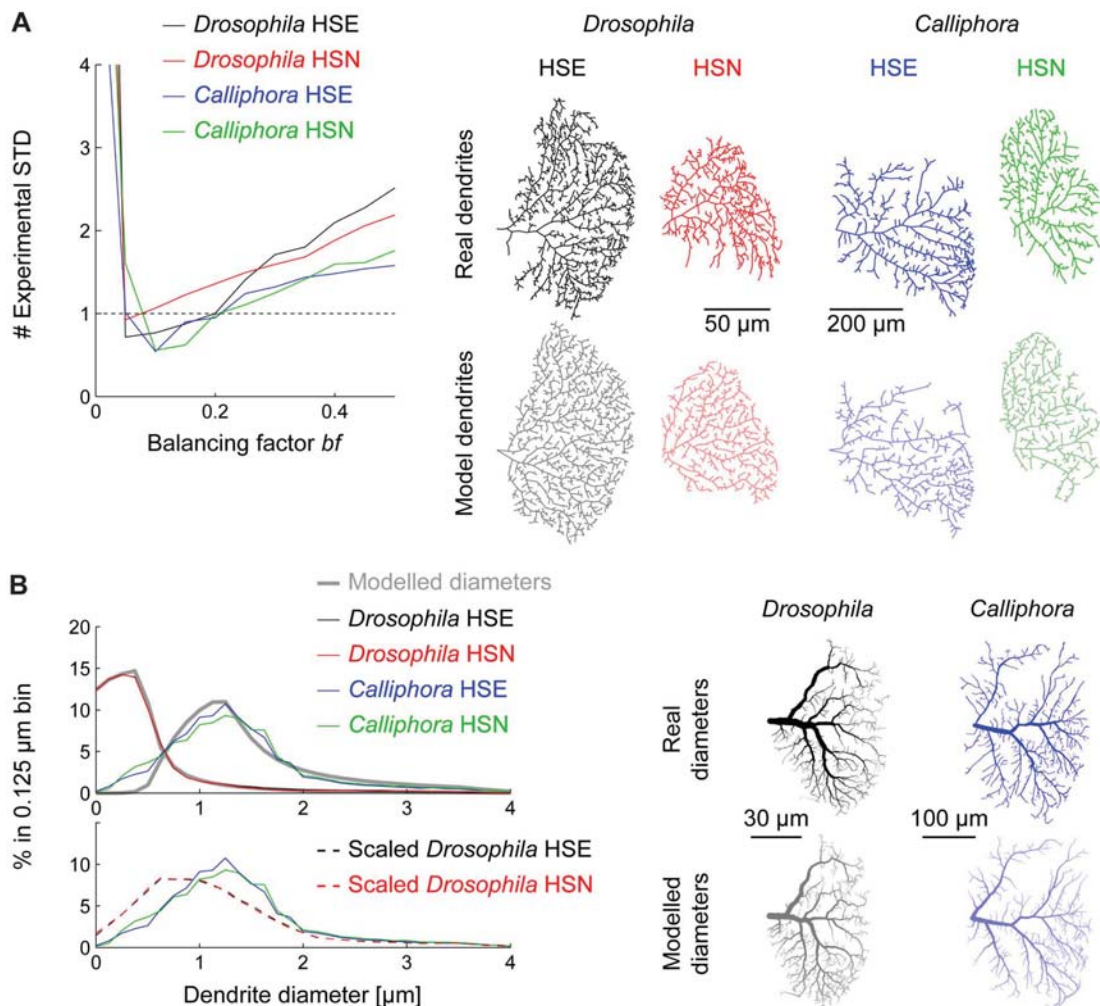


**Figure 2. Morphological model to study the scaling properties of HS cells.** (A) Model error compared to standard deviation of experimental measures as a function of the balancing factor *bf*, the one parameter in the morphological model. To the right, sample model dendrites (lighter colours) with their respective real counterparts for *Drosophila* HSE (black) and HSN (red) and *Calliphora* HSE (blue) and HSN (green). (B) Diameter histograms for all cell types (same colours as in A) and best fits (grey lines) using the quadratic taper fit from our model [12]. Lower panel shows scaled diameters of *Drosophila* cells in comparison to *Calliphora* cells. To the right, sample *Calliphora* and *Drosophila* HSE dendrites comparing real and modelled diameters (in lighter colours).

doi:10.1371/journal.pone.0071540.g002

digitised at 10 kHz via a D/A converter (PCI-DAS6025, Measurement Computing, Norton, MA) with Matlab. Note that electrophysiological and morphological data were not obtained from the same individuals. Input resistance and membrane time constant were measured in responses to 3 × step currents of hyperpolarizing 50 pA each, 30 seconds and 10 minutes after break-in. Membrane time constants were obtained by linear regression on a semi-logarithmic plot corresponding to a single exponential fit to the voltage response, which yielded good results. Both input resistance and membrane time constant increased during the recording period from  $176 \pm 46$  to  $205 \pm 45$  M $\Omega$  and from  $4.3 \pm 1.4$  to  $4.9 \pm 1.3$  ms respectively within 10 minutes (numbers are mean and standard deviation). While the quality of the seal increases with time, the quality of the recording decreases because of clogging of the electrode. It was therefore not clear

which values to use but the differences were small in comparison to the overall variance in experimental values. The later measurements were used for averaged values. Since recordings were obtained in current clamp and the membrane potential measurements were relatively noisy even without any stimulation, we were unable to accurately estimate and compensate for the series resistance. However, our values for the input resistance are in good agreement with data for VS cells in *Drosophila* obtained in voltage clamp [32], suggesting that errors in measurement are minor.

#### Morphological model

To check that *Drosophila* HS cells obeyed optimal wiring constraints we first verified the scaling properties predicted by these constraints (Figure 1D) [33]. Further we performed the complete analysis as previously for *Calliphora* HS cells [28]

**Table 2.** Scaling of dendritic anatomical features.

Size parameters	<i>Calliphora</i>	<i>Drosophila</i>	scale	linear scale
avg. dendrite diameter (μm)	1.92±0.27 (N=25)	0.58±0.08 (N=20)	3.4	3.4

doi:10.1371/journal.pone.0071540.t002

involving the generation of a morphological model based on optimal wiring principles (see Results). Briefly, dendrite spanning fields were obtained for each reconstructed HS dendrite delimiting the area covered by the dendrite such that each point in the dendrite spanning field is within a threshold distance away from the dendrite tree. Target points were then distributed randomly within the spanning fields and connected to dendrite structures satisfying two wiring costs: (1) the total dendrite length should be short and (2) the length of all paths along the dendrite from any point to the root should be short. The second cost was weighted with a balancing factor  $bf$  against the first cost. We verified that our morphological model was useful also for *Drosophila* dendrites using a similar model parameter value  $bf$  as for *Calliphora* HS dendrites. Only few minor adjustments were required in the modelling procedure accounting for the differences in scale: e.g. a finer resolution was used to estimate the dendrite spanning fields.

### Morphological model database

The corresponding database of synthetic dendrites used to studying the electrotonic scaling properties of HS cells were obtained using target point numbers ranging from 625 to 2,300 and scaling down the surface area of a *Calliphora* HS dendrite between 1× and 4.5×. A model for diameter tapering was obtained as discussed previously [12] based on requirements for synaptic democracy. Two sets of parameters (consisting of a terminal branch diameter value and a scaling factor) were obtained by fitting the data from real reconstructions for *Drosophila* and *Calliphora* HS cell dendrites, respectively. All algorithms are available in the Matlab software package (the TREES toolbox, [www.treestoolbox.org](http://www.treestoolbox.org)) [10,30].

## Results

### Morphological analysis

First, we studied the global scaling properties between the two species of flies. Selected size parameters (Table 1) scaled linearly with a factor of about 4 indicating that isometric rather than allometric scaling takes place regarding the body shape thereby conserving the general anatomical proportions [34,35]. In particular, the area of the Lobula Plate (see outlines in Figure 1BC) that is spanned by the HS cells seemed to be scaled linearly with the body length and its shape was well preserved. It is worth noting that HSN dendritic fields cover a similar percentage of the Lobula Plate in *Calliphora* and *Drosophila*, whereas the HSE dendritic field covers a larger percentage in *Drosophila* than in *Calliphora*. We have previously shown that dendrite morphology of LPTCs in fact depends most strongly on the area they span [28]. This indicates that some aspects of LPTC morphology should be conserved and should scale linearly with the Lobula Plate size. To make quantitative assertions, however, full morphological LPTC reconstructions were required consisting of connected cylinders representing the tree structure. Such reconstructions were obtained and discussed previously for the *Calliphora* HS cells [28] (Figure 1B). To quantitatively assess differences in morphology and signal propagation between HS cells of *Calliphora* with those of

*Drosophila*, we acquired the corresponding data from fruit flies. Studying *Drosophila* allows the usage of genetic techniques. We therefore obtained image stacks from flies using the Gal4 driver line NP0282 to express GFP bilaterally in HSN and HSE cells [25,29] (Figure 1C). The dendrite reconstructions were obtained from these image stacks using custom-made Matlab code as done previously for the *Calliphora* HS cells (see Methods and Figure S1).

A major determinant of dendrite shape is a strive for minimising wiring costs and conduction times [10–12,36–38]. It was previously shown that optimal wiring constraints account for inner branching features in the case of *Calliphora* LPTCs [12,28]. Assuming optimal wiring principles, the scaling behaviour of dendrites can be predicted in terms of dendrite length, number of synapses, number of branch points and the surface or volume that a dendrite spans [33]. A 1/2 power between branch point density and dendrite cable density is expected for planar dendrites with a precise calculation of a tight lower bound for the optimal dendrite length (Figure 1D, straight line). Both *Drosophila* and *Calliphora* HS cell dendrites were strictly constrained by this equation with the best fit of 0.49 for the power relation between cable density and branch point density (Figure 1D). As expected, the overall density of dendrites was much larger in the smaller *Drosophila* dendrites. Beyond this relation describing the scaling behaviour in terms of optimal wiring it is useful to compare the absolute dendrite length with the surface covered by the dendrite (Figure 1E). For this relation no prediction in terms of optimal wiring is known. A linear relation (power of 1) would indicate that the cable density is similar in both species, while a power of 1/2 would correspond to a simple isometric scaling without a change in dendrite complexity. Interestingly, the fitted power was 0.33 indicating that the larger dendrites of *Calliphora* HS cells were consistently less complex than their smaller counterparts. This result is particularly counterintuitive since *Drosophila* has a much smaller number of facets in the eye with 700 in *Drosophila* [39] vs. 4,500 in *Calliphora* [40]. Since the underlying neural circuitry is subdivided and organised into retinotopic cartridges corresponding to the ommatidial layout [41], *Drosophila* HS cells should in fact receive fewer inputs to be integrated within their receptive field.

### A morphological model for scaling

In order to understand the change of morphological and electrotonic properties due to scaling we first developed a model that describes the morphology with a few parameters. With the possibility to scale continuously between *Drosophila* and *Calliphora* dendrites the consequences of morphological scaling can then be studied independently from each other while keeping the other features constant. We have recently proposed a morphological model capable of generating synthetic dendrites that match well those of *Calliphora* LPTCs and many other neurons [10,12,28]. The model is based on the assumption that a dendrite strives to connect optimally to its inputs that are distributed in space. In the case of LPTCs, inputs are retinotopically organised elementary motion detectors covering the area of the Lobula Plate. Target points that are distributed within the contours of a real LPTC are connected while minimising cable length and path lengths along

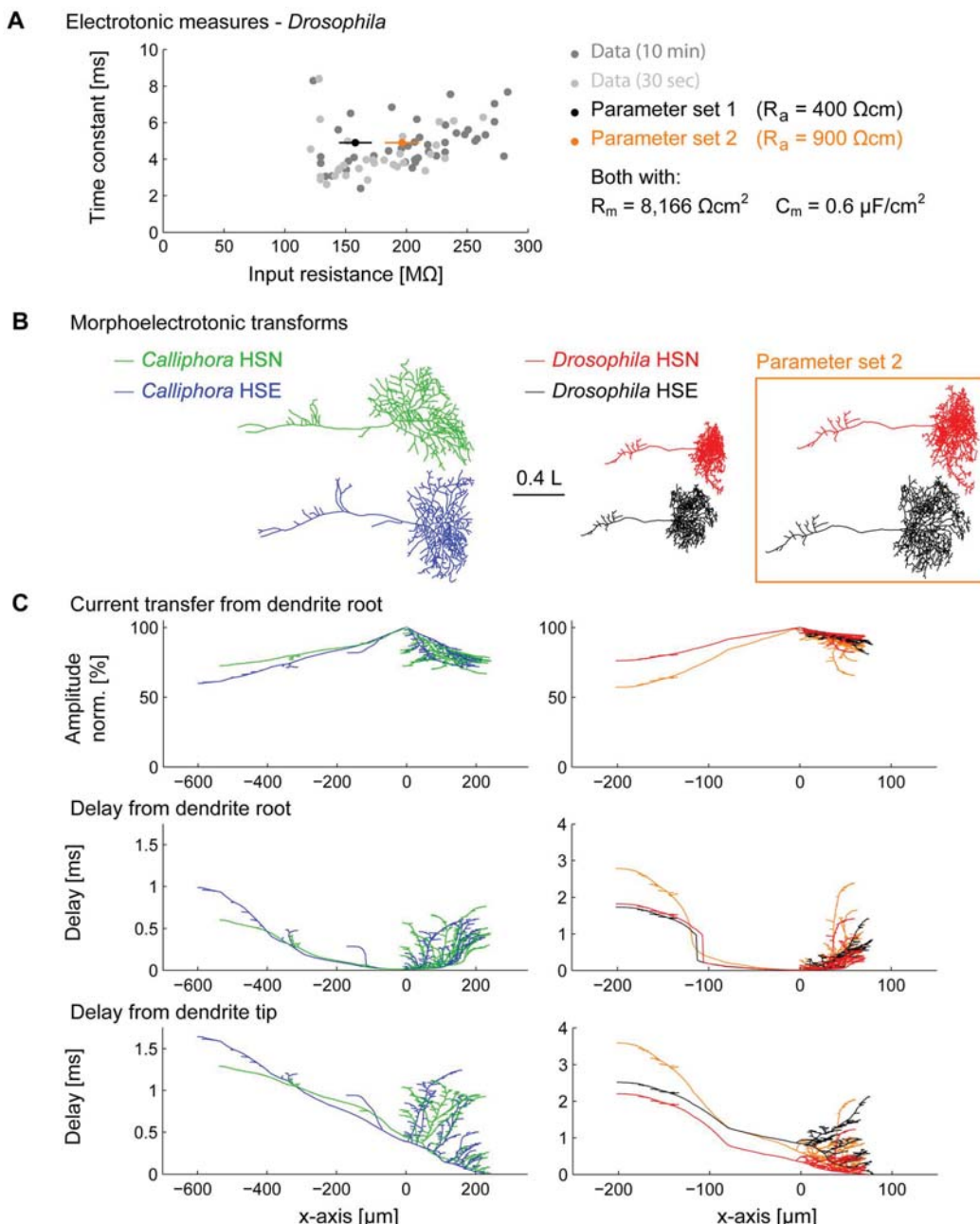


**Figure 3. Signal conduction and dendritic integration in *Drosophila* and *Calliphora* HS cells.** (A) Experimental input resistance and membrane time constant measurements in *Drosophila* HS cells (dark grey –10 min.; light grey –30 sec. after breaking into the cell). The later measurements were used for estimating average values since the patch is more stable then. Two model parameter sets (black and orange) were used in the further study. (B) Morphoelectrotonic transforms of four sample cells where electrotonic lengths are mapped onto the segments of the branched structures [42] (orange box: second parameter set for *Drosophila*). (C) Same four cells as in B but with the amplitude decay from the dendrite root mapped onto the y-axis of the cells (top panels) and delays from the dendrite root (middle panels) and from selected dendrite tips (bottom panels). The *Drosophila* HSN cell results are shown for the second parameter set in orange.

doi:10.1371/journal.pone.0071540.g003

the tree toward the root [28]. A cost for long path lengths is weighted in comparison to the cost of cable length by one parameter of the model, the balancing factor  $bf$ . The same

procedure was previously performed on *Calliphora* dendrites [28] (see Methods). When branching features (total length, branch order and path length distributions) of the resulting model

**Table 3.** Electrophysiological measures.

	<i>Calliphora</i>	<i>Drosophila</i>
Input resistance, $R_m$ (MΩ)	4.95±2.25 (N=5)	205±45 (N=14)
Membrane time constant, $\tau$ (ms)	2.1 (N=5)	4.9±1.3 (N=14)

Data for *Calliphora* are from [17].  
doi:10.1371/journal.pone.0071540.t003

dendrites were linearly combined and compared to the standard deviation in the experimental measures, a small parameter value  $bf = 0.1$  represented a good fit in *Drosophila* as well as in *Calliphora* (Figure 2A, see also sample dendrites and their corresponding model counterparts). The comparably low value for  $bf$  (the typical range is between 0.1 in LPTCs and 0.85 in dentate gyrus granule cells for example) seems to discard fast conduction times in favour of short cable length and reduces the effective electrotonic compartmentalisation in favour of more even integration of signals throughout the dendrite [10].

Next, we studied the scaling property of diameters while further confining our model. Beyond the cable length and dendrite complexity, cable diameters play an important role for conveying electrical signals. While average dendrite diameter values (see Table 2) scaled isometrically with the rest of the global fly measures, diameter distributions were slightly different (Figure 2B, top and bottom panel). When dendrite diameters were scaled to have the overall same average diameter, a higher proportion of thin *Drosophila* dendrites was revealed compared to a higher proportion of medium size diameters for *Calliphora* counterparts. A quadratic diameter taper was previously shown to optimise synaptic current transfer democracy in LPTCs [12] and a method exists for mapping diameters onto a tree structure following the corresponding rules of diameter tapering. Beyond reproducing the diameter taper observed in *Calliphora* LPTCs the method generates good diameter mappings for a number of other dendrites [10,30]. The quadratic diameter taper is parameterised with a parameter for the smallest dendrite tip diameter and a scaling factor determining a neuron's overall leak [12]. To compare diameter values between *Calliphora* and *Drosophila* dendrites we obtained the best fits for these two parameters in the two populations of dendrites. Parameter sets reproducing the diameter distributions were obtained and validated (Figure 2B). This procedure allows us to manipulate diameter values of the morphology using the two different diameter mapping methods as well as a smooth transition between the two. In summary, the morphology of both types of HS cells are essentially scaled versions of each other following similar branching principles but *Drosophila* HS cells are surprisingly more complex than *Calliphora* HS cells.

#### Designing the passive electrotonic model

Next we studied the electrotonic properties of HS cells to determine the following parameters for the corresponding compartmental models: the specific membrane resistance  $R_m$ , the specific axial resistance  $R_a$  and the specific membrane capacitance  $C_m$ . We determined input resistance and membrane time constant in electrophysiological intracellular recordings (Table 3; see Methods). The measured membrane time constants were short in both species, but about 2.3× longer in *Drosophila* (4.9 ms) than in *Calliphora* (2.1 ms). The measured input resistances were much higher (~50×) in *Drosophila* HS cells (205±45 MΩ instead of 4–5 MΩ in *Calliphora*). A common assumption is that the specific membrane capacitance is close to  $C_m = 1\mu\text{F}/\text{cm}^2$ . The specific

membrane resistance  $R_m$  is then fully determined when the measured membrane time constant is known. This is the case since  $\tau = R_m \cdot C_m$  corresponding to the membrane time constant for a current injection in an infinite cable is valid for current injections in complex electrotonic models of neurons including the ones tested here. For *Calliphora* HS cells, a model was selected that corresponding to the measured membrane time constant of 2.1 ms had  $R_m = 2,100 \Omega\text{cm}^2$  and to fit the input resistance  $R_m$  required  $R_a = 100 \Omega\text{cm}$ . This is in agreement with previously measured parameters [17]. The *Drosophila* HS cell electrotonic model has not yet been studied and we performed meticulous intracellular recordings for which experimental  $R_m$  and  $\tau$  are plotted in Figure 3A. With *Calliphora* HS cell membrane parameters, *Drosophila* HS cells exhibit an input resistance of about 40 MΩ. To obtain realistic input resistance values in the model,  $C_m$  was required to be very small and  $R_a$  very large even considering that recordings in *Drosophila* were performed in the soma whereas *Calliphora* input resistances measures were performed in the axon. We considered two model parameter sets both with  $R_m = 8,166 \Omega\text{cm}^2$  and  $C_m = 0.6 \mu\text{F}/\text{cm}^2$  but with different axial resistances of  $R_a = 400 \Omega\text{cm}$  in a model with realistic axial resistance but with low input resistance and with  $R_a = 900 \Omega\text{cm}$  in a model with very high axial resistance but corresponding to the average experimental input resistance (Figure 3A black and orange dots).  $C_m = 0.6 \mu\text{F}/\text{cm}^2$  and  $R_a = 400 \Omega\text{cm}$  are at the boundaries of typically observed values in invertebrates and therefore within the realistic range (see summarising table 4 in [17]).

#### Dendritic integration in the electrotonic models

Since the primary computation in LPTC dendrites is the integration of local motion information, dendritic integration properties of *Calliphora* and *Drosophila* electrotonic HS cell models might reflect the similarity in function. Figure 3B shows morphoelectrotonic transforms [42] of four representative morphologies, one for each HS cell type. Instead of showing metric length relations for the individual segments of the branched structures, this representation maps electrotonic length onto the respective segments. Strikingly, in this representation, HS cells of *Drosophila* exhibit very similar proportions and overall size as HS cells of *Calliphora*. The summed electrotonic lengths were remarkably similar (*Calliphora*: 23.6±3.8 L; *Drosophila*: 21±3.8 L). If anything, this similarity was increased when considering the more unrealistic parameter set 2 that described the experimental data better. Consequently dendritic integration properties affecting synaptic democracy were well conserved. Synaptic democracy in amplitude as expressed in the current transfer between the dendrite root and the rest of the neuron was qualitatively identical between *Calliphora* and *Drosophila* (Figure 3C). Also, temporal synaptic democracy as expressed by the temporal delays between dendrite root or dendrite tip and the rest of the neuron (Figure 3C) was similar but slightly scaled in *Drosophila* because of the difference in the membrane time constant. Again, these similarities were only affected slightly when the alternative set of passive membrane properties was used for the *Drosophila* electrotonic model (Figure 3C, orange).

To test how robust these properties were with morphological changes we designed a morphological model with variable branch point numbers and dendrite surface areas. To do this we selected one sample dendrite contour from a *Calliphora* HSE and generated synthetic morphologies using the method described above but varying both the number of target points and the scaling factor for the surface area. These synthetic dendrites were appended to either a *Calliphora* or a *Drosophila* axon (Figure 4A). Note that the only differences between a *Calliphora* neuron and a

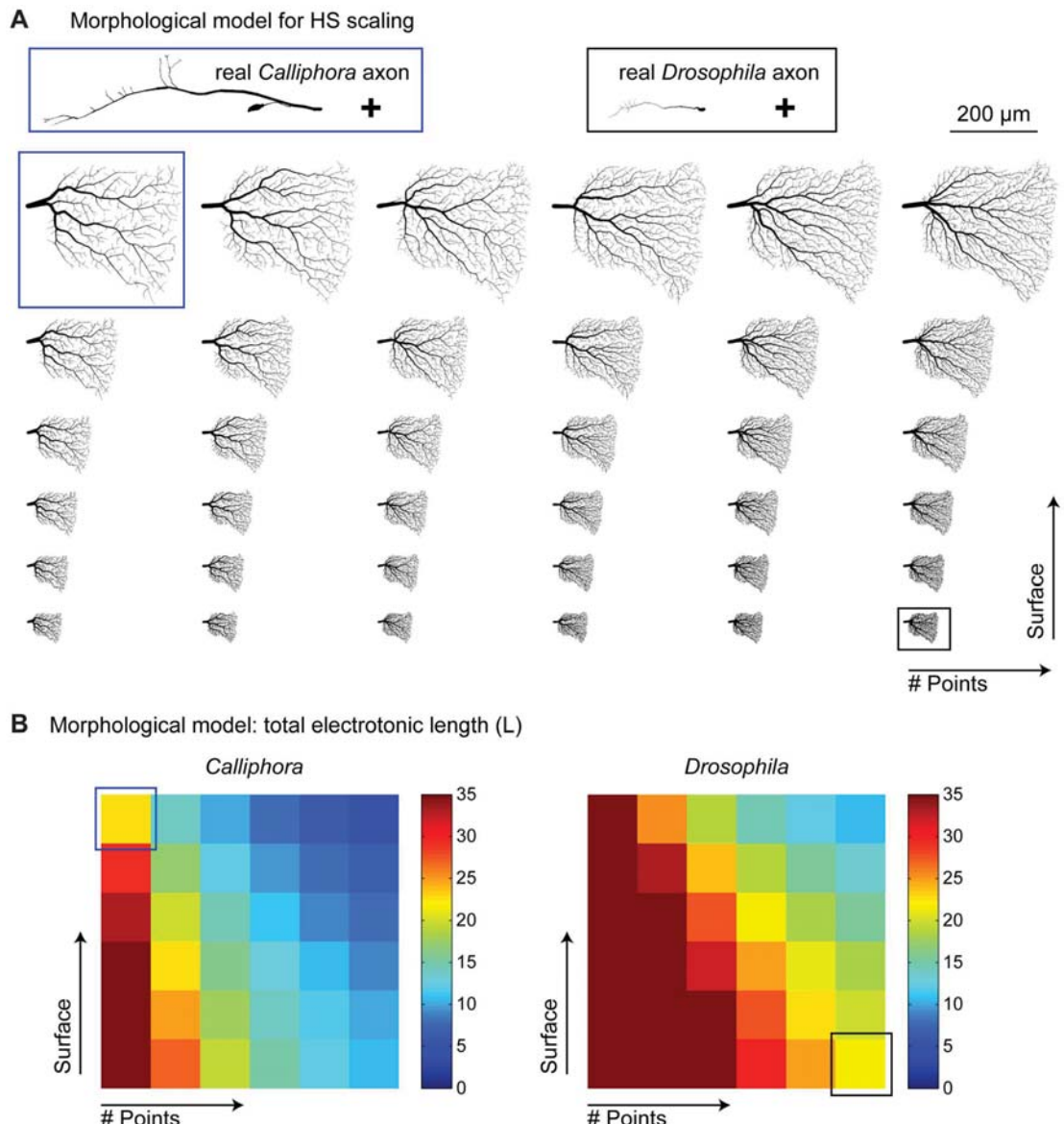


**Figure 4. Electrotonic analysis of a morphological model for scaling HS cells.** (A) Database of models generated by pairing either a sample *Calliphora* (blue box) or a sample *Drosophila* HSE axon (black box) to a synthetic dendrite obtained from a sample *Calliphora* HSE dendrite contour but scaled in overall size (surface) and in complexity (number of branch points). Upper left (blue box) and lower right (black box) model dendrites correspond to *Calliphora* and *Drosophila* dendrite measures respectively. (B) Corresponding to the morphological model databases in A, total electrotonic length is shown for *Calliphora* (left) and *Drosophila* (right) morphological models. Models with realistic morphologies for *Calliphora* (blue box) and *Drosophila* (black box) are in the same range but scaling surface area or number of branch points changes these measures.

doi:10.1371/journal.pone.0071540.g004

*Drosophila* neuron were therefore given by (1) the appended axons, (2) the diameters mapped onto the dendrites and (3) the passive membrane properties. Summed electrotonic length measures for this database of morphological models (Figure 4B) showed that the passive membrane properties are indeed selective for the particular overall morphology. In conclusion however, dendritic integration properties are largely unaffected by the scaling procedure and changes in passive membrane properties are helpful to further stabilise the electrotonic skeleton.

#### Integration of visual responses in HS cells

The model can then be used to study the responses to visual stimulation of HS cells in a comparative way between *Calliphora* and *Drosophila*. We focused here on the integration of large-field visual inputs that have been extensively studied in *Calliphora* HS cells [16]. As mentioned above, the dendritic arrangement of HS cells is retinotopic and the  $\text{Ca}^{2+}$  distribution within the dendrites reproduces the motion image in the visual field [43]. One function of the HS cell dendrite is to integrate democratically the motion

## Responses to visual stimulation

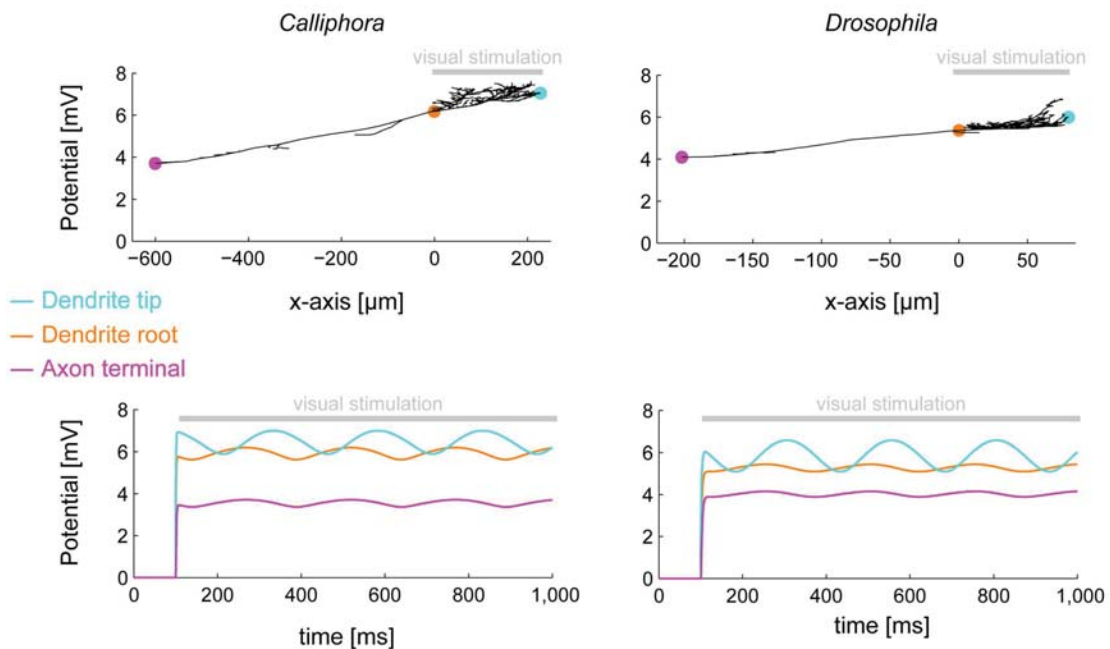


**Figure 5. Visual responses in *Drosophila* and *Calliphora* HS cells.** *Calliphora* (left) vs. *Drosophila* (right) HSE cell model responses to full field visual stimulation (top) and full field sinusoidal conductance injections in the dendrite with the phase corresponding to the x-axis location of the conduction injection site (bottom). Cyan, orange and pink dots in top panels indicate dendrite tip, dendrite root and axon terminal locations respectively for which voltage time traces are plotted in bottom panels. Grey bars indicate stimulation region (top panels) and time onset of stimulation (bottom panels).

doi:10.1371/journal.pone.0071540.g005

vectors present in the individual parts of the visual field and to smooth out irregularities due to textures in the moving background in both space and time [18].

In order to simulate visual responses we distributed a total synaptic conductance in the terminal branches of the dendrites that corresponds to the total input conductance of the cell as derived from visual stimulation recordings in *Calliphora* HS cells [15]. Since the HS cell membrane potential responds to visual stimulation in a graded manner, simulations using passive electrotonic models produced good results. Synaptic conductances of about  $9 \text{ pS} \times 577 = 5.2 \text{ nS}$  were required in the *Drosophila* HS cell model compared to about  $900 \text{ pS} \times 278 = 250 \text{ nS}$  in the *Calliphora* HS cell model (Figure 5, top panels) and achieved voltage responses to large-field visual stimulation of about 5 mV at the electrode location (in the axon or the soma) for both cells. This indicates that the amplitudes of synaptic conductance indeed match the input resistance and therefore that the passive membrane properties of the cell match the synaptic conductance. The voltage distributions throughout the cells were similar; compare in particular the dendritic tip where the synapses were located (Figure 5, cyan dots), the dendrite root where the signals are integrated (Figure 5, orange dots) and the axon tip where signals are conveyed to neurons that descend to the thoracic ganglia involved in flight muscle control (Figure 5, pink dots).

Finally, we studied how dendritic integration averages out modulations in the visual input due to textures in the visual background. We inserted sinusoidally modulated synaptic conductances along the dendrites of the model HS cells reflecting visual inputs due to a moving spatial grating. The phase was

proportional to the x-coordinate for each synaptic input and the sinusoidal input covered the dendritic span with exactly one period. In both *Calliphora* and *Drosophila* model cells, the modulations vanished at the level of the dendrite root and the axon tip (Figure 5, bottom panels; see also movie S1). In conclusion, also the visual response properties between *Calliphora* and *Drosophila* HS cells were qualitatively similar throughout the neuron in the electrotonic compartmental models.

## Discussion

In recent years comparison of *Drosophila* and *Calliphora* Lobula Plate circuits have revealed close similarities in anatomical and computational features [24,25,44,45]. We focused on one type of neuron, the HS cell, to study specifically to which extent it is modified to compensate for the extreme differences in size between both species. We showed that *Drosophila* HS cells follow the same branching principles as *Calliphora* HS cells and that the underlying electrotonic architecture is well conserved. We find also that the morphology obeys essentially isometric scaling and that even drastic scaling alterations do not per se challenge dendritic integration features such as synaptic democracy and responses to visual motion. Furthermore, total length and number of branch points, i.e. dendrite complexity, are strongly linked to each other by optimal wiring constraints (Figure 1D) [33].

Even though the general anatomical features were roughly scaled isometrically, two notable features departed from this rule. Firstly, while the average diameter values were scaled isometrically, the distribution of the branching diameters was altered

possibly to conserve dendritic synaptic democracy. Secondly, and more surprising, the complexity of *Drosophila*'s HS cells was increased compared to *Calliphora*. The lower spatial resolution of the *Drosophila* visual system with roughly 700 ommatidia per eye [39] vs. 4,500 in *Calliphora* [40] would suggest a lower complexity in the retinotopically organised branching structures of LPTCs since their function is to integrate signals from individual columnar elements over large parts of the visual field.

The morphological model of *Drosophila* cells indicated that the trade-off between cable cost and short conduction delays is in favour of short cables in a similar way as had been the case for *Calliphora* cells [12,28]. Together with the planar organisation of LPTCs within the Lobula Plate, this finding sets them functionally in one common group with cerebellar Purkinje cells that were suggested to also maximise their connectivity repertoire [11,46,47]. The low importance of conduction delays in the morphological model for both types of HS cells, thereby indicating less electrotonic compartmentalisation [10] is highly suggestive of a similar functional role. This function does not seem to be affected by general scale.

The electrotonic properties of the cells indicate that the specific membrane properties did not change very much. Changes in membrane resistivity in the scaling process led to higher input resistances without compromising dendritic integration. As a result however, predicted synaptic currents are much smaller in *Drosophila* than in *Calliphora* HS cells. This could in turn result in smaller metabolic costs generally associated with higher input resistances [48]. The differences in electrotonic properties that were seen are hard to resolve since experimental measurements were performed using sharp electrodes in axons of *Calliphora* HS cells but with patch electrodes in somata of *Drosophila* HS cells. While the former have been shown to introduce higher leak conductances, the latter have unknown influences on ion concentrations [49]. Studies performed in maturing invertebrates also describe the conservation of electrophysiological features in the nervous system even with large differences in size [50,51]. Interestingly, the functional syntax (e.g. spike timing), but not the absolute response intensity were conserved within growing cricket neurons, supporting the idea that functional concepts rather than the detailed physical sizes of features are encoded genetically [52,53]. In general the number of detailed electrotonic studies in *Drosophila* is still limited. Antennal lobe projection neurons exhibit different function, morphology and electrotonic properties compared to the HS cells described here [54]. However, input resistance measurements of around  $220\text{ M}\Omega$  in *Drosophila* VS cells, another class of LPTCs, matches our measurements in HS cells [32].

Most strikingly and in accordance with previous electrophysiological recordings [24,25], the dendritic integration properties and the simulated responses to visual stimulation were extremely

similar in the *Calliphora* and *Drosophila* HS cell models. Despite the anatomical scaling of  $60\times$  between the two fly species, the similarity in the electrotonic structure seems to be rather robust. While this requires some adjustments in the set of membrane properties, the range of adequate parameters is rather large. The overall importance of morphology for neural computation has been emphasised in many studies [55–57]. Dendrite structure plays a large role for spiking responses [56] and theoretical discussions on preserving synaptic integration through adjustments of morphological and electrotonic scaling properties of neurons have been held [3,58]. We show here in a combined electrophysiology, morphology and modelling study that iso-electrotonic scaling is feasible with minor adjustments in passive membrane properties and anatomy in the fly HS cell. We have provided evidence that the morphological backbone is important but robust over a wide range of scaling alterations in terms of the implementation of dendritic computations. By dissecting morphological and electrotonic scaling features, we show that neural function and many electrotonic properties are not compromised by scaling. We therefore conclude that a conservative scaling as proposed previously is comparably simple to achieve.

## Supporting Information

**Figure S1 Drosophila HS morphology database.** HSN and HSE cells were genetically tagged with GFP and all HSN and HSE cells from five flies were imaged with confocal microscopy (left two columns) and reconstructed (right two columns; HSN – red, HSE – black). The two columns each represent the left and right lobula plate of the same animal so that each row corresponds to the data obtained from one animal.  
(TIF)

**Movie S1 Responses of Drosophila and Calliphora HS model cells to a moving sinusoidal grating.** The dendrite receives sinusoidally modulated inputs where the phase depends on the x-coordinate and the pattern covers the dendrite with exactly one period of the sinusoidal input. The y-axis shows the local membrane potential instead of the correct HS cell y-coordinate (see Figure 5 for more details).  
(AVI)

## Acknowledgments

We would like to thank P. Jedlička and C. Kapfer for helpful discussions.

## Author Contributions

Conceived and designed the experiments: HC FF AB. Performed the experiments: FF BS GA SVR. Analyzed the data: HC FF. Wrote the paper: HC FF BS GA SVR AB.

## References

1. Niven JE, Farris SM (2012) Miniaturization of nervous systems and neurons. *Curr. Biol.* 22: R323–R329.
2. Tower DB (1954) Structural and functional organization of mammalian cerebral cortex: the correlation of neurone density with brain size. *J. Comp. Neurol.* 101: 19–51.
3. Bekkers JM, Stevens CF (1990) Two different ways evolution makes neurons larger. *Prog. Brain Res.* 83: 37–45.
4. Herculano-Houzel S, Mota B, Lent R (2006) Cellular scaling rules for rodent brains. *Proc. Natl. Acad. Sci. U.S.A.* 103: 12138–12143.
5. Herculano-Houzel S, Collins CE, Wong P, Kaas JH (2007) Cellular scaling rules for primate brains. *Proc. Natl. Acad. Sci. U.S.A.* 104: 3562–3567.
6. Purves D, Lichman JW (1985) Geometrical differences among homologous neurons in mammals. *Science* 228: 298–302.
7. Howarth C, Gleeson P, Attwell D (2012) Updated energy budgets for neural computation in the neocortex and cerebellum. *J. Cereb. Blood Flow Metab.* 32: 1222–1232.
8. Scholvinck ML, Howarth C, Attwell D (2008) The cortical energy needed for conscious perception. *NeuroImage* 40: 1460–1468.
9. Laughlin SB, De Ruyter van Steveninck RR, Anderson JC (1998) The metabolic cost of neural information. *Nat. Neurosci.* 1: 36–41.
10. Cuntz H, Forstner F, Borst A, Häusser M (2010) One rule to grow them all: a general theory of neuronal branching and its practical application. *PLoS Comput. Biol.* 6: e1000877.
11. Wen Q, Chklovskii DB (2008) A cost-benefit analysis of neuronal morphology. *J. Neurophys.* 99: 2320–2328.
12. Cuntz H, Borst A, Segev I (2007) Optimization principles of dendritic structure. *Theor. Biol. Med. Model.* 4: 21.

13. Bakken TE, Stevens CF (2011) Visual system scaling in teleost fish. *J. Comp. Neurol.* 53: 142–153.
14. Borst A, Haag J, Reiff DF (2010) Fly motion vision. *Annu. Rev. Neurosci.* 33: 49–70.
15. Haag J, Theunissen F, Borst A (1997) The intrinsic electrophysiological characteristics of fly lobula plate tangential cells: II. Active membrane properties. *J. Comput. Neurosci.* 4: 349–369.
16. Haag J, Vermeulen A, Borst A (1999) The intrinsic electrophysiological characteristics of fly lobula plate tangential cells: III. Visual response properties. *J. Comput. Neurosci.* 7: 213–234.
17. Borst A, Haag J (1996) The intrinsic electrophysiological characteristics of fly lobula plate tangential cells: I. Passive membrane properties. *J. Comput. Neurosci.* 3: 313–336.
18. Singh S, Borst A (1998) Dendritic integration and its role in computing image velocity. *Science* 281: 1848–1850.
19. Haag J, Borst A (2002) Dendro-dendritic interactions between motion-sensitive large-field neurons in the fly. *J. Neurosci.* 22: 3227–3233.
20. Cuntz H, Haag J, Borst A (2003) Neural image processing by dendritic networks. *Proc. Natl. Acad. Sci. U.S.A.* 100: 11082–11085.
21. Haag J, Borst A (2004) Neural mechanism underlying complex receptive field properties of motion-sensitive interneurons. *Nat. Neurosci.* 7: 628–634.
22. Cuntz H, Haag J, Forstner F, Segev I, Borst A (2007) Robust coding of flow-field parameters by axo-axonal gap junctions between fly visual interneurons. *Proc. Natl. Acad. Sci. U.S.A.* 104: 10229–10233.
23. Elyada YM, Haag J, Borst A (2009) Different receptive fields in axons and dendrites underlie robust coding in motion-sensitive neurons. *Nat. Neurosci.* 12: 327–332.
24. Joesch M, Plett J, Borst A, Reiff DF (2008) Response properties of motion-sensitive visual interneurons in the lobula plate of *Drosophila melanogaster*. *Curr. Biol.* 18: 368–374.
25. Schnell B, Joesch M, Forstner F, Raghu SV, Otsuna H, et al. (2010) Processing of horizontal optic flow in three visual interneurons of the *Drosophila* brain. *J. Neurophys.* 103: 1646–1657.
26. Hausen K (1982) Motion sensitive interneurons in the optomotor system of the fly - I. The horizontal cells: structure and signals. *Biol. Cybern.* 45: 143–156.
27. Hengstenberg R, Hausen K, Hengstenberg B (1982) The number and structure of giant vertical cells (VS) in the lobula plate of the blowfly *Calliphora erythrocephala*. *J. Comp. Physiol. A* 149: 163–177.
28. Cuntz H, Forstner F, Haag J, Borst A (2008) The morphological identity of insect dendrites. *PLoS Comput. Biol.* 4: e1000251.
29. Otsuna H, Ito K (2006) Systematic Analysis of the Visual Projection Neurons of *Drosophila melanogaster*. I. Lobula-Specific Pathways. *J. Comp. Neurol.* 497: 928–958.
30. Cuntz H, Forstner F, Borst A, Häusser M (2011) The TREES toolbox—probing the basis of axonal and dendritic branching. *Neuroinformatics* 9: 91–96.
31. Wilson RI, Laurent G (2005) Role of GABAergic inhibition in shaping odor-evoked spatiotemporal patterns in the *Drosophila* antennal lobe. *J. Neurosci.* 25: 9069–9079.
32. Maimon G, Straw AD, Dickinson MH (2010) Active flight increases the gain of visual motion processing in *Drosophila*. *Nat. Neurosci.* 13: 393–399.
33. Cuntz H, Mathy A, Häusser M (2012) A scaling law derived from optimal dendritic wiring. *Proc. Natl. Acad. Sci. U.S.A.* 109: 11014–11018.
34. Thompson DW (1917) On growth and form. Cambridge University Press. 1116 p.
35. Huxley JS (1932) Problems of relative growth. Methuen, Co. LTD, London. 276 p.
36. Ramón y Cajal S (1911) Histologie du système nerveux de l'homme et des vertébrés. Paris, A. Maloine, translated by Larry W Swanson 1995, Oxford University Press. 986 p.
37. Cherniak C (1992) Local optimization of neuron arbors. *Biol. Cybern.* 66: 503–510.
38. Cherniak C, Changizi MA, Kang DW (1999) Large-scale optimization of neuron arbors. *Phys. Rev. E* 59: 6001–6009.
39. Götz KG (1968) Flight control in *Drosophila* by visual perception of motion. *Kybernetik* 4: 199–208.
40. Sukontason KL, Chaiwong T, Piangjai S, Upakut S, Moophayak K, et al. (2008) Ommatidia of blow fly, house fly, and flesh fly: implication of their vision efficiency. *Parasitol. Res.* 103: 123–131.
41. Braatenberg V (1970) Ordnung und Orientierung der Elemente im Sehsystem der Fliege. *Biol. Cybern.* 7: 235–242.
42. Zador AM, Agmon-Snir H, Segev I (1995) The morphoelectrotomic transform: a graphical approach to dendrite function. *J. Neurosci.* 15: 1669–1682.
43. Borst A, Eggerhaaf M (1992) *In vivo* imaging of calcium accumulation in fly interneurons as elicited by visual motion stimulation. *Proc. Natl. Acad. Sci. U.S.A.* 89: 4139–4143.
44. Fischbach K-F, Heisenberg M (1984) Neurogenetics and behaviour in insects. *J. Exp. Biol.* 93: 65–93.
45. Scott EK, Raabe T, Luo L (2002) Structure of the vertical and horizontal system neurons of the lobula plate in *Drosophila*. *J. Comp. Neurol.* 454: 470–481.
46. Wen Q, Stepaniants A, Elston GN, Grosberg AY, Chklovskii DB (2009) Maximization of the connectivity repertoire as a statistical principle governing the shapes of dendritic arbors. *Proc. Natl. Acad. Sci. U.S.A.* 106: 12536–12541.
47. Cuntz H (2012) The dendritic density field of a cortical pyramidal cell. *Front. Neuroanat.* 6: 2.
48. Niven JE, Anderson JC, Laughlin SB (2007) Fly photoreceptors demonstrate energy-information trade-offs in neural coding. *PLoS biology* 5: e116.
49. Staley KJ, Otis TS, Mody I (1992) Membrane properties of dentate gyrus granule cells: comparison of sharp microelectrode and whole-cell recordings. *J. Neurophys.* 67: 1346–1358.
50. Kämper G, Murphey RK (1994) Maturation of an insect nervous system: constancy in the face of change. *Comp. Biochem. Phys. A* 109: 23–32.
51. Bucher D, Prinz AA, Marder E (2005) Animal-to-animal variability in motor pattern production in adults and during growth. *J. Neurosci.* 25: 1611–1619.
52. Marder E, Goaillard J-M (2006) Variability, compensation and homeostasis in neuron and network function. *Nat. Rev. Neurosci.* 7: 563–574.
53. Borst A (2008) How does nature program neuron types? *Front. Neurosci.* 2: 4–5.
54. Gouwens NW, Wilson RI (2009) Signal propagation in *Drosophila* central neurons. *J. Neurosci.* 29: 6239–6249.
55. Eggerhaaf M, Haag J, Borst A (1994) Processing of synaptic information depends on the structure of the dendritic tree. *NeuroReport* 6: 205–208.
56. Mainen ZF, Sejnowski TJ (1996) Influence of dendritic structure on firing pattern in model neocortical neurons. *Nature* 382: 363–366.
57. London M, Häusser M (2005) Dendritic computation. *Annu. Rev. Neurosci.* 28: 503–532.
58. Hill AA V, Edwards DH, Murphey RK (1994) The effect of neuronal growth on synaptic integration. *J. Comput. Neurosci.* 1: 239–254.

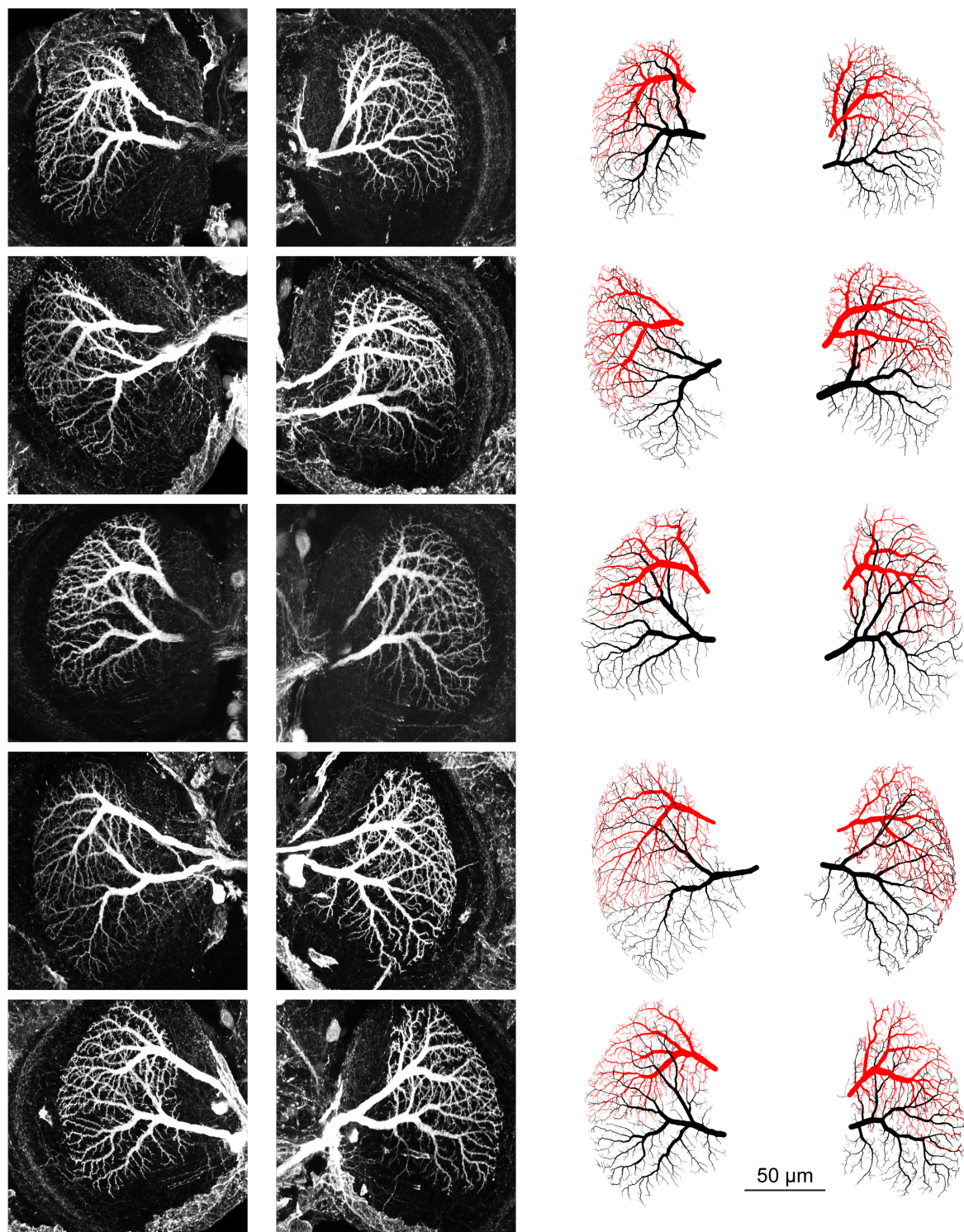


**Figure S1**



### 3. DISCUSSION

#### 3.1 Defining the Algorithm of Motion Detection

An influential essay by Marr and Poggio states that one of the fundamental levels at which nervous systems need to be understood is that at which the algorithms that implement a computation are characterized (Marr and Poggio, 1976). In the case of the computation of motion two alternative algorithms, differentiated by the type of non-linearity that gives rise to direction selectivity, have been suggested. In the Hassenstein-Reichardt (HR) model, this non-linearity is implemented by a multiplication that leads to an enhancement of motion signals in the detector's preferred direction. In the second, Barlow-Levick (BL), model an inhibitory non-linearity suppresses signals in the null direction. A number of recent studies have reported evidence that support either one or the other model (Behnia et al., 2014; Fisher et al., 2015b). A study that determined the temporal properties of medulla cells electrophysiologically (Behnia et al., 2014) has been interpreted as providing evidence that the ON pathway computes motion according to a Hassenstein-Reichardt model (Behnia and Desplan, 2015). Interestingly, these data have also been interpreted as favoring a Barlow-Levick detector mechanism by others (Takemura, 2015). This suggestion was based on two observations: First, a previous EM study has reported that the anatomical receptive fields of Tm3 cells that innervate a given T4 cell are displaced towards the preferred side of the dendrite with respect to Mi1 inputs (Takemura et al., 2013). Second, Mi1 was shown to have a slightly higher filter time constant than Tm3 (Behnia et al., 2014). This arrangement would suggest that Mi1 is inhibitory and provides the null direction inhibition of a Barlow-Levick detector. However, several findings contradict this hypothesis. First, multiple studies showed that Mi1 cells are cholinergic, and therefore assumed to be excitatory (Hasegawa et al., 2011; Pankova and Borst, 2017; Takemura et al., 2017). Furthermore, calcium imaging of T4 and T5 neurons while presenting apparent motion stimuli suggested that both of these cells implement only PD-enhancement (Fisher et al., 2015b). Interestingly, I could show in this thesis that removing Tm3 from the circuit by silencing its electrical activity only impairs ON motion detection at high edge motion velocities (Manuscript 2 - (Ammer et al., 2015)). This is inconsistent with a simple scheme were Mi1 and Tm3 are the two sole arms of a correlation-type motion detector, but suggest that additional mechanisms or cell types are involved as well. Additionally, despite both the HR and the BL model generating direction-selective signals, their responses are not as highly direction selective as those measured in T4 or T5 axon terminals (Maisak et al., 2013). The case is similar for the algorithm implemented in T5 cells. Here, an EM study has found not

only two, but four input elements (Shinomiya et al., 2014). Blocking each of these cells individually impairs responses to OFF motion in downstream tangential cells and behaving flies to different degrees (Serbe et al., 2016). This suggests a partial redundancy of the T5 input elements and argues against a simple two-arm model.

Taken together, the evidence presented above suggests that neither PD-enhancement nor ND-suppression alone can account for the high degree of direction selectivity observed in T4 and T5 cells. A study by Haag and colleagues has finally resolved this discrepancy (Haag et al., 2016). The authors used a telescopic device to stimulate neighboring neuromatidia sequentially and imaged calcium signals in single T4 cells projecting to layer 3 (Figure 5A). When apparent motion stimuli were presented to the fly, the authors found that both mechanisms, PD-enhancement and ND-suppression are realized in T4 cells. Interestingly these two mechanisms segregate with respect to the dendritic subfield of the T4 neuron. While PD-enhancement is predominantly found on the preferred side of the dendrite (corresponding to the dendritic tips), ND-suppression is strongest on the null side (corresponding to the base of the dendrite) (Figure 5B). Combining both of these models in a hybrid detector – the so-called HR/BL detector – generated responses that resembled the experimentally measured ones remarkably well (Figure 5C-D). Thus, both a Hassenstein-Reichardt and a Barlow-Levick-like mechanism are at work in T4 neurons and together generate the high degree of direction selectivity observed in these cells. In addition, a parallel study has provided evidence that T5 cells might implement both of these mechanisms as well (Leong et al., 2016).

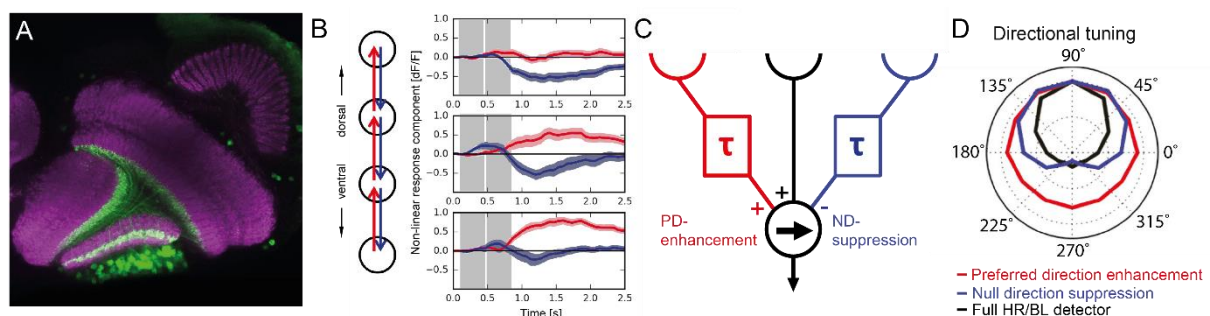


**Figure 5. The HR/BL Motion Detector Unites PD-enhancement and ND-suppression**

(A) Driver line with selective expression of GCaMP6m in T4/T5 cells of subtype c (projecting to lobula plate layer 3) that was used for functional calcium imaging.  
 (B) Single neuro-ommatidium stimulation combined with calcium imaging reveals PD-enhancement (red) on the preferred side and ND-suppression (blue) on the null side of the T4 dendrite.  
 (C) The HR/BL hybrid detector unites the Hassenstein-Reichardt and the Barlow-Levick model.  
 (D) Combining PD-enhancement and ND-suppression in a single model sharpens direction selectivity matching the tuning observed for T4 *in vivo*.  
 (B and D: from Haag et al., 2016)

### 3.2 Towards the Cellular Implementation of Motion Detection

After having established the algorithm for motion detection in the fly visual system, the next step is to map the neural elements to the specific parts of that algorithmic structure. In other words: which specific cell types that are presynaptic to T4 or T5 cells correspond to which arms of the HR/BL detector? This task might at first seem unfeasible for the T4-ON pathway as the HR/BL detector has three input arms whereas only two strong input cells to T4 were described in the medulla connectome (Takemura et al., 2013). This view changed dramatically when a new medulla connectome was acquired using an improved EM method with higher axial resolution (Takemura et al., 2017; Xu et al., 2017). The resultant new wiring diagram (Takemura et al., 2017) revealed that the connection strengths of several T4 inputs had been severely underestimated in the previous study. Instead of Mi1 and Tm3 making up over 85% of synaptic input, they now account only for approximately 50%. The other half of the inputs is contributed by six additional cell types namely Mi4, Mi9, C3, CT1, TmY15 and T4 itself (Figure 6A). Most importantly, the spatial offset between Mi1 and Tm3 reported earlier could not be reproduced. In contrast, large spatial offsets of approximately one ommatidium (corresponding to ~5° of visual space) were reported between all of the other columnar input elements with respect to Mi1, which itself synapses mainly in the center part of the T4 dendrite (Figure 6B-C). Of those, Mi4, C3 and CT1 inputs cluster at the shaft region of the T4 dendrite, while Mi9 provides input at the dendritic tips (Figure 6D). Furthermore, T4 cells connect exclusively to T4 cells of the same subtype in an asymmetric manner by synapsing only onto T4 cells that lie at their null side. In addition, immunohistochemical analyses showed that Mi4, C3, CT1 and TmY15 are GABAergic, Mi9 is glutamatergic and Mi1, Tm3 and T4 are cholinergic. In general, this anatomical layout looks surprisingly similar to the HR/BL detector proposed earlier with three main input clusters that might correspond to the three spatially segregated input lines of the detector. Excitatory inputs (Mi1, Tm3) synapse onto the center of the T4 dendrite, while inhibitory inputs cluster at the shaft (Mi4, C3, CT1, TmY15) and the tips (Mi9), respectively.

How can this anatomical circuit architecture be reconciled with the functional properties of the T4 input cells? Of the newly discovered inputs, only Mi4 and Mi9 provide strictly columnar feedforward input to T4, making them strong candidates for essential parts of the core motion detection circuit (Figure 6E). This prompted us to study the temporal response properties of Mi4, Mi9, Mi1 and Tm3 for the ON pathway (as well as Tm1, Tm2, Tm4 and Tm9 for the OFF pathway) by calcium imaging (Manuscript 3 - (Arenz et al., 2017)). We used white noise stimuli to extract the linear spatiotemporal filter components of these cells. These experiments revealed that Mi4 and Mi9 exhibit almost pure low-pass characteristics, while Mi1 and Tm3 act as band-pass filters. Surprisingly, whereas Mi1, Tm3 and Mi4 had ON-

center/OFF-surround spatial receptive fields, Mi9 showed OFF-center/ON-surround responses. However, given that Mi9 is glutamatergic and thus likely inhibitory (Liu and Wilson, 2013; Takemura et al., 2017), the synapse between Mi9 and T4 should be sign-reversing such that an ON stimulus would release T4 from inhibition of Mi9.

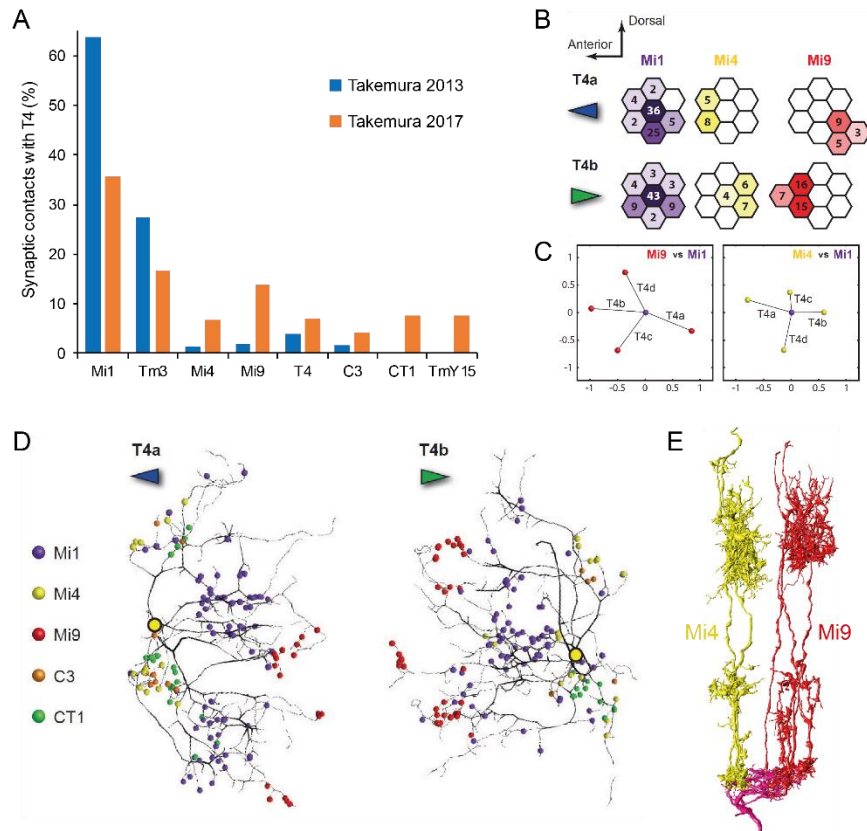


**Figure 6. An Improved Medulla Connectome Reveals Additional Inputs to T4 Cells**

(A) Comparison of “old” (Takemura et al., 2013) and “new” (Takemura et al., 2017) medulla connectome with regard to the synaptic contacts that presynaptic cells form with T4 cells.

(B) Numbers of synaptic contacts that Mi1, Mi4 and Mi9 of different columns form with T4a and T4b cells from the same column.

(C) Anatomical displacement between Mi9 and Mi1 as well as Mi4 and Mi1 that synapse onto T4 cells of a given subtype depicted in units of interommatidial distance.

(D) Reconstructed T4a and T4b neuron with synaptic inputs from medulla neurons depicted as dots.

(E) Single reconstructed T4 cell with all presynaptic Mi4 and Mi9 cells that give strong input illustrates their anatomical displacement.

(B-D: from Takemura et al., 2017; E: skeletons from [emanalysis.janelia.org](http://emanalysis.janelia.org))

How do the temporal properties and the anatomical arrangement of T4 inputs fit with the proposed HR/BL detector architecture? The slow and inhibitory Mi4 inputs are located on the null side of the T4 dendrite, just as the delayed, suppressive arm in the HR/BL model. Thus, Mi4 is well positioned to provide ND-suppression to T4. The also slow and inhibitory Mi9 is located on the preferred side. Disinhibition of T4 by Mi9 during ON-stimuli, when coupled with a non-linearity, could provide the preferred direction enhancement postulated by the

HR/BL model. Mi1 and/or Tm3 would then correspond to the central, fast arms of the detector, which matches their fast and excitatory properties. Such a proposed implementation is compatible with available experimental data. However, functional knock-out experiments are clearly required to confirm this proposal.

Another study performed loss-of-function experiments by blocking synaptic transmission of T4 inputs and measuring calcium responses in T4 cells and behavior as readout of the circuit (Strother et al., 2017). This study found a strong reduction of T4 calcium responses to motion stimuli after blocking Mi1 and a less strong reduction after blocking Tm3, consistent with the work presented in this thesis (Manuscript 2 - (Ammer et al., 2015)). Surprisingly, they detected only a very mild effect on T4 responses when blocking Mi4 or Mi9. However, it is important to note that the authors imaged the dendritic calcium responses of all T4 subtypes simultaneously, which makes it impossible to determine a measure of direction selectivity in these cells. In fact the HR/BL model predicts that a loss of PD-enhancement or ND-suppression alone would lead to increased T4 responses when summing the responses of all four subtypes (Haag et al., 2016).

In addition, Strother and colleagues performed optogenetic activation experiments of all T4 inputs alone and in pairwise combinations (Strother et al., 2017). While activation of single input cells led only to negligible responses, activation of Mi1 and Tm3 in conjunction caused a strong calcium increase in T4. This argues for a supralinear interaction between Mi1 and Tm3. The results summarized above led the authors to speculate that Mi1 and Tm3 represent the core components of a HR motion detector, corresponding to the delayed and non-delayed input line. However, since there is no spatial offset between Mi1 and Tm3, the authors had to postulate differential temporal processing of Mi1/Tm3 cells that synapse onto different parts of the T4 dendrite. Such a scenario could be implemented by a mechanism that is intrinsic to T4 cells, such as passive dendritic filtering. Otherwise, Mi1/Tm3 cells that synapse onto distal regions could be targeting slow, muscarinic ACh-receptors whereas more proximal Mi1/Tm3 inputs could target fast, nicotinic ACh-receptors. However, evidence for both of these mechanisms is currently lacking. In the model of Strother et al., and contrary to our study, Mi4 and Mi9 cells play only a modulatory role by providing weak inhibitory input to T4. Notably, increasing the weights of Mi4 and Mi9 inputs and coupling them to non-linear postsynaptic processes would essentially lead to an architecture that is similar to that of our study (Arenz et al., 2017).

In summary, in the model of Arenz et al. (Arenz et al., 2017) the interaction of Mi1/Tm3 with Mi4 or Mi9 implements ND-suppression and PD-enhancement, respectively. In contrast,

the model of Strother and colleagues ([Strother et al., 2017](#)) argues that a non-linear interaction between Mi1 and Tm3 results in PD-enhancement, whereas ND-suppression is not an explicit feature of the model. In comparison, the model of Arenz et al. is more parsimonious, as it does not necessitate the postulation of any further delay mechanisms or wiring asymmetries. How can the results from Strother and coworkers be reconciled with those from Arenz and colleagues? In the Strother study, no non-linear interaction was found between Mi9 and Mi1 or Tm3 when activating them simultaneously. However, this is to be expected if Mi9 is inhibitory. A non-linear interaction would only be visible if Mi9 was optogenetically inhibited while activating Mi1 or Tm3 at the same time. Furthermore, blocking Mi4 or Mi9 had only a mild effect on motion responses in T4 and behavior. However, as mentioned above, all subtypes of T4 were imaged simultaneously. Thus, no broadening in directional tuning, as would be expected when removing PD-enhancement or ND-suppression alone, can be detected. Furthermore, it was not tested if the block of synaptic output from Mi4 and Mi9 indeed resulted in a complete loss of synaptic release. The relatively weak expression levels of the Split Gal4 driver lines that were used suggest that the block was incomplete, which makes the results difficult to interpret.

### **3.3 Biophysical Implementation of the Core Computations**

Although determining the cellular architecture of the ON and OFF motion detectors in *Drosophila* is within reach, the biophysical mechanisms of the essential computations remain elusive. The mathematical operations central to the HR/BL model are the temporal delay as well as the enhancing and suppressive non-linearity. How might these operations be realized in the biological hardware of the fly brain?

#### **3.3.1 Temporal Delay Mechanism**

The temporal response properties of most major cells presynaptic to T4 and T5 have been characterized in detail. The input cells both to T4 and to T5 span a large range of different temporal filters, ranging from fast band-pass filters to almost pure low-pass filters ([Arenz et al., 2017](#); [Serbe et al., 2016](#)). It is, however, completely unclear which underlying mechanisms give rise to their diverse temporal properties. In principle, a delay can either be implemented cell-intrinsically or synaptically. Cell intrinsic mechanisms can be as simple as passive dendritic filtering. The length and diameter of the neurite and its membrane resistance, for example, determine the conduction velocity of electrical signals. The time constant of a neuron, which describes its passive low-pass filtering properties, depends linearly on its input resistance. It is thus plausible that slower medulla neurons simply have higher resistances.

Besides passive cell properties, voltage gated ion channels can both delay electrical signals or render them more transient (Koch, 1999). To give one example, A-type potassium channels are activated by depolarizing synaptic inputs but become rapidly inactivated. This brief increase in potassium conductance can keep the membrane from reaching a threshold and thereby generate a delay. It has been hypothesized that such a transient A-type potassium current is responsible for the delayed visual response of a subset of cells in the guinea pig lateral geniculate nucleus (McCormick, 1991).

Alternative to cell-intrinsic mechanisms, synaptic transmission can have a profound impact on temporal dynamics in a circuit. Chemical synaptic transmission – the process of neurotransmitter release, its diffusion to the postsynaptic side and binding to a receptor – already imposes a delay of 2-3 milliseconds. Furthermore, the properties of postsynaptic receptors lead to additional temporal filtering. Ionotropic receptors permit direct current flow, whereas metabotropic receptors activate second messenger cascade that in turn activate ionic conductances, which imposes a delay that can be in the order of tens to hundreds of milliseconds. Both T4 and T5 neurons express a wide array of ionotropic and metabotropic neurotransmitter receptors as well as voltage-gated ion channels (Pankova and Borst, 2016), making all of these mechanisms plausible. Additionally, synapses can implement temporal filtering by exhibiting short-term synaptic plasticity (Zucker and Regehr, 2002). Projection neurons in the *Drosophila* olfactory system, for example, were shown to perform a sort of high-pass filtering by responding only transiently to strong synaptic input due to short-term synaptic depression (Kazama and Wilson, 2008).

Another interesting possibility how neurons can realize temporal filtering was recently proposed by Baden and colleagues (Baden et al., 2014). Based on calcium recordings from zebrafish bipolar cells, the authors found that the size of the presynaptic terminal determines the temporal filtering of visual signals. Terminals with smaller volumes transmitted higher stimulus frequencies more effectively whereas larger terminals acted more like low-pass filters. In *Drosophila* medulla cells, however, there does not seem to be such a straightforward correlation between terminal size and temporal dynamics. Mi1, for example, has the largest terminals of all T4/T5 inputs, but cells with smaller terminals, such as Tm9 are much slower.

Medulla cells Mi4, Mi9 and Tm9 have temporal response properties akin to low-pass filters, which makes them prime candidates for corresponding to the delayed lines of the motion detectors (Arenz et al., 2017). Interestingly, Mi9 and Tm9 receive their major input from lamina cell L3, which itself was shown to exhibit slow temporal characteristics (Silies et al., 2013). This raises the intriguing possibility that medulla neurons inherit the temporal properties

from their lamina inputs. Thus, the delay mechanism of both ON and OFF motion detectors might be implemented at the first synapse of the visual system – between photoreceptors and lamina cells. A prediction of this scenario is that flies with dysfunctional L3 cells should be motion-blind. Contrary to that expectation, however, blocking synaptic transmission from L3 has little effect on fly optomotor behavior (Bahl et al., 2015; Silies et al., 2013; Tuthill et al., 2013). In the end, probably an interplay of several biophysical mechanisms will determine the temporal filtering properties of a given neuron in the fly medulla.

### 3.3.2 Mechanism of Non-linear Input Interaction

Both T4 and T5 cells display PD-enhancement and ND-suppression (Haag et al., 2016; Leong et al., 2016). Therefore, two different non-linear mechanisms must act within these cells' dendrites. In the HR/BL detector, PD-enhancement is implemented by a simple multiplication. Clearly, no neuron can perform a true multiplication. However, several biophysical mechanism are conceivable which integrate synaptic inputs in a non-linear manner that resembles a multiplication – at least over a limited range of input strengths. Indeed, one such mechanism exists in the lobula giant movement detector (LGMD) neurons of locusts (Gabbiani et al., 2002). These neurons multiply two synaptic inputs, one of them excitatory and the other one inhibitory. The inputs, which impinge onto different parts of the LGMD dendrite, are summed postsynaptically on a logarithmic scale (Jones and Gabbiani, 2012). This sum is then exponentiated by the exponential transformation of the membrane potential into spike output, which involves voltage-gated sodium channels. By exponentiating the sum of a logarithm, the LGMD neuron thus essentially performs a multiplication.

However, multiple alternative mechanisms could account for the non-linear integration that is necessary for PD-enhancement as well. In general, every voltage-gated cation channel could implement a non-linear summation of inputs. This is because the voltage-dependent gating of the channel leads to ion flow that elevates the membrane potential, which in turn causes the opening of further channels leading to a positive non-linear feedback loop. Indeed, in cortical neurons it was shown that a combination of the non-linear voltage-gating of NMDA-receptors together with a dendritic impedance gradient is sufficient to render their dendrites direction selective (Branco et al., 2010). As mentioned before, voltage-gated ion channels of several different subtypes are expressed in T4 and T5 neurons (Pankova and Borst, 2016). The fact that calcium signals in the dendrites of T4 and T5 are strongly direction selective might already be a hint that voltage-gated calcium channels are directly involved in the mechanism for PD-enhancement.

In a manuscript included in this thesis, we suggest that a non-linear interaction between the OFF-responsive, inhibitory Mi9 and the ON-responsive, excitatory Mi1 leads to PD-enhancement in T4 cells (Arenz et al., 2017). In such a scenario, an ON motion stimulus that passes the receptive field of a T4 cell would first decrease the activity of Mi9, which in turn releases the Mi9-mediated inhibition of T4. This disinhibition by itself could bring the T4 membrane potential close to threshold for an active conductance. Subsequent excitatory input from Mi1 onto T4 could then lead to a crossing of this threshold and thus a non-linear amplification. Alternatively, the inhibition caused by Mi9 could activate a hyperpolarization-activated conductance (e.g. an  $I_h$  current). Disinhibition of T4 would then lead to a depolarizing rebound that opens a time window in which excitation from Mi1/Tm3 can exert a non-linear effect.

The implementation of the divisive ND-suppression seems to be more straightforward. In general, inhibition can exhibit a divisive effect on excitatory inputs if two requirements are fulfilled (Koch, 1999; Torre and Poggio, 1978). First, the reversal potential of the inhibitory conductance must be close to the membrane potential. Second, the inhibitory conductance must be much larger than the excitatory conductance. Such a form of inhibition is termed shunting- or divisive inhibition. In the ON pathway, shunting inhibition might be provided by GABAergic input impinging from Mi4 onto T4 cells.

### 3.4 Parallels with Direction-selective Circuits in the Mammalian Retina

Similar to the visual system of the fly, direction-selective circuits in the mammalian retina have been studied for more than a half-century (Vaney et al., 2012). Here, the direction-selective cells to be first described were the direction-selective retinal ganglion cells (DSGCs) (Barlow and Hill, 1963). DSGCs receive input from several types of bipolar cells, and multiple types of amacrine cells, among them the starburst amacrine cells (SACs) (Briggman et al., 2011; Helmstaedter et al., 2013). SACs represent the first direction-selective stage in the mammalian retina (Euler et al., 2002; Yonehara et al., 2013). These cells have radially protruding dendrites that respond preferentially when being stimulated in an outward fashion (i.e. from base to tip). SACs in turn render DSGCs direction selective by providing asymmetric GABAergic inhibition specifically to the null side of DSGC dendrites (Briggman et al., 2011). Consequently, the central question is how the dendrites of SACs, which receive input from glutamatergic, excitatory bipolar cells and mixed cholinergic/GABAergic input from neighboring SACs, become direction selective. Several different mechanism have been suggested to underlie the emergence of direction selectivity in SACs (Borst and Helmstaedter, 2015; Mauss et al., 2017). Interestingly, one of the recently proposed models bears remarkable resemblance to the fly

visual circuits discussed above. A calcium imaging study showed that different bipolar cell types span a range of different temporal response profiles (Baden et al., 2013), ranging from fast transient to slow sustained, just as the medulla cells in *Drosophila*. Subsequent anatomical studies found asymmetric wiring of bipolar cells to the dendrites of both ON and OFF starburst amacrine cells (Greene et al., 2016; Kim et al., 2014). A bipolar cell subtype shown to be slow preferentially contacts the proximal part of the SAC dendrite, while a fast subtype contacts the distal part. These observations are consistent with a Hassenstein-Reichardt-like computation in which the delay is implemented already presynaptically to the SACs. However, while some studies found supporting evidence for this model (Fransen and Borghuis, 2017), other studies could not detect any difference in the temporal kinetics of excitatory input to proximal versus distal SAC dendrites (Stincic et al., 2016). Thus, direction selectivity in flies and mammals may arise by similar mechanisms. Definitive evidence, however, must await further experiments in both species.

### 3.5 Limitations of Current Anatomical and Genetic Tools

In the recent decade much progress has been made towards elucidating the mechanisms that generate direction selectivity both in *Drosophila* and in mice. The reason for this success is largely based on the development of novel tools - both genetic and anatomical - that permit a cell type-specific investigation of neural circuits (Briggman and Bock, 2012; Luo et al., 2008; Venken et al., 2011). Despite these tools having a tremendous impact, all of them suffer from certain problems that require caution in interpreting experimental results.

#### 3.5.1 Tools for Blocking Synaptic Transmission

Correlation alone does not prove causation. Functional dissection of neural circuits requires proving that individual neurons are necessary for a given computation (Katz et al., 2016; Wiegert et al., 2017). In *Drosophila*, this is usually accomplished by using the Gal4/UAS system to overexpress a protein that interferes with vesicle release or electrical activity of a neuron. Due to the overexpression, the effectiveness of the block is dependent on the expression strength of the Gal4 driver line. Additionally, a subset of synapses seems to be resistant to some of the blocking agents (Rister and Heisenberg, 2006). Therefore, any experiment in which a cell type is blocked would in theory require a control that shows that the block is indeed completely effective. This could be done by recording electrophysiologically from postsynaptic cells while activating the blocked neuron. Alternatively, neurotransmitter release could be monitored indirectly by visualizing exocytosis with synaptophluorin (Miesenbock et al., 1998) or directly by neurotransmitter sensors such as iGluSnFR (Marvin

et al., 2013). The experimental difficulty of such controls, however, makes them impractical and therefore they are rarely carried out. Consequently, false negatives can normally not be excluded from experimental results. In addition, quantitative statements about results of synaptic blocks have to be interpreted with caution. Small effects might simply be caused by weaker blocking of neural activity.

A novel tool to disrupt synaptic transmission that does not depend on the expression strength of the driver line would be highly valuable. Here, newly emerging tools for genome engineering provide a promising solution (Fisher et al., 2017; Heidenreich and Zhang, 2016; Zhang et al., 2014). Conditional knockout alleles of genes that are necessary for synaptic transmission can easily be generated and are thus promising candidates. Recombinase-mediated disruption of the gene of interest is a unitary event and thus not proportional to the levels of recombinase expressed. However, other confounding effects must be taken into consideration. Depending on the stability of the mRNA and protein of the targeted gene, the time interval between gene knockout and experiment needs to be adjusted. Furthermore, the knockout must be efficient enough to ensure a loss-of-function allele on both chromosomes. Ideally, it should be shown that the protein is indeed strongly depleted by measuring protein levels using immuno-stainings or western blots.

A further problem encountered with currently available blocking reagents is that they are not connection-specific. Silencing a certain cell type will silence synaptic transmission to all of its postsynaptic targets. In the fly visual system, this is especially problematic because of its high degree of interconnectedness (Takemura et al., 2013; Takemura et al., 2015). As an example, Mi4 and Mi9 cells have very strong reciprocal connections. For this reason, silencing one of these cells will very likely have a large impact on the function of the other cell. This makes it difficult to disambiguate the functional role of the synaptic connections between each of these cells and T4. Thus, blocking one cell type can have profound effects on the function of the circuit as a whole, leading to potential second-order effects.

A solution to such confounding effects would be given by the development of connection-specific blockers. Such a hypothetical tool could for example be based on a split-protein approach similar to the GRASP technique (Gordon and Scott, 2009). Expressing two complementary halves of a protein in the pre- and postsynaptic neurons, respectively, that, for example, quickly degrades neurotransmitters or allows tethering of pharmacological inhibitors of neurotransmitter receptors (Shields et al., 2017), would allow blocking of synaptic transmission specifically between two genetically defined cell types.

### 3.5.2 Connectomic Circuit Reconstruction

Parallel to the development of genetic tools, the anatomical reconstruction of neural circuits has entered a new era with recently developed EM-techniques for dense connectomic reconstructions (Dorkenwald et al., 2017; Kasthuri et al., 2015; Xu et al., 2017). Yet similarly, all of these techniques have their limitations and results need to be interpreted accordingly. The ultimate goal of connectomics is to reconstruct every single neuron and every single connection within a neural circuit or even a whole brain. However, it is unclear at which point a connectome can be considered complete. Due to the fact that no positive control can exist, it is impossible to rule out that fine neurites or individual connections have been missed. Indeed, a connectomic reconstruction of an entire medulla column that was claimed to contain all strong connections to T4 (Takemura et al., 2013) was shown to be incomplete after a superior method was applied to the same neuropil (Takemura et al., 2017). Furthermore, the present techniques applied to *Drosophila* brain areas only allow the resolution of chemical synaptic connections, but do not resolve electrical synapses. Given the prominence of electrical synapses in the lobula plate of blowflies (Haag and Borst, 2005) and in the mammalian retina (Bloomfield and Volgyi, 2009) it would be surprising if they do not play a crucial role in visual processing in *Drosophila* as well. However, despite these limitations, high-resolution circuit reconstruction remains a powerful method for building and refuting hypotheses about functional network structures.

### 3.6 Downstream Circuits and Behavior

How is the information about motion direction that is computed in the optic lobe utilized by downstream circuits to ultimately guide fly behavior? Several studies in which synaptic transmission from T4 and T5 cells was blocked, one of which is a part of this cumulative thesis (Bahl et al., 2013), uncovered essential roles of these cells in visually guided behaviors. In that study, we demonstrated that T4 and T5 cells are necessary for fly optomotor behavior. Flies in which the synaptic output of these cells were blocked turned out to be completely motion-blind. Subsequent papers showed their involvement in figure-ground-discrimination (Fenk et al., 2014) and in the avoidance of expanding stimuli as well as in the landing response (Schilling and Borst, 2015). How are direction-selective signals from T4/T5 cells routed to the central brain and motor areas? The most direct link between motion-sensitive neurons and motor circuits is provided by lobula plate tangential cells that project to the posterior slope of the central brain. Unilateral optogenetic activation of HS cells induces yaw turning responses of the head and the wings during tethered flight (Haikala et al., 2013). Furthermore, blocking the synaptic output of VS and HS cells with an inwardly rectifying potassium channel (Kir2.1)

impairs the head optomotor response to a large degree, and has a weaker effect on wing steering (Kim et al., 2017). Thus, LPTCs are thought to drive, at least in part, the optomotor response of *Drosophila*. Surprisingly, the temporal frequency tuning of the behavioral optomotor response in flying flies is markedly broader and shifted to higher frequencies than that of HS cells measured under the same conditions. A study suggests that calcium buffering in the axon terminals of HS cells acts as an integrator that can account for this discrepancy (Schnell et al., 2014).

In the central brain, LPTCs synapse onto descending neurons that in turn contact motor neurons (Strausfeld et al., 1987; Suver et al., 2016). Interestingly, some of these descending neurons often respond only weakly to visual stimuli alone, but become strongly activated when input from other sensory modalities is presented simultaneously (Haag et al., 2010; Huston and Krapp, 2009). Additionally, many of the descending neurons receive bilateral visual input, which is thought to increase their optic flow field specificity (Huston and Krapp, 2008; Wertz et al., 2009).

The detection of motion not only guides hard-wired and stereotyped reflexes, but also provides input to more sophisticated higher brain circuits. Recently, it was shown that a structure in the central brain that is implicated in fly navigation – the central complex – harbors cells that respond in a direction-selective manner (Weir et al., 2014). Furthermore, optic flow drives central complex neurons that are required for updating the flies internal representation of heading direction (Green et al., 2017). During prey capture, dragonflies even compute an abstract internal model of prey motion that guides their targeted steering during prey approach (Mischiati et al., 2015). Consequently, this internal model must receive input from motion-sensitive circuits. Whether these higher central brain circuits inherit their direction selectivity from T4/T5 cells or whether it is computed de-novo elsewhere in the brain remains to be tested. In conclusion, direction-selective cells convey information to various downstream circuits that orchestrate essential behavioral programs.

### 3.7 Visual Circuit Function during Natural Behaviour

An open question is how motion detection circuits operate during unrestrained behavior. Recently, it has become clear that the activity and tuning properties of visual circuits, both in mice and flies, exhibit state-dependent modulations (Maimon, 2011). As mentioned in the introduction, some neurons in the fly visual system become more active and shift their temporal response optima to higher speeds when the animal is moving (Chiappe et al., 2010; Jung et al., 2011; Maimon et al., 2010). All of these experiments, however, were performed

in restrained flies navigating in a virtual visual environment. A freely walking or flying fly experiences not only visual cues, but also proprioceptive cues detected by the halteres and the antennae (Mamiya et al., 2011; Sandeman and Markl, 1980). Higher multimodal circuits combine multiple of these cues, usually in a non-linear manner (Haag et al., 2010; Huston and Krapp, 2009). Thus, the activity of visually responsive neurons might be completely different during tethered versus free flight. Furthermore, for tethered flying flies the feedback loop is usually restricted to one dimension, the yaw axis. During free flight, however, flies perform much more complex maneuvers, often consisting of rotations and translations of head and body along multiple axes (Muijres et al., 2014). Such maneuvers are difficult, if not impossible, to re-enact in a restrained setting. Consequently, to fully understand the function of a visual circuit, it should ideally be studied during natural behavior. This is feasible in larger animals, which can carry head-mounted microscopes, head-stages or fiber optics, but is extremely challenging in the tiny fruit fly. Nonetheless, large progress towards achieving this goal has been made in the last years. The position of walking or flying fruit flies can be tracked on-line with high precision in 2D and 3D. This information can be used to update either the visual surrounding or a laser that targets the fly for thermo- or optogenetic activation of nerve cells (Bath et al., 2014; Stowers et al., 2014; Straw et al., 2011). Thereby, the activity of a subset of neurons can be manipulated during natural behavior, contingent on a specific behavioral action that the fly performs or a visual stimulus that it experiences. Recently, it became even possible to perform functional imaging in freely walking flies, albeit with low spatial resolution (Grover et al., 2016). Together, these promising tools will help to gain insight into how individual nerve cells and visual circuits operate under near-natural conditions.

### 3.8 Conclusions and Outlook

During the last years, as reflected by the manuscripts that constitute this thesis, we have witnessed a large progress in the characterization of the neural elements that compute motion direction in *Drosophila*. Perhaps most importantly, T4 and T5 were discovered as the neurons corresponding to the elementary motion detectors. Thereafter, the neurons that are presynaptic to T4 and T5 were identified and their physiological properties characterized. In parallel, the algorithmic structures of the motion detectors were refined making it possible to map the neural elements to those structures. Furthermore, new insights have been gained into how ON and OFF motion detectors have adapted to natural surroundings and how flies use motion and other visual cues to navigate their environment.

Despite these accomplishments, many of the central questions remain unanswered. Several functional roles have been proposed for the individual cell types presynaptic to T4 and

T5, yet no commonly accepted assignment of function to any single of these cells has been possible. Furthermore, it is unclear which mechanisms account for the temporal filtering and non-linear processing of signals in the circuit. Finding answers to this question has been hampered in part by the fact that all functional studies so far have recorded calcium levels in T4 and T5 neurons. Measuring the membrane potential of these neurons directly and with high temporal resolution using novel genetically encoded voltage indicators (Gong et al., 2015; Yang et al., 2016) or electrophysiological recordings will likely provide valuable insights in the near future. First, the biophysical processes that are central to generating direction selectivity occur on fast timescales that cannot be resolved with calcium indicators. Second, synaptic inhibition plays a central role, which again is difficult to visualize with calcium indicators. Ideally, whole-cell voltage clamp recordings of T4 and T5 cells would provide access to the conductance and currents that interact to generate direction-selective signals. Such recordings, however, are methodologically highly demanding and suffer from very low throughput (Pimentel et al., 2016). Therefore, the generation and improvement of voltage indicators will likely be essential in revealing subthreshold as well as hyperpolarizing signals in T4 and T5 cells.

In the end, the membrane potential of T4 and T5 is determined by the opening and closing of ion channels. Thus, it will be necessary to know the subcellular distribution of these proteins on the dendrites of the cells. This can be accomplished by high-resolution light- or electron microscopy. Unfortunately, the functional properties of invertebrate ion channels are less well characterized than those of their mammalian counterparts (Littleton and Ganetzky, 2000; Podlaski et al., 2017). As a consequence, their detailed biophysical characterization, either in heterologous systems or, preferentially, in *Drosophila* neurons *in vivo* is an extensive and important task for the future. Additionally, it will be necessary to manipulate individual ion channels in a cell type-specific manner. Here, recently developed genetic approaches to engineer their endogenous genomic loci will be of central importance. In the light of all these unanswered questions, enough challenges remain ahead for future researchers studying motion detection in the *Drosophila* visual system.



## 4. REFERENCES

Adams, M.D., Celniker, S.E., Holt, R.A., Evans, C.A., Gocayne, J.D., Amanatides, P.G., Scherer, S.E., Li, P.W., Hoskins, R.A., Galle, R.F., *et al.* (2000). The genome sequence of *Drosophila melanogaster*. *Science* 287, 2185-2195.

Adelson, E.H., ed. (2000). Lightness perception and lightness illusions (Cambridge, MA: MIT Press).

Akerboom, J., Chen, T.W., Wardill, T.J., Tian, L., Marvin, J.S., Mutlu, S., Calderon, N.C., Esposti, F., Borghuis, B.G., Sun, X.R., *et al.* (2012). Optimization of a GCaMP calcium indicator for neural activity imaging. *J Neurosci* 32, 13819-13840.

Ammer, G., Leonhardt, A., Bahl, A., Dickson, B.J., and Borst, A. (2015). Functional specialization of neural input elements to the *Drosophila* ON motion detector. *Curr Biol* 25, 2247-2253.

Arenz, A., Drews, M.S., Richter, F.G., Ammer, G., and Borst, A. (2017). The temporal tuning of the *Drosophila* motion detectors is determined by the dynamics of their input elements. *Curr Biol* 27, 929-944.

Baden, T., Berens, P., Bethge, M., and Euler, T. (2013). Spikes in mammalian bipolar cells support temporal layering of the inner retina. *Curr Biol* 23, 48-52.

Baden, T., Nikolaev, A., Esposti, F., Dreosti, E., Odermatt, B., and Lagnado, L. (2014). A synaptic mechanism for temporal filtering of visual signals. *PLoS Biol* 12, e1001972.

Bahl, A., Ammer, G., Schilling, T., and Borst, A. (2013). Object tracking in motion-blind flies. *Nat Neurosci* 16, 730-738.

Bahl, A., Serbe, E., Meier, M., Ammer, G., and Borst, A. (2015). Neural mechanisms for *Drosophila* contrast vision. *Neuron* 88, 1240-1252.

Baines, R.A., Uhler, J.P., Thompson, A., Sweeney, S.T., and Bate, M. (2001). Altered electrical properties in *Drosophila* neurons developing without synaptic transmission. *J Neurosci* 21, 1523-1531.

Barlow, H.B. (1961). Possible principles underlying the transformation of sensory messages. *Sensory Communication*, 18.

Barlow, H.B., and Hill, R.M. (1963). Selective sensitivity to direction of movement in ganglion cells of the rabbit retina. *Science* 139, 412-412.

Barlow, H.B., and Levick, W.R. (1965). The mechanism of directionally selective units in rabbit's retina. *J Physiol* 178, 28.

Bath, D.E., Stowers, J.R., Hormann, D., Poehlmann, A., Dickson, B.J., and Straw, A.D. (2014). FlyMAD: rapid thermogenetic control of neuronal activity in freely walking *Drosophila*. *Nat Methods* 11, 756-762.

Bausenwein, B., Dittrich, A.P., and Fischbach, K.F. (1992). The optic lobe of *Drosophila melanogaster*. II. Sorting of retinotopic pathways in the medulla. *Cell Tissue Res* 267, 17-28.

Behnia, R., Clark, D.A., Carter, A.G., Clandinin, T.R., and Desplan, C. (2014). Processing properties of ON and OFF pathways for *Drosophila* motion detection. *Nature* 512, 427-430.

Behnia, R., and Desplan, C. (2015). Visual circuits in flies: beginning to see the whole picture. *Curr Opin Neurobiol* 34, 125-132.

Bloomfield, S.A., and Volgyi, B. (2009). The diverse functional roles and regulation of neuronal gap junctions in the retina. *Nat Rev Neurosci* 10, 495-506.

Borst, A. (2009). *Drosophila*'s view on insect vision. *Curr Biol* 19, R36-47.

Borst, A. (2014a). Fly visual course control: behaviour, algorithms and circuits. *Nat Rev Neurosci* 15, 590-599.

Borst, A. (2014b). Neural circuits for elementary motion detection. *J Neurogenet* 28, 361-373.

Borst, A., Haag, J., and Reiff, D.F. (2010). Fly motion vision. *Annu Rev Neurosci* 33, 49-70.

Borst, A., and Helmstaedter, M. (2015). Common circuit design in fly and mammalian motion vision. *Nat Neurosci* 18, 1067-1076.

Boyden, E.S., Zhang, F., Bamberger, E., Nagel, G., and Deisseroth, K. (2005). Millisecond-timescale, genetically targeted optical control of neural activity. *Nat Neurosci* 8, 1263-1268.

Branco, T., Clark, B.A., and Häusser, M. (2010). Dendritic discrimination of temporal input sequences in cortical neurons. *Science* 329, 1671-1675.

Brand, A.H., and Perrimon, N. (1993). Targeted gene-expression as a means of altering cell fates and generating dominant phenotypes. *Development* 118, 401-415.

Briggman, K.L., and Bock, D.D. (2012). Volume electron microscopy for neuronal circuit reconstruction. *Curr Opin Neurobiol* 22, 154-161.

Briggman, K.L., Helmstaedter, M., and Denk, W. (2011). Wiring specificity in the direction-selectivity circuit of the retina. *Nature* 471, 183-188.

Buchner, E., Buchner, S., and Bulthoff, H. (1984). Deoxyglucose mapping of nervous activity induced in *Drosophila* brain by visual movement. I. Wildtype. *J Comp Physiol* 155, 471-483.

Cajal, S.R., and Sanchez, D. (1915). Contribucion al conocimiento de los centros nerviosos de los insectos (Madrid: Imprenta de Hijos de Nicholas Moja).

Cao, G., Platisa, J., Pieribone, V.A., Raccuglia, D., Kunst, M., and Nitabach, M.N. (2013). Genetically targeted optical electrophysiology in intact neural circuits. *Cell* 154, 904-913.

Carandini, M., Demb, J.B., Mante, V., Tolhurst, D.J., Dan, Y., Olshausen, B.A., Gallant, J.L., and Rust, N.C. (2005). Do we know what the early visual system does? *J Neurosci* 25, 10577-10597.

Carandini, M., and Heeger, D.J. (2011). Normalization as a canonical neural computation. *Nat Rev Neurosci* 13, 51-62.

Chalasani, S.H., Chronis, N., Tsunozaki, M., Gray, J.M., Ramot, D., Goodman, M.B., and Bargmann, C.I. (2007). Dissecting a circuit for olfactory behaviour in *Caenorhabditis elegans*. *Nature* 450, 63-70.

Chalfie, M., Tu, Y., Euskirchen, G., Ward, W.W., and Prasher, D.C. (1994). Green fluorescent protein as a marker for gene-expression. *Science* 263, 802-805.

Chen, T.W., Wardill, T.J., Sun, Y., Pulver, S.R., Renninger, S.L., Baohan, A., Schreiter, E.R., Kerr, R.A., Orger, M.B., Jayaraman, V., *et al.* (2013). Ultrasensitive fluorescent proteins for imaging neuronal activity. *Nature* 499, 295-300.

Chiappe, M.E., Seelig, J.D., Reiser, M.B., and Jayaraman, V. (2010). Walking modulates speed sensitivity in *Drosophila* motion vision. *Curr Biol* 20, 1470-1475.

Clark, D.A., Fitzgerald, J.E., Ales, J.M., Gohl, D.M., Silies, M.A., Norcia, A.M., and Clandinin, T.R. (2014). Flies and humans share a motion estimation strategy that exploits natural scene statistics. *Nat Neurosci* 17, 296-303.

Cook, R. (1979). The courtship tracking of *Drosophila*. *Biol Cybernetics* 34, 16.

Cuntz, H., Forstner, F., Schnell, B., Ammer, G., Raghu, S.V., and Borst, A. (2013). Preserving neural function under extreme scaling. *PLoS One* 8, e71540.

Denk, W., Briggman, K.L., and Helmstaedter, M. (2012). Structural neurobiology: missing link to a mechanistic understanding of neural computation. *Nat Rev Neurosci* 13, 351-358.

Denk, W., and Horstmann, H. (2004). Serial block-face scanning electron microscopy to reconstruct three-dimensional tissue nanostructure. *PLoS Biol* 2, e329.

Denk, W., Strickler, J.H., and Webb, W.W. (1990). Two-photon laser scanning fluorescence microscopy. *Science* 248, 73-76.

Dietzl, G., Chen, D., Schnorrer, F., Su, K.C., Barinova, Y., Fellner, M., Gasser, B., Kinsey, K., Oppel, S., Scheiblauer, S., *et al.* (2007). A genome-wide transgenic RNAi library for conditional gene inactivation in *Drosophila*. *Nature* 448, 151-156.

Dorkenwald, S., Schubert, P.J., Killinger, M.F., Urban, G., Mikula, S., Svara, F., and Kornfeld, J. (2017). Automated synaptic connectivity inference for volume electron microscopy. *Nat Methods* 14, 435-442.

Dvorak, D., Srinivasan, M.V., and French, A.S. (1980). The contrast sensitivity of fly movement-detecting neurons. *Vision Res* 20, 397-407.

Dvorak, D.R., Bishop, L.G., and Eckert, H.E. (1975). On the identification of movement detectors in the fly optic lobe. *J Comp Physiol A Neuroethol Sens Neural Behav Physiol* 100, 19.

Eichner, H., Joesch, M., Schnell, B., Reiff, D.F., and Borst, A. (2011). Internal structure of the fly elementary motion detector. *Neuron* 70, 1155-1164.

Euler, T., Detwiler, P.B., and Denk, W. (2002). Directionally selective calcium signals in dendrites of starburst amacrine cells. *Nature* 418, 845-852.

Exner, S. (1891). Die Physiologie der facettirten Augen von Krebsen und Insecten (Leipzig und Wien: Franz Deuticke).

Exner, S. (1894). Entwurf zu einer physiologischen Erklärung der psychischen Erscheinungen (Leipzig und Wien: Franz Deuticke).

Fenk, L.M., Poehlmann, A., and Straw, A.D. (2014). Asymmetric processing of visual motion for simultaneous object and background responses. *Curr Biol* 24, 2913-2919.

Fenno, L., Yizhar, O., and Deisseroth, K. (2011). The development and application of optogenetics. *Annu Rev Neurosci* 34, 389-412.

Fermi, G., and Reichardt, W. (1963). Optomotorische Reaktionen der Fliege *Musca domestica*. *Kybernetik*, 14.

Fischbach, K.F., and Dittrich, A.P.M. (1989). The optic lobe of *Drosophila melanogaster*. I. A golgi analysis of wild-type structure. *Cell Tissue Res* 258, 35.

Fisher, Y.E., Leong, J.C., Sporar, K., Ketkar, M.D., Gohl, D.M., Clandinin, T.R., and Silies, M. (2015a). A class of visual neurons with wide-field properties is required for local motion detection. *Curr Biol* 25, 3178-3189.

Fisher, Y.E., Silies, M., and Clandinin, T.R. (2015b). Orientation selectivity sharpens motion detection in *Drosophila*. *Neuron* 88, 390-402.

Fisher, Y.E., Yang, H.H., Isaacman-Beck, J., Xie, M., Gohl, D.M., and Clandinin, T.R. (2017). FlpStop, a tool for conditional gene control in *Drosophila*. *Elife* 6.

Fransen, J.W., and Borghuis, B.G. (2017). Temporally diverse excitation generates direction-selective responses in ON- and OFF-type retinal starburst amacrine cells. *Cell Rep* 18, 1356-1365.

Gabbiani, F., Krapp, H.G., Koch, C., and Laurent, G. (2002). Multiplicative computation in a visual neuron sensitive to looming. *Nature* 420, 320-324.

Gjorgjieva, J., Sompolinsky, H., and Meister, M. (2014). Benefits of pathway splitting in sensory coding. *J Neurosci* 34, 12127-12144.

Gong, Y., Huang, C., Li, J.Z., Grewe, B.F., Zhang, Y., Eismann, S., and Schnitzer, M.J. (2015). High-speed recording of neural spikes in awake mice and flies with a fluorescent voltage sensor. *Science* 350, 1361-1366.

Gordon, M.D., and Scott, K. (2009). Motor control in a *Drosophila* taste circuit. *Neuron* 61, 373-384.

Götz, K.G. (1964). Optomotorische Untersuchung des visuellen Systems einiger Augenmutanten der Fruchtfliege *Drosophila*. *Kybernetik* 2, 16.

Green, J., Adachi, A., Shah, K.K., Hirokawa, J.D., Magani, P.S., and Maimon, G. (2017). A neural circuit architecture for angular integration in *Drosophila*. *Nature* 546, 101-106.

Greene, M.J., Kim, J.S., Seung, H.S., and EyeWirers (2016). Analogous convergence of sustained and transient inputs in parallel on and off pathways for retinal motion computation. *Cell Rep* 14, 1892-1900.

Grienberger, C., and Konnerth, A. (2012). Imaging calcium in neurons. *Neuron* 73, 862-885.

Grover, D., Katsuki, T., and Greenspan, R.J. (2016). Flyception: imaging brain activity in freely walking fruit flies. *Nat Methods* 13, 569-572.

Haag, J., Arenz, A., Serbe, E., Gabbiani, F., and Borst, A. (2016). Complementary mechanisms create direction selectivity in the fly. *Elife* 5.

Haag, J., and Borst, A. (2005). Dye-coupling visualizes networks of large-field motion-sensitive neurons in the fly. *J Comp Physiol A Neuroethol Sens Neural Behav Physiol* 191, 445-454.

Haag, J., Wertz, A., and Borst, A. (2010). Central gating of fly optomotor response. *Proc Natl Acad Sci U S A* 107, 20104-20109.

Haikala, V., Joesch, M., Borst, A., and Mauss, A.S. (2013). Optogenetic control of fly optomotor responses. *J Neurosci* 33, 13927-13934.

Harris, K.M., Perry, E., Bourne, J., Feinberg, M., Ostroff, L., and Hurlburt, J. (2006). Uniform serial sectioning for transmission electron microscopy. *J Neurosci* 26, 12101-12103.

Hasegawa, E., Kitada, Y., Kaido, M., Takayama, R., Awasaki, T., Tabata, T., and Sato, M. (2011). Concentric zones, cell migration and neuronal circuits in the *Drosophila* visual center. *Development* 138, 983-993.

Hassenstein, B., and Reichardt, W. (1956). Systemtheoretische Analyse der Zeit-, Reihenfolgen- und Vorzeichenauswertung bei der Bewegungsperzeption des Rüsselkäfers *Chlorophanus*. *Z Naturforsch B* 11b, 12.

Hausen, K. (1982). Motion sensitive interneurons in the optomotor system of the fly. *Biol Cybern* 45, 14.

Heidenreich, M., and Zhang, F. (2016). Applications of CRISPR-Cas systems in neuroscience. *Nat Rev Neurosci* 17, 36-44.

Heisenberg, M., and Buchner, E. (1977). The role of retinula cell types in visual behavior of *Drosophila melanogaster*. *J Comp Physiol A Neuroethol Sens Neural Behav Physiol* 117, 36.

Helmchen, F., and Denk, W. (2005). Deep tissue two-photon microscopy. *Nat Methods* 2, 932-940.

Helmstaedter, M., Briggman, K.L., Turaga, S.C., Jain, V., Seung, H.S., and Denk, W. (2013). Connectomic reconstruction of the inner plexiform layer in the mouse retina. *Nature* 500, 168-174.

Hengstenberg, R. (1982). Common visual response properties of giant vertical cells in the lobula plate of the blowfly *Calliphora*. *J Comp Physiol A Neuroethol Sens Neural Behav Physiol* 149, 15.

Herry, C., Ciocchi, S., Senn, V., Demmou, L., Muller, C., and Luthi, A. (2008). Switching on and off fear by distinct neuronal circuits. *Nature* 454, 600-606.

Hildebrand, D.G.C., Cicconet, M., Torres, R.M., Choi, W., Quan, T.M., Moon, J., Wetzel, A.W., Scott Champion, A., Graham, B.J., Randlett, O., et al. (2017). Whole-brain serial-section electron microscopy in larval zebrafish. *Nature* 545, 345-349.

Hubel, D.H., and Wiesel, T.N. (1962). Receptive fields, binocular interaction and functional architecture in the cat's visual cortex. *J Physiol* 160, 51.

Huston, S.J., and Krapp, H.G. (2008). Visuomotor transformation in the fly gaze stabilization system. *PLoS Biol* 6, e173.

Huston, S.J., and Krapp, H.G. (2009). Nonlinear integration of visual and haltere inputs in fly neck motor neurons. *J Neurosci* 29, 13097-13105.

Jenett, A., Rubin, G.M., Ngo, T.T., Shepherd, D., Murphy, C., Dionne, H., Pfeiffer, B.D., Cavallaro, A., Hall, D., Jeter, J., *et al.* (2012). A GAL4-driver line resource for *Drosophila* neurobiology. *Cell Rep* 2, 991-1001.

Joesch, M., Plett, J., Borst, A., and Reiff, D.F. (2008). Response properties of motion-sensitive visual interneurons in the lobula plate of *Drosophila melanogaster*. *Curr Biol* 18, 368-374.

Joesch, M., Schnell, B., Raghu, S.V., Reiff, D.F., and Borst, A. (2010). ON and OFF pathways in *Drosophila* motion vision. *Nature* 468, 300-304.

Jones, P.W., and Gabbiani, F. (2012). Logarithmic compression of sensory signals within the dendritic tree of a collision-sensitive neuron. *J Neurosci* 32, 4923-4934.

Jung, S.N., Borst, A., and Haag, J. (2011). Flight activity alters velocity tuning of fly motion-sensitive neurons. *J Neurosci* 31, 9231-9237.

Kandel, E.R. (2001). The molecular biology of memory storage: a dialogue between genes and synapses. *Science* 294, 9.

Karmeier, K., Tabor, R., Egelhaaf, M., and Krapp, H.G. (2001). Early visual experience and the receptive-field organization of optic flow processing interneurons in the fly motion pathway. *Vis Neurosci* 18, 1-8.

Kasthuri, N., Hayworth, K.J., Berger, D.R., Schalek, R.L., Conchello, J.A., Knowles-Barley, S., Lee, D., Vazquez-Reina, A., Kaynig, V., Jones, T.R., *et al.* (2015). Saturated reconstruction of a volume of neocortex. *Cell* 162, 648-661.

Katz, L.N., Yates, J.L., Pillow, J.W., and Huk, A.C. (2016). Dissociated functional significance of decision-related activity in the primate dorsal stream. *Nature* 535, 285-288.

Kazama, H., and Wilson, R.I. (2008). Homeostatic matching and nonlinear amplification at identified central synapses. *Neuron* 58, 401-413.

Kim, A.J., Fenk, L.M., Lyu, C., and Maimon, G. (2017). Quantitative predictions orchestrate visual signaling in *Drosophila*. *Cell* 168, 280-294 e212.

Kim, J.S., Greene, M.J., Zlateski, A., Lee, K., Richardson, M., Turaga, S.C., Purcaro, M., Balkam, M., Robinson, A., Behabadi, B.F., *et al.* (2014). Space-time wiring specificity supports direction selectivity in the retina. *Nature* 509, 331-336.

Kitamoto, T. (2001). Conditional modification of behavior in *Drosophila* by targeted expression of a temperature-sensitive shibire allele in defined neurons. *J Neurobiol* 47, 81-92.

Klapoetke, N.C., Murata, Y., Kim, S.S., Pulver, S.R., Birdsey-Benson, A., Cho, Y.K., Morimoto, T.K., Chuong, A.S., Carpenter, E.J., Tian, Z., *et al.* (2014). Independent optical excitation of distinct neural populations. *Nat Methods* 11, 338-346.

Koch, C. (1999). Biophysics of computation: information processing in single neurons (New York, Oxford: Oxford University Press).

Krapp, H.G., and Hengstenberg, R. (1996). Estimation of self-motion by optic flow processing in single visual interneurons. *Nature* 384, 463-466.

Kvon, E.Z., Kazmar, T., Stampfel, G., Yanez-Cuna, J.O., Pagani, M., Schernhuber, K., Dickson, B.J., and Stark, A. (2014). Genome-scale functional characterization of *Drosophila* developmental enhancers in vivo. *Nature* 512, 91-95.

Lai, S.L., and Lee, T. (2006). Genetic mosaic with dual binary transcriptional systems in *Drosophila*. *Nat Neurosci* 9, 703-709.

Land, M.F., and Collett, T.S. (1974). Chasing behavior of houseflies (*Fannia Canicularis*) - A description and analysis. *J Comp Physiol* 89, 331-357.

Leong, J.C., Esch, J.J., Poole, B., Ganguli, S., and Clandinin, T.R. (2016). Direction selectivity in *Drosophila* emerges from preferred-direction enhancement and null-direction suppression. *J Neurosci* 36, 8078-8092.

Leonhardt, A., Ammer, G., Meier, M., Serbe, E., Bahl, A., and Borst, A. (2016). Asymmetry of *Drosophila* ON and OFF motion detectors enhances real-world velocity estimation. *Nat Neurosci* 19, 706-715.

Lin, J.Y., Knutson, P.M., Muller, A., Kleinfeld, D., and Tsien, R.Y. (2013). ReaChR: a red-shifted variant of channelrhodopsin enables deep transcranial optogenetic excitation. *Nat Neurosci* 16, 1499-1508.

Littleton, J.T., and Ganetzky, B. (2000). Ion channels and synaptic organization: analysis of the *Drosophila* genome. *Neuron* 26, 35-43.

Liu, W.W., Mazor, O., and Wilson, R.I. (2015). Thermosensory processing in the *Drosophila* brain. *Nature* 519, 353-357.

Liu, W.W., and Wilson, R.I. (2013). Glutamate is an inhibitory neurotransmitter in the *Drosophila* olfactory system. *Proc Natl Acad Sci U S A* 110, 10294-10299.

Luan, H., Peabody, N.C., Vinson, C.R., and White, B.H. (2006). Refined spatial manipulation of neuronal function by combinatorial restriction of transgene expression. *Neuron* 52, 425-436.

Luo, L., Callaway, E.M., and Svoboda, K. (2008). Genetic dissection of neural circuits. *Neuron* 57, 634-660.

Maimon, G. (2011). Modulation of visual physiology by behavioral state in monkeys, mice, and flies. *Curr Opin Neurobiol* 21, 559-564.

Maimon, G., Straw, A.D., and Dickinson, M.H. (2010). Active flight increases the gain of visual motion processing in *Drosophila*. *Nat Neurosci* 13, 393-399.

Maisak, M.S., Haag, J., Ammer, G., Serbe, E., Meier, M., Leonhardt, A., Schilling, T., Bahl, A., Rubin, G.M., Nern, A., et al. (2013). A directional tuning map of *Drosophila* elementary motion detectors. *Nature* 500, 212-216.

Mamiya, A., Straw, A.D., Tomasson, E., and Dickinson, M.H. (2011). Active and passive antennal movements during visually guided steering in flying *Drosophila*. *J Neurosci* 31, 6900-6914.

Mank, M., Santos, A.F., Direnberger, S., Mrsic-Flogel, T.D., Hofer, S.B., Stein, V., Hendel, T., Reiff, D.F., Levelt, C., Borst, A., et al. (2008). A genetically encoded calcium indicator for chronic in vivo two-photon imaging. *Nat Methods* 5, 805-811.

Marder, E., and Goaillard, J.M. (2006). Variability, compensation and homeostasis in neuron and network function. *Nat Rev Neurosci* 7, 563-574.

Marr, D., and Poggio, T. (1976). From understanding computation to understanding neural circuitry. *AI Memo* 357, 22.

Marvin, J.S., Borghuis, B.G., Tian, L., Cichon, J., Harnett, M.T., Akerboom, J., Gordus, A., Renninger, S.L., Chen, T.W., Bargmann, C.I., *et al.* (2013). An optimized fluorescent probe for visualizing glutamate neurotransmission. *Nat Methods* 10, 162-170.

Mauss, A.S., and Borst, A. (2017). Motion vision in arthropods. In *The Oxford Handbook of Invertebrate Neurobiology*, p. 45.

Mauss, A.S., Vlasits, A., Borst, A., and Feller, M. (2017). Visual circuits for direction selectivity. *Annu Rev Neurosci*.

McCormick, D.A. (1991). Functional properties of a slowly inactivating potassium current in guinea pig dorsal lateral geniculate relay neurons. *J Neurophysiol* 66, 1176-1189.

McCulloch, W.S., and Pitts, W. (1943). A logical calculus of the ideas immanent in nervous activity. *Bulletin of Mathematical Biophysics* 5, 19.

Meier, M., Serbe, E., Maisak, M.S., Haag, J., Dickson, B.J., and Borst, A. (2014). Neural circuit components of the *Drosophila* OFF motion vision pathway. *Curr Biol* 24, 385-392.

Miesenbock, G., De Angelis, D.A., and Rothman, J.E. (1998). Visualizing secretion and synaptic transmission with pH-sensitive green fluorescent proteins. *Nature* 394, 192-195.

Mischiati, M., Lin, H.T., Herold, P., Imler, E., Olberg, R., and Leonardo, A. (2015). Internal models direct dragonfly interception steering. *Nature* 517, 333-338.

Morgan, T.H. (1910). Sex limited inheritance in *Drosophila*. *Science* 32, 120-122.

Muijres, F.T., Elzinga, M.J., Melis, J.M., and Dickinson, M.H. (2014). Flies evade looming targets by executing rapid visually directed banked turns. *Science* 344, 172-177.

Pankova, K., and Borst, A. (2016). RNA-Seq transcriptome analysis of direction-selective T4/T5 neurons in *Drosophila*. *PLoS One* 11, e0163986.

Pankova, K., and Borst, A. (2017). Transgenic line for the identification of cholinergic release sites in *Drosophila melanogaster*. *J Exp Biol* 220, 1405-1410.

Parise, C.V., and Ernst, M.O. (2016). Correlation detection as a general mechanism for multisensory integration. *Nat Commun* 7, 11543.

Perkins, L.A., Holderbaum, L., Tao, R., Hu, Y., Sopko, R., McCall, K., Yang-Zhou, D., Flockhart, I., Binari, R., Shim, H.S., *et al.* (2015). The transgenic RNAi project at harvard medical school: resources and validation. *Genetics* 201, 843-852.

Pfeiffer, B.D., Jenett, A., Hammonds, A.S., Ngo, T.T., Misra, S., Murphy, C., Scully, A., Carlson, J.W., Wan, K.H., Laverty, T.R., *et al.* (2008). Tools for neuroanatomy and neurogenetics in *Drosophila*. *Proc Natl Acad Sci U S A* 105, 9715-9720.

Pick, B., and Buchner, E. (1979). Visual movement detection under light- and dark-adaptation in the fly, *Musca Domestica*. *J Comp Physiol* 134, 45-54.

Pimentel, D., Donlea, J.M., Talbot, C.B., Song, S.M., Thurston, A.J., and Miesenbock, G. (2016). Operation of a homeostatic sleep switch. *Nature* 536, 333-337.

Podlaski, W.F., Seeholzer, A., Groschner, L.N., Miesenbock, G., Ranjan, R., and Vogels, T.P. (2017). Mapping the function of neuronal ion channels in model and experiment. *Elife* 6.

Ratliff, C.P., Borghuis, B.G., Kao, Y.H., Sterling, P., and Balasubramanian, V. (2010). Retina is structured to process an excess of darkness in natural scenes. *Proc Natl Acad Sci U S A* 107, 17368-17373.

Reiff, D.F., Plett, J., Mank, M., Griesbeck, O., and Borst, A. (2010). Visualizing retinotopic half-wave rectified input to the motion detection circuitry of *Drosophila*. *Nat Neurosci* 13, 973-978.

Rister, J., and Heisenberg, M. (2006). Distinct functions of neuronal synaptobrevin in developing and mature fly photoreceptors. *J Neurobiol* 66, 1271-1284.

Rister, J., Pauls, D., Schnell, B., Ting, C.Y., Lee, C.H., Sinakevitch, I., Morante, J., Strausfeld, N.J., Ito, K., and Heisenberg, M. (2007). Dissection of the peripheral motion channel in the visual system of *Drosophila melanogaster*. *Neuron* 56, 155-170.

Rivera-Alba, M., Vitaladevuni, S.N., Mishchenko, Y., Lu, Z., Takemura, S.Y., Scheffer, L., Meinertzhagen, I.A., Chklovskii, D.B., and de Polavieja, G.G. (2011). Wiring economy and volume exclusion determine neuronal placement in the *Drosophila* brain. *Curr Biol* 21, 2000-2005.

Rubin, G., and Spradling, A. (1982). Genetic transformation of *Drosophila* with transposable element vectors. *Science* 218, 348-353.

Salazar-Gatzimas, E., Chen, J., Creamer, M.S., Mano, O., Mandel, H.B., Matulis, C.A., Pottackal, J., and Clark, D.A. (2016). Direct measurement of correlation responses in *Drosophila* elementary motion detectors reveals fast timescale tuning. *Neuron* 92, 227-239.

Sandeman, D.C., and Markl, H. (1980). Head movements in flies (*Calliphora*) produced by deflection of the halteres. *Journal of Experimental Biology* 85, 43-60.

Schiller, P.H. (1992). The ON and OFF channels of the visual system. *Trends Neurosci* 15, 86-92.

Schilling, T., and Borst, A. (2015). Local motion detectors are required for the computation of expansion flow-fields. *Biol Open* 4, 1105-1108.

Schnell, B., Joesch, M., Forstner, F., Raghu, S.V., Otsuna, H., Ito, K., Borst, A., and Reiff, D.F. (2010). Processing of horizontal optic flow in three visual interneurons of the *Drosophila* brain. *J Neurophysiol* 103, 1646-1657.

Schnell, B., Raghu, S.V., Nern, A., and Borst, A. (2012). Columnar cells necessary for motion responses of wide-field visual interneurons in *Drosophila*. *J Comp Physiol A Neuroethol Sens Neural Behav Physiol* 198, 389-395.

Schnell, B., Weir, P.T., Roth, E., Fairhall, A.L., and Dickinson, M.H. (2014). Cellular mechanisms for integral feedback in visually guided behavior. *Proc Natl Acad Sci U S A* 111, 5700-5705.

Serbe, E., Meier, M., Leonhardt, A., and Borst, A. (2016). Comprehensive Characterization of the Major Presynaptic Elements to the *Drosophila* OFF Motion Detector. *Neuron* 89, 829-841.

Shapiro, A.G., and Hamburger, K. (2007). Last but not least. *Perception* 36, 1104-1107.

Shields, B.C., Kahuno, E., Kim, C., Apostolides, P.F., Brown, J., Lindo, S., Mensh, B.D., Dudman, J.T., Lavis, L.D., and Tadross, M.R. (2017). Deconstructing behavioral neuropharmacology with cellular specificity. *Science* 356.

Shinomiya, K., Karuppusudurai, T., Lin, T.Y., Lu, Z., Lee, C.H., and Meinertzhagen, I.A. (2014). Candidate neural substrates for off-edge motion detection in *Drosophila*. *Curr Biol* 24, 1062-1070.

Silies, M., Gohl, D.M., Fisher, Y.E., Freifeld, L., Clark, D.A., and Clandinin, T.R. (2013). Modular use of peripheral input channels tunes motion-detecting circuitry. *Neuron* 79, 111-127.

Simoncelli, E.P., and Olshausen, B.A. (2001). Natural image statistics and neural representation. *Annu Rev Neurosci* 24, 1193-1216.

Single, S., and Borst, A. (1998). Dendritic integration and its role in computing image velocity. *Science* 281, 1848-1850.

Srinivasan, M.V., and Dvorak, D.R. (1980). Spatial processing of visual information in the movement-detecting pathway of the fly. *J Comp Physiol A Neuroethol Sens Neural Behav Physiol* 140, 23.

Stincic, T., Smith, R.G., and Taylor, W.R. (2016). Time course of EPSCs in ON-type starburst amacrine cells is independent of dendritic location. *J Physiol* 594, 5685-5694.

Stowers, J.R., Fuhrmann, A., Hofbauer, M., Streinzer, M., Schmid, A., Dickinson, M.H., and Straw, A.D. (2014). Reverse engineering animal vision with virtual reality and genetics. *Computer* 47, 38-45.

Strausfeld, N.J., and Lee, J.K. (1991). Neuronal basis for parallel visual processing in the fly. *Vis Neurosci* 7, 13-33.

Strausfeld, N.J., Seyan, H.S., and Milde, J.J. (1987). The neck motor system of the fly *Calliphora erythrocephala*. *J Comp Physiol A Neuroethol Sens Neural Behav Physiol* 160, 20.

Straw, A.D., Branson, K., Neumann, T.R., and Dickinson, M.H. (2011). Multi-camera real-time three-dimensional tracking of multiple flying animals. *J R Soc Interface* 8, 395-409.

Strother, J.A., Nern, A., and Reiser, M.B. (2014). Direct observation of ON and OFF pathways in the *Drosophila* visual system. *Curr Biol* 24, 976-983.

Strother, J.A., Wu, S.T., Wong, A.M., Nern, A., Rogers, E.M., Le, J.Q., Rubin, G.M., and Reiser, M.B. (2017). The emergence of directional selectivity in the visual motion pathway of *Drosophila*. *Neuron* 94, 168-182 e110.

Suver, M.P., Huda, A., Iwasaki, N., Safarik, S., and Dickinson, M.H. (2016). An array of descending visual interneurons encoding self-motion in *Drosophila*. *J Neurosci* 36, 11768-11780.

Suver, M.P., Mamiya, A., and Dickinson, M.H. (2012). Octopamine neurons mediate flight-induced modulation of visual processing in *Drosophila*. *Curr Biol* 22, 2294-2302.

Sweeney, S.T., Broadie, K., Keane, J., Niemann, H., and O'Kane, C.J. (1995). Targeted expression of tetanus toxin light chain in *Drosophila* specifically eliminates synaptic transmission and causes behavioral defects. *Neuron* 14, 11.

Takemura, S.Y. (2015). Connectome of the fly visual circuitry. *Microscopy (Oxf)* 64, 37-44.

Takemura, S.Y., Bharioke, A., Lu, Z., Nern, A., Vitaladevuni, S., Rivlin, P.K., Katz, W.T., Olbris, D.J., Plaza, S.M., Winston, P., et al. (2013). A visual motion detection circuit suggested by *Drosophila* connectomics. *Nature* 500, 175-181.

Takemura, S.Y., Karuppudurai, T., Ting, C.Y., Lu, Z., Lee, C.H., and Meinertzhagen, I.A. (2011). Cholinergic circuits integrate neighboring visual signals in a *Drosophila* motion detection pathway. *Curr Biol* 21, 2077-2084.

Takemura, S.Y., Nern, A., Chklovskii, D.B., Scheffer, L.K., Rubin, G.M., and Meinertzhagen, I.A. (2017). The comprehensive connectome of a neural substrate for 'ON' motion detection in *Drosophila*. *Elife* 6.

Takemura, S.Y., Xu, C.S., Lu, Z., Rivlin, P.K., Parag, T., Olbris, D.J., Plaza, S., Zhao, T., Katz, W.T., Umayam, L., et al. (2015). Synaptic circuits and their variations within different columns in the visual system of *Drosophila*. *Proc Natl Acad Sci U S A* 112, 13711-13716.

Torre, V., and Poggio, T. (1978). A synaptic mechanism possibly underlying directional selectivity to motion. *Proc R Soc Lond B* 202, 9.

Tuthill, J.C., Nern, A., Holtz, S.L., Rubin, G.M., and Reiser, M.B. (2013). Contributions of the 12 neuron classes in the fly lamina to motion vision. *Neuron* 79, 128-140.

Tuthill, J.C., Nern, A., Rubin, G.M., and Reiser, M.B. (2014). Wide-field feedback neurons dynamically tune early visual processing. *Neuron* 82, 887-895.

Van Hateren, J.H. (1992). Theoretical predictions of spatiotemporal receptive fields of fly LMCs, and experimental validation. *J Comp Physiol A Neuroethol Sens Neural Behav Physiol* 171, 14.

Van Hateren, J.H. (1993). Spatiotemporal contrast sensitivity of early vision. *Vision Res* 33, 257-267.

Vaney, D.I., Sivyer, B., and Taylor, W.R. (2012). Direction selectivity in the retina: symmetry and asymmetry in structure and function. *Nat Rev Neurosci* 13, 194-208.

Varshney, L.R., Chen, B.L., Paniagua, E., Hall, D.H., and Chklovskii, D.B. (2011). Structural properties of the *Caenorhabditis elegans* neuronal network. *PLoS Comput Biol* 7, e1001066.

Venken, K.J., Simpson, J.H., and Bellen, H.J. (2011). Genetic manipulation of genes and cells in the nervous system of the fruit fly. *Neuron* 72, 202-230.

Vinje, W.E., and Gallant, J.L. (2000). Sparse coding and decorrelation in primary visual cortex during natural vision. *Science* 287, 1273-1276.

Wardill, T.J., List, O., Li, X., Dongre, S., McCulloch, M., Ting, C.Y., O'Kane, C.J., Tang, S., Lee, C.H., Hardie, R.C., and Juusola, M. (2012). Multiple spectral inputs improve motion discrimination in the *Drosophila* visual system. *Science* 336, 925-931.

Warrant, E.J. (2016). Sensory matched filters. *Curr Biol* 26, R976-R980.

Wehner, R. (1987). Matched filters - Neural models of the external world. *J Comp Physiol A Neuroethol Sens Neural Behav Physiol* 161, 511-531.

Weir, P.T., Schnell, B., and Dickinson, M.H. (2014). Central complex neurons exhibit behaviorally gated responses to visual motion in *Drosophila*. *J Neurophysiol* 111, 62-71.

Wertz, A., Gaub, B., Plett, J., Haag, J., and Borst, A. (2009). Robust coding of ego-motion in descending neurons of the fly. *J Neurosci* 29, 14993-15000.

White, J.G., Southgate, E., Thomson, J.N., and Brenner, S. (1986). The structure of the nervous system of the nematode *Caenorhabditis elegans*. *Philosophical Transactions of the Royal Society B: Biological Sciences* 314, 1-340.

Wiechert, M.T., Judkewitz, B., Riecke, H., and Friedrich, R.W. (2010). Mechanisms of pattern decorrelation by recurrent neuronal circuits. *Nat Neurosci* 13, 1003-1010.

Wiegert, J.S., Mahn, M., Prigge, M., Printz, Y., and Yizhar, O. (2017). Silencing neurons: Tools, applications, and experimental constraints. *Neuron* 95, 504-529.

Xu, C.S., Hayworth, K.J., Lu, Z., Grob, P., Hassan, A.M., Garcia-Cerdan, J.G., Niyogi, K.K., Nogales, E., Weinberg, R.J., and Hess, H.F. (2017). Enhanced FIB-SEM systems for large-volume 3D imaging. *Elife* 6.

Yamaguchi, S., Wolf, R., Desplan, C., and Heisenberg, M. (2008). Motion vision is independent of color in *Drosophila*. *Proc Natl Acad Sci U S A* 105, 4910-4915.

Yang, H.H., St-Pierre, F., Sun, X., Ding, X., Lin, M.Z., and Clandinin, T.R. (2016). Subcellular imaging of voltage and calcium signals reveals neural processing in vivo. *Cell* 166, 245-257.

Yapici, N., Kim, Y.J., Ribeiro, C., and Dickson, B.J. (2008). A receptor that mediates the post-mating switch in *Drosophila* reproductive behaviour. *Nature* 451, 33-37.

Yonehara, K., Farrow, K., Ghanem, A., Hillier, D., Balint, K., Teixeira, M., Juttner, J., Noda, M., Neve, R.L., Conzelmann, K.K., and Roska, B. (2013). The first stage of cardinal direction selectivity is localized to the dendrites of retinal ganglion cells. *Neuron* 79, 1078-1085.

Yu, J.Y., Kanai, M.I., Demir, E., Jefferis, G.S., and Dickson, B.J. (2010). Cellular organization of the neural circuit that drives *Drosophila* courtship behavior. *Curr Biol* 20, 1602-1614.

Zhang, X., Koolhaas, W.H., and Schnorrer, F. (2014). A versatile two-step CRISPR- and RMCE-based strategy for efficient genome engineering in *Drosophila*. *G3 (Bethesda)* 4, 2409-2418.

Zucker, R.S., and Regehr, W.G. (2002). Short-term synaptic plasticity. *Annu Rev Physiol* 64, 355-405.

## ACKNOWLEDGEMENTS

First and foremost I want to thank my supervisor Axel Borst. Axel has always been able to motivate me during the long phases where there was no progress with my main project. But even more importantly, he has allowed me to work on my ‘pet projects’ on the side (and now even mainly) and completely independently. Axel’s general attitude towards science, paired with his enthusiasm for specific scientific questions, is surely a big factor that makes his lab so pleasant to work in.

This thesis is highly representative of the collaborative environment in our lab. None of the papers would have been possible without the help of several colleagues. Here, I would like to mention especially Armin, Aljoscha, ET and Matthias. Our collaborations started with an all-night patch marathon and culminated in the ‘paper matrix’.

Additionally, I want to thank many other ‘Borstis’ for scientific discussion and help throughout my PhD. Franz, Hubert and Jones for getting started in the lab. Alexander, Bulle and Alex for troubleshooting technical problems, proofreading and sharing their scientific expertise. Michi and Flo as co-fighters in the CDM project. Jesus, Sandra and Liesl for science small talk.

I would also like to thank my ‘mentors’ back from Vienna days, Barry Dickson, Michael Kiebler and Sigi Huck for always supporting me, even long after I have left their labs.

Apart from all the scientific contributions, I am also grateful to many present and former people from the institute for all of the social activities we have done together. Be it the Tuesday soccer sessions, climbing, slacklining, or the uncountable parties, conferences and happy hours.

Lastly, I want to thank my family and Irene for their unconditional support and belief in me.



## LIST OF PUBLICATIONS AND AUTHOR CONTRIBUTIONS

### Manuscript I - A Directional Tuning Map of *Drosophila* Elementary Motion Detectors

Matthew S. Maisak\*, Juergen Haag\*, **Georg Ammer**, Etienne Serbe, Matthias Meier, Aljoscha Leonhardt, Tabea Schilling, Armin Bahl, Gerald M. Rubin, Aljoscha Nern, Barry J. Dickson, Dierk F. Reiff, Elisabeth Hopp, and Alexander Borst

\*equal contribution

**Nature** 500, 212-216. doi: 10.1038/nature12320.

M.S.M. and J.H. jointly performed and, together with A.Bo., evaluated all calcium imaging experiments. **G.A.**, E.S. and M.M. recorded from tangential cells. A.L., T.S. and A.Ba. performed the behavioural experiments. G.R., B.D. and A.N. generated the driver lines and characterized their expression pattern. D.F.R. performed preliminary imaging experiments. E.H. helped with programming and developed the PMT shielding for the two-photon microscope. A.Bo. designed the study and wrote the manuscript with the help of all authors.

### Manuscript II - Functional Specialization of Neural Input Elements to the *Drosophila* ON Motion Detector

**Georg Ammer**\*, Aljoscha Leonhardt, Armin Bahl, Barry J. Dickson, and Alexander Borst\*

\*corresponding authors

**Current Biology** 25, 2247-2253. doi: 10.1016/j.cub.2015.07.014

**G.A.** and A. Borst designed the study. **G.A.** performed electrophysiological experiments and anatomical characterization of expression patterns, analyzed the data, and wrote the manuscript with the help of A. Borst, A.L., and A. Bahl. A.L. and A. Bahl performed behavioral experiments and analyzed data. B.J.D. generated SplitGal4 fly lines and hosted G.A. for characterization of Gal4 lines. A. Borst performed computational modeling.

### Manuscript III - The Temporal Tuning of the *Drosophila* Motion Detectors Is Determined by the Dynamics of Their Input Elements

Alexander Arenz\*, Michael S. Drews\*, Florian G. Richter, **Georg Ammer**, and Alexander Borst

\*equal contribuiton

**Current Biology** 27, 929-944. doi: 10.1016/j.cub.2017.01.051.

A.A., M.S.D., and A.B. conceived the study and designed the experiments. A.A. conducted and analyzed the measurements of T4/T5 cell responses. M.S.D. designed the projector-based stimulation arena and performed and analyzed the measurements of the OFF-pathway elements. F.G.R. performed and analyzed the experiments describing the ON-pathway neurons. **G.A.** performed and analyzed the patch-clamp recordings from lobula plate tangential cells. M.S.D. performed the computer simulations. A.A. wrote the manuscript with the help of all authors.

### Manuscript IV - Asymmetry of *Drosophila* ON and OFF Motion Detectors Enhances Real-World Velocity Estimation

Aljoscha Leonhardt\*, **Georg Ammer**\*, Matthias Meier, Etienne Serbe, Armin Bahl, and Alexander Borst

\*equal contribution

**Nature Neuroscience** 19, 706-715. doi: 10.1038/nn.4262.

A.L., **G.A.** and A. Borst designed the study. A.L. performed behavioral experiments, associated data analysis and all modeling work. **G.A.**, M.M. and E.S. performed electrophysiological

experiments. **G.A.** performed calcium imaging. A.L. and **G.A.** analyzed physiological data. A. Bahl designed the behavioral apparatuses and performed behavioral experiments. A.L. wrote the manuscript with help from all of the authors.

#### **Manuscript V - Object Tracking in Motion-Blind Flies**

Armin Bahl, **Georg Ammer**, Tabea Schilling, and Alexander Borst

**Nature Neuroscience** 16, 730-738. doi: 10.1038/nn.3386.

A. Bahl set up the locomotion recorder and the stimulus display, and wrote the software for reading the behavioral output and displaying the stimulus. A. Bahl and T.S. performed all of the behavioral experiments and evaluated the data. **G.A.** performed the electrophysiological recordings and analyzed the data. A. Bahl and A. Borst designed the study. A. Borst carried out the modeling work. A. Borst and A. Bahl wrote the manuscript with the help of the other authors.

#### **Manuscript VI - Neural Mechanisms for *Drosophila* Contrast Vision**

Armin Bahl, Etienne Serbe, Matthias Meier, **Georg Ammer**, and Alexander Borst

**Neuron** 88, 1240-1252. doi:10.1016/j.neuron.2015.11.004

A.Ba. and A.Bo. designed the study. E.S. and M.M. performed electrophysiological recordings. **G.A.** provided the Mi1, Tm3, and Mi1/Tm3-Gal4 lines and did the immunostainings. A.Ba. built the behavioral setup, programmed the visual stimuli, performed the behavioral experiments, and analyzed the data. A.Ba. wrote the paper with help from the other authors.

#### **Manuscript VII - Preserving Neural Function under Extreme Scaling**

Hermann Cuntz, Friedrich Forstner, Bettina Schnell, **Georg Ammer**, Shamprasad Varija Raghu, and Alexander Borst

**PLoS One** 8, e71540. doi: 10.1371/journal.pone.0071540.

Conceived and designed the experiments: HC FF AB. Performed the experiments: FF BS **GA** SVR. Analyzed the data: HC FF. Wrote the paper: HC FF BS **GA** SVR AB.

I hereby certify that the information above is true and accurate.

.....  
Georg Ammer  
(author)

.....  
Alexander Borst  
(supervisor)

.....  
Aljoscha Leonhardt  
(co-first author manuscript 4)

## **AFFIDAVIT**

### **Eidesstattliche Versicherung/Affidavit**

Hiermit versichere ich, Georg Ammer, an Eides statt, dass ich die vorliegende Dissertation „Functional Dissociation of Neural Circuits for Motion Vision in *Drosophila*“ selbstständig angefertigt habe, mich außer der angegebenen keiner weiteren Hilfsmittel bedient und alle Erkenntnisse, die aus dem Schrifttum ganz oder annähernd übernommen sind, als solche kenntlich gemacht und nach ihrer Herkunft unter Bezeichnung der Fundstelle einzeln nachgewiesen habe.

I hereby confirm that the dissertation “Functional Dissociation of Neural Circuits for Motion Vision in *Drosophila*” is the result of my own work and that I have only used sources or materials listed and specified in the dissertation.

München, den 23. August 2017  
(Munich, date)

.....  
Georg Ammer  
Unterschrift (signature)

